Characterisation of laser-driven radiation beams: Gamma-ray dosimetry and Monte Carlo simulations of optimised target geometry for record-breaking efficiency of MeV gamma-sources

Dissertation
zur Erlangung des Doktorgrades
der Naturwissenschaften

vorgelegt beim Fachbereich Physik
der Johann Wolfgang Goethe - Universität
in Frankfurt am Main

von
Nadiya Zahn
aus Kupyansk, Ukraine

Frankfurt 2022
(D 30)

vom Fachbereich Physik der
Johann Wolfgang Goethe - Universität als Dissertation angenommen.

Dekan:	Prof. Dr. Roger Erb
Gutachter:	Apl. Prof. Dr. Olga Rosmej
	Prof. Dr. Joachim Jacoby
Datum der Disputation:	

“*Fac quod debes facere fiat quod fiet.*”

This thesis is dedicated to the memory
of my beloved grandmother
Valentina.

Abstract

This Ph. D. thesis with the title "Characterisation of laser-driven radiation beams: Gamma-ray dosimetry and Monte Carlo simulations of optimised target geometry for record-breaking efficiency of MeV gamma-sources" is dedicated to the study of the acceleration of electrons by intense sub-picosecond laser pulses propagating in a sub-millimeter plasma with near-critical electron density (NCD) and resulting generation of the gamma bremsstrahlung and positrons in the targets of different materials and thickness.

Laser-driven particle acceleration is an area of increasing scientific interest since the recent development of short pulse, high-intensity laser systems. The interaction of intense high-energy, short-pulse lasers with solid targets leads to the production of high-energy electrons in the relativistic laser intensity regime of more than $10^{18}\,W/cm^2$. These electrons play the leading role in the first stage of the interaction of laser with matter, which leads to the creation of laser sources of particles and radiation. Therefore, the optimisation of the electron beam parameters in the direction of increasing the effective temperature and beam charge, together with a slight divergence, plays a decisive role, especially for further detection and characterisation of laser-driven photon and positron beams.

In the context of this work, experiments were carried out at the PHELIX laser system (Petawatt High-Energy Laser for Heavy Ion eXperiments) at GSI Helmholtz Center for Heavy-Ion Research GmbH in Darmstadt, Germany. This thesis presents a thermoluminescence dosimetry (TLD) based method for the measurement of bremsstrahlung spectra in the energy range from 30 keV to 100 MeV. The results of the TLD measurements reinforced the observed tendency towards the strong increase of the mean electron energy and number of super-ponderomotive electrons. In the case of laser interaction with long-scale NCD-plasmas, the dose caused by the gamma-radiation measured in the direction of the laser pulse propagation showed a 1000-fold increase compared to the high contrast shots onto plane foils and doses measured perpendicular to the laser propagation direction for all used combinations of targets and laser parameters.

In this thesis I present novel characterisation method using a combination of TLD measurements and Monte Carlo FLUKA simulations applicable to laser-driven beams. The thermoluminescence detector-based spectrometry method for simultaneous detection of electrons and photons from relativistic laser-induced plasmas initially developed by Behrens et al. (Behrens et al., 2003) and further applied in experiments at PHELIX laser (Horst et al., 2015) delivered good spectral information from keV

energies up to some MeV, but as it was presented in (Horst et al., 2015) this method was not really suitable to resolve the content of photon spectra above 10 MeV because of the dominant presence of electrons. Therefore, I created new evaluation method of the incident electron spectra from the readings of TLDs. For this purpose, by means of MatLab programming language an unfolding algorithm was written. It was based on a sequential enumeration of matching data series of the dose values measured by the dosimeters and calculated with of FLUKA-simulations. The significant advantage of this method is the ability to obtain the spectrum of incident electrons in the low energy range from 1 keV, which is very difficult to measure reliably using traditional electron spectrometers.

The results of the evaluation of the effective temperature of super-ponderomotive electrons retrieved from the measured TLD-doses by means of the Monte-Carlo simulations demonstrated, that application of low density polymer foam layers irradiated by the relativistic sub-ps laser pulse provided a strong increase of the electron effective temperature from 1.5 - 2 MeV in the case of the relativistic laser interaction with a metallic foil up to 13 MeV for the laser shots onto the pre-ionized foam and more than 10 times higher charge carried by relativistic electrons.

The progressive simulation method of whole electron spectra described with two - temperatures Maxwellian distribution function has been developed and the results of dose simulations were compared with the acquired experimental data. The advanced feature of this method, which distinguishes it from the results of the simulation of the photon spectrum using the interaction with the target of mono-energetic electron beams (Nilgün Demir, 2013; Nilgün Demir, 2019) or the initial electron spectrum expressed as a function of one electron temperature (Fiorini, 2012), is the ability to simulate the initial electron spectrum described by the Maxwellian distribution function with two temperatures.

The important objective of this thesis was dedicated to the study and characterisation of laser-driven photon beams. In addition to this, the positron beams were evaluated. The investigation of bremsstrahlung photons and positrons spectra from high Z targets by varying the target thickness from 10 μm to 4 mm in simulated models of the interactions of electron spectra with Maxwellian distribution functions allowed to define an optimal thickness when the fluences of photons and positrons are maximal. Furthermore based on the results of FLUKA simulations the gold material was found to be the most suitable for the future experiments as $e-\gamma$ target because of its highest bremsstrahlung yield.

Additionally Monte Carlo simulations were performed applying the obtained electron beam parameters from the electron acceleration process in laser-plasma interactions simulated with particle-in-cell (PIC) code for two laser energies of 20 J and 200 J. The corresponding electron spectra were imported into a Monte Carlo code FLUKA to simulate the production process of bremsstrahlung photons and positrons in Au converter. FLUKA simulations showed the record conversion of efficiency in

MeV gammas can reach 10%, which reinforces the generation of positrons. The obtained results demonstrate the advantages of long-scale plasmas of near critical density (NCD) to increase the parameters of MeV particles and photon beams generated in relativistic laser-plasma interaction. The efficiency of the laser-driven generation of MeV electrons and photons by application of low-density polymer foams is essentially enhanced.

Zusammenfassung

Diese Dissertation mit dem Titel "Characterisation of laser-driven radiation beams: Gamma-ray dosimetry and Monte Carlo simulations of optimised target geometry for record-breaking efficiency of MeV gamma-sources" widmet sich der Untersuchung der Beschleunigung von Elektronen durch intensive Sub-Pikosekunden-Laserpulse, die sich in einem Sub-Millimeter-Plasma mit nahezu kritischer Elektronendichte (NCD) ausbreiten und der daraus resultierenden Erzeugung von Gamma-Bremsstrahlung und Positronen in den Targets aus unterschiedlichen Materialien und Dicken.

Die wesentlichen Verbesserungen in der Lasertechnologie während des letzten Jahrzehnts führten zu hohen Laserintensitäten von bis zu $10^{21}\,W/cm^2$. Bereits bei Intensitäten von $10^{18}\,W/cm^2$ ist die Elektronenenergie im Laserfeld vollständig relativistisch, was durch Bremsstrahlungserzeugung zur Erzeugung hochintensiver und -energetischer Gammastrahlen führt. Die laserinduzierten Photonenstrahlen machen den hochintensiven Laser zu einem effektiven Werkzeug zur Untersuchung von Kernreaktionen.

Die lasergetriebene Teilchenbeschleunigung ist seit der letzten Entwicklung hochintensiver Kurzpuls-Lasersysteme ein Bereich von zunehmendem wissenschaftlichem Interesse. Die Wechselwirkung intensiver hochenergetischer Kurzpulslaser mit festen Targets führt zur Erzeugung hochenergetischer Elektronen im relativistischen Laserintensitätsbereich von mehr als $10^{18}\,W/cm^2$. Diese Elektronen spielen die führende Rolle in der ersten Phase der Wechselwirkung von Laser mit Materie, die zur Entstehung von Laserquellen für Teilchen und Strahlung führt. Daher spielt die Optimierung der Elektronenstrahlparameter bei der Erhöhung der effektiven Temperatur und Strahlladung zusammen mit einer geringen Divergenz eine entscheidende Rolle, insbesondere für die weitere Detektion und Charakterisierung von lasergetriebenen Photonen- und Positronenstrahlen.

Im Rahmen dieser Arbeit werden die experimentellen Ergebnisse zur Wechselwirkung relativistischer Sub-Pikosekunden-Laserpulse, die vom PHELIX System erzeugt werden, mit ausgedehnten, sub-mm langen, nahekritischen Elektronendichteplasmen präsentiert. Um die hydrodynamisch stabilen, großflächigen, quasi-homogenen Plasmen zu erzeugen, wurden Polymerschaumschichten niedriger Dichte ($2\,mg/cc$ Triacetate-Cellulose $C_{12}H_{16}O_8$) mit einer Dicke von 300 und $500\,\mu m$ als Targets verwendet. Die Wechselwirkung des relativistischen Laserpulses mit großräumigen NCD-Plasmen gewährleistete einen langen Beschleunigungsweg und sorgte für eine effektive Kopplung der Laserenergie in schnelle MeV-energetische Elektronen und der daraus resultierenden Erzeugung von Gamma-Bremsstrahlung und Positronen in den Targets aus

unterschiedlichen Materialien und Dicken.

Die detaillierte Beschreibung der Verteilung der durch eine Wechselwirkung relativistischer Elektronenstrahlen mit unterschiedlichen Targetmaterialien induzierten Photonenemission und die Definition der Eigenschaften der erzeugten Bremsstrahlungsphotonen wie Energie, Intensität und Winkelverteilung ist sehr wichtig für die Optimierung der Photonenquelle und für die Schätzung der entsprechenden Umwandlungseffizienz der Laserenergie in die Energie von Gammas. Die Intensität der Bremsstrahlung hängt von der Energie der einfallenden Elektronen, der Ordnungszahl (Z) und der Dicke des Strahlermaterials ab. Die Optimierung der High-Z-Targetgeometrie ermöglicht es, eine ultrahohe MeV-Photonenzahl von $\approx 10^{12}$ pro Schuss bei einer moderaten relativistischen Laserintensität von $10^{19}\ W/cm^2$ zu erreichen.

Zur Untersuchung der Erzeugung und Charakterisierung ultrarelativistischer heißer Elektronen, die in unterdichten vorionisierten Schaumtargets beschleunigt werden und der folgenden Wechselwirkungen von Elektronen mit festen Targets, die die Erzeugung hochenergetischer Photonen in Form von Bremsstrahlung induzieren, wurden zwei experimentelle Kampagnen mit dem PHELIX-Laser durchgeführt. Das erste Pilotexperiment **P138** zur Erzeugung ultrarelativistischer heißer Elektronen, die durch den Mechanismus der direkten Laserbeschleunigung (DLA) in vorionisierten Schaumtargets beschleunigt wurden, zeigte einen enormen Anstieg der Gesamtladung und -energie der laserbeschleunigten Elektronen, wie von der Theorie (Pugachev et al., 2016) vorgesagt, der viel höher ist als durch das Gesetz von Wilks definiert (Wilks et al., 1992). Das Ziel des anschließenden Experiments **P176** war die Charakterisierung von MeV-Bremsstrahlungsquellen, die durch die Wechselwirkung von DLA-Elektronen mit Hoch-Z-Konvertertargets entstehen.

In dieser Arbeit wurde ein TLD-Spektrometer basierend auf der Thermolumineszenz-Dosimetriemethode für die Diagnostik in Experimenten mit Hochintensitätslasern eingesetzt. Dieses Spektrometer wurde für einen Energiebereich von 30 keV bis 100 MeV entwickelt und absolut kalibriert. Die als Stapel angeordneten Absorber unterschiedlicher Materialien und Dicken verursachten ein unterschiedliches Ansprechen jedes TLD-Detektors, die dann als Informationen über das Spektrum der einfallenden Strahlenbündel verwendet wurden. Bei der Laserinteraktion mit langskaligen NCD-Plasmen zeigte die in Richtung der Laserpulsausbreitung gemessene Dosis durch die Gammastrahlung eine 1000-fache Erhöhung im Vergleich zu den Hochkontrastschüssen auf ebene Folien (siehe Figure 1) und senkrecht zur Laserausbreitungsrichtung gemessene Dosen für alle verwendeten Kombinationen von Targets und Laserparametern. Die Messungen zeigten auch eine hohe Direktionalität des Beschleunigungsprozesses.

Die Experimente wurden durch Monte-Carlo-Simulationen unterstützt, die das Targetmaterial und die Geometrie des Versuchsaufbaus berücksichtigten. Die Responsefunktionen des TLD-Spektrometers auf monoenergetische Elektronenstrahlung im Energiebereich von 100 keV - 100 MeV wurden unter Verwendung des Monte-Carlo-Codes FLUKA als Dosiswerte in den TLD-Detektoren simuliert, die in einem Stapel

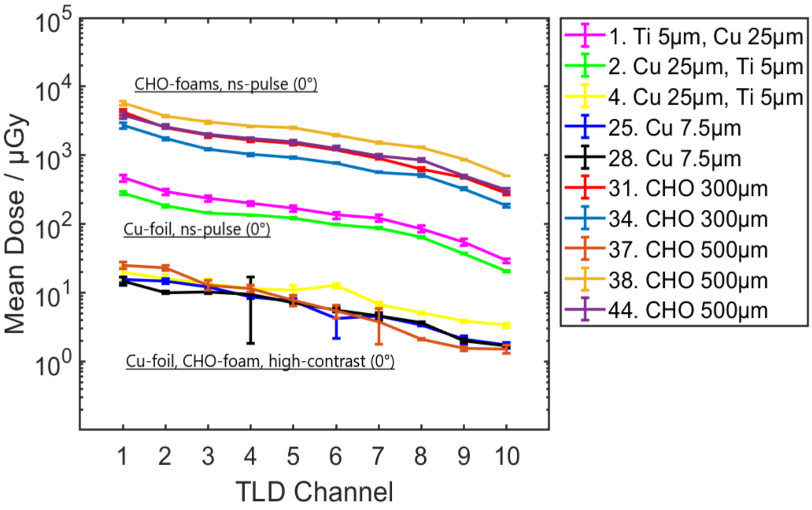

FIGURE 1: Dosisverteilung, gemessen mit dem 10-Kanal-TLD-Spektrometer, das in Richtung der Laserpulsausbreitung für Schüsse bei verschiedenen Bedingungen platziert wurde. Die Schüsse 31, 34, 38, 44 wurden auf präionisiertem Schaum durchgeführt. Schüsse 1, 2 wurden auf vorionisierten Folien gemacht. Die Schüsse 4, 25, 28, 37 wurden bei höchstem Laserkontrast auf Folie oder Schaum durchgeführt.

aus verschiedenen Materialien angeordnet waren. Unterschiedliche Steigungen und Schwellen dieser Responsefunktionen ermöglichten die Durchführung der Rekonstruktion (Entfaltung) der Elektronenspektren. Die Auswertung der Elektronenspektren aus den Messwerten von TLDs wurde in 20 Energiebins aufgelöst und erfolgte unter Anwendung eines Entfaltungsalgorithmus basierend auf einer sequentiellen Aufzählung übereinstimmender Datenreihen der von den Dosimetern gemessenen und mittels FLUKA-Simulationen berechneten Dosiswerte. Es wurde festgestellt, dass die Elektronenverteilungsfunktionen durch zwei Temperatur-Maxwell-Verteilungen beschrieben werden. Die effektive Temperatur von superponderomotorischen Elektronen, die aus den gemessenen TLD-Dosen mit Hilfe der Kombination von Monte-Carlo-Simulationen und Entfaltungsalgorithmen ermittelt wurde, erreichte 11–12 MeV. Figure 2 zeigt die resultierenden Werte von T_{e1} und T_{e2} für ausgewählte Laserschüsse auf verschiedene Targets im Experiment **P138**. Bei der Laserinteraktion mit vorionisierten Schäumen wurde die beste Anpassung aller zehn TLD-Signale für $T_{e1} \simeq 12$ MeV und $T_{e2} \simeq 2 - 5$ MeV erhalten. Die Anwendung von CHO-Schäumen als Targets erhöht wesentlich die Temperatur und Anzahl der in Vorwärtsrichtung beschleunigten Elektronen, was mit der DLA-Skalierung übereinstimmt, während die Temperatur für Elektronen in großen Winkeln zur Laserausbreitungsrichtung mit der ponderomotorischen Skalierung übereinstimmt. Diese Beobachtung der Richtung von in NCD-Plasmen erzeugten superponderomotorischen Elektronen wurde theoretisch vorhergesagt (Pugachev et al., 2016; Pugachev et al., 2019). Bei den Schüssen mit höchstem Laserkontrast betragen beide Elektronentemperaturen $T_{e1} \simeq T_{e2} \simeq 0.5 - 2.5$ MeV. Diese Ergebnisse stellten eine sehr gute Korrelation mit den experimentellen

Bedingungen und mit den Ergebnissen der direkten Messungen durch das Elektronenspektrometer dar (Zaehter, 2020).

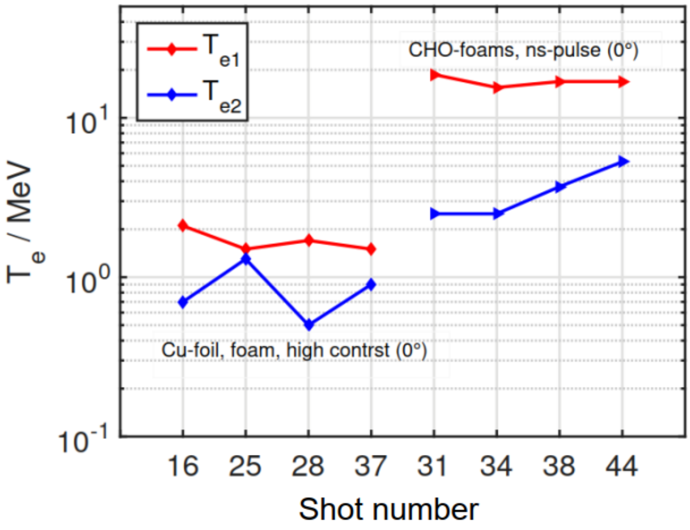

FIGURE 2: Elektronentemperaturen, die aus den gemessenen TLD-Dosen (Experiment **P138**) über den Entfaltungsalgorithmus unter Verwendung von FLUKA-Simulationsergebnissen ausgewertet wurden, die eine reale Geometrie des Versuchsaufbaus und der Umgebung berücksichtigten und eine Zwei Elektronentemperaturen Näherung verwendeten.

Der hochenergetische beschleunigte Elektronenstrahl, der mit einem Targetmaterial mit hohem Z wechselwirkte, erzeugte einen Kaskadenschauer von Bremsstrahlung und die kontinuierlichen Spektren von Photonen, Positronen und Sekundärelektronen. Unter Verwendung des Monte-Carlo-Codes FLUKA wurden die durch die Wechselwirkung der entfalteten Elektronenspektren mit unterschiedlichen Strahlermaterialien erzeugten Bremsstrahlungsspektren und austretenden Elektronen- und Positronenspektren simuliert. Die Photonen-, Elektronen- und Positronenfluenzen wurden aus der Simulation der Wechselwirkung der Elektronenspektren mit Au-Targets unterschiedlicher Dicke erhalten und sind in Figure 3 dargestellt. Das Differential der Energie von Teilchenfluenzen wurde über den Raumwinkel im Bereich der Teilchenausbreitung integriert.

Die Bremsstrahlungsphotonen bieten die Möglichkeit, verschiedene Experimente durchzuführen, wie z. B. die Untersuchung der Kernstrukturen, verschiedener Wechselwirkungsmechanismen und die Entwicklung und Detektion verschiedener Materialien. Daher ist es wünschenswert, dass der Photonenstrahl eine maximale Intensität und einen minimalen Streuwinkel hat. Da die Intensität der Bremsstrahlungsphotonen von der Ordnungszahl Z des Materials, der Dichte und der Materialdicke abhängt, wurde dann durch das Variieren der Targetdicke in simulierten Modellen der Wechselwirkungen von Elektronenspektren mit Maxwellscher Verteilung mit Targets mit hohem Z eine optimale Dicke gefunden, wenn die Photonen- und Positronenflüsse maximal waren. Die in Figure 4 dargestellten Ergebnisse der Monte-Carlo-Simulation zeigten, dass der Photonenfluss den maximalen Wert erreichte, wenn Au oder W mit

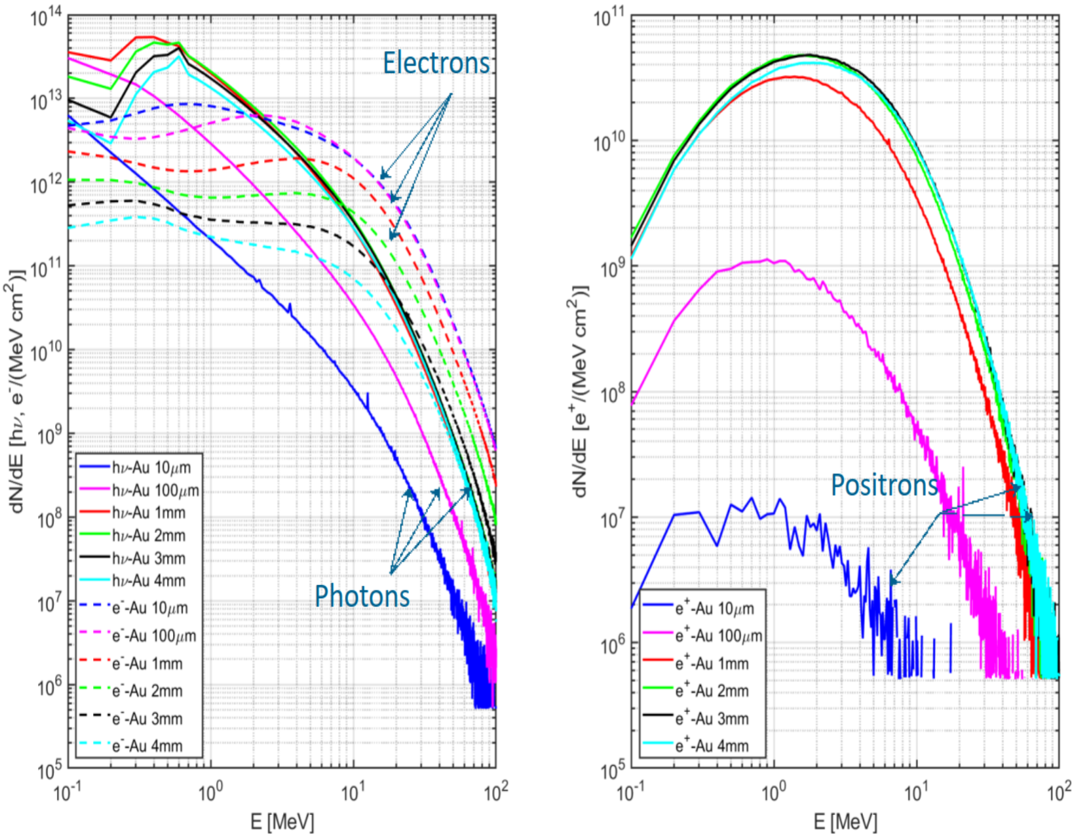

FIGURE 3: Differenzielle Fluenzen von Photonen, Primär- und Sekundärelektronen und Positronen als Funktion der entsprechenden Energie, werden über Raumwinkel 2π in Vorwärtsrichtung integriert und von der Rückseite direkt von Au-Targets von 10 μm, 100 μm, 1 mm, 2 mm, 3 mm, 4 mm Dicke detektiert.

einer Dicke von 1 mm als Strahler-Targets verwendet wurden. Die Experimente mit dem TLD-Spektrometer bestätigten auch das höchste Signal, das mit TLD-Karten gemessen wurde, wenn Au-Folie von 1 mm als Target verwendet wurde. Gemäßden Simulationsergebnissen wurde die effizienteste Erzeugung von Positronen durch die Verwendung von Au- oder W-Targets mit einer Dicke von 2 - 3 mm realisiert.

Die Simulationsergebnisse der Optimierung der High-Z-Targetgeometrie zeigten eine ultrahohe MeV-Photonenzahl von $\approx 5 \cdot 10^{13}$ und eine Positronenzahl von $\approx 10^{11}$ pro Schuss bei moderater relativistischer Laserintensität von $10^{19}\, W/cm^2$. Figure 5 (a) zeigt die Gesamtzahl von Photonen, Elektronen und Positronen von Au-Targets mit einer Dicke von 10 μm, 100 μm, 1 mm, 2 mm, 3 mm, 4 mm. Die Simulationsergebnisse zeigten die Dominanz des Elektronenflusses für dünne Au-Targets von 10 μm, 100 μm Dicke. Die Dominanz der Photonenfluenz wurde für dicke Targets von 1 - 4 mm Dicke erhalten, was durch eine Zunahme der Wechselwirkungslänge im Prozess der Erzeugung von Bremsstrahlungsphotonen erklärt wird. Figure 5 (b) zeigt die Gesamtzahl der Photonen in drei Energieintervallen von $1\, keV - 1\, MeV$, $1\, MeV - 7.5\, MeV$, $7.5\, MeV - 100\, MeV$, die von Au-Targets mit 10 μm, 100 μm,

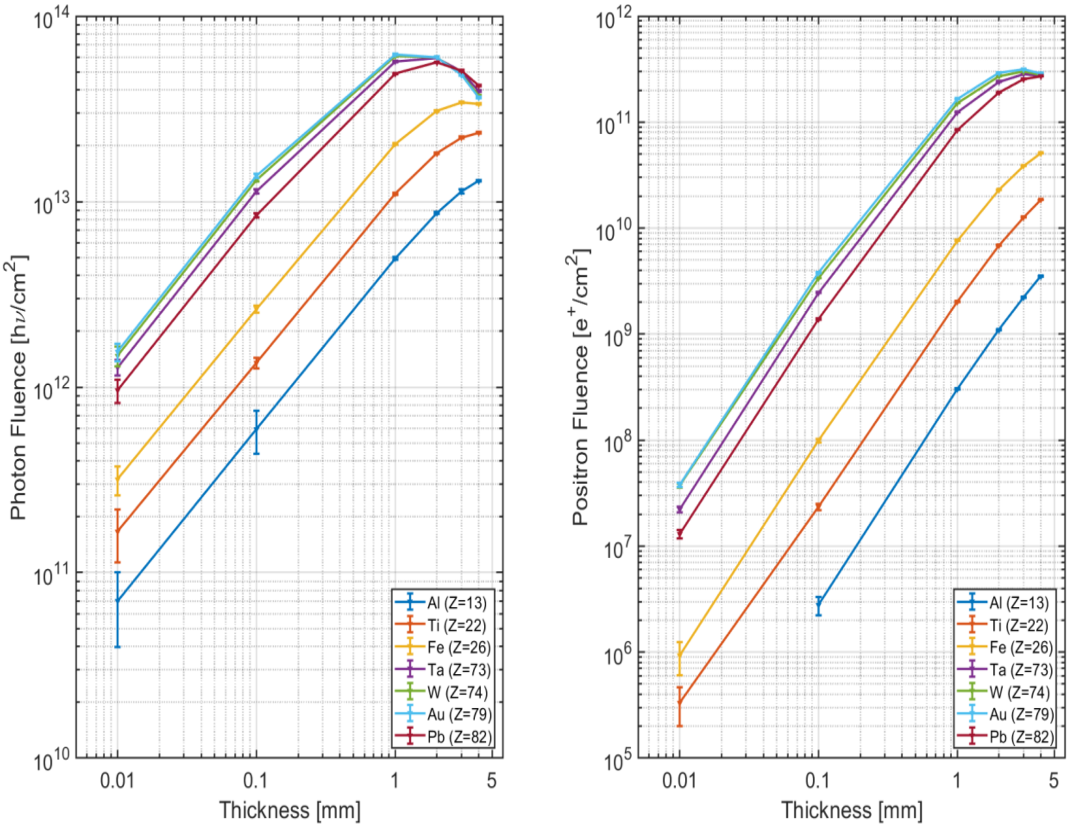

FIGURE 4: Integrierte Fluenzen von Bremsstrahlungsphotonen und Positronen von Al, Ti, Fe, Ta, W, Au, Pb Targets in Abhängigkeit zu Targetdicken von $10\,mm$, $100\,mm$, 1 mm, 2 mm, 3 mm, 4 mm.

1 mm, 2 mm, 3 mm, 4 mm Dicke bestrahlt wurden. Die maximalen Photonenausbeuten mit Energien von $1\,keV - 1\,MeV$ wurden von dem Au-Target mit einer Dicke von 1 mm emittiert, die maximalen Photonenausbeuten mit Energien von $1\,MeV - 7.5\,MeV$ wurden von dem Au-Target mit einer Dicke von 2 mm emittiert und die maximalen Photonenausbeuten mit Energien von $7.5\,MeV - 100\,MeV$ wurden von dem Au-Target mit einer Dicke von $2 - 3$ mm emittiert. Die Erfassung der Anzahl von Photonen innerhalb bestimmter Energieintervalle und die Betrachtung der maximalen Produktion in 2π-Vorwärtsrichtung gibt die Möglichkeit, lasererzeugte Bremsstrahlungsphotonen auf die Initiierung von photonuklearen Reaktionen zu untersuchen. Das Spektrum der erzeugten Gammas ist energetisch breit und reicht bis in den Bereich der Riesendipolresonanz. Somit kann es als Quelle dienen, um ultraschnelle Neutronenstrahlen durch photonukleare Reaktion zu erzeugen. Die Ergebnisse dieser Simulationen können verwendet werden, um die Auswahl der Targetmaterialien und -dicken für die weiteren Laserexperimente zu leiten.

Zusätzlich wurden die mit Particle-in-Cell (PIC)-Code simulierten Elektronenspektrenparameter für zwei Laserenergien von 20 J und 200 J in einen Monte-Carlo-Code FLUKA importiert, um den Produktionsprozess von Bremsstrahlungsphotonen und -positronen in Au-Konvertern zu simulieren um die Ergebnisse der Umwandlungseffizienz der hohen Elektronenenergie in Photonen zu vergleichen. Figure 6 zeigt

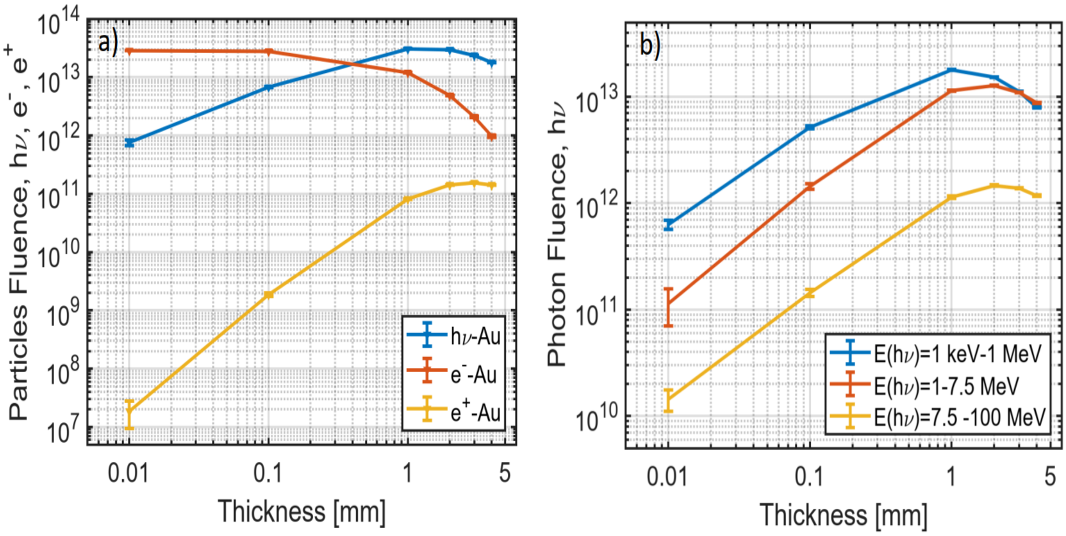

Figure 5: (a) Simulierte Photonenelektronen- und Positronenfluenzen von Au-Targets mit einer Dicke von 10 μm, 100 μm, 1 mm, 2 mm, 3 mm, 4 mm Dicke. (b) Simulierte Photonenfluenzen, aufgeteilt in drei Energieintervalle. Die Anzahl der Photonen, Elektronen und Positronen wurde in Vorwärtsrichtung des 2π Raumwinkels detektiert und durch die Anzahl der anfänglich simulierten Elektronen normiert.

die Umwandlungseffizienz von Laserenergie in Photonenerzeugung durch Elektronenstrahl mit Maxwellscher Energieverteilung auf Au-Targets unterschiedlicher Dicke für 20 J und 200 J Laserenergie. Die Ergebnisse der Simulationen zeigten, dass der Rekord der Konversionseffizienz in MeV-Gammas 10% erreichen kann, was die Erzeugung von Positronen verstärkt. Die weitere Anwendung des vorgeschlagenen robusten Zielschemas, das keine hohe Laserausrichtungsstabilität, keine ultrahohe Laserintensität und keinen hohen Laserkontrast erfordert, ebnet den Weg zu einem neuen Level des diagnostischen Potenzials von PW-Lasern der kJ-Klasse.

Die Ergebnisse der Monte-Carlo-Simulationen zeigen, dass die Wechselwirkung von gezielten relativistischen Hochstromelektronen mit Au-Targets zu einer effektiven Erzeugung von MeV-Bremsstrahlung mit ultrahoher Fluenz führt. Die Simulationen demonstrierten eine extrem hohe Eignung der gezielten relativistischen Hochstrom-Elektronenstrahlen zur Verwendung in neuartigen lasergestützten Anwendungen unter Verwendung bereits bestehender hochenergetischer Sub-PW- und PW-Klasse-Lasersysteme. Dieser Ansatz ist sehr wichtig für Anwendungen, die eine starke Verbesserung der Leistung von Laserquellen für Teilchen und Photonen versprechen.

Zusammenfassend demonstrieren die experimentellen Ergebnisse und die Ergebnisse der numerischen Simulationen, über die in dieser Arbeit berichtet wird, die Vorteile von langskaligen Plasmen nahe der kritischen Dichte (NCD) zur Erhöhung der Parameter von MeV-Partikeln und Photonenstrahlen, die in relativistischer Laser-Plasma-Wechselwirkung erzeugt werden. Die Effizienz der lasergetriebenen Erzeugung von MeV-Elektronen und -Photonen durch Anwendung von Polymerschäumen

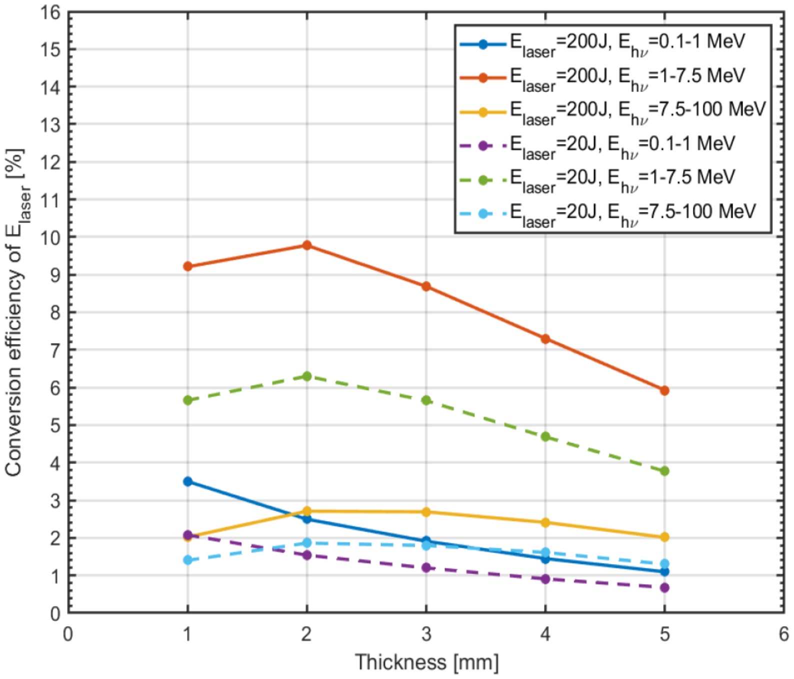

FIGURE 6: Umwandlungseffizienz von Laserenergie in Photonenerzeugung durch Elektronenstrahl mit Maxwellscher Energieverteilung auf Au-Targets unterschiedlicher Dicke für 20 J und 200 J Laserenergie.

mit niedriger Dichte wird wesentlich verbessert. Diese Elektronen sind ein hervorragendes Werkzeug für viele Anwendungen, die eine große Menge an MeV Gammastrahlung in Wechselwirkung mit einem Zielkonverter mit hohem Z erzeugen, der verwendet werden kann, um Gamma-getriebene Kernreaktionen und die Erzeugung von Elektron-Positron-Paaren auszulösen. Dies bringt auch neue Aspekte bezüglich der laserinduzierten Beschleunigung von Elektronen und der Erzeugung von MeV-Gammas in zukünftigen Experimenten.

Contents

List of Abbreviations

CLT	**C**entral **L**imit **T**heorem
CSDA	**C**ontinuous **S**lowing **D**own **A**pproximation
DCS	**D**ifferential **C**ross **S**ection
DLA	**D**irect **L**aser **A**cceleration
EMF	**E**lectro **M**agnetic **F**LUKA
FAIR	**F**acility for **A**ntiprotons and **I**on **R**esearch
FWHM	**F**ull **W**idth at **H**alf **M**aximum
FLUKA	**FLU**ktuierende **KA**skade
GSI	**G**esellschaft für **S**chwer**i**onenforschung
HED	**H**igh **E**nergy **D**ensity
LWFA	**L**aser **W**ake **F**ield **A**cceleration
MC	**M**onte **C**arlo method
MPI	**M**ulti **P**hoton **I**onisation
NCD	**N**ear **C**ritical **D**ensity
PDF	**P**robability **D**istribution **F**unction
PHELIX	**P**etawatt **H**ight-**E**nergy **L**aser for Heavy **I**on e**X**periments
SP	**S**topping **P**ower
TAC, CHO	**Tr**i**a**cetate **C**ellulose $\mathbf{C}_{12}\mathbf{H}_{16}\mathbf{O}_{8}$
TLD	**T**hermo **L**uminescence **D**etector

Physical Constants

Quantity	**Symbol**	= **Value**
Avogadro's number	N_A	$= 6.022\,142 \times 10^{23}\,\mathrm{mol}^{-1}$
Bohr radius	$a_B = \hbar^2/(m_e e^2)$	$= 5.291\,772\,109\,03(80) \times 10^{-11}\,\mathrm{m}$
Boltzmann constant	k_B	$= 1.380\,649 \times 10^{-23}\,\mathrm{J\,K}^{-1}$
Classical electron radius	$r_e = e^2/(m_e c^2)$	$= 2.817\,940 \times 10^{-15}\,\mathrm{m}$
Elementary charge	e	$= 1.602\,176\,634 \times 10^{-19}\,\mathrm{C}$
Electron rest mass	m_e	$= 9.109\,383\,701\,5 \times 10^{-31}\,\mathrm{kg}$
Electron rest energy	$m_e c^2$	$= 0.510\,998\,9\,\mathrm{MeV}$
Planck Constant	h	$= 6.626\,070\,15 \times 10^{-34}\,\mathrm{J\,s}$
Reduced Planck's constant	$\hbar = h/(2\pi)$	$= 1.054\,571\,817 \times 10^{-34}\,\mathrm{J\,s}$
Speed of light in vacuum	c_0	$= 2.997\,924\,58 \times 10^{8}\,\mathrm{m\,s}^{-1}$
Vacuum permittivity	ϵ_0	$= 8.854\,187\,812\,8(13) \times 10^{-12}\,\mathrm{F\,m}^{-1}$

Chapter 1

Introduction

Today femtosecond laser pulses of the relativistic intensities generated by the high power laser systems have significant potential for numerous applications. The relativistic laser-plasma interactions lead to the directed acceleration of electrons and ions. Laser-driven relativistic electron beams are excellent tools for generation of ultrashort multi-MeV photon beams produced via bremsstrahlung radiation of laser accelerated high current beams of energetic relativistic electrons interacting with targets of different materials and thickness (Wang et al., 2020; Norreys, 1999; Hatchet, 2000; Zhu et al., 2020). These ultrashort x-ray and gamma-ray beams are in the same time scale as the laser pulses and can be used as a powerful tool for ultrafast probing of moving object (Ben-Ismail et al., 2011), production of ultra-fast positron (Sarri et al., 2013; Xu et al., 2016; Gu et al., 2019; Zhu et al., 2016; Ridgers, 2012) and neutron sources (Pomerantz, 2014). The laser-driven photon beams can have very small size of $\approx 10\,\mu m$ and high luminosity, which can be used for radiographic studies of dense objects, probing of high energy density matter and non-destructive inspection of manufacturing defects with a resolution of tens of micrometer (Ravasio, 2008; Li et al., 2014). Additionally, laser-driven gamma-ray sources can be applied for nuclear photonics and laser driven nuclear physics (Negoita, 2016; Habs and Köster, 2011; Ma et al., 2019). Gamma rays with energies from 10 to 30 MeV are ideal to initiate photo-nuclear reactions in the giant dipole resonance region, which is conducive to the generation of ultrashort-pulsed neutron source (Pomerantz, 2014), transmutation of radioactive nuclear materials and production of medical isotopes for positron emission tomography (PET) (Li et al., 2017). Another applications can be found in the field of laser driven nuclear and plasma physics (Schlenvoigt et al., 2008; Brambrink et al., 2016; Negoita, 2016; Habs and Köster, 2011; Ma et al., 2019).

Two mechanisms of laser-driven acceleration are very productive for the generation of high energy electrons in near-critical plasmas. The first one is the laser wake field acceleration (LWFA) (Esarey, Schroeder, and Leemans, 2009), when the intense laser pulse drives strong plasma waves that can trap and accelerate electrons. The LWFA works very effectively in very under-dense plasmas and ultra-short laser pulses, shorter than the plasma wavelength. The second mechanism is the direct laser acceleration (DLA) in a plasma channel created by a relativistic laser pulse (Pukhov, Sheng, and Vehn, 1999). In this case, the electron acceleration occurs in the presence of strong quasi-static electric and magnetic fields generated in plasma (Pukhov, Sheng, and Vehn, 1999; Pukhov, 2003). Ponderomotive expulsion of background plasma electrons from the channel caused by a relativistic laser pulse creates a radial electrostatic field and at the same time, the current of accelerated electrons generates the azimuthal magnetic field (Pukhov, 2003; Arefiev A V and M, 2016; Willingale, 2018). The DLA works efficiently in near critical density (NCD) plasmas and for sub-picosecond laser pulses like petawatt high energy laser for ion experiments (PHELIX) at GSI (Bagnoud, 2010). DLA generates electrons with the effective temperature of tens of MeV and Boltzmann-like distributions carrying mega-ampere currents. Interaction of a relativistic sub-ps laser pulses with extended, sub-mm long near critical electron density (NCD) plasmas ensures a long acceleration path of electrons and consequent effective coupling of the laser energy with fast MeV energetic electrons (Rosmej et al., 2019). The interaction of the ponderomotively accelerated electrons in the pre-plasma region with high atomic number Z solid targets resulting in the subsequent deceleration of relativistic electrons in high-Z targets producing continuous MeV-bremsstrahlung radiation. The energy of bremsstrahlung photons can reach the maximum value equal to the energy of the accelerated electrons. The generation of high-energy bremsstrahlung photons allows to investigate laser-induced gamma reactions in different materials resulting in neutron production (Pomerantz, 2014).

The goal of this thesis is to demonstrate the advantages of long-scale plasmas of near critical density (NCD) to increase strongly the parameters of energetic electrons tens of MeV energy and photon beams generated in relativistic laser-plasma interactions. The study of production of bremsstrahlung photons via high intensity laser matter interactions follows three stages: 1. the generation of MeV electrons in the high-intensity laser plasma interactions, 2. conversion of the MeV electrons into MeV photons through the bremsstrahlung process in a high Z solid targets, 3. characterization of the bremsstrahlung spectrum and optimization of conversion efficiency between electrons and photons.

In order to create such type of hydrodynamic stable, large scale, quasi-homogeneous plasmas low density polymer foam layers (Triacetate-Cellulose $C_{12}H_{16}O_8$) of $2\,mg/cm^{-3}$ volume density with a thickness of 300 and 500 μm were used as targets. In this foam target, the sub-mm long NCD-plasma was produced by a mechanism of super-sonic ionization (Gus'kov et al., 2011; Nicolai, 2012) when a well-defined separate ns-pulse was sent onto the foam target forerunning the relativistic main pulse. In the case of fully ionized plasma, it corresponds to $0.64 \cdot 10^{21}\,cm^{-3}$ electron density or $0.64 \cdot n_{cr}$, where $n_{cr} = 10^{21}\,cm^{-3}$ (Rosmej et al., 2019; Rosmej et al., 2020).

The application of sub-mm thick low density foam layers provided a substantial increase of the electron acceleration path in a NCD-plasma compared to the case of freely expanding plasmas created in the interaction of the ns-laser pulse with solid foils. The performed experiments on the electron heating by a 100 J, 750 fs short laser pulse of $2-5 \cdot 10^{19}\,W/cm^2$ intensity demonstrated that the effective temperature of supra-thermal electrons increased from 1.5–2 MeV in the case of the relativistic laser interaction with a metallic foil at high laser contrast up to 13 MeV for the laser shots onto the pre-ionized foam. The observed tendency towards a strong increase of the mean electron energy and the number of ultra-relativistic laser-accelerated electrons was reinforced by the results of gamma-yield measurements that showed a 1000-fold increase of the measured doses. The thermoluminescence dosimetry based method was used for the measurement of bremsstrahlung spectra in the energy range from 30 keV to 100 MeV in ultrashort pulsed radiation fields generated during operation of the PHELIX laser (Rosmej et al., 2019).

Additionally the experiments were supported by Monte-Carlo FLUKA simulations, which considered the target material and the geometry of the experimental set-up. Both, measurements and simulations showed a high directionality of the acceleration process, since the strongest increase in the electron energy, charge and corresponding gamma-yield was observed close to the direction of the laser pulse propagation. The charge of super-ponderomotive electrons with energy above 30 MeV reached a very high value of 78 nC (Rosmej et al., 2019).

The detailed description of the distribution of the photon emission induced by an interaction of relativistic electron beams with different target materials and definition of the characteristics of the produced bremsstrahlung photons such as energy, intensity and angular distribution is very important for optimization of the photon source and estimation of the corresponding conversion efficiency of the laser energy into the energy of gammas. The intensity of bremsstrahlung depends on the energy of the incoming electrons, the atomic number (Z) and the thickness of the radiator material. The optimization of the high-Z target geometry allows to reach an ultra-high MeV photon number of $\approx 10^{12}$ per shot at moderate relativistic laser intensity of $10^{19}\, W/cm^2$.

In this thesis I present novel characterisation method using a combination of TLD measurements and Monte Carlo FLUKA simulations applicable to laser-driven beams. The thermoluminescence detector-based spectrometry method for simultaneous detection of electrons and photons from relativistic laser-induced plasmas initially developed by Behrens et al. (Behrens et al., 2003) and further applied in experiments at PHELIX laser (Horst et al., 2015) delivered good spectral information from keV energies up to some MeV, but as it was presented in (Horst et al., 2015) this method was not really suitable to resolve the content of photon spectra above 10 MeV because of the dominant presence of electrons. Therefore, I created new evaluation method of the incident electron spectra from the readings of TLDs. For this purpose, by means of MatLab programming language an unfolding algorithm was written. It was based on a sequential enumeration of matching data series of the dose values measured by the TLD dosimeters and calculated by means of Monte Carlo FLUKA simulations. The significant advantage of this method is the ability to obtain the spectrum of incident electrons in the low energy range from 1 keV, which is very difficult to measure reliably using traditional electron spectrometers. This method gives the additional information for the investigation of the electron spectra characteristics.

The results of the evaluation of the effective temperature of super-ponderomotive electrons retrieved from the measured TLD-doses by means of the Monte-Carlo simulations demonstrated, that application of low density polymer foam layers irradiated by the relativistic sub-ps laser pulse provided a strong increase of the electron effective temperature from 1.5-2 MeV in the case of the relativistic laser interaction with a metallic foil up to 13 MeV for the laser shots onto the pre-ionized foam and more than 10 times higher charge carried by relativistic electrons (Rosmej et al., 2019).

The progressive simulation method of whole electron spectra described with two - temperatures Maxwellian distribution function has been developed and the results of dose simulations were compared with the acquired experimental data. The advanced feature of this method, which distinguishes it from the results of the simulation of the photon spectrum using the interaction with the target of mono-energetic electron beams (Nilgün Demir, 2013; Nilgün Demir, 2019) or the initial electron spectrum expressed as a function of one electron temperature (Fiorini, 2012), is the ability to simulate the initial electron spectrum described by the Maxwellian distribution function with two temperatures.

The important objective of this thesis was dedicated to the study and characterisation of laser-driven photon beams. In addition to this, the positron beams were evaluated. The investigation of bremsstrahlung photons and positrons spectra from high Z targets by varying the target thickness from 10 μm to 4 mm in simulated models of the interactions of electron spectra with Maxwellian distribution functions allowed to define an optimal thickness when the fluences of photons and positrons are maximal. Furthermore based on the results of FLUKA simulations the gold material was found to be the most suitable for the future experiments as $e-\gamma$ target because of its highest bremsstrahlung yield.

Additionally Monte Carlo simulations were performed applying the obtained electron beam parameters from the electron acceleration process in laser-plasma interactions simulated with particle-in-cell (PIC) code for two laser energies of 20 J and 200 J. The corresponding electron spectra were imported into a Monte Carlo code FLUKA to simulate the production process of Bremsstrahlung photons and positrons in Au converter. FLUKA simulations showed the record conversion of efficiency in MeV gammas can reach 10%, which reinforces the generation of positrons. The obtained results demonstrate the advantages of long-scale plasmas of near critical density (NCD) to increase the parameters of MeV particles and photon beams generated in relativistic laser-plasma interaction. The efficiency of laser-driven generation of MeV electrons and photons by application of low-density polymer foams is essentially enhanced.

The results of the numerical simulations allowed to conclude that interaction of high-current well-directed relativistic electrons with Au targets leads to effective production of MeV bremsstrahlung radiation with the ultra-high fluence. The simulations demonstrated an extremely high capability of the well-directed high-current relativistic electron beams to be used in novel laser assisted applications using already existed high-energy sub-PW and PW-class laser systems. This approach is very important for applications that promise a strong improvement in the performance of laser sources of particles and photons.

The structure of this thesis is organised as following:

- Introduction Chapter 1
- Chapter 2 gives theoretical overview to the physics of the interaction of relativistic laser with matter. The description of the laser propagation in vacuum, interaction of a single electron with the electro-magnetic wave and the occurrence of laser-plasma ionisation processes is presented. The theory of the interaction of electromagnetic waves with plasma and mechanisms of the electron acceleration in plasma also discussed in this chapter.
- Chapter 3 describes in detail the interaction of electromagnetic radiation with matter. The discussions about photon and electron interactions are presented.
- Chapter 4 presents a general theory and a review of a thermoluminescence dosimetry based method for measurements of bremsstrahlung spectra in the energy range from 1 keV to 100 MeV. The thermoluminescence dosimetry method was applied at the PHELIX laser experiments P138 and P176.
- Chapter 5 describes the experimental facilities at the PHELIX laser system that was used for the experiments. Brief descriptions of the experimental device and the applied TLD diagnostic techniques are given. Additionally the selection of the target materials is discussed.
- Chapter 6 presents the obtained results of the dose measurements with TLD spectrometer. Comparison of the experimental results acquired outside of the vacuum chamber (in experiment P138) and experimental results acquired inside of the vacuum chamber (in experiment P176) under different types of target materials are presented. These results demonstrated a 1000-fold increase of the measured doses in the case of the relativistic laser interaction with pre-ionized foam. Moreover the achieved experimental results showed the dependence on different experimental parameters as target material and thickness, pre-pulse duration, laser-pulse intensity and emission angle. The profound effect of these parameters on the electron acceleration demonstrated high directionality of the acceleration process, the strong increase in the electron energy, charge and corresponding gamma-yield.
- Chapter 7 describes the Monte Carlo method for calculations of radiation interactions and particle transport implemented in computer code FLUKA. The specific details of the Monte Carlo simulations are presented. The FLUKA code was used for production and transport of lectrons, photons and positrons

through different targets. The simulations are very important in order to obtain information about particles produced in electron interactions with matter.

- Chapter 8 deals with the study and characterization of Bremsstrahlung radiations from different target materials of low Z (Titanium $Z = 22$) to high Z (Gold $Z = 79$, Lead $Z = 82$) elements and the exact analysis of bremsstrahlung spectra and spectra of released electrons and positrons. Simulations of Monte Carlo code FLUKA provided the results of bremsstrahlung photons, electrons and positrons fluences from target surfaces of various thicknesses. Additionally the response functions of the TLD spectrometers to mono-energetic electron beams were simulated for the deconvolution of the electron spectra from the measured dose readings of the dosimeters. Using an unfolding algorithm based on a sequential enumeration of matching data series the electron spectra were calculated for all variants of targets that were used in the experiments. This method has been also validated with the cross checking simulations of the TLD dose values.

- Chapter 9 presents the results of FLUKA Simulations of laser driven photon, electron and positron spectra. Varying the target thickness in simulated models of the interactions of electron spectra with Maxwellian distribution with high Z targets, an optimal thickness has been defined that the photon beam has a maximal intensity and minimal scattering angle.

- Chapter 10 describes the enhancement of efficiency of laser-driven generation of MeV particles and photon beams and demonstrates the advantages of long-scale plasmas of near critical density (NCD) to increase parameters of MeV particles and photon beams generated in relativistic laser-plasma interaction. The high energy electrons are an excellent tool for many applications producing vast amount of MeV gamma radiation in interaction with high Z target-convertor. The convertor can be used to trigger gamma-driven nuclear reactions and electron-positron pair production. In this chapter, electron acceleration process in laser-plasma interactions was simulated with particle-in-cell (PIC) code for two laser energies of 20 J and 200 J, and the obtained electron beam parameters were imported into a Monte Carlo code FLUKA to simulate the production process of Bremsstrahlung photons and positrons in Au converter. Monte Carlo FLUKA simulations show the record conversion of efficiency in MeV gammas can reach 10%, which reinforces the generation of positrons. Application of proposed robust target scheme, which does not require a high laser pointing stability, an ultra-high laser intensity and a high laser contrast, paves the way to a new level of diagnostic potential of kJ-class PW laser facilitates.

- Finally, Chapter 11 summarises this work and gives the general conclusions of the performed investigations of laser-plasma interactions.

- Appendix A presents FLUKA input file used for simulations of the interactions of the electron beam with different targets.
- Appendix B gives the results of simulations of electrons, positrons, and bremsstrahlung photons fluences from different target materials.

Chapter 2

Interaction of Relativistic Laser with Matter

The interaction of ultra-shot relativistic laser pulses having intensities higher then $10^{18}\,\mathrm{W/cm^2}$ with extended, sub-mm long near critical electron density (NCD) plasmas induces a long acceleration path of electrons and consequent effective coupling of the laser energy into fast MeV energetic electrons. A big fraction of the energy of the laser pulse with relativistic intensity is transferred into kinetic energy of relativistic electrons, which are accelerated to velocities close to the speed of light by the oscillating electric field of laser wave, while the magnetic field changes the electron direction from transversal (along electric field, where electrons get accelerated) to longitudinal (along laser axis) one. The enormous increase of total charge and energy of the laser-accelerated electrons was predicted by the theory (Pugachev et al., 2016) and confirmed experimentally (Rosmej et al., 2019; Rosmej et al., 2020). This chapter gives a brief introduction into the physics of the interaction of a laser pulse of relativistic intensity with matter. The first sections introduce the mechanism of the interaction of electromagnetic wave with a single electron. Then the interaction of the laser with plasma and different processes of electron acceleration are described.

2.1 Description of the Laser Propagation in Vacuum

The laser-light wave is an electromagnetic wave which is a combination of an alternating electric $\vec{E}$ and magnetic $\vec{B}$ fields propagating in space and varying with the same frequency. Both fields are perpendicular to each other and to the propagation direction. The propagation direction of the electromagnetic wave is expressed by the wave vector $\vec{k}$. The electromagnetic field of the laser is described by the Maxwell's equations. A linear polarized in $\vec{e}_x$ direction plane electromagnetic wave propagating in $\vec{e}_z$-direction can be described by its vector potential $\vec{A}(z,t)$, that varies only in space z and time t

$$\vec{A} = \vec{e}_x \cdot A_0 sin(kz - \omega_L t), \tag{2.1}$$

where ω_L is the angular frequency of the laser, $\omega_L/2\pi$ is the laser frequency, $k = 2\pi\eta_r/\lambda_L$ is the wave number, η_r is the refractive index, $\lambda_L = 2\pi c/\omega_L$ is the laser wave length in vacuum and c is the speed of light. The refractive index in a vacuum is $\eta_r = 1$. In the absence of electrostatic potential $\Phi_{el} = 0$ in the vacuum and with the Coulomb gauge $\vec{\nabla} \cdot \vec{A} = 0$, then the electric $\vec{E}_L$ and magnetic $\vec{B}_L$ fields of the laser can be expressed as

$$\vec{E_L} = -\frac{\partial \vec{A}}{\partial t} = \vec{E_0} cos(kz - \omega_L t), \quad \vec{E_0} = \vec{e_x} \cdot \omega_L A_0, \tag{2.2}$$

$$\vec{B_L} = -\vec{\nabla} \times \vec{A} = \vec{B_0} cos(kz - \omega_L t), \quad \vec{B_0} = \vec{e_y} \cdot k A_0 = \vec{e_y} \frac{\eta_r E_0}{c}. \tag{2.3}$$

In experiments using high-intensity lasers the key parameter describing laser interactions is the laser intensity. It is defined as the absolute value of the Poynting vector $\vec{S_L}$, temporally averaged over a single period $T_L = 2\pi/\omega_L$ of the fast oscillation of the laser field:

$$(2.4) I_L = \langle |\vec{S_l}| \rangle_T = \frac{1}{\mu_o} \langle |\vec{E_L} \times \vec{B_L}| \rangle_T =$$

$$(2.5) \qquad = \frac{E_0 B_0}{\mu_o} \frac{1}{T_L} \int_0^{T_L} [cos(kz - \omega_L t)]^2 dt = \frac{E_0 B_0}{2\mu_o} = \frac{c^2 \epsilon_0}{2} E_0 B_0 = \frac{c \epsilon_0}{2} E_0^2,$$

where ϵ_0 is the permittivity of the vacuum and μ_o is the permeability of the vacuum, which are connected with the speed of light c by the relation $\epsilon_0 \mu_o = \frac{1}{c^2}$.
In order to reach peak intensities, it is necessary to concentrate as much light energy in a short time in as small area as possible. During experiments the quantities of the laser energy E_L, its distribution in space within a certain area A_{focus}, and the pulse duration τ_L can be measured in order to evaluate the laser intensity

$$I_L = \frac{E_L}{\tau_L \cdot A_{focus}} = \frac{P_L}{A_{focus}}, \tag{2.6}$$

where the laser power P_L for a Gaussian pulse in time is expressed as

$$P_L = 2\sqrt{\frac{\ln(2)}{\pi}} \frac{E_L}{\tau_L} \approxeq \frac{E_L}{\tau_L}, \tag{2.7}$$

Therefore, the peak intensity can be calculated from the measurements of energy, duration, and spot size, when the shape of the laser beam is known (Cros, 2016; Saleh and Teich, 2007; Kaluza, 2004). Due to the usually high spatial coherence of lasers, the energy can be focused on very small areas. Nevertheless, the minimum focus size is limited to the order of λ_L^2 (Kneubühl and Sigrist, 2005). For a laser with a wavelength of $\lambda_L = 1053 nm$, this corresponds to a minimum focus of approximately $1.1 \mu m^2$.

2.2 Interaction of a Single Electron with a Plane Electro Magnetic Wave

The relativistic description of motion of a single electron with charge $-e$ and the rest mass m_e in the electric $\vec{E}$ and magnetic $\vec{B}$ fields is expressed by the Lorentz equation of motion

$$\vec{F_L} = \frac{d\vec{p}}{dt} = \frac{d}{dt}(\gamma_e m_e \vec{v_e}) = -e\left(\vec{E} + \vec{v_e} \times \vec{B}\right), \tag{2.8}$$

where $\vec{p}$ and $\vec{v_e}$ are the electron momentum and velocity, γ_e is the relativistic Lorentz factor $\gamma_e = 1/\sqrt{1-\beta^2} = 1/\sqrt{1-v_e^2/c^2} = \sqrt{1+(p/m_e c)^2}$, and $\beta = v_e/c$ defines the normalized velocity. The kinetic energy of the electron is given by

$$E_{kin} = (\gamma_e - 1)m_e c^2. \tag{2.9}$$

The temporal evolution of the kinetic energy depends only on the electric field and the electron velocity

$$\frac{dE_{kin}}{dt} = -e\vec{v_e} \cdot \vec{E}. \tag{2.10}$$

In the non-relativistic regime, when $\beta \ll 1$ and $\gamma_e \approx 1$, the electron motion is mostly regulated by the electric field. The magnetic field is by a factor of v/c smaller and in the first order can be neglected. Then the equation 2.8 becomes simply

$$\frac{d\vec{p}}{dt} = -e\vec{E} = e\frac{\partial \vec{A}}{\partial t}. \tag{2.11}$$

Integrating this equation of motion for initial conditions of the electron at rest $z_0 = 0$, $x_0 = 0$ and $v_0 = 0$, it delivers the solution for electron velocity $\vec{v_e} = \vec{e_x}\frac{eE_0}{\omega_L m_e} sin(kz - \omega_L t)$ and the displacement $x = \frac{eE_0}{\omega_L^2 m_e}(cos(kz - \omega_L t) - 1)$. Therefore, in the analytically simple case of a planar, infinitely extended electrical wave the electron undergoes harmonic phase-shifted oscillations with amplitudes $x_0 = \frac{eE_0}{\omega_L^2 m_e}$ and $v_0 = \frac{eE_0}{\omega_L m_e}$ in the direction of the electric field.

It is common to define a normalized vector potential, also called the laser strength as the ratio of the velocity amplitude v_0 and c

$$a_0 = \frac{eE_0}{\omega_L m_e c} = \frac{eA_0}{m_e c}. \tag{2.12}$$

The normalized vector potential a_0 determines the mode of interactions of laser light with matter. When $a_0 \ll 1$ the electron motion is in non-relativistic, classical regime. When $a_0 \approx 1$ the electron velocity reaches the speed of light, the classical description is not valid and the electron motion is fully relativistic. When $a_0 \gg 1$ the regime of electron motion is ultra-relativistic. The amplitudes of electric and magnetic fields

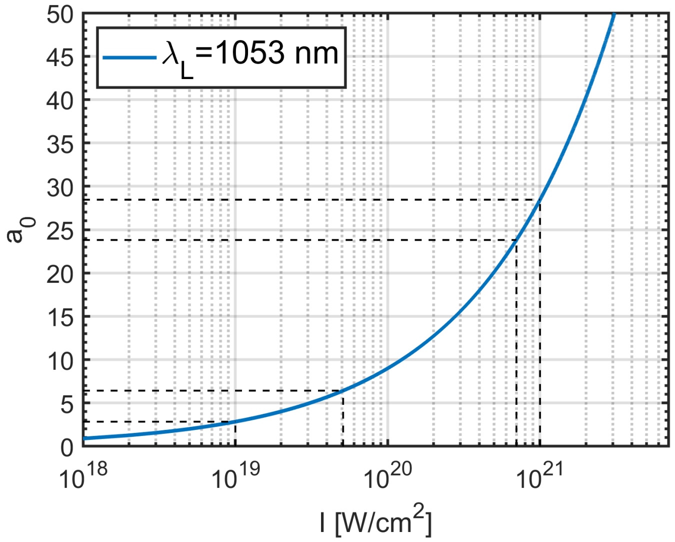

FIGURE 2.1: Representation of the normalized vector potential. The dashed lines show the ranges of the operating modes of the PHELIX laser intensity.

and the laser intensity can be expressed in terms of a_0 and $\lambda_L = \frac{2\pi c}{\omega_L}$ as

$$E_0 = \frac{a_0}{\lambda_L} \cdot 3.21 \times 10^{12} \frac{V}{m} \cdot \mu m \tag{2.13}$$

$$B_0 = \frac{a_0}{\lambda_L} \cdot 1.07 \times 10^{4} T \cdot \mu m \tag{2.14}$$

$$I_L = \frac{a_0^2}{\lambda_L^2} \cdot 1.37 \times 10^{18} \frac{W}{cm^2} \cdot \mu m^2 \tag{2.15}$$

For the wave length of the PHELIX laser of $\lambda_L = 1053nm$ the normalized vector potential is $a_0 = 1$ when laser intensity is of $I_L = 1.24 \cdot 10^{18} \frac{W}{cm^2}$. In experiments performed at the PHELIX laser and described further in this thesis, the laser operated in two regimes of laser intensities $(1 - 5.1) \cdot 10^{19} \frac{W}{cm^2}$ and $(7 - 10) \cdot 10^{20} \frac{W}{cm^2}$. This leads to a normalized vector potential of $a_0 = 2.8 - 6.4$ and $a_0 = 23.8 - 28.4$ correspondingly. The results of the calculated normalized vector potential for different regimes of the PHELIX laser are shown in Figure 2.1. In the relativistic regime, the solution of the equation of motion 2.8 leads to different results compared to the classical case. The spatial components of the electron trajectory are:

$$x = \frac{c}{\omega_L} a_0 \left(1 - cos\Phi\right), \tag{2.16}$$

$$y = 0, \tag{2.17}$$

$$z = \frac{c}{\omega_L} \frac{a_0^2}{4} \left(\Phi - \frac{1}{2} cos(2\Phi)\right), \tag{2.18}$$

where $\Phi = kz - \omega_L t$. Since the x component is identical to the classical case, the electron is pushed forward in laser direction for $a_0 \geq 1$. This forward motion is a drift in laser direction with the velocity

$$\vec{v_D} = \frac{a_0^2}{4 + a_0^2} c \cdot \vec{e}_z. \tag{2.19}$$

For $a_0 \rightarrow \infty$ the drift velocity $v_D \rightarrow c$. The oscillation of the electron in longitudinal $\vec{e}_z$ direction scales with the square of the laser strength as a_0^2, while the transverse oscillation in $\vec{e}_x$ direction linearly depends on the laser strength as a_0. Hence, for $a_0 \gg 1$, the longitudinal motion of the electron dominates the transverse oscillation, that make the shape of "figure 8" motion of the electron with v_D as it is shown in Figure 1.2. The electron velocity is always positive in the z direction, the $\vec{v} \times \vec{B}$ part of the Lorentz force accelerates the electron in forward direction during laser pulse. But, when the laser pulse of finite duration is over the electron stops. It does not gain energy from the laser. The overall net energy effect is only to transfer the electron to a new longitudinal position. In experiments, where laser pulses are tightly focused to achieve high intensity, the laser intensity is not uniform but Gaussian-like in the transverse plane. The ponderomotive force associated with the laser intensity gradient excites a plasma wave, as the plasma plays the role of a transformer, to transfer laser energy to electrons (Cros, 2016).

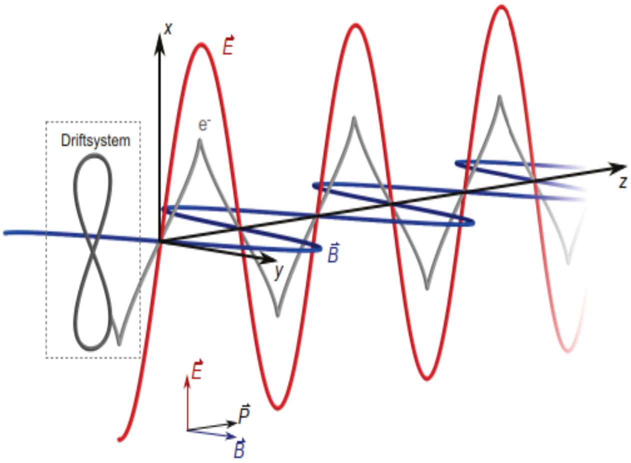

FIGURE 2.2: Drift of the free electron in a plane electromagnetic wave (Königstein, 2013).

2.2.1 The Ponderomotive Force

A ponderomotive force $\vec{F}_{pond}$ is a nonlinear force that a charged particle experiences in an inhomogeneous oscillating electromagnetic field. The particle moves towards the area of the weaker field strength, rather than oscillating around its initial point as in a case of a homogeneous field. This occurs since the particle sees a greater magnitude of force during the half of the oscillation period while it is in the area with the stronger field. The net force during its period in the weaker area in the second half of the oscillation does not compensate the net force in the first half of the oscillation. Therefore, this makes the particle move towards to the area of smaller force over a complete cycle (Freeman, Bucksbaum, and McIlrath, 1988; Burton et al., 2017). The ponderomotive force of the laser acting on the electron is expressed by the following equation

$$\vec{F}_{pond} = -\frac{e^2}{4m_e\omega_L^2}\vec{\nabla}(\vec{E}_0^2(\vec{r},t)). \tag{2.20}$$

The relativistic description of the ponderomotive force is

$$\vec{F}_{pond} = -\frac{e^2}{4\langle\gamma_e\rangle m_e\omega_L^2}\vec{\nabla}(\vec{E}_0^2(\vec{r},t)), \tag{2.21}$$

where $\langle\gamma_e\rangle$ is the Lorentz faktor averaged over the fast oscillations of the laser field. Using the relation $\vec{F}_{pond} = -\vec{\nabla}\varphi_{pond}$ between a conservative force and the associated potential the ponderomotive potential is expressed as

$$\varphi_{pond} = \frac{e^2}{4m_e\omega_L^2}\vec{E}_0^2. \tag{2.22}$$

If the ponderomotive potential is not spatially constant, the electron can gain the kinetic energy of the ponderomotive potential of its initial starting position which is the laser axis where the amplitude of the spatially depending electric field is the peak electric field of the focussed laser pulse. In the relativistic case the equation for the ponderomotive potential is

$$\varphi_{pond} = \frac{e^2}{4\langle\gamma_e\rangle m_e\omega_L^2}\vec{E}_0^2. \tag{2.23}$$

The electron can be ejected from high-intensity region of the laser focus of finite diameter, which is comparable to or smaller than the amplitude of the electron's quiver motion. It leaves the focus under an angle θ to the laser axis with a finite velocity by ponderomotive scattering. Since the electron starts on the laser axis, where the fields are maximal, it will be displaced sideways during the first laser-half cycle into regions of reduced intensity. Thus, the restoring force acting on the electron is smaller, when the fields change the sign. Hence, it does not return to its initial position in the next laser-half period, and finally leaves the focus with a finite velocity (Kaluza, 2004; Hartemann et al., 1995; Hartemann et al., 1998). The scattering angle θ is determined by the ratio of transversal and longitudinal momentum of the electron (Hartemann et al., 1995)

$$\theta = \arctan\left(\frac{p_x}{p_z}\right) = \arctan\left(\sqrt{\frac{2}{\gamma_e - 1}}\right). \tag{2.24}$$

This equation has been proved by experimental observations of the scattering of single electrons from the laser focus by Moore et al. (Moore, Knauer, and Meyerhofer, 1995). The relations derived in this section describe the interaction of a single electron with the electromagnetic fields of a laser pulse. A focussed laser pulse was described by a plane wave. Any electrostatic potentials arising from laser-induced charge separations during the interaction of the laser with a plasma have been neglected. But the situation will be different, when such effects are taken into account. The collective effects of a large number of plasma electrons interacting with an intense laser pulse give rise to strong electric fields that vary on the time scale of the pulse duration and not of the laser period. On these much longer time scales, also the ions in the plasma can be accelerated to MeV-energies. The basic properties of a plasma and collective effects of the plasma electrons will be described in the next section.

2.3 Laser-Plasma Ionisation Processes

Plasmas are created via ionization of matter, which can occur through different mechanisms: through collisions of fast particles with atoms, through photoionization by electromagnetic radiation, or via electrical breakdown in strong electric fields. The last two are examples of *field ionization.* When an intense laser pulse is focused on the matter, it can get ionized via different ionization mechanisms depending on the laser parameters of intensity, wavelength and pulse duration, the amount of laser energy, which has to be transferred from the laser to the bound electrons of the target as well as the nature of the target. The field ionization occurs at the typical field strength required to detach electrons from the hydrogen atom

$$E_a = \frac{e}{4\pi\epsilon_0 a_B^2} \simeq 5.1 \cdot 10^9 \frac{V}{cm}, \tag{2.25}$$

where a_B is the Bohr radius

$$a_B = \hbar^2/(m_e e^2) = 5.29 \cdot 10^{-9} cm. \tag{2.26}$$

Therefore, the threshold of the atomic intensity can be expressed as

$$I_a = \frac{\epsilon_0 c E_a^2}{2} \simeq 3.51 \cdot 10^{16} \frac{W}{cm^2} \tag{2.27}$$

When the laser intensity is $I_L > I_a$ then the laser is able to ionize a target material. Hence, the ionization occurs if the laser has an electric field of the order of magnitude of the Coulomb field of an atom. The atom is directly ionised by a single photon with enough energy to detach the electron out of the electron shell. This process is called *optical field ionization.* However ionization can also occur below this threshold due to the mechanism of *multi-photon ionization* (MPI) (Gibbon, 2005). MPI describes the transition of a bound electron to a free state due to the absorption of multiple photons with an energies below the ionization threshold when the photons can combine their energies to ionize an atom. The ionisation rate Γ_N is expressed by the equation

$$\Gamma_N = \sigma_N I_L^N, \tag{2.28}$$

where N is the number of photons involved in a single ionisation process, σ_N is the generalised cross-section and I_L is the laser intensity (Protopapas, Keitel, and Knight, 1997). Due to the decrease in the cross-sections with an increasing number of photons N, the MPI only plays a role for laser intensities between $10^{10} W/cm^2$ and $10^{12} W/cm^2$ (Gibbon, 2005; Mulser and Bauer, 2010). In modern high-power lasers, such intensities are usually achieved by the amplified spontaneous emission (ASE) preceding the intensity maximum or by compressed pre-pulses.

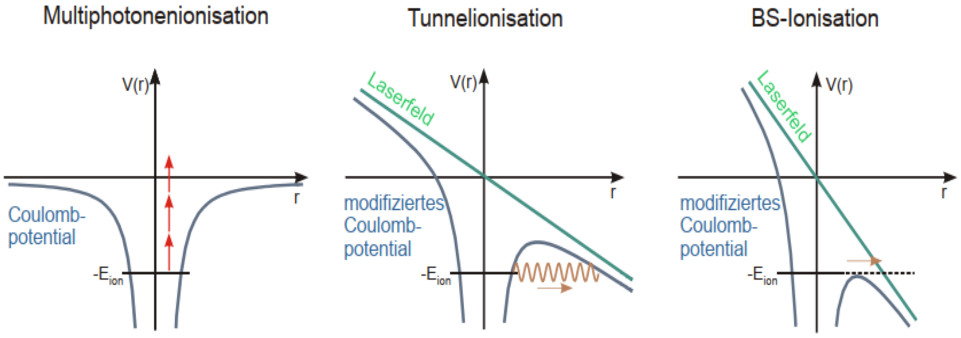

FIGURE 2.3: Schematic representation of the ionization mechanisms: multi-photon ionization (MPI), tunnel ionization (TI) and barrier suppression ionization (BSI). Here $V(r)$ describes the potential depending on the location r and E_i the ionization energy of the undisturbed atom (Wagner, 2014).

Another possible ionisation process is the *tunnel-ionisation* (TI) (Keldysh, 1965). Even below I_a intensity limit, the Coulomb potential can be modified by the laser field. The Coulomb barrier can be essentially lowered that the electron can tunnel quantum mechanically through the remaining barrier. This effect is known as tunnel ionization. If the barrier is reduced even below the energy level of the electron due to the higher laser-intensity and higher laser-field, so that the Coulomb potential is completely compensated and the electron can leave the atom spontaneously. This kind of ionisation is called *barrier suppression* (BSI) ionization. The corresponding laser intensity for the hydrogen atom is $I_{BS} = 1.4 \cdot 10^{14} W/cm^2$ (Gibbon, 2005). Figure 2.3 shows the different ionization mechanisms. The Keldish parameter γ_K is applied as a reference point distinguishing the above mentioned ionisation mechanisms,

$$\gamma_K = \omega_L \sqrt{\frac{2E_i}{I_L}}, \tag{2.29}$$

where ω_L is the laser frequency, E_i is the ionization energy and I_L is the laser intensity (Keldysh, 1965). For $\gamma_K \geq 1$ the MPI is dominant, a bound electron can gain maximum half of the energy necessary for the ionisation. For $\gamma_K \leq 1$ tunnel ionization is the predominant process. If the laser intensity further increases, the electron leaves the atom directly without tunnelling, then the at condition of $\gamma_K \ll 1$ a barrier suppression ionization takes place. Which ionization mechanism is the determining process in plasma generation depends on the parameters of laser energy, pulse duration and focal spot size, as well as on material properties, as atomic number and phase of the matter. In laser plasma experiments on electron acceleration carried out within the scope of this work, the maximum of the reached laser intensities are measured in the range of $10^{19} - 10^{21} W/cm^2$. The following section describes interaction of the electromagnetic laser wave with the plasma.

2.4 Interaction of Electromagnetic Waves with Plasma

The propagation of a high frequency electromagnetic wave in plasma is modified from its vacuum propagation by the presence of the free plasma electrons. Due to the complete or partial ionization of the matter the electromagnetic forces occur between the charged particles which can interact and thus show a collective behaviour typical for the plasma state. One of the important characteristics of the plasma is the ability to shield externally applied electric fields. The potential of the individual charge carriers in the plasma is shielded by the surrounding charges. On a macroscopic scale the differently charged particles arrange in a way that an electric field of the opposite orientation is generated that tends to cancel the external field that makes plasma to be quasi-neutral. On a microscopic scale, the positive ions are surrounded by plasma electrons which screen the electric potential of the ions. For a single ion with charge Ze this shielding results in the Debye potential which differs from the Coulomb potential by an exponential drop

$$\Phi_D(r) = \frac{Ze}{4\pi\epsilon_0 r} \exp\left(-\frac{r}{\lambda_D}\right), \tag{2.30}$$

where λ_D is the characteristic shielding length, called the Debye length of the plasma, which depends on the electron temperature T_e and the electron density n_e:

$$\lambda_D = \sqrt{\frac{\epsilon_0 k_B T_e}{n_e e^2}} = 743 \left(\frac{T_e}{eV}\right)^{1/2} \left(\frac{n_e}{cm^{-3}}\right)^{-1/2} cm. \tag{2.31}$$

The Debye length describes the range of an electric potential inside a plasma, which is much smaller than the range in vacuum (Chen, 1974).

The plasma parameter N_D is defined by the number of particles in the Debye sphere. This can be calculated for the particle density n_e of the plasma within the spherical volume of the Debye length as

$$N_D = \frac{4\pi}{3} \lambda_D^3 n_e \gg 1. \tag{2.32}$$

The plasma electrons have a characteristic frequency called the plasma frequency, which is the oscillation frequency of the electrons when they are displaced from the background ions and restored by the resultant electric fields arising from the charge separation. The strong restoring electric field associated with deviations from quasi-neutrality causes a harmonic oscillation of electrons around the position of charge equilibrium with a characteristic electron plasma frequency ω_{pe}

$$\omega_{pe} = \sqrt{\frac{n_e e^2}{\epsilon_0 m_e}} \simeq 5.6 \cdot 10^4 \left(\frac{n_e}{cm^{-3}}\right)^{1/2} s^{-1}. \tag{2.33}$$

This electron plasma frequency depends only on the density n_e of the plasma electrons and does not depend on the temperature. Substituting the electron mass for the mass of the corresponding ions m_i, the ion plasma frequency is derived then as

$$\omega_{pi} = \sqrt{\frac{n_e Z^2 e^2}{\epsilon_0 m_i}}, \tag{2.34}$$

with Z the charge state of the ion. As the ions can also move slightly out of phase with the electrons the total frequency of plasma oscillations ω_p is given by the following equation

$$\omega_p^2 = \omega_{pe}^2 + \omega_{pi}^2. \tag{2.35}$$

If the assumprion of infinite ion mass is made $m_i \gg m_e$, then the plasma frequency is $\omega_p \approx \omega_{pe}$. Any perturbed charge density oscillated at the plasma frequency. The characteristic plasma scale length, the thermal electron velocity $\upsilon_{te} = \sqrt{\frac{k_B T_e}{m_e}}$ and frequency are related by the equation

$$\lambda_D = \frac{\upsilon_{te}}{\omega_{pe}}. \tag{2.36}$$

For a thermal plasma with temperature T_e a characteristic response time to disturbances from external laser fields is defined as

$$t_D = \frac{\lambda_D}{\upsilon_{te}} = \sqrt{\frac{\epsilon_0 k_B T_e}{n_e e^2} \cdot \frac{m_e}{k_B T_e}} = \left(\frac{n_e e^2}{\epsilon_0 m_e}\right)^{-1/2} = \omega_{pe}^{-1}. \tag{2.37}$$

Plasma oscillations are damped in time by collisions and can also be damped collisionless by mechanism of Landau damping. In the case of a laser pulse that excites the oscillation of the electrons at relativistic speeds, the relativistic plasma frequency is expressed as

$$\omega_{pe,rel} = \frac{\omega_{pe}}{\langle\gamma_e\rangle}, \tag{2.38}$$

where the time average of the gamma factor $\langle\gamma_e\rangle$ of the electrons is

$$\langle\gamma_e\rangle = \frac{1}{\tau}\int_0^\tau \frac{1}{\sqrt{1-\left(\frac{\upsilon_e(t)}{c}\right)^2}} dt \approx \sqrt{1+\frac{a_0^2}{2}}. \tag{2.39}$$

The reduction in the plasma frequency for relativistic laser radiation can be interpreted as a consequence of the increase in mass of the oscillating electrons, which thus have a higher inertia. The propagation of the electromagnetic light wave with frequency ω_L in a plasma is described with the dispersion relation, that can be written as

$$k_L^2 c^2 = \omega_L^2 - \omega_{pe}^2. \tag{2.40}$$

Depending on the frequency of the electromagnetic wave interacting with the plasma and on the plasma frequency, three different regimes can be established. The light wave can either be transmitted, damped, or reflected in the plasma. If the frequency of the electromagnetic wave of the laser light is lower than the plasma frequency $\omega_L < \omega_{pe}$, the radiation is reflected because the disturbance of the oscillation of the free electrons is relatively high in this case. The electrons can follow the interference frequency and thus reflect the radiation. If the radiation frequency is greater than the plasma frequency $\omega_L > \omega_{pe}$, the electrons are too inert to follow the varying field and the external radiation can be transmitted in the plasma. In a case when the radiation frequency and the plasma frequency are equal $\omega_L = \omega_{pe}$ the resonant absorption of the electromagnetic wave takes place. The electron density at which this occurs is called the critical plasma density n_{cr} and the density contour is called the critical surface.

$$n_{cr} = \frac{\epsilon_0 \langle\gamma_e\rangle m_e \omega_L^2}{e^2} = \frac{1.11 \cdot 10^{21} cm^{-3}}{\lambda_L^2} \cdot \langle\gamma_e\rangle \cdot \mu m^2. \tag{2.41}$$

For a PHELIX laser wave length of $\lambda_L = 1053$ nm, resulting critical density is of $n_{cr} = 1.005 \cdot 10^{21} cm^{-3}$. When electron density is significantly smaller then the critical density $n_e \ll n_{cr}$, the plasma is called under-dense or under-critical, when $n_e <\sim n_{cr}$ the plasma is called near critical and when it is opposite $n_e > n_{cr}$ the plasma is called over-dense or over-critical. The laser-driven wakefield relies on the excitation of a plasma wave in the under-critical regime. If a laser hits an overcritical plasma, only an evanescent wave enters the plasma up to the so-called skin depth. The skin depth is defined as the distance to the surface at which the amplitude of the wave is exponentially attenuated. The skin depth is then given as

$$L_{skin} = \frac{c}{\sqrt{\omega_{pe}^2 - \omega_L^2}}. \tag{2.42}$$

The smaller the difference between the laser frequency and the plasma frequency the deeper can the laser wave penetrate into plasma. In the limit case of $\omega_L = \omega_{pe}$, the skin depth is infinite and plasma becomes transparent for the laser beam. Using the equation for refractive index η_r of the plasma, that is defined as

$$\eta_r = \sqrt{1 - \left(\frac{\omega_{pe}}{\omega_L}\right)^2} = \sqrt{1 - \left(\frac{n_e}{n_{cr}}\right)}. \tag{2.43}$$

Therefore, the refractive index η_r can be modified by the relativistic Lorentz factor γ_e or by the density distribution n_e. The phase and group velocities of the electromagnetic field in plasma can be calculated from equation 2.40 and expressed by the following equations:

$$\upsilon_{ph} = \frac{\omega_L}{k} = \sqrt{c^2 + \frac{w_p^2}{k^2}} = \frac{c}{\eta_r}, \tag{2.44}$$

$$\upsilon_{gr} = \frac{d\omega_L}{dk} = \frac{c^2}{\upsilon_{ph}} = \frac{c^2}{\sqrt{c^2 + \frac{w_p^2}{k^2}}} = \eta_r \cdot c. \tag{2.45}$$

When $n_e < n_{cr}$, the refractive index for a plasma is $0 < \eta_r < 1$, the radiation penetrates plasma, the phase velocity is dependent on the local electron density and $\upsilon_{ph} > c$, the group velocity is $\upsilon_{gr} < c$.

When plasma has over-critical electron density n_e and hence is non transparent for a sub-relativistic light wave with $a_0 \ll 1$, it can become transparent for a laser pulse with $a_0 \leq 1$, when the following condition is fulfilled

$$\frac{\epsilon_0 m_e \omega_L^2}{e^2} < n_e < \frac{\epsilon_0 m_e \omega_L^2}{e^2} \cdot \sqrt{1 + a_0^2/2}. \tag{2.46}$$

This effect is called *self-induced transparency* (Lefebvre and Bonnaud, 2002).

If the laser pulse has moderate intensity, which is low enough to be treated classically but also sufficiently high that can significantly enhance the ionisation degree of the plasma by optical field ionisation, the electron density in the centre of the focus is increased due to the ionisation, while outside the focus the density remains unchanged. This leads to a lower refractive index in the centre of the beam, what in turn increases the phase velocity, $\upsilon_{ph} = \frac{c}{\eta_r}$, of the laser wave in the centre. Therefore, the plasma acts as a negative lens, defocusing the laser beam. This effect is called *ionisation defocusing*.

When the laser pulse of relativistic intensity is focused into plasma, the averaged electron mass $\gamma_e m_e$ increases more during the oscillation of the laser field, the higher the local intensity is. This leads to a decrease in the refractive index at the laser axis compared to the edges of the focus. If this effect dominates the ionisation defocusing, the plasma acts as a positive lens increasing further the intensity compared to the focusing in vacuum. This effect is called *relativistic self-focusing*. Furthermore, the electrons are ponderomotively scattered out of the centre of the laser focus where the intensity is higher, decreasing the local electron density. This effect, that further enhances the laser-beam focusing, is called *ponderomotive self-focusing*. The power threshold above which relativistic self-focusing dominates over the ionisation defocusing is given by the following equation

$$P_{RSF} = 2\frac{m_e c^2}{e}\frac{4\pi\epsilon_0 m_e c^3}{e} \cdot \left(\frac{n_{cr}}{n_e}\right) = 17.4GW \cdot \left(\frac{n_{cr}}{n_e}\right), \tag{2.47}$$

where $4\pi\epsilon_0 m_e c^3/e$ is the Alfvén current, which is the maximum current that can be transported through vacuum (Alfven, 1939; Sun et al., 1987; Kaluza, 2004). Such effect is beneficial for laser-driven particle acceleration, since it helps increasing the length of the interaction between laser and plasma.

2.5 Electrons Acceleration Mechanisms in Plasma

Interaction of the high-intensity laser pulse with plasma becomes more complex compared to the interaction with a single electron due to the variety of non-linear effects associated with the collective behaviour of the electrons in plasma. The plasma electrons can increase kinetic energy and be accelerated by high-intensity laser pulses. In contrast to the pure heating of a plasma, which results in almost isotropic velocity distribution, the fraction of the laser pulse energy can be converted into electrons energy of the MeV-range forming a directed electron beam. The different collective effects potentially influence each other, therefore, the description of the whole plasma behaviour is very complicated and can be realised by using numerical PIC simulations. The investigation of the interactions of focused intense laser pulses with plasmas has high relevance for a wide range of applications over a large interval of laser intensities, spanning thermonuclear fusion (Atzeni and vehn, 2004), laboratory astrophysics (Remington et al., 2000), or laser-driven particle acceleration (Daido, Nishiuchi, and Pirozhkov, 2012; Macchi, Borghesi, and Passoni, 2013).

Depending on the experimental conditions different electron acceleration mechanisms take place, which can be divided into two groups. The first mechanism is when electrons are accelerated at or close to the surface of the over-critical plasma, where the laser pulse is stopped and partly reflected. These effects play a role in experiments with solid targets, where such layer appears. The second mechanism is when electrons are accelerated in under-dense plasma regions, they occur in gas or foam targets, or long-scale length pre-plasmas created in front of the solid targets. These effects are essential when the laser pulse can propagate through under-dense plasma regions over a distance that is much longer compared to its minimal diameter in the focus (Kaluza, 2004).

2.5.1 Electron Acceleration at the Critical Surface

In experiments with solid targets, the intense laser pre-pulse can be used to generate a pre-plasma at the front side of the target. The interactions of the main pulse with targets make significant differences between experimental results with and without pre-plasmas from the perspective of dominant electron acceleration processes and energy coupling to plasmas. When the following main laser pulse hits an inhomogeneous plasma with a very large density gradient (with the over-dense plasma surface $\backsim 10^{21} cm^{-3}$) that is parallel to the initial target surface, it is reflected in the critical density range. If a linearly polarized electromagnetic wave is incident at an angle θ with respect to its direction of propagation and the direction of the density gradient there will be a reflection at the density $n_e = n_{cr} \cos^2 \theta$ (Kruer, 2003). Sience the laser beam is not able to propagate through this overcritical surface, the field gradient is maximal there and directed normal to the overcritical surface. The ponderomotive force is directed along the field gradient and drives electrons perpendicular to the surface of the over-critical plasma layer into the target. The initially parallel to the

target surface the critical plasma surface is getting deformed during the interaction with the laser pulse as it pushes electrons and the critical surface sideways and in forward direction (Kaluza, 2004). This effect is referred as a laser hole boring. To explain the electron acceleration at the critical surface process, 2D PIC simulations were performed. Due to this effect, the direction of electron acceleration is not only perpendicular to the target surface, but also in a direction between target normal and direction of the laser (Pukhov and Vehn, 1997; Ruhl et al., 1999).
From PIC simulations performed by S. Wilks et al. (Wilks et al., 1992) it was deduced that due to the ponderomotive force the electrons spectrum resembles a relativistic Maxwellian distribution with the effective electron temperature T_e and the effective electron energy $k_B T_e$ given by the following equation

$$\begin{aligned} k_B T_e &= m_e c^2 \left(\sqrt{1 + a_0^2} - 1 \right) \\ &= 0.511 MeV \cdot \left(\sqrt{1 + \frac{I_L \lambda_L^2}{1.37 \cdot 10^{18} W/cm^2 \mu m^2}} - 1 \right). \end{aligned} \tag{2.48}$$

This relation has been experimentally confirmed by G. Malka et al. (Malka and Miquel, 1996) in the case of a thin $(10 - 100 \mu m)$ metal foil targets. Therefore, if plasma is generated due to the interaction of the high-intensity laser pulse in a thin metal foil, in which the electrons are accelerated by the ponderomotive force and these ponderomotive electrons are capable to reach relativistic velocities the parameter of the effective temperature is used to describe the energy distribution of the electrons and this temperature depends on the laser intensity and the laser contrast.

In the case when p-polarised laser pulse is incident onto a solid target with a very large density gradient and thus a very small scale length, which is in the range of the laser wavelength $L_p \approx \lambda_L$, plasma waves can be resonantly excited directly at the critical density. As in the vacuum, the transverse electric field of the laser wave accelerates electrons sideways. In vacuum the electrons would oscillate symmetrically around the laser axis, but in regions close to the critical surface of the solid the electrons only experience the electric field of the laser in areas of under-critical density. In the first half-wave of the laser the electrons are moved in the direction of the vacuum and in the second half-wave they are accelerated back into the solid target, where they do not experience the restoring forces of the laser fields which are not able to penetrate into over-dense regions. The laser pulse is reflected at the critical density, whereas the electrons accelerated into the solid and propagate further without the influence of the laser. This acceleration mechanism is called vacuum heating or not-so-resonant, resonant absorption and *Brunel heating mechanism*. The absorption of laser energy can be very effective for intensities around $10^{16}\ W/cm^2$ and very small scale lengths (Brunel, 1987).

2.5.2 Electron Acceleration in Under-Dense Plasma

During the propagation of the short and intense laser pulse through the under-dense plasma, the ponderomotive force acts on the plasma electrons in the direction of lower irradiance expelling electrons from the focal region. In the field of descending edge, the electrons are accelerated in the opposite direction. This results in the oscillation of the charge density distribution that follows the laser pulse in its wake and propagates with the group velocity $\upsilon_{gr} = \eta_r \cdot c < c$ of the laser pulse in the plasma. The longitudinal electric field in the plasma wave traps electrons, increasing kinetic energy when electrons travel with the wave. This acceleration mechanism is called *Laser Wake-Field Acceleration* (LWFA) and was proposed by T. Tajima et al. (Tajima and Dawson, 1979) The efficiency of the electrons acceleration by this mechanism is very high when the group velocity of the laser pulse is only slightly greater or equal to the phase velocity of the plasma wave. These conditions are particularly important for small density gradients, at moderate plasma density. At relativistic laser pulses, the electrons receive energies of several 10 MeV. The LWFA works very effectively in tenuous, very under-dense plasmas and ultra-short laser pulses, shorter than the plasma wavelength.

2.5.3 Direct Laser Acceleration (DLA)

In the case when the relativistic laser pulse interacts with a plasma in the Near Critical Density (NCD) regime and the power threshold, described by the equation 2.47, above which relativistic self-focusing dominates over the ionisation defocusing is reached, the mechanism of self-focusing of the laser pulse takes place. In this process the focal diameter of the laser beam is getting reduced and the laser intensity increases compared to the focusing in vacuum. A formation of the plasma channel is initiated along the laser axis where, the ponderomotive forces of the laser radially expel electrons and drive a strong electron current along the channel. This results in the formation of strong radial electric fields due to the lack of plasma electrons in the channel and strong azimuthal magnetic fields due to the high current. An electron running under small initial pitch angles to the axis of the channel is bent back by the strong electric and magnetic fields and starts to oscillate in these fields. If this electron oscillation is in resonance with the Doppler-shifted laser-light oscillation, and if the phases between electron and laser field match, the electrons can gain a large amount of energy directly from the laser fields (Kaluza, 2004). This mechanism for the generation of ultra-relativistic laser accelerated electrons is called *Direct Laser Acceleration* (DLA) and has been described by Z. M. Sheng, A. Pukhov and J. Meyer-ter-Vehn (Pukhov, Sheng, and Vehn, 1999). The theoretical results of Particle in Cell (PIC) simulations (Pukhov and Vehn, 1996; Pukhov and Vehn, 1997; Pukhov and Vehn, 1998) and the results of experimental investigation (Key, 1998; Wharton, 1998; Malka, 1997) have shown significant efficiency of the laser energy conversion which can reach up to $30 - 40\%$.

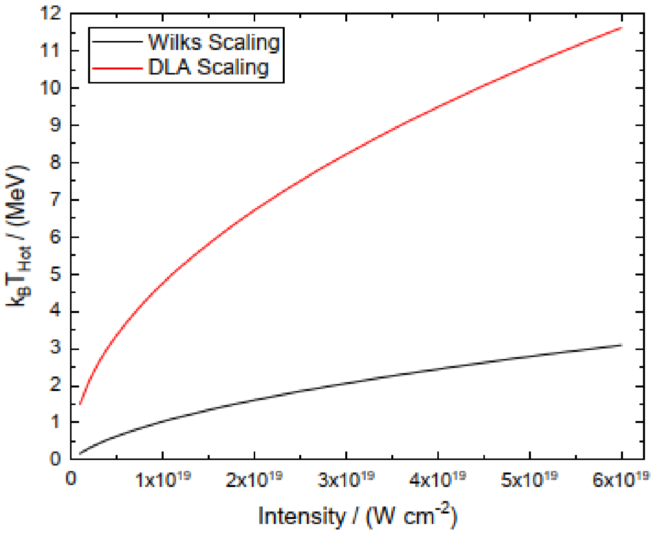

FIGURE 2.4: Comparison of the electron temperature scaling laws of Wilks et al. (Wilks et al., 1992) and in DLA by Pukhov et al. (Pukhov, Sheng, and Vehn, 1999).

The most important process for the generation of the high energy electrons during relativistic laser plasma interaction is ponderomotive acceleration. The spectral distribution of these relativistic electrons has a quasi-thermal Maxwellian-like behaviour, which can be characterised by an exponential slope with effective temperature. The normal ponderomotive scaling in the spectra is substituted by the tail of these spectra. The electron acceleration in laser - plasma channels is very different to the simple picture of a single free electron in a plane electromagnetic wave (Pukhov, 2003). This is the relativistically correct Maxwell distribution in three dimensions. The ponderomotorically accelerated relativistic electrons propagate predominantly in the forward direction (Norreys, 1999; Günther et al., 2011). This means that the velocity distribution of these high-energy electrons can be described relativistically correctly by a one-dimensional Maxwell-Jüttner distribution. For very high energies ($E \gg m_ec^2$), as treated in this work, the one-dimensional Maxwell-Jüttner distribution assumes the form of the one-dimensional Boltzmann distribution. In the discussed velocity distributions, the high energy part of the distribution is exponential. That corresponds to the number of high-energy electrons in the range of several MeV and as a function of energy can be calculated using the simple distribution function

$$N_e(E) = N_0 \exp\left(\frac{-E}{k_BT_e}\right). \tag{2.49}$$

The results of the numerical PIC simulations performed by Pukhov et al. (Pukhov, Sheng, and Vehn, 1999; Pukhov, 2003) obtained DLA temperature scaling where effective temperature grows like the square root of the laser intensity

$$k_BT_e \approx 1.5\sqrt{\frac{I_L}{10^{18}W/cm^2}}. \tag{2.50}$$

These results in a significantly higher electron temperature due to the creation of a long laser channel and the mechanism of DLA. Figure 2.4 presents the comparison of the electron temperature scaling laws of Wilks et al. (Wilks et al., 1992) and in DLA by Pukhov et al. (Pukhov, Sheng, and Vehn, 1999).

The number of electrons accelerated in the forward direction can be calculated using the following relationship

$$N_e \approx \frac{\eta E_L}{k_B T_e}. \tag{2.51}$$

It is the ratio of the laser pulse energy to the average energy of the accelerated electrons. The absorption efficiency η describes the portion of the laser energy that is converted to generate the high-energy electrons. In general, the efficiency scales as well as the mean electron energy with the laser energy.

Chapter 3

Interaction of Electromagnetic Radiation with Matter

This chapter is focused on the interaction of electromagnetic radiation with matter. It is important to distinguish the interactions of charged electrons and photons. Charged particles lose their energy in a different way compared to the uncharged photons. An individual photon incident on a target material may pass through it without interactions and therefore without energy loss. Otherwise it can interact and lose energy in one of the described further events. By contrast, a charged particle, being surrounded by its Coulomb electric force field, interacts with one or more electrons or with nucleus of practically every atom it passes. The discussion of these interactions is described in the following sections.

3.1 Photon Interactions

This sections reviews the basic processes of the interactions with matter of high-energy photons, which are called in the energy range of $1 - 100$ keV as X-rays and with energies higher then 100 keV as γ-rays. Photons can be produced in a variety of processes, for example: bremsstrahlung, emitted through electron–nucleus interactions; characteristic X rays, emitted in transitions of orbital electrons from one allowed orbit to a vacancy in another allowed orbit; annihilation radiation, emitted through positron–electron annihilation; gamma-de-excitation after nuclear reactions, particle decay, radiative neutron capture. When passing through a matter, photons interact with atoms, electrons and nuclei, as a result of which the intensity of photon beam decreases. There are five types of interactions which dominate for different photon energies:

- Photoelectric effect
- Compton scattering (incoherent)
- Pair production
- Photonuclear interactions
- Rayleigh scattering (coherent)

In these processes, the photon is either absorbed or scattered by a wide angle. In the energy range up to 10 MeV, the most significant processes are the photoelectric effect, the Compton scattering, and the formation of electron-positron pairs. At the energy of photons above 10 MeV, the threshold of photonuclear reactions is exceeded, and as a result of the interaction of photons with nuclei, reactions (γ, p), (γ, n), (γ, α) become possible. The mechanisms and relative importance of these interactions are briefly described here and discussed in detail by Robley Evans (Evans, 1955).

3.1.1 Photoelectric Effect

The photoelectric effect was discovered in 1887 by G. Herz and was systematically studied later in experimental research works of A. G. Stoletov. The photoelectric effect or photoionisation is the process of absorption of a photon by an atomic electron, which is removed from one of the inner shells of an atom and can either be raised to a higher atomic shell or can be released as free photoelectron. This interaction is dominant for low energy of photons with energies higher than the ionization energy of atoms E_i and less than 100 keV. The kinetic energy of the electron E_e is then the difference between the photon energy E_γ and the ionization energy E_i, which is also called as the binding energy of the electron.

$$E_e = E_\gamma - E_i, \tag{3.1}$$

The ionization energy E_i depends on the shell where the electron was. This equation is also called as Einstein relation for the photoelectric effect. The Nobel Prize of Physics in 1921 was awarded to Einstein for his important physical and mathematical research, and especially for the discovery of the laws of the photoelectric effect. After the emission of a photoelectron, the opened vacancy in the atomic shell can be filled by another electron of a higher shell. The transition of less bound electrons to vacant levels is accompanied by the release of energy, which can be transferred to one of the electrons of the upper shells of the atom, which leads to its escape from the atom - Auger effect or transform into the energy of characteristic X-ray radiation. Thus, during the photoelectric effect, part of the energy of the primary photon is converted into the energy of electrons - photoelectrons and Auger electrons, and part is released in the form of a characteristic radiation. The photoelectric process is not possible for a free electron, accordingly to the law of conservation momentum. The cross section of photoelectric interaction, integrated over all angles of photoelectrons emission is expressed as

$$\sigma_{p.e.} \cong const \cdot \frac{Z^n}{E_\gamma^m} \quad [cm^2], \tag{3.2}$$

where the exponent on the atomic number Z changes the value from 4 for low energy $E_\gamma < 100$ keV to 4.6 for high energy $E_\gamma > 500$ keV and the exponent on E_γ changes the value from 3 to 1 correspondingly. The photoelectric cross section is a steeply decreasing function of photon energy with sharp peaks corresponding to the cases when

$E_\gamma = E_i$ for deeper layers of electrons. Angular distributions of the photoelectrons are described by theory of Sauter (Sauter, 1931a). Simple estimation of the speed of electrons υ_e emitted e.g. from K shell of the Au foil ($E_i = 80.729$ keV) after interaction of photon with energy of 100 keVdetermines the value of $\upsilon_e = 7.998 \cdot 10^7 m/s$, which is $\approx 27\%$ of the speed of light c.

3.1.2 Incoherent Compton Scattering

American physicist A. H. Compton studying the scattering of monochromatic X-rays by boron and graphite discovered that additionally to the radiation of the primary wavelength λ the radiation of the longer wavelength λ^* is also observed. In 1927 Arthur Holly Compton was awarded the Nobel Prize for his discovery of the effect named after him. In this process a photon interacts with a weakly bound electron and transfers some part of its energy to the electron. The photon is scattered by the quasi-free electron that leads to the change of photons wavelength. Particular cases of the Compton effect are not only the scattering of X-rays by the electronic shells of atoms but also the scattering of γ-rays by atomic nuclei. The scattering is incoherent since the photons do not interfere before and after scattering. The difference between the wavelength of the scattered and primary radiation $\Delta\lambda$ does not depend on the properties of the material and the wavelength of the primary radiation. With an increase of the atomic number of the material, the intensity of the unbiased line increases and the intensity of the shifted line decreases. The solution of the kinetic equations for elastic collision based on the conservation of momentum and energy provides the dependency of the energy of the scattered photon E^*_γ on the energy of primary photon E_γ and the photon scattering angle ϕ. The following equation 3.3 describes the kinematic of Compton interactions.

$$E^*_\gamma = \frac{E_\gamma}{1 + (E_\gamma / m_e c^2)(1 - \cos\phi)}, \tag{3.3}$$

$$E_e = E_\gamma - E^*_\gamma, \tag{3.4}$$

$$\cot\theta = (1 + \frac{E_\gamma}{m_e c^2}) \tan(\frac{\phi}{2}), \tag{3.5}$$

Equation 3.4 provides the kinetic energy of the scattered electron E_e and equation 3.5 expresses scattering angle θ . Figure 3.1 (a) shows the kinematic relationship between E_γ and E^*_γ where for $E_\gamma < 0.01$ MeV all curves for different values of ϕ converge along diagonal line. This means that $E_\gamma \cong E^*_\gamma$ regardless of the photon scattering angle and the electron obtains almost no kinetic energy in this interaction. For incident photons of high energy the side-scattered photons have essentially higher energy than the back-scattered photons. Figure 3.1 (b) shows the relationship of the electron scattering angle θ and the photon scattering angle ϕ in the Compton effect. For all photon energies when $\phi = 0°$, $\theta = 90°$, and when $\phi = 180°$, $\theta = 0°$. For low photon energies the electron scattering angle gradually decreases from 90° to 0° while the photon scattering angle increases from 0° to 180°. For high photon energies the variation of

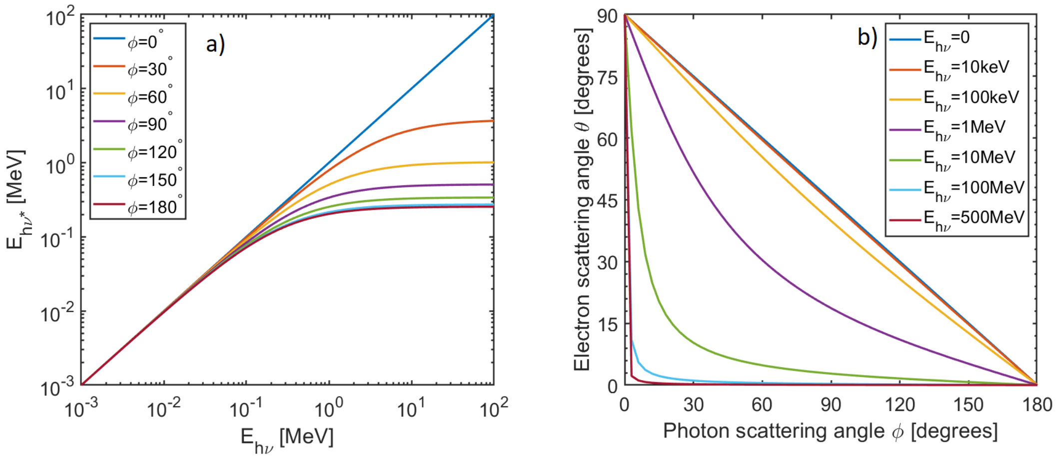

FIGURE 3.1: **a)** Representation of the kinematic relationship of E_γ and E^*_γ in the Compton effect, **b)** ralationship of the electron scattering angle θ and the photon scattering angle ϕ.

θ is collected at small ϕ angles and vice versa. The maximum energy is transferred to recoil electron when it is forwarded with $\theta = 0°$ and the photon is scattered back with $\phi = 180°$. The amount of energy transferred to the electron depends on the photon energy. For low photon energy, very small amount of energy is transferred, despite of the probability of this process. For example when $E_\gamma = 5.11$ keV the maximum electron energy will be $E_e = 0.1$ keV which is only 2% of photon energy. When photon energy reaches $E_\gamma = 5.11$ MeV the maximum electron energy is then $E_e = 4.87$ MeV which makes 95% of transferred energy.

From relativistic and quantum mechanical calculations the value of the Compton scattering cross section can be derived. The Klein-Nishina formula describes the total cross section of Compton scattering $\sigma_{Compton}$ of photon by an electron (Klein and Nishina, 1929)

$$\sigma_{Compton} = 2\pi r_e^2 \left(\frac{1+\epsilon}{\epsilon^2} \left[\frac{2(1+\epsilon)}{1+2\epsilon} - \frac{1}{\epsilon} \ln(1+2\epsilon) \right] + \frac{1}{2\epsilon} \ln(1+2\epsilon) - \frac{1+3\epsilon}{(1+2\epsilon)^2} \right) [cm^2] \tag{3.6}$$

where $\epsilon = \dfrac{E_\gamma}{m_e c^2}$, in which E_γ is to be expressed in MeV and $m_e c^2 = 0.511 MeV$, $r_e = \dfrac{e^2}{m_e c^2}$ is the classical electron radius. For photon energies $E_\gamma \ll m_e c^2$ the scattering is isotropic and the back-scattering is equally probable as the scattering in the forward direction. If the photon energies $E_\gamma \gg m_e c^2$ the scattering is pointed into the forward direction.

3.1.3 Pair Production

If the photon energy is $E_\gamma > 2m_e c^2 = 1.022$ MeV the photon can interact in the strong electric field of the nucleus, annihilate and produce an electron-positron pair. Accordingly to the conservation of momentum and energy, this process occurs in the presence of the third body, which is in this case is the nucleus. The process of the positron generation is called the Bethe-Heitler process (Bethe and Heitler, 1934). The energy conservation equation for this process is following

$$E_\gamma = 2m_e c^2 + E_{e^-} + E_{e^+}. \tag{3.7}$$

where E_{e^-} and E_{e^+} are the kinetic energies of electron and positron. Another process that initiates the production of positrons via electron-ion pair production is referred to as the Trident process. This process begins when the kinetic energy of electron exceeds $2m_e c^2$, it scatter from a nuclear charge, exchanging a virtual photon that immediately decays into a positron-electron pair (Bhabha, 1935). The Bethe-Heitler and Trident pair production yields depend on the target atomic number, areal density, electron and photon energies.

The total cross section of the Trident process, σ_T, has been approximated for electron energies from the production threshold of $2m_e c^2$ up to 100 MeV by the following equation

$$\sigma_T = 5.22 Z^2 ln^3 \left[\frac{2.3 + E_0}{2.53}\right] \quad [\mu barn], \tag{3.8}$$

where E_0 is the kinetic energy of the incident electron in MeV (Gryaznykh, Kandiev, and Lykov, 1998). The probability of a pair production by the Trident process is $dP_T = n_i \sigma_T d \propto Z^2 N_A \rho d/A$, where n_i is the ion number density, Z is atomic number, d is thickness of the target material and N_A is Avogadro's number.

The probability of pair generation via Bethe-Heitler is the product of creating a bremsstrahlung photon $dP_b = n_i \sigma_b d$ and creating a photo-ion positron-electron pair $dP_{e^+e^-} = n_i \sigma_{e^+e^-} d^{'}$ where σ_b and $\sigma_{e^+e^-}$ are the bremsstrahlung and photon-ion pair production cross sections and $d^{'}$ is the distance between the location of photon creation event and the rear side of the target. The bremsstrahlung differential radiation cross section can be expressed by the Bethe-Heitler equation using a relativistic Born approximation and assuming an unscreened nucleus as

$$\sigma_b = \frac{4Z^2 r_0^2}{137} \frac{dE_{h\nu}}{E_{h\nu}} \left[1 + \frac{E^2}{E_0^2} - \frac{2E}{3E_0}\right] \left[\ln \frac{2EE_0}{E_{h\nu}} - \frac{1}{2}\right] \quad [barn], \tag{3.9}$$

where r_0 is the classical electron radius, $E_{h\nu}$ is the energy of the emitted photon, and E_0 and E are the initial and final energy of the electron, respectively (Koch and Motz, 1959; Bethe and Heitler, 1934). The unscreened, relativistic Bethe-Heitler equation for pair production by a photon is expressed as

$$d\sigma_{e^+e^-} = 4Z^2 r_0^2 \left[E_{e^+}^2 + E_{e^-}^2 + \frac{2}{3} E_{e^+} E_{e^-}\right] / 137 E_{h\nu}^3 \times \left[\ln(2E_{e^+} E_{e^-}/E_{h\nu}) - \frac{1}{2}\right] dE_{e^+} [barn], \tag{3.10}$$

where the total energy of the created positrons is E_{e^+} and electrons E_{e^-} (Motz, Olsen, and Koch, 1969; Bethe and Heitler, 1934). Since both σ_b and $\sigma_{e^+e^-}$ scale as Z^2, the total Bethe-Heitler process has a birth yield proportional to $Z^4 \rho^2 d(d - x)/A^2$, where x is the distance from the target front to the creation depth of the bremsstrahlung photon. Therefore, the Bethe-Heitler and Trident pair generation

are each proportional to the term $(Z^2\rho d/A)^n$, where $n = 1$ for Trident and $n = 2$ for Bethe-Heitler process. This relation shows that for thick high-Z targets, Bethe-Heitler will be the dominant process, where for an Au target, the pair production yield mechanism is balanced at a thickness of $\approx 20\mu m$. For the mm-scale target thicknesses in this study, the Trident contribution is estimated to be between 2% and 12% (Nakashima and Takabe, 2002; Myatt et al., 2009; Williams et al., 2016).
The number of emitted positrons will be reduced by several scattering and absorption processes including ionization, low energy bremsstrahlung emission, photo-nuclear absorption, electronic energy loss and Compton scattering, the later two are the dominant mechanisms that reduce pair yield from the Z^4 proportionality of the simple model. The collisional energy loss for electrons and positrons is linearly dependent on Z, as is the Compton scattering cross section in the high energy limits $(> 1\,MeV)$. From these loss mechanisms, the final pair production dependency can be roughly estimated as Z^2 for different nuclei (Williams et al., 2016).

Materials with high atomic number more likely convert photons into electron-positron pair than materials with low atomic number. At high photon energies $E_\gamma > 50$ MeV in all materials the pair production and bremsstrahlung dominate. The process of the pair production produces an increase of the charged particles – electrons and positrons, and the bremsstrahlung of these particles again produces more photons. Hence, these processes develop in a cascade form resulting in conversion of particles with high energies into copies of the particles with low energies. Less probable, but still possible process occurs when one of the electrons in the atomic shells interacts with the incoming photon and becomes a third body in this interaction. The photon divides its energy between the electron-positron pair and ejected electron. This process is called triplet-production. The energy conservation equation of pair production in the electron field is

$$E_\gamma = 2m_e c^2 + E_{e^+} + E_{e_1^-} + E_{e_2^-}. \tag{3.11}$$

The threshold for this interaction is $E_\gamma > 4m_0c^2 = 2.044$ MeV. The cross section of the pair production in the field of the atomic electrons σ_e scales as Z.

3.1.4 Photonuclear Interaction

This phenomenon was discovered by Chadwick and Goldhaber in 1934. The photonuclear interaction is also named as Photonuclear absorbtion or Photodisintegration. Similar to photoelectric effect in this process energetic photon gets absorbed in a nucleus. When the energy of the photon is higher than the binding energy of the neutron the excited nucleus can emit a neutron or proton. Due to the Coulomb threshold, the probability of neutron emission is greater than that of protons. The photon energy is transferred to kinetic energy of neutron and residual nucleus. Neutrons are produced via different mechanisms which depend on the incident photon energy. These mechanisms are Giant Resonance interaction at $E_\gamma \approx 10 - 20$ MeV, Quasi-Deuteron effect at $E_\gamma \approx 50 - 150$ MeV, Delta Resonance production at $E_\gamma \approx 150 - 400$ MeV and Vector Meson Dominance at higher energies (Fasso, 2005). For light nuclei with $A < 40$ the photoneutron production threshold energy varies in a range from 8 to 19 MeV and for heavy nuclei in a range of $6 - 8$ MeV. But there are few exceptions e.g. for deuterium and beryllium the threshold energies are 2.2 MeV and 1.67 MeV respectively (Mobley and Laubenstein, 1950).

3.1.5 Coherent Rayleigh Scattering

Rayleigh interaction is a coherent elastic scattering of photons from atoms. In this process photon does not lose its energy, hence its wave length is not changed. The photon scattering angle depends on E_γ and Z. The cross section of the Rayleigh interaction is one order of magnitude smaller then the cross section of the photoelectric effect and has a form of

$$\sigma_{Rayleigh} \cong const \cdot \frac{Z^2}{E_\gamma^2} \quad [cm^2]. \tag{3.12}$$

At high energies $E_\gamma > 1$ MeV the photon is deviated in a small angle relatively to the initial direction of the propagation. When $E_\gamma < 100$ keV the scattering angle increases, especially for high Z materials.

3.1.6 Relative Importance of Various Processes

The photoelectric effect, Compton effect and pair production are very important processes by means of which the part of the energy of primary photons is transferred to kinetic energies of electrons and positrons and then to matter in various Coulomb-force interactions along their tracks. The other part of the energy of primary photons is transformed to the energy of the secondary photons. The relative importance of these processes depends on the photon energy E_γ and atomic number Z of the absorbing medium. Figure 3.2 shows the regions where each of the interactions predominate. The curves represent the cases when two interactions are equally probable. The photoelectric effect is dominant at the lower photon energies in the range of $\approx 1 - 100$ keV. For materials with high Z the Compton scattering dominates in the narrow energy range of ≈ 100 keV $- 1$ MeV. At the same time for materials with low Z the region where the Compton scattering dominates can extend from ≈ 20 keV to ≈ 30 MeV. At the higher energies the pair production process dominates.

The relative importance of Rayleigh scattering is quite small and for materials with high Z it can be disregarded in competition of other processes such as photoelectric effect of Compton scattering. However, the role of this process increases for low Z materials.

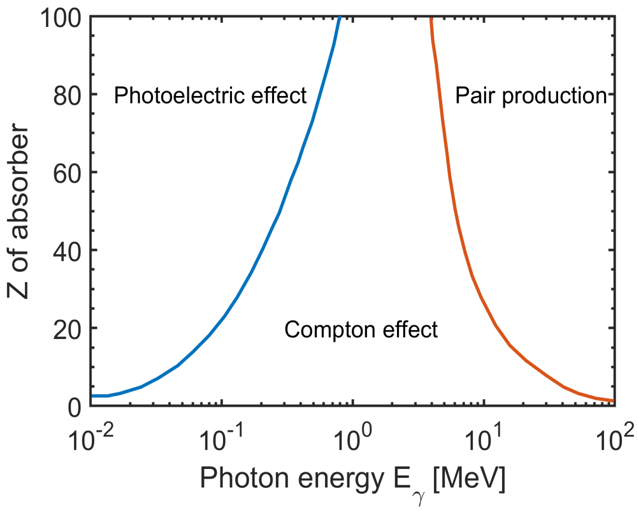

FIGURE 3.2: Representation of the relative importance of the photoelectric effect, Compton scattering and pair production process. The curves show the values of E_γ and Z where two types of effect are equal.

3.1.7 Attenuation and Mean Free Path of Photons in Different Materials

When the photon beam with an incident intensity I_0 penetrates any form of matter, it will be partly transmitted and partly absorbed. Therefore, in a layer of material with the thickness x and density ρ, the photon beam undergoes exponential attenuation. The resulting intensity I is decreased according to the Beer-Lambert law (Swinehart, 1962; Creagh and Hubbell, 1987) that is expressed by the equation

$$I(x) = I_0 \exp\left(-\mu_l x\right) \tag{3.13}$$

where μ_l is the linear attenuation coefficient of the material. It can be substituted with the photon mass attenuation coefficient $\mu_m = \frac{\mu_l}{\rho}$, which is used to quote the integrated cross section in such a way that it is independent on the aggregation state. Subsequently in equation 3.13 the thickness x should be substituted to the mass thickness. The values of μ_m are tabulated. Its inverse function $\frac{1}{\mu_m} = \frac{\rho}{\mu_l} = \lambda\rho$ is photon mass attenuation length, or mass absorption length, where $\lambda = 1/\mu_l = 1/n\sigma = M/\rho N_a \sigma$ is mean free path of photons. The total mass attenuation coefficient for all photon interaction is given as

$$\frac{\mu_l}{\rho} = \frac{\sigma_{p.e.}}{\rho} + \frac{\sigma_{Compton}}{\rho} + \frac{\sigma_{e^+e^-}}{\rho} + \frac{\sigma_{nuc}}{\rho} + \frac{\sigma_{Rayleigh}}{\rho} \tag{3.14}$$

For compounds and mixtures the total attenuation coefficient can be calculated from Bragg's rule

$$\frac{\mu_l}{\rho} = \omega_1 \left(\frac{\mu}{\rho}\right)_1 + \omega_2 \left(\frac{\mu}{\rho}\right)_2 + \omega_3 \left(\frac{\mu}{\rho}\right)_3 + \cdots + \omega_i \left(\frac{\mu}{\rho}\right)_i \tag{3.15}$$

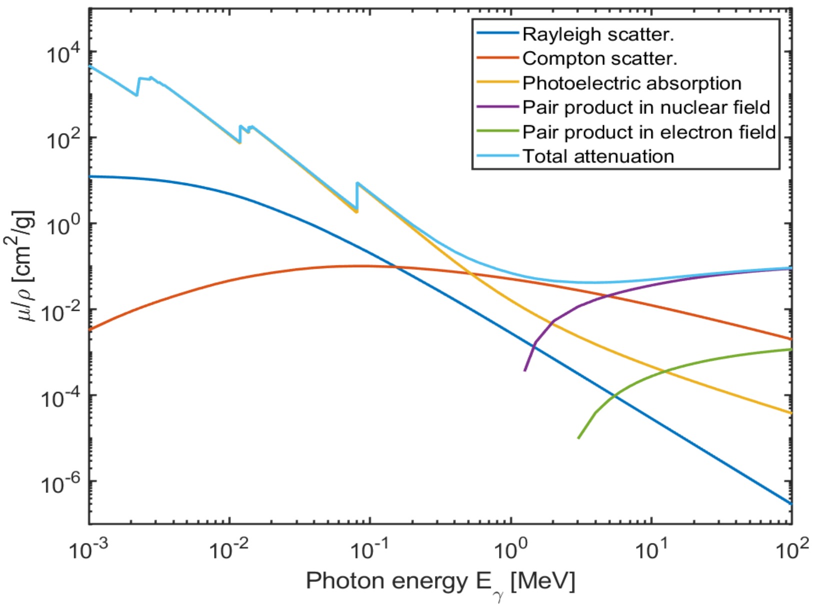

FIGURE 3.3: The photon mass attenuation coefficient for Au. Representation of the relative importance of the photoelectric effect, Compton scattering, pair production process and Rayleigh scattering.

where ω_i is the weight fraction of each element in the compound and $\left(\frac{\mu_l}{\rho}\right)_i$ their mass absorption coefficients. The relative importance of various photon interactions by means of mass attenuation coefficients versus photon energy is shown for Au in Figure 3.3. Figure 3.4 shows the calculated mean free paths of photons λ as a function of photon energy E_γ in different representative materials: Al (Z=13), Ti (Z=22), Fe (Z=26), Cu (Z=29), Au (Z=79), Pb (Z=82). Therefore, in order to absorb high-energy gamma rays the detectors of high Z and large thickness are needed.

3.2 Electron Interactions

In first approximation it is possible to consider the matter as a mixture of free electrons and nuclei at rest. When an electron passes through some matter it will interact with the electrons and nuclei present in the material through the electromagnetic force and undergo elastic and inelastic collisions with these objects. These interactions can be classified as follows:

- Elastic collisions with atomic electrons,
- Elastic collisions with atomic nuclei, resulting in elastic scattering that is characterized by a change in direction but no energy loss,
- Inelastic collisions with atomic electrons, resulting in ionization and excitation of atoms and termed collisional or ionization loss,

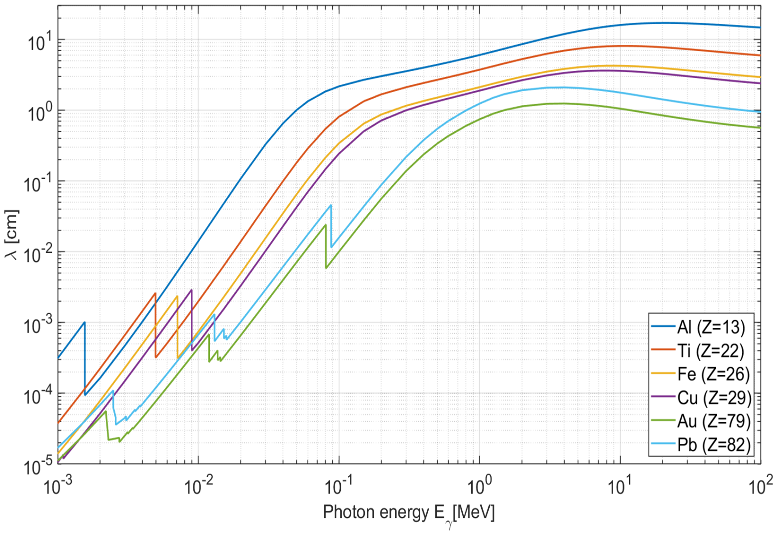

Figure 3.4: Mean free path of photons λ as a function of photon energy in different materials: Al (Z=13), Ti (Z=22), Fe (Z=26), Cu (Z=29), Au (Z=79), Pb (Z=82).

- Inelastic collisions with atomic nuclei, resulting in bremsstrahlung production and radiative energy loss.

Due to the small rest mass, electron experiences relatively large change of momentum in each collision, which causes a noticeable change in the direction of motion of this electron and as a result an electromagnetic radiation. Therefore, electrons lose energy due to collisions and radiation, change initial trajectory and generate secondary electrons, that endure the same processes. Generated due to the Bremsstrahlung photons make impact to ionization, interact with matter via processes described in previous section 3.1 and generate secondary electrons and positrons. The whole process is coupled to electron-photon transport problem. In contrast to photons, which can path through the matter without interactions or can lose the energy in one or few processes, the electron interacts with one or more electrons or with the nucleus almost every atom it passes. Finally the electron is slowed down in an absorbing material and brought to rest. The process of gradual losses of kinetic energy is denominated as the "Continuous Slowing-Down Approximation" (CSDA) and the average pass length of any charged particle passing through the material is called CSDA range. The rate of the energy loss suffered by the charge particles per unit path length in the medium is equal to the total Stopping Power (NIST, 2017).
The transport of electrons and positrons is described by the following interactions:

- Large energy loss Møller scattering $(e^-e^- \rightarrow e^-e^-)$,
- Large energy loss Bhabha scattering $(e^+e^- \rightarrow e^+e^-)$,
- Hard bremsstrahlung emission $(e^{\pm}N- \rightarrow e^{\pm}\gamma N)$,
- Positron annihilation "in flight" and at rest $(e^+e^- \rightarrow \gamma\gamma)$,

- Low-energy Møller-Bhabha scattering,
- Atomic excitation ($e^{\pm}N \rightarrow e^{\pm}N^{*}$),
- Impact ionization and production of fluorescence photons and Auger electrons
- Elastic electron (positron) multiple scattering from atoms ($e^{\pm}N \rightarrow e^{\pm}N$).

The physical models and energy-differential cross sections for these processes are described in an articles of S. Seltzer and M. Berger (Berger and Selzer, 1968; Selzer, 1991). Therefore, the electron lose its energy dE during propagation through the matter on penetration length dx in two ways: losses due to collisions and radiative losses due to Bremsstrahlung emission. This results in a total energy loss, which is given by the following equation

$$\left(\frac{dE}{dx}\right)_{total} = \left(\frac{dE}{dx}\right)_{collision} + \left(\frac{dE}{dx}\right)_{radiative} \tag{3.16}$$

The energy losses of electron moving through a material with density ρ can also be described in tearms of the total mass-energy stopping power $\left(\frac{S}{\rho}\right)_{total}$.

$$\left(\frac{S}{\rho}\right)_{total} = -\frac{1}{\rho}\left(\frac{dE}{dx}\right)_{total} \tag{3.17}$$

$$\left(\frac{S}{\rho}\right)_{total} = \left(\frac{S}{\rho}\right)_{collision} + \left(\frac{S}{\rho}\right)_{radiative} \tag{3.18}$$

The two terms of equation 3.18 are briefly described in the following sections 3.2.1 and 3.2.2. A detailed discussion of stopping-power theory can be found in the following reviews and articles (ICRU, 1984; Bethe, 1930; Bethe, 1932; Rohrlich and Carlson, 1954; Bethe and Jackiw, 1973; Bethe and Ashkin, 1953; Fano, 1963). In addition, section 3.2.3 deals with a limiting criterion that allows to determine at which initial energy of the electrons which energy loss process dominates.

3.2.1 Collision Stopping Power

The collision stopping power $S_{collision}$ or the collision losses are the average rate of energy loss per unit path length due to interactions in which the energy of the electrons is transferred to the particles of the matter through inelastic collisions. These inelastic Coulomb collisions lead to an excitation or ionization of the atoms of the matter. If the number of electrons is sufficiently high, these processes can serve as a heating process for matter. The value of the energy loss of the incident electrons depends on the kinetic energy of the electrons and on the properties of the stopping material. The mass collisional stopping power is described by integrating of the following Bethe's evaluation of the stopping-power over the cross section σ for inelastic scattering:

$$\frac{1}{\rho}S_{collision} = \frac{N_a Z}{A}\int W \frac{d\sigma}{dW}\, dW \tag{3.19}$$

where $\frac{N_a Z}{A}$ represents the number of atomic electrons per gram of the medium. N_a is Avogadro's number, and Z and A are the atomic number and atomic weight, the energy W transferred in inelastic collisions to atomic electrons. The stopping power S_{col} is divided into two regimes based on the energy transfer depending on whether a cut-off value for the energy transfer W_c smaller or larger compared to the binding energies of the atomic electrons of the stopping medium. The mass collision stopping power is expressed as the sum of two components where the atomic electron remains bound to the nucleus, and where the atomic electron is ionized.

$$\frac{1}{\rho}S_{collision} = \frac{1}{\rho}S_{collision}(W < W_c) + \frac{1}{\rho}S_{collision}(W > W_c) \tag{3.20}$$

$$\frac{1}{\rho}S_{collision}(W < W_c) = \frac{2\pi N_a r_e^2 m_e c^2 Z z^2}{A\beta^2}\left[ln\frac{2m_e c^2\beta^2 W_c}{(1-\beta^2)I^2} - \beta^2\right] \tag{3.21}$$

where r_e is the classical electron radius, $m_e c^2$ is the electron rest energy, β is the velocity of the incident particle divided by the velocity of light, z is the projectile charge in units of the electron charge, Z and A are the atomic number and atomic weight of the target atoms, and I is the mean excitation energy. The equation 3.21 is valid when the velocity of the projectile is large compared to the velocities of the atomic electrons. This result of the Bethe theory is applicable to electrons and heavy charged particles. The stopping power due to large energy transfers can be evaluated assuming that the atomic electrons are free and at rest.

$$\frac{1}{\rho}S_{collision}(W > W_c) = \frac{N_a Z}{A}\int_{W_c}^{W_m} W\frac{d\sigma}{dW}\,dW, \tag{3.22}$$

$$W_m = 2\tau(\tau+2)m_e c^2/[1 + 2(\tau+1)(m_e/M) + (m_e/M)^2], \tag{3.23}$$

where $\frac{d\sigma}{dW}$ is the differential cross section for energy transfer W in a collision with a free electron, W_m is the largest possible energy transfer, $\tau = E_e/mc^2$ is the kinetic energy of the projectile in units of its rest mass and m_e/M is the ratio of the electron mass to the mass of the projectile. For the projectile electrons the large energy transfers to atomic electrons is given by the Møller cross section (Moller., 1932), where relativity, spin effects and exchange effects associated with the indistinguishability of the incident and target electrons

$$d\sigma = \frac{2\pi r_e^2 m_e c^2}{\beta^2}\frac{dW}{W^2}\left[1 + \frac{W^2}{(E_e - W)^2} + \frac{\tau^2 W^2}{(\tau+1)^2 E_e} - \frac{(2\tau+1)W}{(\tau+1)^2(E_e - W)}\right]. \tag{3.24}$$

The equation for the complete electron mass collision stopping power can be obtained using equations 3.19, 3.20 and 3.22. It is given by the following equation according to ICRU Report No. 37 (ICRU, 1984)

$$\frac{1}{\rho}S_{collision} = \frac{2\pi N_a r_e^2 m_e c^2}{\beta^2}\frac{Z}{A}\left[ln(E_e/I)^2 + ln(1+\tau/2) + F^-(\tau) - \delta - \frac{2C}{Z}\right], \tag{3.25}$$

where

$$F^{-}(\tau) = (1-\beta^2)\left[1+\tau^2/8-(2\tau+1)ln2\right]. \tag{3.26}$$

The factor δ has been added into the equation 3.25 for the collisional stopping power represents the relativistic density-effect correction. For electrons passing through high density materials the stopping power is reduced by the polarization of the medium. This is the polarization of the absorber atoms due to the relativistically distorted field of the incoming charged particle in the vicinity of the particle trajectory. The degree of polarization depends on the local charge density and on the absorber density, because the electron density and the mass density are proportional to one another. The polarized atoms shield areas of the absorber that are further away from the electric field of the incoming particle. A summary of current density effect correction models can be found in ICRU Report (ICRU, 1984). The equation for mass collision stopping-power for positrons is the same as for electrons, except the factor F^{-} is replaced by following equation

$$F^{+}(\tau) = 2ln2-(\beta^2/12)\left[23+14/(\tau+2)+10/(\tau+2)^2+4/(\tau+2)^3\right]. \tag{3.27}$$

The shell corrections term $2C/Z$ can be neglected in the formula of the electron stopping power that results in relatively small errors in the calculation at low energies. At the electron energy above 100 keV the errors in the collision stopping powers are estimated to be 1-2% (Seltzer and Berger, 1982).

3.2.2 Bremsstrahlung and Radiative Stopping Power

The bremsstrahlung is electromagnetic radiation produced by the acceleration or deceleration of electron when deflected by strong electromagnetic fields of target high-Z (proton number) nuclei. The name bremsstrahlung comes from the German. The literal translation is ‘braking radiation’. From classical theory, when a charged particle is accelerated or decelerated, it must radiate energy.

Bremsstrahlung radiation is a result of Coulomb interactions between a charged particle and the atomic field of the medium. When the incident electron propagates in the field of the atomic nucleus it gets decelerated and loses part of its kinetic energy in the form of bremsstrahlung photons (radiative loss). Photons with energies ranging from zero to the kinetic energy of the incident electron $0 < h\nu < E_e$ may be produced, that results in a continuous bremsstrahlung spectrum. Bremsstrahlung is an important physical phenomenon which is the result of coupling of the electromagnetic field with matter. Therefore it is an important tool for the experimental investigations in nuclear, plasma, solid-state and elementary particle physics and has a wide range of technical applications.

Bremsstrahlung may be internal or external. The process of internal bremsstrahlung arises from the creation of the electron and its loss of energy due to the strong electric field in the region of the nucleus undergoing decay as it leaves the nucleus. During beta decay there is an emission of photon along with the beta particles and neutrinos or anti neutrinos. The emitted photons possess a continuous spectrum. Therefore, the internal bremsstrahlung is due to the Coulomb interaction between the beta particles and the daughter nucleus. The external bremsstrahlung process is produced in the material of the target due to the Coulomb interaction of the incident charged particles with the target nucleus. The bremsstrahlung spectrum produced in a given target depends on the kinetic energy of the incident electron and on the thickness and atomic number Z of the target. According to the range of electrons of a given kinetic energy E_e in the target material, the external bremsstrahlung is divided into two groups: thin target bremsstrahlung, where a thickness of a thin target is much smaller than the electron range, and thick target bremsstrahlung, where the thickness of a thick target is similar to the range. It is assumed that in the thin target there is no loss of energy due to ionization, the electrons do not suffer any significant elastic collision and there is no second radiative collision. For thin target bremsstrahlung radiation, the radiated energy is proportional to the product $E_e Z$, where Z is the atomic number of the target. The intensity of radiation emitted in each photon energy interval versus photon energy or photon spectrum is constant from zero to the kinetic energy E_e of the incident electron, and zero for all energies above E_e. Intensity of photons $I(h\nu)$ is proportional to product of number of photons and photon energy. Intensity is also proportional to atomic number Z. Hense, the photon of energy $E_1/2$ is produced with $\times 2$ probability of photon of energy E_1, the photon of energy $E_1/10$ is produced with $\times 10$ probability of photon of energy E_1. The lowest energy photons have the highest probability of production via thin target bremsstrahlung radiation. When the thickness of the target is a significant fraction of the mean range of the electrons in a certain material, the resulting external bremsstrahlung is called thick target bremsstrahlung. In this case, a thick target can be considered as consisting of a large number of superimposed thin targets. The intensity $I(h\nu)$ of a thick target spectrum is expressed by the following equation:

$$I(h\nu) = CZ(E_e - h\nu) \tag{3.28}$$

where C is a proportionality constant (Podgorsak, 2005). The bremsstrahlung of thick targets is very attractive field for experimental investigations and a subject of theoretical modelling presented in this thesis. A radiative mechanism of energy loss is possible due to the small mass of the electrons. The larger the change in acceleration a charged electron undergoes, the more energetic bremsstrahlung photon can be emitted. The bremsstrahlung photons have a continuous energy distribution that ranges until the maximum energy equal to the kinetic energy of the incoming electron. Radiative stopping power is an average rate of electron energy loss per unit path length due to collisions with atoms and atomic electrons in which bremsstrahlung quanta are emitted (NIST, 2017). The radiative mass stopping power can be calculated from the bremsstrahlung cross sections as it is expressed in the following equation (Seltzer and Berger, 1982):

$$\frac{1}{\rho}S_{radiative} = \frac{N_a}{A}\left[\int_0^T k\frac{d\sigma_n}{dk}\,dk + Z\int_0^{T'} k\frac{d\sigma_e}{dk}\,dk\right] \tag{3.29}$$

where $d\sigma_n/dk$ is the differential cross section for the emission of a photon of energy k due to the interaction of the electron with the Coulomb field of the atomic nucleus, and σ_e/dk is the corresponding cross section due to the Coulomb interaction with one of the atomic electrons. The upper limit of the energy of the photons that can be emitted in electron-electron interactions is

$$T' = mc^2T\left[T + 2mc^2 - \beta(T + mc^2)\right]^{-1} \tag{3.30}$$

The average energy loss per unit length of charged particles due to bremsstrahlung in the Coulomb field of the nucleus can be calculated with the following equation

$$-\left(\frac{dE}{dx}\right)_{radiative} = 4\alpha N_a\rho\frac{Z^2}{A}z^2\left(\frac{1}{4\pi\epsilon_0}\frac{e^2}{mc^2}\right)^2 E\,ln\frac{183}{Z^{1/3}}. \tag{3.31}$$

Accordingly to this equation the bremsstrahlung losses are inversely proportional to the square of the projectile mass $1/m^2$ and proportional to the energy of the incident particle E. This means that the energy loss due to bremsstrahlung for heavy charged particles plays essential role only at very high energies in a range of GeV. For the particle energies of MeV range considered in this thesis, the loss of bremsstrahlung energy only plays a role for the electrons because of their small rest mass of 511 keV. The efficiency of bremsstrahlung radiation in elements of different atomic number Z varies nearly as Z^2. Thus, for electrons of a given energy, bremsstrahlung losses are considerably greater in high-Z materials, such as Au, than in low-Z materials, such as Al. Also bremsstrahlung losses depend on the size of the atom, represented by its atomic weight A. For the electrons, the following equation is applied for the calculation of bremsstrahlung loss

$$-\left(\frac{dE}{dx}\right)_{radiative} = 4\alpha N_a\rho\frac{Z(Z+1)}{A}r_e^2E\,ln\frac{183}{Z^{1/3}}, \tag{3.32}$$

where $r_e = \frac{1}{4\pi\epsilon_0}\frac{e^2}{m_ec^2}$ is the electron radius. Furthermore, the equation 3.32 gives the approximated analytical formula for the radiation length. The radiation length X_0 is the average thickness of the material in which a relativistic charged particle will reduce to $1/e$ ($\approx 67\%$) of its energy in terms due to radiation losses.

$$X_0 = \frac{A}{4\alpha N_a\rho Z(Z+1)r_e^2E\,ln\frac{183}{Z^{1/3}}}, \tag{3.33}$$

Hence, equation 3.32 reads

$$-\left(\frac{dE}{dx}\right)_{radiative} = \frac{E}{X_0}. \tag{3.34}$$

The radiation length of a multicomponent mixture or compound can be approximated as

$$X_0 = \frac{1}{\sum_{i=0}^{n} g_i/X_0^i}, \tag{3.35}$$

where g_i is the mass fraction of the i-th component with the radiation length X_0^i.

3.2.3 Critical Energy

The total energy loss of electrons due to the atomic interaction is given by the equation 3.16. It essentially depends on the electron energy and the material properties of the absorber. The energy of the electrons at which the collision energy loss are equal to the radiative energy loss for the same properties of the absorber material is called the Critical Energy E_c for the electrons in the particular material.

$$-\left(\frac{dE}{dx}(E_c)\right)_{collision} = -\left(\frac{dE}{dx}(E_c)\right)_{radiative} \tag{3.36}$$

The relative importance of the collision and radiative stopping power as well as total stopping power as a function of incident electron kinetic energy for solid density titanium Ti (Z=22) and gold Au (Z=79) are shown in Figure 3.5. The data are obtained from (Berger, 1993). The vertical dashed lines mark the critical energies for titanium Ti (Z=22) and gold Au (Z=79). The collision energy losses are predominating at low

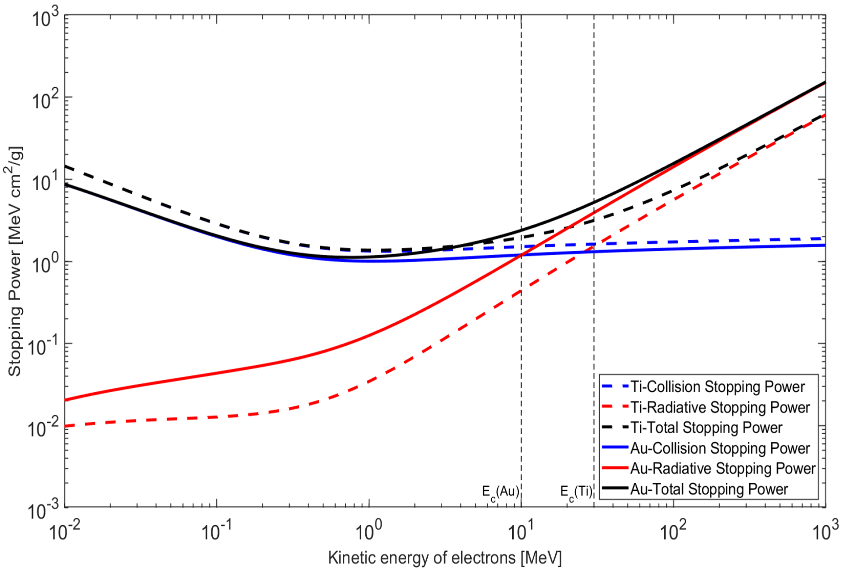

FIGURE 3.5: Stopping Powers of electrons in titanium Ti (Z=22) and gold Au (Z=79). The vertical lines mark the critical energies for each material respectively.

electron energies while radiative losses start becoming essential only at high electron energies. Since the energy loss through ionization is proportional to the Logarithm and the radiative energy loss is linearly proportional to the projectile energy, the loss of energy due to bremsstrahlung processes dominates above the critical energy. The rate of radiative energy losses is approximately proportional to the electron energy and to Z^2. This means that X-ray production through radiative losses is more efficient for higher energy electrons and higher atomic number of materials. Radiative losses starts to dominate collisional losses for high Z materials at lower electron energies compared to the case of low Z materials. These energies are $E_e > 10$ MeV for Au and $E_e > 30$ MeV for Ti. As a result, the total energy loss rises above the value of critical energy E_c with increasing electron energy.

Therefore, when the electron crosses the matter, it undergoes many different collisions with atoms in its path. The particle loses energy and changes its direction after each collision. The path length of a single electron is the total distance travelled along its trajectory until the electron comes to rest, regardless of the direction of movement. A very close approximation to the average path length travelled by the electron as it slows down to rest is continuous slowing-down approximation or CSDA range. In this approximation, the rate of energy loss at every point along the track is assumed to be equal to the total stopping power. Energy-loss fluctuations are neglected. The CSDA range is obtained by integrating the reciprocal of the total stopping power with respect to energy (NIST, 2017). The CSDA range is purely a calculated quantity that represents the mean path length along the electron's trajectory and not the depth of penetration in the defined direction.

3.2.4 Characteristic Lines in X-Ray Spectra

As it is described in the section 3.2.2, the electrons are slowed down when they penetrate matter and the energy is emitted in the form of radiation. The photon radiation spectrum represents a superposition of the continuous bremsstrahlung spectrum (contains all photon energies or frequencies in a range) with a characteristic line spectrum (discrete, contains only certain energies in a range). The continuous spectrum is formed by the deceleration of electrons close to the nuclei of atoms in the target metal. The range of possible photon energies is continuous. The characteristic line spectrum is formed by the ejection of orbital electrons from inner energy shells and the subsequent transitions of electrons from outer shells. Transitions in metals with large atomic number Z result in emission of the photons with energies in the X-ray range also called fluorescence x-rays. The development process of the characteristic X-ray radiation is illustrated in Figure 3.6. Historically, X-ray spectral lines were labelled with letters (K, L, M, N, . . .). These letters correspond to the atomic shells (n=1, 2, 3, 4, . . .). The electrons lose energy through the collisions with bound electrons. If the kinetic energy of the incident electron during the collision is greater than the binding energy of the electron on the K(n=1) shell $E_e > E_i$, it leads to the

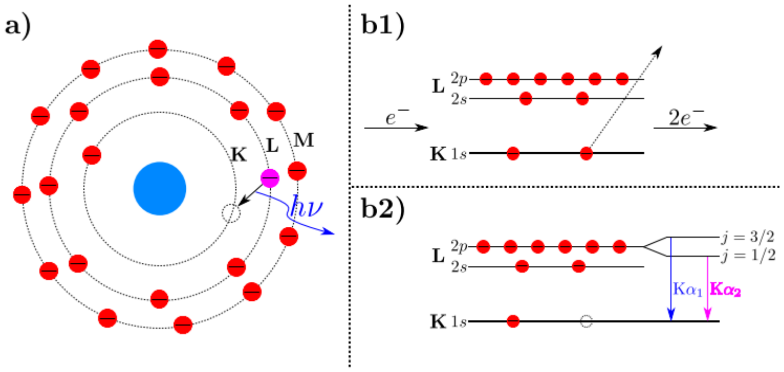

FIGURE 3.6: Schematic representation of the characteristic X-ray radiation. (a) Shell model of K_α radiation. (b1) Ionization of K-Shell. (b2) Level diagram of the K_α radiation (Schönlein, 2015).

ejection of a K(n=1) shell electron out of the atom (Fig. 3.6 (b1)). The generated by the ionization of the K-shell vacancy is then filled by a transition of an electron from a higher state. The energy difference of the two energy levels is emitted in the form of radiation of a photon. When a vacancy on the K(n=1) shell is filled, the radiation emitted in this way is called K(n=1)-line radiation. Radiation that is emitted when the vacancy of L(n=2)-shell is filled is analogously called as L(n=2)- line radiation. Another convention indicates which higher energy level is involved in the transition. If the next higher shell is concerned, the transition is called the α-radiation, for the second higher shell it is β-radiation, etc. For K-line radiation this means that X-rays produced in a transition of an electron from L(n=2) to K(n=1) shell are called K_α radiation (Fig. 3.6 (a)), X-rays produced in a transition from the M(n=3) to the K(n=1) shell is K_β radiation, X-rays produced in a transition from the N(n=4) to the K(n=1)shell are called K_γ X-rays. Transitions from higher shells to L and M shells are labelled similarly. Figure 3.6 (b2) shows another differentiation of the emission lines. There are eight electrons on the L-shell. Two in the $2s(l = 0)$ and six in the $2p(l = 1)$ orbital. Due to the selection rule for electrical dipoles ($\Delta l = \pm 1$), the transition $2s \to 1s$ with $\Delta l = 0$ is forbidden. Hence, only the electrons of the $2p$ orbital take part in a transition. However, this level is degenerate due to the spin-orbital coupling with $j = \dfrac{3}{2}$ (four electrons) and $j = \dfrac{1}{2}$ (two electrons). Therefore, two different transitions from the $2p$ orbital are possible. Since the transition is equally probable for each electron, but the transition $2p^{3/2} \to 1s$ can be carried out by four electrons and the transition $2p^{1/2} \to 1s$ can only be carried out by two electrons, the relative intensity of the transition from $j = \dfrac{3}{2}$ is also twice as high. The more intensive high energetic state is assigned by the index 1. The resulting emission lines are therefore referred to as K_{α_1} and K_{α_2} (Schönlein, 2015).

The characteristic radiation has a quantum nature, each line of the X-ray spectrum appears as a result of the transition of an atom from one energy state to another, where the energy of the photons is determined by the Mosley's law

$$E_{ph} = h\nu = E_{n_i} - E_{n_f} = Z_{eff}^2 R_y^{'} (\frac{1}{n_i^2} - \frac{1}{n_f^2}), \tag{3.37}$$

where n_i and n_f are the main quantum numbers of the initial and final energy levels involved in the transition, and $R_y^{'}$ is the Rydberg unit of energy for the corresponding element the atomic mass M

$$R_y^{'} = R_y(\frac{1}{1 + \frac{m_e}{M}}), \tag{3.38}$$

The effective atomic number Z_{eff} or effective nuclear charge of an atom arises from the fact that the charge actually prevailing in the nucleus is shielded by inner-shell electrons. The electron involved in the transition therefore does not see the full nuclear charge Z, but an effective nuclear charge reduced by a shielding factor S ($Z_{eff} = Z - S$). Radiated photon energy has strong quadratic dependence on Z_{eff} that explains why the radiation is described as characteristic and shows that the shielding of the core also plays a decisive role for the radiated energy. The probability that a fluorescence x-rays will be emitted by a certain atom is called the fluorescence yield, defined Y_K for a K-shell vacancy and Y_L for a L-shell vacancy. Y_K and Y_L are plotted in Figure 3.7 for materials of different Z. The production of fluorescence x-rays appears for elements with atomic numbers higher than 10. Y_K increases rapidly with Z to about of 0,95 for tangsten (Z=74), which because of this property is most often used in X-ray tube targets. For the L-shell the yield Y_L remains relatively low, since the L-shell binding energy is smaller then K-shell binding energy (Attix, 1986). The extensive database of measured and calculated cross sections for the ionization by electron impact of the K shell and the L and M sub-shells of all elements from

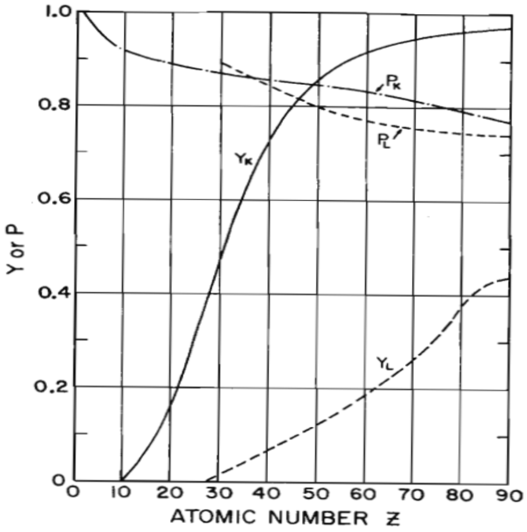

FIGURE 3.7: Fluorescence yield $Y_{K,L}$ and fractional participation in the photoelectric effect $P_{K,L}$ by K and L-shell electrons. Y_K was calculated from tables of Ledere and Shirley (1979), and Y_L from Burhop (1952) (Attix, 1986).

hydrogen to einsteinium (Z=1 to Z = 99) depending on the energy of the incident electrons and positrons with kinetic energies up to 1 GeV can be found in article (Llovet et al., 2014). The authors described the essentials of classical and semi-classical models of quantum approximations for computing ionization cross sections and developed a systematic method for evaluating cross sections for emission of x rays and Auger electrons based on atomic transition probabilities from the Evaluated Atomic Data Library of Perkins et al. [Lawrence Livermore National Laboratory, UCRL-ID-50400, 1991]. The emphasis was on the recent formulation of the distorted-wave Born approximation by Bote and Salvat (Bote and Salvat, 2008) that has been used to generate the cross sections.

3.2.5 Electromagnetic Cascades

Electromagnetic cascades or electron-photon showers arise as a result of multiple successive interactions of high-energy electrons or photons with matter. The electron of sufficiently high energy $E_e > E_c$ interacting with the matter on its first unit path emits Bremsstrahlung photons some of which will have the energy of the same order of magnitude as the electron. The emerged photons with a large probability will generate on the next unit path electron-positron pairs or experience Compton scattering. The components of the pair again undergo deceleration on the next unit path and again emit bremsstrahlung photons, etc. The process of multiplication of particles grows like an avalanche until the average energy of the newly created particles will drop to the critical energy E_c, below which the ionisation energy losses prevail over radiation losses. After reaching the maximum number of particles the cascade begins to fade due to the absorption of particles energy via ionisation losses. Similar cascades are generated by photons with an energy of $E_{ph} > 2m_ec^2$.

After n radiation lengths up to the breakdown of the cascade, there will be created 2^n particles with the critical energy of E_c. Therefore, for particle with the initial energy of E_0 the following equations take place

$$E_0 = 2^n E_c, \tag{3.39}$$

$$n \ln 2 = \ln \frac{E_0}{E_c}. \tag{3.40}$$

Using the equations (3.32), (3.36) and (3.40) it is possible to estimate the number of radiation lengths until the electromagnetic cascade will be completely stopped. The main objective of the theory describing the development and damping of electromagnetic cascades is to find the distribution function of particles at different depths in terms of energies and angles, and hence, in terms of distances from the shower axis or from the direction of motion of the primary particle. The longitudinal dimensions of the shower are much larger than its transverse dimensions. The transverse dimensions of the shower are determined mainly by the angle of multiple scattering ϑ, which is inversely proportional to the energy of the electron. The lower energy has the particle, then the higher angle it will be dissipated at. The largest scattering angle will be at the energy of electrons $E_e \approx E_c$, since particles of lower energies are quickly absorbed due to ionization losses. This multiple scattering of charged particles is described by the theory of G. Molière. The transverse dimension of the fully contained electromagnetic showers initiated by an incident high energy electron or photon in any material is characterised by the Molière radius R_M. This is the radius of a cylinder containing on average 90% of the shower's energy deposition. Two Molière radii contain 95% of the shower's energy deposition. It is related to the radiation length X_0 by the approximate relation $R_M = 0.0265 \cdot X_0(Z + 1.2)$, where Z is the atomic number (Moliere, 1948).

Chapter 4

Thermoluminescence Dosimetry at the PHELIX Laser

Thermoluminescence dosimetry (TLD) is one of the most flexible dosimetric techniques for the assessment of dose from ionising radiation. It can be used in various radiation dose measurement applications such as radiation protection, environmental dose monitoring, medical and health physics, radiotherapy and diagnostic applications. This chapter presents a review of a thermoluminescence dosimetry based method for measurements of bremsstrahlung spectra in the energy range from 1 keV to 100 MeV.

4.1 General Theory of TLD

Thermoluminescence is a form of luminescence that is exhibited by certain crystalline materials, when previously absorbed energy from electromagnetic radiation or other ionizing radiation is re-emitted as a light upon heating of the material (McKinlay, 1981). The first medical use of TLD was reported in 1953 by Daniels et al. (Daniels, Boyd, and Saunders, 1953). In 1971 TLDs were used for personnel dosimetry (Wilson, 1987), in 1972 for environmental dosimetry (Denham, Kathren, and Corley, 1972) and in 1977 for nuclear accident dosimetry (Glenn and Bramson, 1977). Since then TLD method has been significantly developed and a lot of materials have been studied for applications in different areas of dosimetry investigations (ICRU, 1992). TL dosimeters are non-conducting crystals, which conduction band is empty. In solid-state physics, the electronic band structure of a solid matter describes the range of energy levels that electrons may have within the band. Additionally band gaps or forbidden bands are the ranges of energy that electrons can not have. At room temperature all electrons in a crystal are confined in the valence band. When the crystal is irradiated, some electrons gain sufficient energy to move from the valence to the conduction band where they can move freely. The conduction band is separated from the valence band by the forbidden band gap. The energy difference between the de-localised bands is E_g. Therefore, in absence of electron e^- a positively charged hole (h) remains in the valence band, which can also move inside the crystal. Due to impurities, imperfections and doping in the crystal, e^- and h traps are created in the band gap between the valence and the conduction band. Thus e^- and h are trapped at defects, as it schematically shown in Figure 4.1. A simple TL model assumes two energy levels in the forbidden gap: one situated below the bottom of the conduction band and the other situated above the top of the valence band. The highest level indicated by T is situated above the equilibrium Fermi level E_f and in the equilibrium state is empty, before the exposure to radiation and the creation of electrons and holes. It is therefore a potential electron trap. The other level, indicated by R is a potential hole trap and can function as a recombination centre (Bos, 2006). If these traps are deep, the electrons and holes will not have enough energy to escape. If the distance between the energy level of the trap and the conduction band is sufficiently large, there is only a small probability per unit time at normal room temperatures that the electron will escape the trap by being thermally excited back to the conduction band. For this reason, exposure of this kind of material to a continuous source of radiation leads to a progressive build-up of trapped electrons. By heating the crystal their energy is increasing, therefore they can leave the traps and recombine at luminescence centres. As a result the light is emitted (see Figure 4.1 (c)). The amount of emitted light depends on the temperature and the number of the trapped electrons and holes, therefore on the absorbed dose in the crystal. The TLD can be considered as an integrating detector, where the number of the trapped e^- and h is proportional to the number of the original e^- and h pairs produced during the exposure. Ideally, every trapped e^- and h emits one photon. Consequently, the number of emitted photons is equal to the number of charge pairs, which are also proportional to the absorbed by the crystal dose (McKinlay, 1981; Dam and Morenello, 2006; Knoll, 2000). The probability of a charge carrier to escape from the trap per unit time is described by the Arrhenius equation

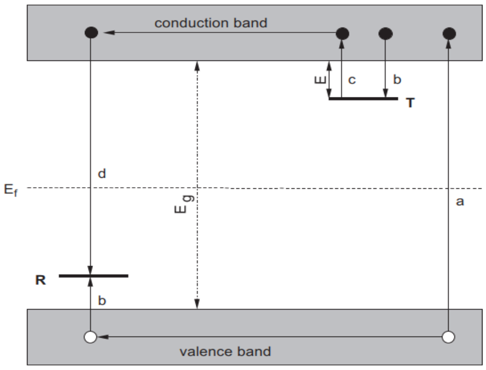

FIGURE 4.1: Energy band model of the electronic transitions in a TL material according to a simple two-level model: (a) generation of electrons and holes; (b) electron and hole trapping; (c) electron release due to thermal stimulation; (d) recombination. Solid circles are electrons, open circles are holes. Level T is a electron trap, level R is a recombination centre, E_f is Fermi level, E_g is the energy band gap (Bos, 2006).

$$p = s \cdot \exp\left(\frac{-E}{k_B T}\right), \tag{4.1}$$

where p is the probability per unit time, s is the frequency factor or attempt-to-escape factor associated with a particular defect and considered to be independent on the temperature, E is the trap depth or activation energy, which is needed to release an electron from the trap into the conduction band, k_B is Boltzmanns constant and T is the absolute temperature. The intensity of the emitted by the TL crystal light $I_{el}(t)$ at any time t during heating is proportional to the recombination rate of holes and electrons at R. The recombination rate is proportional to the concentration of free electrons n and the concentration of holes m trapped at R:

$$I_{el}(t) = \frac{mA_m ns \exp\left(\frac{-E}{k_B T}\right)}{(N-n)A_n + mA_m}, \tag{4.2}$$

where A_m is the recombination probability, N is the concentration of electron traps and A_n is the probability of re-trapping. The equation 4.2 can not be solved analytically without additional assumptions. From equation 4.2, the different orders of kinetics equations can be derived. The Randall-Wilkins theory (Randall and Wilkins, 1945) is applicable with the assumption of the first order TL kinetics, higher order kinetics are discussed by R. Chen (Chen, 1969). Randall and Wilkins assumed negligible re-trapping during the heating stage that $mA_m \gg (N-n)A_n$. Therefore, equation 4.2 can be written as

$$I_{el}(t) = -\frac{dn}{dt} = n \cdot s \cdot \exp\left(\frac{-E}{k_B T}\right), \tag{4.3}$$

The solution of the equation 4.3 for the number electrons n, released at time t when T and p are constant is expressed as following

$$n(t) = n_0 \exp\left(-st \exp(-\frac{E}{kT})\right), \tag{4.4}$$

where n_0 is the initial number of the trapped electrons. But if the temperature T varies in time p is not longer a constant and the solution of the differential equation 4.3 becomes

$$I_{el}(t) = -\frac{dn}{dt} = n_0 \cdot s \cdot \exp\left(\frac{-E}{k_B T(t)}\right) \cdot \exp\left(-s\int_0^t \exp\left(\frac{-E}{k_B T(t)}\right) dt\right), \tag{4.5}$$

With increase of the temperature, the intensity initially increases because of detrapping of the trapped charge carriers and recombination takes place, than the intensity reaches a maximum and finally decreases, as the number of charges carriers becomes depleted. The intensity has thus the shape of a peak which is called a first-order glow peak (Bos, 2006). The equation 4.3 can be used for the evaluation of glow curves applying a stepped temperature cycle for TL readout. The glow curves for corresponding TLD materials consist of the individual glow peaks which are associated with different traps (Kron, 1994). The light yield is recorded as a function of the increasing temperature in a glow curve, which is dependent on the TLD type. The

related to the radiation deposition signal represents total number of emitted photons, accessible by the area under the glow curve. This curve shows the intensity of the signal plotted against temperature and consists of a large number of overlapping peaks occurring at different temperatures. These peaks are related to the electron traps present in the sample. The area under each peak is related to the number of filled traps, which, in turn is related to the amount of initial radiation.
The principle of TLD can be summarised in the following equation:

$$I_{ir} = f \cdot I_{el}, \tag{4.6}$$

where I_{ir} is the intensity of the ionising radiation incident on the TL crystal, I_{el} is the intensity of the emitted light and the factor f is a complex function of TLD material, geometry of the TL dosimeter, the thermal and radiation history of the TLD material, the time between irradiation and read out, the total dose, the dose rate and the radiation quality. The conversion of I_{ir} to absorbed dose D is explained by the extended Bragg-Gray cavity theory (Paliwal and Almond, 1975). The absorbed dose D means the average energy imparted by ionizing radiation to the matter in a volume element per unit mass of irradiated material. The absorbed dose is expressed in units of rad (or gray) ($1\,rad = 0.01\,gray$). The conversion of the emitted visible light I_{el} to a quantitative parameter of reading r is accomplished using a photo multiplier. Therefore, the equation 4.6 can be expressed as following

$$D = f_D \cdot I_{ir} = f_D \cdot f \cdot I_{el} = f_D \cdot f \cdot f_R \cdot r, \tag{4.7}$$

where f_D summarising all factors converting radiation detected by the TL dosimeter to dose in the surrounding medium and f_R represents all factors in the readout chain (Kron, 1994). The theory of thermoluminescence is broad, so that detailed description would be beyond the scope of the present work. Further information of the physics of TLD can be found in the monograph of J. Cameron et al. (Cameron, Suntharalinharn, and Kenny, 1968) and in a review articles of Y. Horowitz, T. Kron and A.J.J. Bos (Horowitz, 1981; Kron, 1994; Bos, 2006).

4.2 Characteristics of TLD-700 and TLD-700H Detectors

In this work **Harshaw TLD-700** and **TLD-700 H** cards each with four Lithium Fluoride (LiF) based crystals are used for the measurement of bremsstrahlung spectra in ultrashort-pulsed radiation fields. The cards are manufactured by Thermo-Fisher Scientific company. Lithium Fluoride is an alkali halide with atomic number equal to $Z = 8.2$, that is near human tissue-equivalent of 7.4 and hence is widely used for personnel monitoring. It provides an excellent energy response, without the need for extensive mathematical computations to determine dose, improving overall accuracy and reducing the errors. LiF based TLD materials can be found in many forms namely chips or pellets, single crystals, rods, powders, ribbons and gel. **TLD-700** is broadly applied as it has a LiF crystal doped with magnesium **Mg** and titanium **Ti**. Magnesium is used to increase the number of trapping centres in the lattice and titanium is used in order to increase the number of luminescent recombination centres at which the de-trapped electrons and holes recombine after being released from the trapping centres during the readout process. **TLD-700 H** is has a LiF crystal doped with magnesium **Mg**, copper **Cu** and phosphorus **P**. This crystal has higher sensitivity to γ-rays in the low dose range. The tolerance of these materials against high dose rates is experimentally verified for dose rates is up to $10^{10}\,Gy/s = 10\,mGy/ps$. Additionally, LiF based materials are not sensitive to light, enabling added flexibility in dosimeter handling and processing for improved productivity and process efficiency. The fading factor of TLD-700 is $< 5\%$ in 3 months after exposure. The fading factor of TLD-700 H is negligible in 3 months and $< 5\%$ up to 2 years after exposure. The characteristics of TLD-700 and TLD-700H are shown in Table 4.1 (Scientific, 2016).

Type	Material	Dosimetry Application	Linear Range
TLD-700 $(99.99\%^7Li$ and $0.01\%^6Li)$	LiF: Mg, Ti	Gamma, Beta	$10\mu Gy - 1Gy$
TLD-700H $(99.97\%^7Li$ and $0.03\%^6Li)$	LiF: Mg, Cu, P	Gamma, Beta, Environmental	$1\mu Gy - 10Gy$

TABLE 4.1: TLD specifications and ordering information (Scientific, 2016).

The figure 4.2 gives the relative response obtained for ^{137}Cs exposure of TLD-700 and TLD-700H cards. This graph shows that relative response of both cards types at photon energies higher then 500 keV is equal to 1 and at lower photon energies the over-response of TLD-700 is obtained. The similar results were reported in the literature (Miljanic, Ranogajec-Komor, and Vekic, 2002; Lakshmanan, Raffnsre, and Tuyn, 1984; Edwards et al., 2005). The application of the TLD cards has many advantages: relatively cheap and easy to use and then again reuse, versatile - TLDs are available in many forms, high spatial resolution, no angular dependence, no dependence on temperature and pressure of the environment, high dose-rates response. The thermoluminesence dosimetry systems have also certain disadvantages such as: accurate calibration required, precision of the measurements require strict operational procedures, long reading and annealing process. In general, the dosimetric application of the chosen TLD cards has optimum measurement capability to provide correct results of the measured doses.

4.3 Calibration and Linearity of TLD Readings

The calibration of both TLD-700 and TLD-700H cards was performed by means of the X-ray tube which converted electrical input power into X-rays. A high voltage

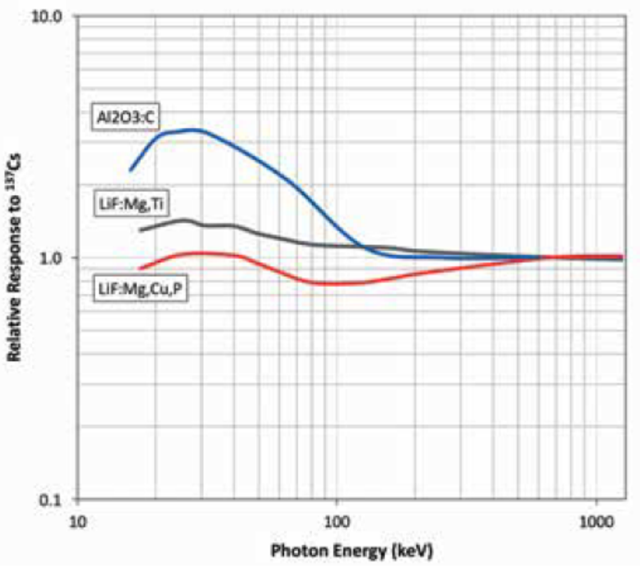

FIGURE 4.2: Response curves of TLD-700 (LiF: Mg, Ti) (black) and TLD-700H (LiF: Mg, Cu, P) (rad). (Scientific, 2016).

power source of 250 kV was connected across cathode and anode to accelerate the electrons. Electrons from the cathode collided with the anode material (made of tungsten) and accelerated other electrons, ions and nuclei within the anode material. As the result of generation of X-ray bremsstrahlung radiation the calibration dose was established to be 5 mGy. This dose was used to determine the calibration factor or the conversion coefficient k for the card reader. Thus, a relationship was established between the dose measured by each of the TLD cards and the dose achieved after reading of the irradiated cards. The calibration equation is $D_{measur} = k \cdot D_{reader}$. This relation was used for the calculation of the dose from each TLD cards with corresponding conversion coefficient, so that it allowed directly obtain the dose in Gy. The background, acquired from non irradiated TLD cards, was subtracted from the values of the irradiated TLD chips, so that the best precision was provided for experimental measurements.

In order to prove that TLD readings are directly proportional to the irradiated dose five TLD-700 and TLD-700H cards were exposed at different doses from 1 mGy to 100 mGy. Figure 4.3 shows the results of mean doses averaged over four chips of each TLD card. The small standard deviation from mean value represents the stability and repeatability of the measured results as well as the correctness of the calibration factor. The averaged over five cards signals are shown in Figure 4.4. The dose response remains linearly related to the absorbed dose value in the selected range from 1 mGy to 100 mGy. This is the most useful range for measurements. The dose range can be considered to stay linear up to 10 Gy and at higher doses TLD readings tends to be supralinear (Geiß, Krämer, and Kraft, 1998).

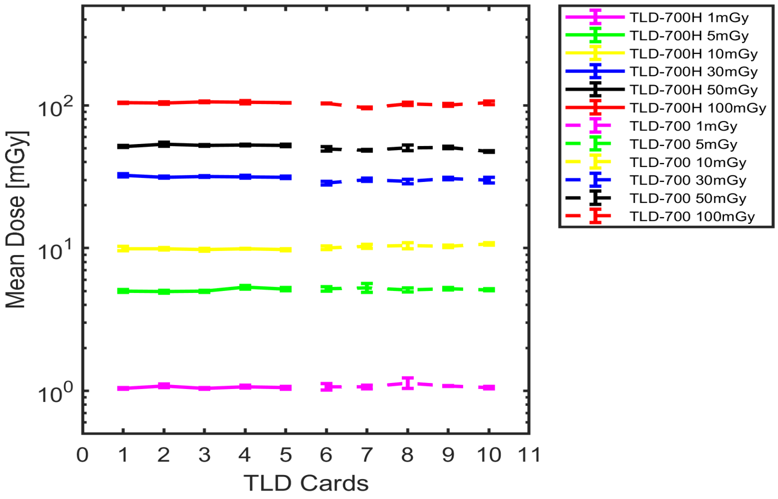

FIGURE 4.3: Dose response for X-ray exposure of TLD-700 and TLD-700H cards.

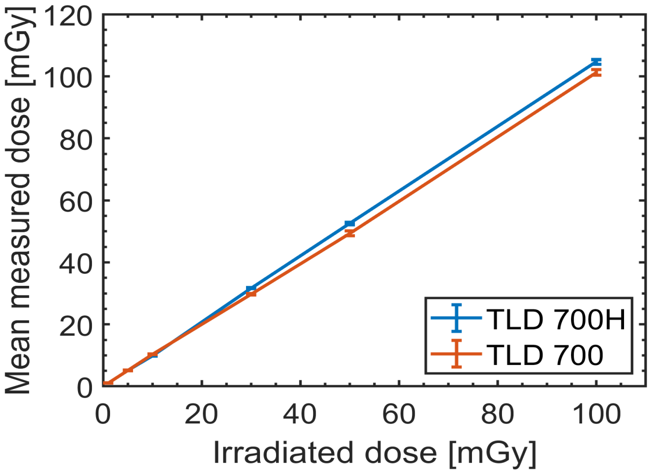

FIGURE 4.4: Variation of the mean measured dose response of TLD cards with the given irradiated dose in the linear dose range.

4.4 TLD Reader and Procedure of Dose Evaluation

TLD Reader of Harshaw Model 6600 PLUS was used for the current research work. The TLD cards were placed into a metal container inside the reader's chamber. The TLD reader implements a contact heating that produces linearly ramped temperatures with accuracy within $\pm 1°C$ to $400°C$. Each TLD card is heated by a heating coil, which is connected to the metal tray holding the TLD. A thermocouple is used to measure the temperature of the heating cycle in the chamber. For improvement of the accuracy of low-exposure readings, a nitrogen gas is injected to flow around the tray. The nitrogen gas eliminates oxygen in the TLD area, hence eliminates unwanted oxygen-induced TL signals. The nitrogen is also used to reduce the signal produced from impurities in the air and is routed through the photomultiplier tube chamber to eliminate moisture caused by condensation.

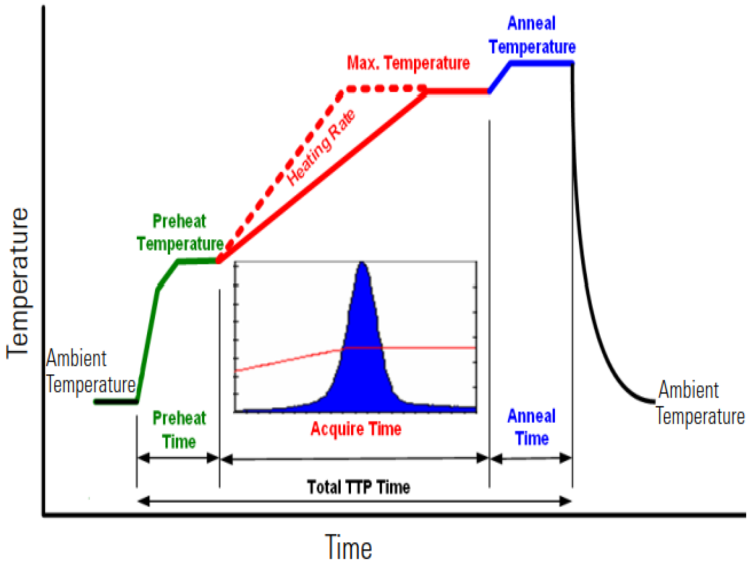

FIGURE 4.5: Time-Temperature Profile of the TLD reader during the readout proses (Scientific, 2010).

Due to the thermoluminescence effect light is emitted. It passes through optical filters and enters through the light guide a photomultiplier tube (PMT) and then it is measured as an electrical signal. The output of the PMT is proportional to the number of generated photons and it is proportional to the absorbed dose when the output is integrated. This total light output by the TL crystal can be calibrated to be proportional to the absorbed dose. A TLD glow curve is a result of the dependency the light intensity given out by the TLD from the heating temperature. According to Arrhenius law, the probability of releasing trapped electrons and holes from their trapping sites increases exponentially with the temperature. At low temperatures, some electrons may gain enough energy to escape the trapping sites and de-excite without much increase in temperature. This causes a problem, as it will affect the sensitivity of the dosimeter. The solution of this was to remove the peaks at low temperatures by pre-heating the TLDs before the readout procedure. This pre-heating also removes the background signal, resulting the dosimetry peak to be much more distinct as shown in TLD reader measures the glow curve by heating of the TLD. During the data acquisition, it has a constant heating rate of $15°C/s$, up to a maximum temperature of $255°C$. This Time-Temperature Profile is pre-set in the TLD reader to allow pre-heat, acquisition, and annealing as shown in Figure 4.5. After reading the signal, the TLD must be annealed at the temperature higher than the readout temperature of $400°C$. This annealing process releases any trapped electrons and holes that are not released during readout so that the TLD could be reused for subsequent measurements. The reader device is connected to a PC and the measured results are either stored in the hard disk of the PC or printed out (Scientific, 2010; Xiang, 2013).

The statistical uncertainty of the readings of these TLD cards relative to the mean dose as a function of the mean absorbed dose has been experimentally determined by the irradiation of TLD cards with different doses. This dependence is presented in Figure 4.6. It shows that doses of at least 10 μGy are needed for reliable readings. From the Figure 4.6 it have been found that the variation of the relative standard

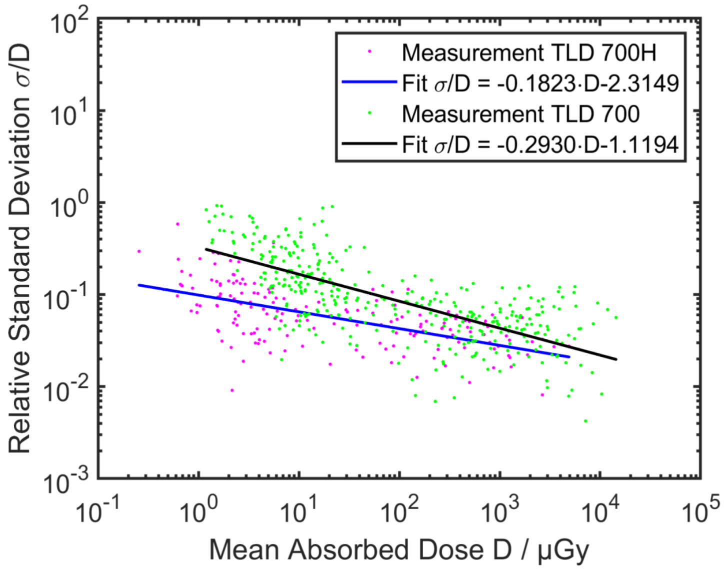

FIGURE 4.6: Relative standard deviation σ/D of the readings from the single LiF crystals in the Harshaw TLD-700 and TLD-700 H cards as a function of the mean absorbed dose D.

deviations σ/D of TLD readings versus mean absorbed dose of TLD readings D can be fitted using the linear regression fit with equations, which are represented in the description to the figure. These regression fits can be used to make a predictive model to an observed data set of values of the response and explanatory variables of the measured absorbed doses for both TLD-700 and TLD-700 H cards and to quantify the strength of the relationship between the response and the explanatory variables of the measured absorbed doses.

In general, the characteristics of the properties of TLD materials of TLD-700 and TLD-700 H cards make it possible to use cards of both types for thermoluminescence dosimetry based measurements of bremsstrahlung spectra during the interaction of PHELIX laser with various targets. Notably, that TLD-700 H cards have a higher sensitivity than TLD-700 cards, so they are preferred for small doses in order of $< 10\,mGy$. For higher doses, the TLD-700 cards give good application results that are in a linear dose range.

Chapter 5

Experimental Facilities and Diagnostic Description

The investigation of plasmas produced by the interaction of ultra-intense and ultra-short laser pulses with matter became to very attractive research field since the laser radiation intensity exceeds $10^{19}\,W/cm^2$. The laser-matter interaction leads to the formation of plasma, the part of the laser energy is transmitted to electrons in the target material. These electrons are accelerated from the interaction zone and reach relativistic velocities and collide with the rest of plasma and with solid target producing bremsstrahlung. In order to compare existing theories of acceleration mechanisms within plasma, detailed measurements of all emitted components have to be realised. This thesis demonstrates the capabilities of characterisation of interaction processes by means of the radiation emitted due to the interaction between the target and electrons. Therefore, this chapter will first introduce the PHELIX laser system and the parameters of the generated laser pulses used for the experiments presented in this thesis. A general overview of the whole laser system is followed by a description of the experimental setup and the diagnostic techniques used to investigate this problem. Finally, the application of the TLD bremsstrahlung spectrometer, including details of the experimental implementation, design and a description of the dosimeters are discussed.

5.1 The PHELIX Laser System

The experiments described in this thesis were carried out using the **P**etawatt **H**igh-**E**nergy **L**aser for Heavy **I**on E**X**periments (**PHELIX**) system at the GSI Helmholtz Center for Heavy-Ion Research in Darmstadt. The PHELIX laser is a versatile laser facility producing the beams with maximum focused intensity higher than the $10^{21}\,W/cm^2$, with energies up to 1 kJ and powers up to 500 TW. It employs two frontends to produce femtosecond pulses (fs-frontend) and nanosecond pulses (ns-frontend), a pre-amplifier, and the main amplifier. The main amplifier section of the laser is based on flash-lamp-pumped Nd:glass amplifier modules. The fundamental wavelength of the laser is 1053 nm. The laser pulses from both frontends are directed to pre-amplifiers and afterwards amplified in main amplifier. By using a compressor

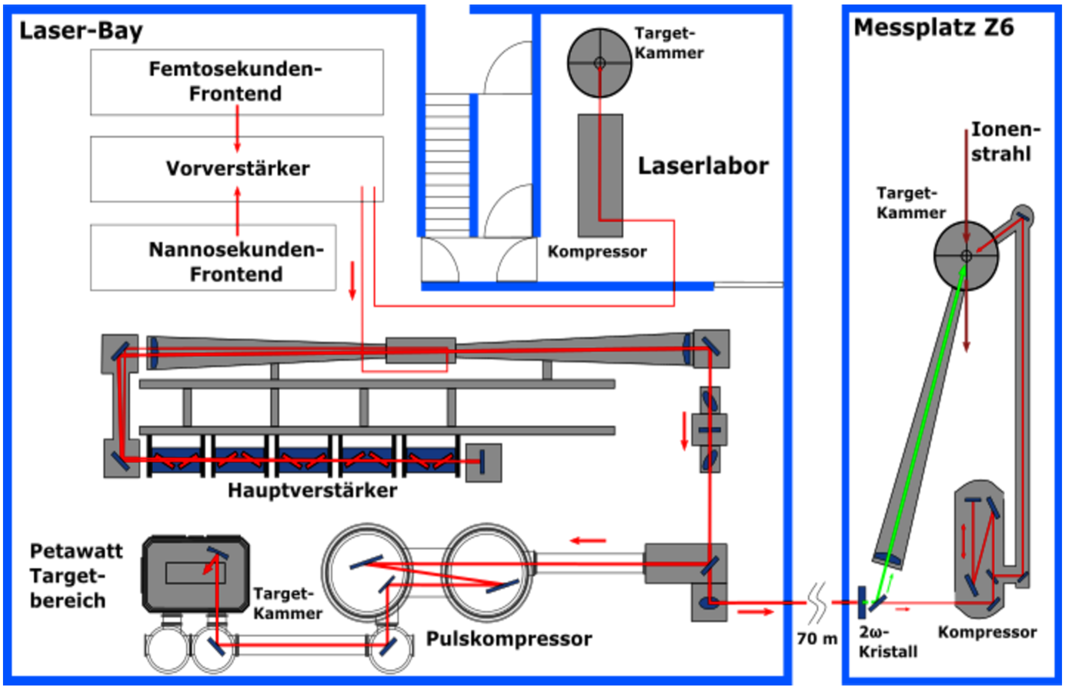

FIGURE 5.1: A schematic view of the PHELIX laser system with experimental areas (Heavy-Ion Research GmbH, 2018).

consisting of large dielectric grids, the pulse is compressed. Then the laser beam can be optionally directed into three different target chambers. These are the Z6 target area, where combined experiments of high-intensity laser and heavy-ion beams from the UNILAC can be performed, target chamber in the laser test laboratory for laser powers under 10 TW and in the PHELIX-building (laser bay) target chamber for intense laser experiments where all experiments described in this thesis were carried out. The schematics of the PHELIX laser facility with experimental areas is shown in Fig. 5.1. The available laser parameters of the PHELIX laser system are shown in Tab. 5.1. For the generation of extreme laser intensities of $> 10^{20}\, W/cm^2$ without damages to the laser optics the Chirped Pulse Amplification scheme (CPA) is used where a sub-picosecond laser pulse is stretched in time, amplified and recompressed afterwards. High energy beams are generated by the nanosecond frontend, which delivers arbitrary pulse shapes and pulse durations between 700 ps and 10 ns (Heavy-Ion Research GmbH, 2018). When the beam is guided into the target chamber several focusing options exist, based on off-axis parabolas with different focal distances and total deviation angles. Depending on the requirements of the experiments the PHELIX laser can also realize the double-pulse option. It can be used to generate two co-propagating pulses with a time delay of 0-1 ns with the same pulse duration or 0.1-5 ns delay with different pulse durations of 500 fs to 1 ns (Heavy-Ion Research GmbH, 2018). The best achievable ratio between the intensities of the pre-pulse and the main pulse is expressed in the value of the contrast. Since the intensity is proportional to the power of the laser pulse a contrast of 100 dB corresponds to a ratio of the intensity of 10^{10}.

Laser Parameters		
	Long Pulse	Short Pulse
Pulse length	1–10 ns	0.5–20 ps
Energy E	0.3–1 kJ	up to 200 J
Max intensity I_{max}	$3 \cdot 10^{16}\, W/cm^2$	$2 \cdot 10^{21}\, W/cm^2$
Contrast	50 dB $\equiv 10^{-6}$	up to 120 dB $\equiv 10^{-10}$
Repetition rate at maximum power	1 shot every 90 min	1 shot every 90 min

TABLE 5.1: The available operational parameters of the PHELIX laser system.

5.2 Experimental Setup

This section describes the experimental setup for the laser acceleration of electrons in **N**ear **C**ritical **D**ensity (NCD) plasmas. For the investigation of the generation and characterisation of ultra-relativistic hot electrons accelerated in under-dense pre-ionised foam targets and the following interactions of electrons with solid targets inducing the generation of high energetic photons in the form of bremsstrahlung two experimental campaigns were carried out. The first pilot experiment **P138** on the generation of ultra-relativistic hot electrons accelerated by the direct laser acceleration (DLA) mechanism in pre-ionized foam targets was carried out at the PHELIX laser in 2017. This experiment on the interaction of relativistically intense laser pulses with near-critical plasmas showed the enormous increase of the total charge and energy of the laser-accelerated electrons as predicted by the theory (Pugachev et al., 2016), which is much higher than defined by Wilks law (Wilks et al., 1992). For these experiments the s-polarized laser pulse of 1.053 μm fundamental wavelength, 80–100 J energy and 750 ± 250 fs pulse duration was focused onto the target by means of a 150 cm 90° off-axis parabola under 5° to the target normal. In this way, up to 60% of the laser energy was concentrated in the focal spot with a FWHM-size of $14 \pm 1 \times 19 \pm 1\, \mu m^2$. Shot-to-shot deviations of the laser energy and 30% uncertainties in the laser pulse duration resulted in the rather large confidential interval of the laser intensities ranging from 2.1 up to $5.1 \cdot 10^{19}\, W/cm^2$. The corresponding normalized vector potentials are $a_0 = 3.9 - 6.0$. The ns laser contrast was kept at the highest level between 10^{-11} and 10^{-12}. In order to create the NCD plasma, a foam layer and foils were irradiated by a 1.5 ns long pulse with a triangular temporal shape and 1–3 J energy forerunning the relativistic short main pulse. The delay between the peak of the ns pulse and the relativistic main pulse was varied from 0 up to 5 ns (Rosmej et al., 2019).

The aim of the subsequent experiment **P176**, carried out in 2019, was to characterize MeV bremsstrahlung sources arising from the interaction of DLA electrons with high-Z converter targets. For this experimental campaign also the s-polarized laser pulse of 1.053 μm fundamental wavelength was sent onto targets at 5 - 7 degrees to the target

Parameters of the PHELIX laser used in experiments	
Main pulse	
Wavelength λ	1053 nm
Polarisation	S
Contrast	$10^{-6} - 10^{-10}$
Pulse duration τ	750 fs
Parabolic mirror with a focal length of 150 cm	
Energy E	80 J - 100 J
Max intensity in the focal spot I_{max}	$1.1 - 2.6 \cdot 10^{19}\, W/cm^2$
Focus size	$19.2 \pm 1.4 \mu m \times 11.8 \pm 1.2\, \mu m$
Parabolic mirror with a focal length of 40 cm	
Energy E	180 J
Max intensity in the focal spot I_{max}	$5 - 7 \cdot 10^{20}\, W/cm^2$
Focus size	$2.9 \pm 0.3 \mu m \times 2.7 \pm 0.3\, \mu m$
Pre-pulse	
Wavelength λ	1053 nm
Energy E	20 J
Pulse duration τ	1.5 ns
Contrast	10^{-4}
Time interval between the pre-pulse and the main pulse dt	2–5 ns

TABLE 5.2: Parameters of the PHELIX laser system during the experiments.

normal. Two different focusing off-axis parabolic mirrors were used providing peak laser intensities of $1 - 2.5 \cdot 10^{19}\, W/cm^2$ ($a_0 = 2.7 - 4.27$) and $7 - 10 \cdot 10^{20}\, W/cm^2$ ($a_0 = 22.6 - 27.0$). The duration of the laser pulse was 750 ± 250 fs. In the case of a moderate relativistic laser intensity of $1 - 2.5 \cdot 10^{19}\, W/cm^2$, $90 \pm 10\, J$ laser energy measured after the main amplifier was focused by means of a 150 cm off-axis parabolic mirror into an elliptical focal spot with FWHM diameters $12 \pm 2\, \mu m$ and $18 \pm 2\, \mu m$ containing a laser energy of $E_{FWHM} \cong 17 - 22\, J$. In the case of the ultra-relativistic laser intensity, 180 J laser energy was focused into a $2.7 \pm 0.2\, \mu m \times 3.2 \pm 0.2\, \mu m$ focal spot by a 40 cm off-axis parabolic mirror. The laser energy in the focal spot was 20% of that after the main amplifier and reached $E_{FWHM} \cong 36 - 40\, J$. The laser spot size on target and the laser energy in the focal spot were controlled in every shot. Experiments on the direct laser acceleration of electrons in plasmas of near critical density were performed using the mentioned off-axis parabolic mirror with a focal length of 150 cm. In the case of ultra-high laser intensity, shots were done only onto metallic foils (Rosmej et al., 2020). The laser parameters used in the experiments **P176** are summarized in the Tab. 5.2.

The schematic view of the experiment **P138** is shown in Figure 5.2. The diagnostics setup included two portable electron spectrometers with 250 mT static magnets.

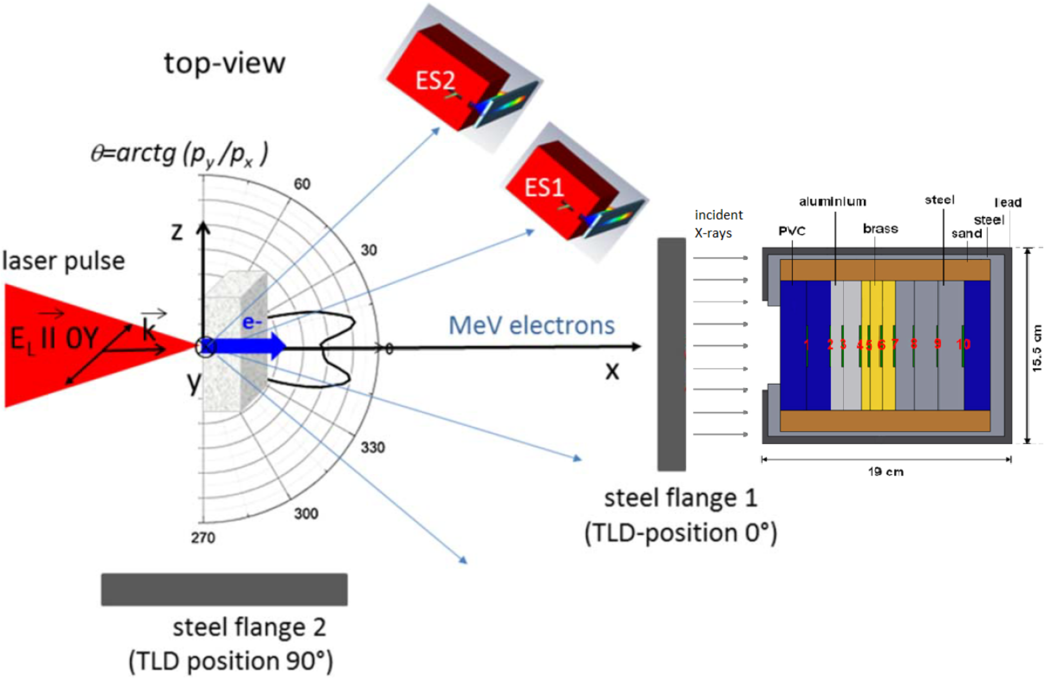

FIGURE 5.2: Schematic view of the orientation of the laser beam relative to the target, electron spectrometers ES1 and ES2, and a ten channel TLD-detector for characterization of the gamma-radiation spectral distribution in experiment P138. The laser pulse (red) irradiates the foam target and propagates along the x-axis (Rosmej et al., 2019).

The spectrometers were placed in the target chamber in a horizontal plane perpendicular to the laser polarization vector. The distance between the interaction point and the entrance holes of both spectrometers was 450 mm. In order to measure an angular distribution of super ponderomotive electrons predicted in simulations (Pugachev et al., 2016), the first spectrometer ES1 was placed under 18° and the second one ES2 under 44° to the laser pulse propagation direction. A thermo-luminescence dosimetry (TLD)-based ten channel system was used for the spectrometry of the hard bremsstrahlung radiation caused by MeV electrons interacting with a 17 mm thick **Fe**-flange which separated the evacuated target chamber from the environment. The flange was located at a distance of 868 mm from the target in the laser pulse direction. Ten TLD-cards were placed inside a shielding cylinder with a collimator window between the absorbers, which are manufactured from lower to higher Z materials of different thickness (Horst et al., 2015). The incident gammas penetrate different absorbers and cause a corresponding TLD-signal (dose) in all ten channels. The TLD-detector was placed for one set of shots in the direction of the laser pulse propagation and for another set in perpendicular direction to measure an angular dependence of the MeV bremsstrahlung radiation produced by supra-thermal electrons. The schematic view of the experiment **P176** is shown in Figure 5.3. The main difference of the experiment **P176** was in the implementation of radiators from high Z materials such as W, Au as targets simultaneously with polymer foam layers. The interaction of the super-ponderomotive electrons with high-Z materials increased the generation of MeV bremsstrahlung radiation. Additionally, a cylindrical diagnostic, which was made of a stack of three stainless steel cylindrical plates of 3 mm thickness each, was used for the measurement of the angular distribution of electrons in a wide range of angles. The TLD-spectrometer was replaced by a more compact version consisting of 8 channel and placed during whole experimental campaign inside the vacuum chamber under 16° to the laser pulse propagation direction. This TLD spectrometer was used to characterize MeV bremsstrahlung radiation generated in the interaction of the super-ponderomotive electrons with high Z materials. Therefore, in described experiments electrons were accelerated in plasma of near critical density. The electron energy distribution was directly analysed by applying a static magnetic field and indirectly by measuring the bremsstrahlung radiation.

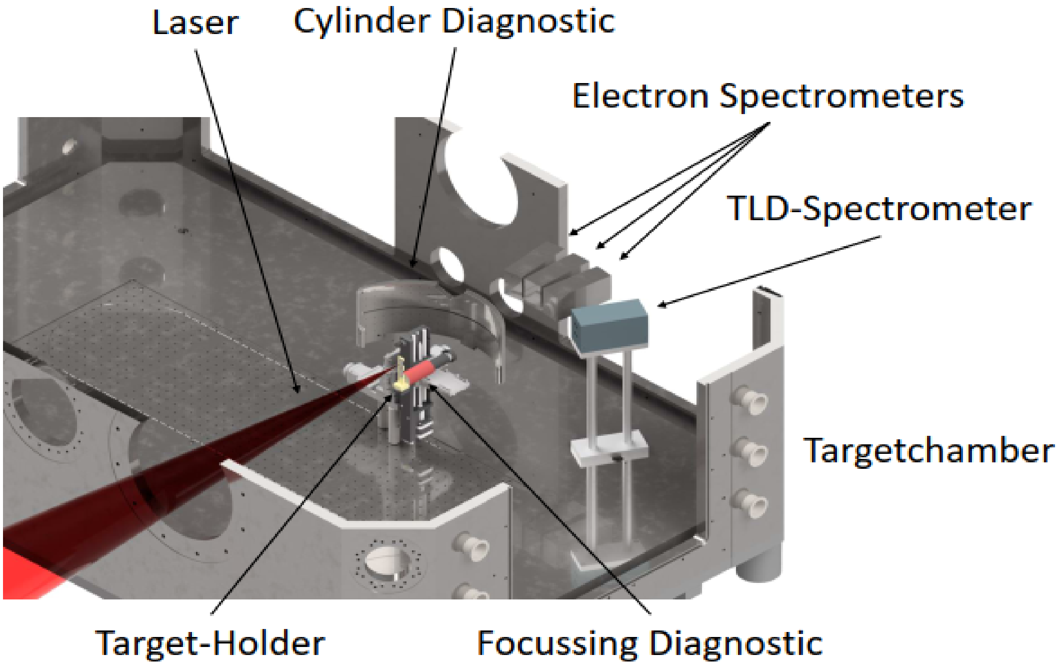

FIGURE 5.3: Section of the experimental setup: in the vacuum chamber the laser beam (red) irradiates the target, cylinder diagnostic, three magnetic spectrometers and 8-channel TLD-spectrometer for characterization of the gamma-radiation spectral distribution in experiment P176 (Zaehter, 2020).

5.3 Selection of the Target Materials

Low density polymer foam layers of 2 mg cm^{-3} density and $300 - 500\,\mu m$ thickness were used as targets in order to to create hydrodynamically stable, large scale, quasi-homogeneous plasmas with a slightly under-critical electron density (Khalenkov, 2006; Borisenko, 2006; Borisenko, 2007; Rosmej et al., 2019). Triacetate Cellulose (TAC, $C_{12}H_{16}O_8$)-layers are optically transparent and characterized by a highly uniform 3D network structure consisting of $1 - 2\,\mu m$ pores, $0.1\,\mu m$ thick and $1\,\mu m$ long fibres with density of approximately $0.1\,gcm^{-3}$. The density fluctuations on the focal spot size

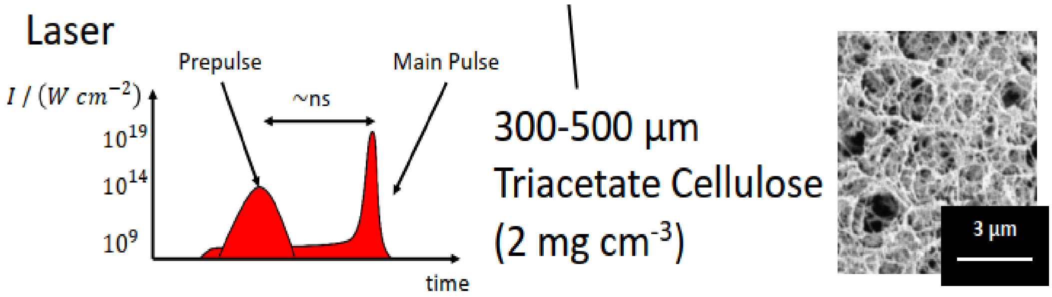

FIGURE 5.4: A schematic view of the PHELIX laser pulses and a vertical cut of the foam target (Zaehter, 2020).

area of 100 μm^2 do not exceed 0.5%.Due to their open cell structure, air contained by pores can be evacuated. The mean volume density of 2 mg cm^{-3} TAC - foam corresponds to $1.7 \cdot 10^{20}$ atoms cm^{-3} and a mean ion charge of $Z_{mean} = 4.2$. Full ionization of all CHO-atoms would correspond to an electron density of $7 \cdot 10^{20}\, cm^{-3}$, which is slightly lower than critical density of $10^{21} cm^{-3}$ for the fundamental wavelength of the Nd:glass laser $\lambda = 1.053\, \mu m$. When the laser interacts with the foam surface, it starts to heat and the solid fibres get ionized. In foams, the NCD plasma was produced by a mechanism of super-sonic ionization when a well defined separate ns-pulse with 1 - 3 J energy was sent onto the foam-target forerunning the relativistic main pulse. The plasma created by the ionization of 0.1 gcm^{-3} ($8 \cdot 10^{21}$ atoms cm^{-3}) dense, 100 nm thick fibres has an overcritical electron density and the fibres thickness is larger than the thickness of the skin layer of $\approx 30nm$. Consequently, it takes time until the created plasma will expand into the pores reaching under-critical electron density and allowing further propagation of the laser pulse into the 3D-like aerogel structure. The energy and intensity of the ns-pulse were well matched to the mean volume density of the target and the thickness of foam layers in such a way that the velocity of the supersonic ionization wave front will be much faster than the ion acoustic velocity. During the propagation of the supersonic ionization wave, the heated high aspect ratio plasma region does not undergo notable expansion. Additionally conventional metallic foils (Cu, Ti) were used as targets. In order to create the NCD plasma, foam or foil layers were irradiated by a well-defined 1.5 ns long pulse with a triangular temporal shape and 1 - 3 J energy, which was sent onto the target forerunning the relativistic short main pulse. The delay between the peak of the ns pulse and the relativistic main pulse was varied from 0 up to 5 ns. The application of sub-mm thick low density foam layers provided a essential increase of the electron acceleration path in a NCD-plasma compared to the case of freely expanding plasmas created in the interaction of the ns-laser pulse with solid foils (Rosmej et al., 2019; Rosmej et al., 2020). In next chapter new experimental results on the interaction of relativistic sub-picosecond laser pulses with sub-mm long NCD plasmas will be presented.

5.4 Description of TLD Spectrometers

Due to the short duration of the sub-picosecond time scale of the laser pulses and the small size of the accelerating fields, an active measurement of x-ray spectra under these conditions is very difficult to implement. Additionally very high number of accelerated electrons on the order of $10^{12} - 10^{13}$ creates essential difficulties for conventional spectroscopic methods. For that reason passive ionizing radiation detectors, such as thermoluminescence dosimeters (TLDs) or image plates are usually applied for the diagnostics in high intensity laser experiments. This section describes 10 and 8 channels absolute calibrated TLD spectrometers, which are based on the thermoluminescence dosimetry method, described in chapter 4, for measurements of the bremsstrahlung spectra in ultrashort-pulsed radiation fields. Implementation of TLD spectomenters is a further development of a work from Behrens et al. (Behrens et al., 2003). The spectral resolution is achieved by use of a set of differently filtered TLD detectors and application of deconvolution techniques. The TLD-cards were placed in a stack between absorbers of different thicknesses and materials, leading to an increasing low-energy cut-off for each subsequent detector. The absorbers were fabricated from different materials of increasing Z. For 10 channels TLD spectrometer these were PVC (Polyvinyl chloride), aluminium, brass and steel. A schematic view is shown in Figure 5.5. The incident x-rays penetrate the TLD cards. The absorbers cause different response of every TLD, which can be used as information about the spectrum of the incident x-rays. For 8-channels TLD detector these were copper, iron and lead. Figure 5.6 shows the schematic drawing of the 8-channels TLD spectrometer. The spectrometers are designed for an energy range from 30 keV to 100 MeV. These few channels spectrometers allow to measure simultaneously the spectral fluences of pulsed electron and photon radiation. The materials of the TLD cards are pieces of doped lithium fluoride in two variations: TLD 700 (7LiF: Mg, Ti) and TLD 700 H (7LiF: Mg, Cu, P). They are suitable for the detection of fast pulsed radiation. The response of the detectors is based on the excitation of the individual decoupled atoms. TLDs absorb radiation and emit photons proportionally to the deposited dose when heated to a few hundred degrees Celsius and have reduced residual signal. TLD cards were calibrated for low- to high-dose ranges and have a very good dose-response and linearity at much higher doses. The detailed description is given in section 4.3. Consequently, the dose readings measured in the different detector layers are made by the dose contributions from electrons and photons with different energies. Therefore, the deconvolution of the spectral fluence of electrons and photons requires knowledge of the dose response of all the detector layers to monoenergetic particles namely response matrix. This response matrix was calculated using the Monte Carlo code FLUKA which is described in chapter 7.

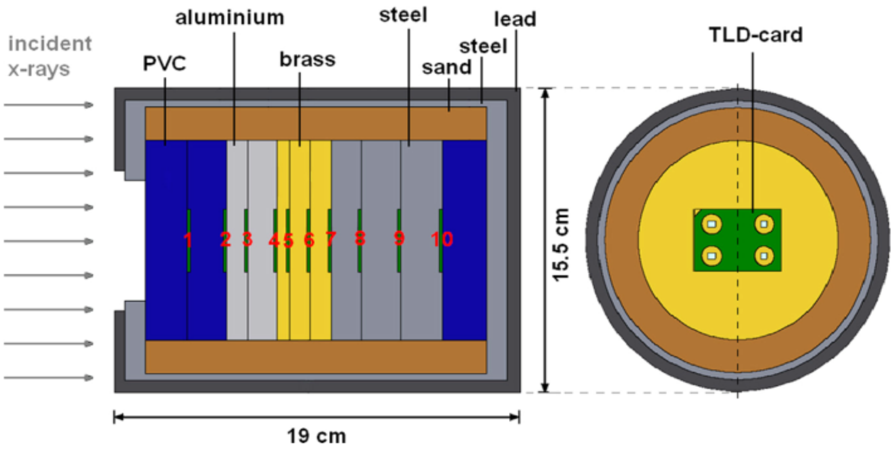

FIGURE 5.5: Schematic view of the TLD-spectrometer: 10 TLD-Cards are placed between absorbers of different materials and thicknesses from lower to higher Z materials inside a shielding (sand-steel-lead) with a collimator window in the front (Horst et al., 2015).

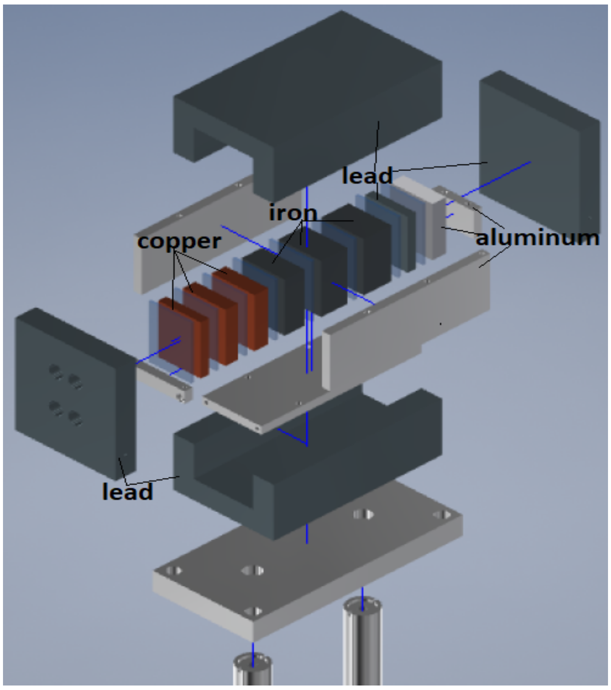

FIGURE 5.6: Schematic view of the TLD-spectrometer: 8 TLD-Cards are placed between absorbers of different materials and thicknesses from lower to higher Z materials inside a lead shielding with four collimator windows in the front.

Chapter 6

Results of the Dose Measurements with TLD Spectrometer

Using pre-ionized by the ns-prepulse low-density CHO-plasma with a mean density near to the PHELIX-laser critical density $n_e = 10^{21} cm^{-3}$ it is possible to increase dramatically amount of 20-100 MeV electrons compared to the case of the laser interaction with foil and thus gain increase of the MeV gamma-rays. Main mechanisms leading to extreme high electron energies are the laser beam self-focusing in the NCD plasma and mechanism of direct laser acceleration of electrons (Pukhov, Sheng, and Vehn, 1999). The following section discusses experimental results on the interaction of relativistic sub-picosecond laser pulses with sub-mm long NCD plasmas. The observed tendency towards the strong increase of the mean electron energy and number of MeV laser-accelerated electrons is reinforced by the results of the gamma-yield measurements.

6.1 Comparison of the Experimental Results Acquired Outside the Vacuum Chamber With Different Types of Target Materials (P138)

In experiment **P138** the bremsstrahlung radiation was produced by MeV electrons passing through a 17 mm thick steel flange, located at a distance of 868 mm from the target in the laser pulse direction. Figures 6.1 and 6.2 show the measured dose readings that were obtained by the 10-channel TLD-spectrometer for laser shots generated at different conditions of target types, high contrast interaction or application of the ns-pulse prior to the relativistic main pulse and position of the TLD-spectrometer: 6.1 at 0° and 6.2 at 90° to the laser pulse propagation direction. When the TLD-spectrometer was placed at 0°, the lowest dose values were measured for shots onto Cu-foils (shots 4, 25, 28) and 500 μm thick CHO-foams (shots 37) that used the high ns contrast $< 10^{-11}$. The results are presented in Figure 6.1. For high contrast laser shots no dependence of the TLD-doses on the target material and the target

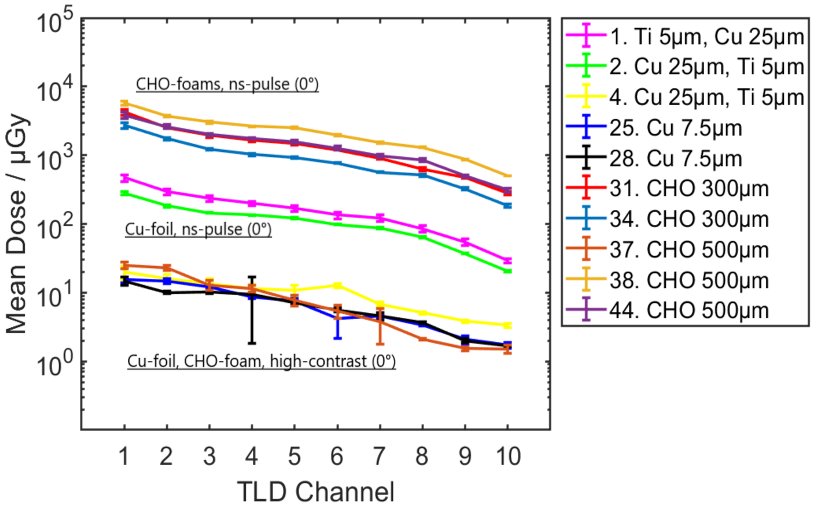

FIGURE 6.1: Dose distribution measured by the 10-channel TLD-spectrometer placed in the direction of the laser pulse propagation for shots made at different conditions. Shots 31, 34, 38, 44 were made onto pre-ionized foam. Shots 1, 2 were made onto pre-ionized foils. Shots 4, 25, 28, 37 were made onto foil or foam at the highest laser contrast.

structure was measured. Shots 1, 2 deal with the case when the main laser pulse interacts with expanded plasma created by the ns-pulse that hit the 25 μm Cu-foil and 5 μm Ti-foil. The density profile of the expanded plasma comprises a relatively short NCD-region, where the effective electron acceleration takes place. Experimentally, we observe a strongly increased level of electromagnetic perturbations in the laser-bay outside the target chamber and one order of magnitude increase in the dose of the gamma-radiation measured by the TLD-detectors. At relativistic laser interaction

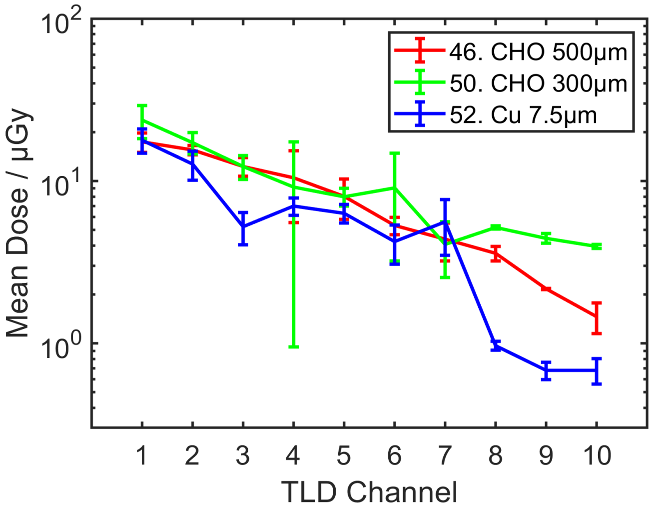

FIGURE 6.2: Dose distribution measured by the ten-channel TLD-spectrometer placed perpendicular to the laser pulse propagation.

with pre-ionized CHO-foams, the creation of the $300 - 500\,\mu m$ long NCD plasmas ensures a longer acceleration path than in the case of freely expanding plasmas, which results in an even more effective coupling of the laser energy into energetic electrons. For example, this effect was clearly observed in the shots 31, 34, 38, 44, where the relativistic laser pulse interacted with pre-ionized CHO-foam. TLD-measurements made in the direction of the laser pulse after its propagation through the long scale NCD-plasma showed a 1000-fold increase of the measured doses in all 10 channels compared to the high contrast case. In the perpendicular direction (Figure 6.2), the measured TLD doses in the case of pre-ionized Cu-foil (shot 52) and CHO-foam layers (shots 46, 50) are very similar. The dose values are close to those measured in the direction of the laser pulse propagation at high laser contrast (Figure 6.1). Therefore, in the case of laser interaction with long-scale NCD-plasmas, the dose caused by the gamma-radiation measured by means of 10 channel TLD spectrometer in the direction of the laser pulse propagation showed a 10^3-fold increase compared to the high contrast shots onto plane foils and doses measured perpendicular to the laser propagation direction for all used combinations of targets and laser parameters. The results of the gamma-yield measurements reinforced the observed tendency towards the strong increase of the mean electron energy and number of super-ponderomotive electrons of 20-100 MeV electrons pre-ionized by the ns-prepulse low density CHO-foams with a mean density near to PHELIX-laser critical density ($n_e = 10^{21}\,cm^{-3}$) compared to the case of the laser interaction with foil.

6.2 Comparison of the Experimental Results Acquired Inside the Vacuum Chamber With Different Types of Target Materials (P176)

In the experiment **P176** the TLD-based diagnostic was used to characterize MeV bremsstrahlung radiation generated in the interaction of the super-ponderomotive electrons with high Z materials such as W, Au as targets simultaneously with polymer foam layers. For this experiment also the s-polarized laser pulse of $1.053\,\mu m$ fundamental wavelength was sent onto targets at 5 - 7 degrees to the target normal, but two different focusing off-axis parabolic mirrors were used providing peak laser intensities of $1 - 2.5 \cdot 10^{19}\,W/cm^2$ ($a_0 = 2.7 - 4.27$) and $7 - 10 \cdot 10^{20}\,W/cm^2$ ($a_0 = 22.6 - 27.0$). The duration of the laser pulse was 750 ± 250 fs. The detailed description of the laser parameters and experimental setup can be found in section 5.2. The TLD-spectometer was placed inside the vacuum chamber at 16° with respect to the laser axis. The distance between the spectrometer and the target was 36 cm. Figure 6.3 shows the dose distribution inside the 8-channel TLD-spectrometer after measurements at PHELIX laser with laser intensities of $1 - 2.5 \cdot 10^{19}\,W/cm^2$. The presented shots were made onto a $10\,\mu m$ thin Ti-foil (shot 15), pre-ionized foam of $500\,\mu m$ thickness (shot 18), pre-ionized foam combined with a $10\,\mu m$ Au-foil attached to the rear side (shot 35) and pre-ionized foam combined with radiators of Au 1mm, 2 mm and W 2mm thickness (shots 31, 33, 34). In the case of the pre-ionized foam, the results of TLD spectrometer showed a 2,5 fold enhancement of the TLD signal averaged over all channels starting from the third channel compared to the results of 10 μm Ti-foil target. The first and the second channels are essentially influenced by the high number of low energy electrons. In the case of the pre-ionized foam combined with a 10 μm Au-foil, the results of TLD spectrometer showed a 12 fold enhancement of the TLD signal starting from the third channel compared to the results of 10 μm Ti-foil target. These results demonstrate the advantages of application foams as targets and a combination of foam layers with thin metallic foils in shots at $1 - 2.5 \cdot 10^{19}\, W/cm^2$ laser intensity and indicate on increased production of high-energy electrons, confirming the electron spectrometer measurements. The results of the electron spectrometer showed that in the case of the foil target, the maximum of the measured electron energy lays in the area up to 15 MeV, while for shots onto the pre-ionized foam stacked together with the Au-foil, the maximum electron energy reached 95–100 MeV (Rosmej et al., 2020). These high-energy and high-current well-directed electron beams are perfectly suited for the production of ultra-intense gammas by the interaction with radiator layers of high Z materials. Figure 6.3 shows the results of increased doses when pre-ionized foam was combined with radiators of Au 1mm, 2 mm and W 2mm thickness (shots 31, 33, 34). It is noteworthy that the highest dose values were obtained using 1 mm thick gold as a radiator, which indicates the optimal thickness for the production of bremsstrahlung photons. Also, the use of tungsten with a thickness of 2 mm gave almost the same results as the result of using gold of a similar thickness. This shows that due to the properties of tungsten and the similar density values for tungsten ($\rho = 19.25\, g/cm^3$) and gold ($\rho = 19.30\, g/cm^3$), this metal can be used as a substitute for gold.

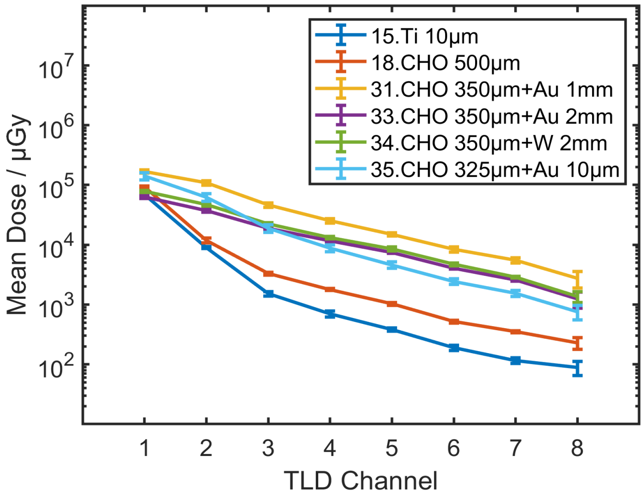

FIGURE 6.3: Dose distribution measured inside the 8-channel TLD-spectrometer placed inside the vacuum chamber for measurements at PHELIX laser with laser intensities of $1 - 2.5 \cdot 10^{19}\, W/cm^2$.

In this experimental campaign, the TLD dose distribution distribution was also measured in the interaction of ultra-relativistic laser pulses of $10^{21}\,W/cm^2$ intensity with metallic foils. Figure 6.4 shows the dose distribution inside the 8-channel TLD-spectrometer after laser shots onto a $10\,\mu m$ thin Ti-foil (shot 8) and radiators of Au 1mm, 2 mm thickness (shots 13, 12). The results obtained at moderate laser intensities of $1-2.5\cdot10^{19}\,W/cm^2$ compared to the results at relativistic laser intensity of $9\cdot10^{20}\,W/cm^2$ in the shots onto Ti-foils (shots 15 and 8) are 2,6 times higher and 7 times higher for shot onto pre-ionized foam (shot 18) than for direct laser shots onto Ti-foil (shot 8) at ultra-relativistic laser intensity. These results correlate good with the measurements of the electron spectrometer. The measured with electron spectrometers effective electron temperature and the maximum of the electron energy were twice higher for shots onto pre-ionized foams at $10^{19}\,W/cm^2$ than for direct laser shots onto standard foils at ultra-relativistic laser intensity of $10^{21}\,W/cm^2$ (Rosmej et al., 2020). The application of the high-Z targets of Au 1mm, 2 mm thickness additionally confirmed the production of high doses for 1 mm Au target but the results of TLD spectrometer showed 2 times higher TLD signal at moderate laser intensity of $10^{19}\,W/cm^2$. Summarizing the results presented in both figures, it is possible to conclude that interaction of high-current well-directed relativistic electrons with high Z targets leads to effective production of MeV bremsstrahlung radiation with the ultra-high photon fluence at moderate laser intensity of $10^{19}\,W/cm^2$. A good agreement between the experimental data and the results of the Monte Carlo code Fluka simulations will be demonstrated in the next chapters.

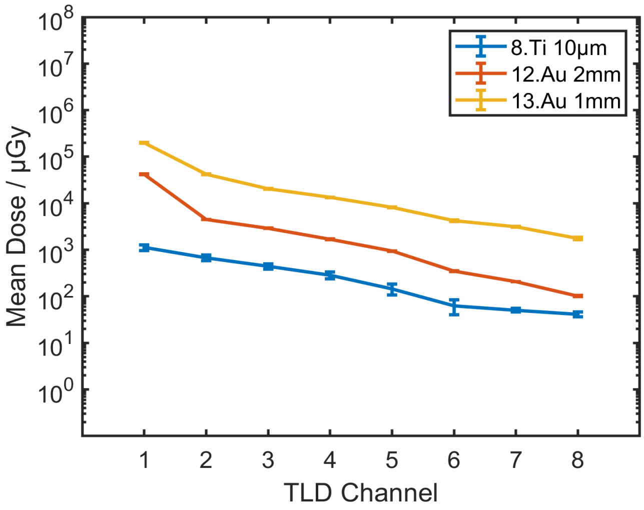

FIGURE 6.4: Dose distribution measured inside the 8-channel TLD spectrometer placed inside the vacuum chamber for measurements at PHELIX laser with relativistic laser intensities of $7-10\cdot10^{20}\,W/cm^2$.

Chapter 7

Monte Carlo Method for Calculations of Radiation Interactions and Particle Transport

The production and transport of the electrons, photons and positrons through different targets are difficult to study only based on the correct experimental results. Therefore, the simulations with an appropriate theoretical model are very important and useful in order to obtain information about particles produced when high intensity laser beam hits the matter. The collisionless particle-in-cell (PIC) codes are usually used for the simulations of the laser-matter interactions. These codes predict with a good precision the processes of production and distribution in space of electrons generated by the laser beam interacting with targets of small densities. But the simulations become impossible for the interactions of electrons with targets of different solid materials with thicknesses of the order of mm, when the collisional energy lost of the electron beam is not negligible. In this case generally used in particle and nuclear physics Monte Carlo codes are very helpful for the simulations of the electron beam moving inside the matter to get information about all produced particles. Monte Carlo codes are not suited for simulations of laser-matter or laser-plasma interactions, but the codes can very good reproduce the transport of laser induced particles and interactions with matter.

7.1 Introduction to Monte Carlo Simulation

The history of Monte Carlo (MC) method began from the early discoveries in probability and statistics and then continued with the search for solutions to complicated diffusion problems that were encountered in first works on atomic energy. French natural scientist Georges-Louis Leclerc, Comte de Buffon (1707–1788) applied probability to a number of his investigations and documented a use of random sampling to solve mathematical problems (Buffon, 1749–1803). The Buffon's needle problem was used for approximation of the π number. Later in 1786 french mathematician, physicist and astronomer Pierre-Simon, marquis de Laplace also suggested that π number could be evaluated by random sampling (Laplace, 1812). Lord Kelvin used the random sampling for evaluation of time integrals associated with the kinetic theory of gases. In 1930 Enrico Fermi applied random sampling to study the properties of the newly discovered neutron and to calculate its moderation. In 1947 John von Neumann, Stanislaw Ulam, Nicholas Metropolis, Enrico Fermi and others developed computer-oriented methods at Los Alamos. Stanislaw Ulam and Nicholas Metropolis coined the term Monte Carlo in 1949 in honour of the games of chance played in the casino in the Principality of Monaco (Metropolis, 1987). This method was effectively used during the Manhatten Project for designing of thermonuclear weapons. Nowadays, the Monte Carlo techniques are widely used for solving difficult physical (e.g. computer simulation of physical processes, particle physics, quantum field theory, astrophysics, molecular modelling, applications in radiation transport, statistical physics and many-body quantum theory) and mathematical problems (e.g. mathematical method for numerical integration, random sampling techniques, convergence, variance reduction techniques, financial market and traffic flow simulations) when it is impossible to use other approaches (James, 1980; James, 1990; Rubinstein, 1981; Kalos and Whitlock, 2008).

Monte Carlo simulation is a technique of estimating the values of an unknown quantity using inferential statistics. The key concepts of inferential statistics are the population, which is a set of examples and the sampling of a proper subset of this population. The important issue is a random sample that tends to exhibit the same properties as the population from which it is drawn. The Monte Carlo methods are mainly used in three problem classes: optimization, numerical integration, and generating draws from a probability distribution. The main idea behind this method is that the results are computed based on repeated random sampling and statistical analysis in order to simulate the real-world phenomena.

The Central Limit Theorem (CLT) provides the needed mathematical foundation of the Monte Carlo method. In probability theory CLT declares that, in many situations, when independent random variables are added, their properly normalized sum tends toward a normal distribution even if the original variables themselves are not normally distributed. In one dimensional case for a variable x, which is distributed accordingly to a function $f(x)$, the average of another function of the same variable $A(x)$ over an interval $[a,b]$ is given by the equation

$$\bar{A} = \frac{\int_a^b A(x) f(x) dx}{\int_a^b f(x) dx}. \tag{7.1}$$

Introducing the normalized distribution $f'(x)$

$$f'(x) = \frac{f(x)}{\int_a^b f(x) dx}, \quad \bar{A} = \int_a^b A(x) f'(x) dx. \tag{7.2}$$

In multi-dimensional case of n variables $x, y, z, ...$, which are distributed according to the normalized functions $f'(x), g'(y), h'(z)...$, the mean value of the function $A(x, y, z,...)$ over n-dimensional domain D is expressed as

$$\bar{A} = \int_x \int_y \int_z ... \int_n A(x, y, z,...) f'(x) g'(y) h'(z)...dxdydz... \tag{7.3}$$

It is impossible to calculate the multi-dimensional integrals with traditional methods, but it is possible to sample N values of A with probability $f'g'h'...$ and divide the sum of the sampled values by N.

$$S_N = \frac{\sum_{i=1}^{N} A(x_i,y_i,z_i...)}{N}. \tag{7.4}$$

In obedience to CLT, for large values of N, the distribution of averages (normalized sums of S_N) of N independent and identically distributed random variables (according to any distribution with mean and variance $\neq \infty$) tends to a normal distribution with mean $\bar{A}$ and variance σ_A^2/N.

$$\lim_{N\to\infty} S_N = \lim_{N\to\infty} \frac{\sum_{i=1}^{N} A(x_i,y_i,z_i...)}{N} = \bar{A}, \tag{7.5}$$

$$\lim_{N\to\infty} P(S_N) = \frac{1}{\sqrt{2\pi \frac{\sigma_A^2}{N}}} \exp\left[-\frac{(S_N - \bar{A})^2}{2\frac{\sigma_A^2}{N}} \right]. \tag{7.6}$$

For any observable A, that can be expressed as the result of a convolution of random processes, the average value of A can be obtained by sampling many values of A according to the probability distributions P of the random processes. The theorem is a key concept in probability theory because it implies that probabilistic and statistical methods that work for normal distributions can be applicable to many problems involving other types of distributions. Initially the Monte Carlo method was not a simulation method, but a technique to solve a multidimensional integro-differential equation by building a stochastic process in such way that some parameters of the resulting distributions would satisfy the equation and then sampling the results of random processes. The accuracy of a MC estimator depends on the number N of samples and converges as $\frac{1}{\sqrt{N}}$ independently on the number of dimensions, while the traditional numerical integration methods converge to the true value as $N^{-1/n}$, where n is the number of dimensions.

In MC the transport or generation of some number of particles dN is described by the evolution of a probability density function $f(\vec{r},\vec{p},t,\alpha)$ with space position within $\vec{dr}$ of $\vec{r}$, momentum $\vec{dp}$ of $\vec{p}$, at time dt of t and α, which includes n other variables like particle species, spin, etc. It is can be expressed by the Boltzmann integro-differential equation, based on the balance in phase space:

$$f_{detector}(\vec{r},\vec{p},t,\alpha) = \int d^3\vec{r_0} \int d^3\vec{p_0} \int dt_0 \int d\alpha_0 G(\vec{r},\vec{p},t,\alpha;\vec{r_0},\vec{p_0},t_0,\alpha_0) f_{source}(\vec{r_0},\vec{p_0},t_0,\alpha_0), \tag{7.7}$$

where $f_{source}(\vec{r_0},\vec{p_0},t_0,\alpha_0)$ is initial particle-number density, $f_{detector}(\vec{r},\vec{p},t,\alpha)$ is a detector of particle-number density after propagating through any material, G is a multi-dimensional operator that encompasses all the microscopic processes, for example: geometry boundary conditions, scattering through various interaction mechanisms, generation of secondary particles, effect of external fields (e.g. magnetic field).

In particular, the Monte Carlo simulation of the radiation transport a particle undergoes represents random series of free flights and interaction events where this particle changes its direction of motion, loses energy and produces secondary particles. This sequential process is called *particle's history*. The Monte Carlo simulation of given experimental conditions consists of the numerical generation of random histories. The created for simulation of these histories corresponding interaction model accomplishes computing calculations of a set of equations with differential cross-sections (DCS) for the relevant interaction mechanisms. The DCSs determine the probability distribution functions (PDF) of the random variables which characterize a track: free path between successive interaction events, type of interactions, energy loss and angular deflection of the particle. When PDFs are known the random histories can be generated by using appropriate sampling methods. If the number of generated histories is large enough, then the quantitative information on the transport process may be obtained by averaging over the simulated histories (Salvat, 2015).

Monte Carlo methods are divided into two types of the performing procedure. First is an analog MC, where the natural laws are presefved the for the solving physical problem and the history of each particle is simulated exactly, it follows the natural PDF. The second is non-analog, also known as biased simulation where in order to reduce required computational time the strict analog simulation of particle histories is bounded. With the biased sampling the resulting scoring is corrected by assigning weights to each history in order to produce a corrected, unbiased estimate of the expected value. In such non-analog MC simulations, the sample variance reduction techniques of the estimated expectation values are applied (FLUKA, 2019a). The simulations described in this thesis were performed by means of the Monte Carlo code FLUKA (Ferrari et al., 2005a; Battistoni et al., 2015; Bohlen et al., 2014). The next sections of this chapter give description concerning of the implemantation of the FLUKA code.

7.2 FLUKA Short Description

FLUKA (**FLU**ktuierende **KA**skade) is a multi-purpose tool for calculations of particle transport and interactions in matter developed at CERN in collaboration with INFN (Insituto Nazionale di Fisica Nucleare). The history of FLUKA begins from

1962 (Ferrari et al., 2005a). The code is developed in Fortran programming language. It has a big variety of applications such as accelerator shielding, target or detector design, activation, calorimetry, radiotherapy and dosimetry, hadrotherapy, neutrino physics, space radiation etc. FLUKA can perform the high accuracy simulations of transport and interaction of 63 different particles, including photons and electrons from 100 eV - 1 keV to thousands of TeV, neutrinos, muons, hadrons of energies up to 20 TeV and all the corresponding antiparticles, neutrons down to thermal energies and heavy ions (Ferrari et al., 2005b). FLUKA code versions 2018, 2019 and 2020 have been used to calculate the results described in this thesis. FLUKA is not a toolkit, it has fully integrated and updated physical models, which are based on original and well-tested microscopic models and optimized by comparing them with experimental data at a single interaction level. FLUKA provides also very good predictivity in cases where no experimental data are directly available. The FLUKA code design has self-consistency, full cross-talk between components and the same level of accuracy for all components. In contrast to other Monte Carlo codes FLUKA has double capability to be used in a biased and fully analogue modes. Therefore, it can be used for simulations of fluctuations, signal coincidences and other correlated events. FLUKA contains a wide set of statistical techniques that can be used to investigate rare events in connection with attenuations by many orders of magnitude. FLUKA can realize very complex geometries, using an improved version of Combinatorial Geometry (CG) package. The FLUKA CG has been designed to track correctly also charged particles in the presence of magnetic or electric fields (Ferrari et al., 2005b). With regard to the simulation of the electron and photon beams FLUKA has been chosen for the improved multiple and single scattering model and for clarity of the implementation of the program routines. A brief introduction to the packages used in FLUKA for the simulations of electromagnetic interactions relevant for this work follows in the next sections.

7.3 Electro Magnetic FLUKA: Transport of Electrons, Positrons and Photons

The **E**lectro **M**agnetic **F**LUKA (**EMF**) is a FLUKA option that activates detailed transport of electrons, positrons and photons. It is obligatory to set EMF either explicitly or implicitly via option DEFAULTS for solving any problems including electrons, positrons and photons interactions. FLUKA uses an original transport algorithm for charged particles (Ferrari et al., 1992), including a complete multiple Coulomb scattering treatment. The Bethe-Bloch theory for energy loss mechanism is applied. The variations with energy of the discrete event cross sections and of the continuous energy loss in each transport step are taken into account precisely. The differences between positrons and electrons are taken into account in both stopping power and bremsstrahlung (Kim et al., 1986). The bremsstrahlung differential cross sections of Seltzer and Berger (Seltzer and Berger, 1985; Seltzer and Berger, 1986) have been extended and the angular distribution of bremsstrahlung photons is accurately sampled. The Landau-Pomeranchuk-Migdal suppression effect (Landau and Pomeranchuk, 1953b; Landau and Pomeranchuk, 1953a; Migdal, 1956; Migdal, 1957) and the Ter-Mikaelyan polarisation effect in the soft part of the bremsstrahlung spectrum (Ter-Mikaelyan, 1954) are also implemented. Electrohadron production (only above ρ mass energy 770 MeV) via virtual photon spectrum and Vector Meson Dominance Model (Moehring, 1989). Positron annihilation in flight and at rest. Delta-ray production via Bhabha and Moeller scattering is also implemented in FLUKA. The lowest transport limit for electrons is 1 keV. The minimum recommended energy for primary electrons is about 50 to 100 keV for low-Z materials and 100-200 keV for heavy materials, unless the single scattering algorithm is used (Ferrari et al., 2005b). In present work the minimum for primary electrons was selected of 100 keV and the lowest transport limit of 10 keV.

For photons pair production with actual angular distribution of electrons and positrons. Landau-Pomeranchuk-Migdal pair production suppression effect (Landau and Pomeranchuk, 1953b; Landau and Pomeranchuk, 1953a; Migdal, 1956; Migdal, 1957). Compton effect with Doppler broadening using a fit of the Compton profiles (Biggs, Mendelsohn, and Mann, 1975; Ribberfors, 1975), and account for atomic bonds through use of inelastic Hartree-Fock form factors. Photoelectric effect with actual photoelectron angular distribution (Sauter, 1931b; Sauter, 1931c), according to the fully relativistic theory of Sauter. Interactions sampled separately for each component element and for each edge. The edge fine structure is taken into account. Parameterisations/tabulations for photoelectric cross sections including all known edges up to Z = 100 and down to a few eV. Optional emission of fluorescence photons and approximate treatment of Auger electrons for all K and most L lines. Rayleigh scattering. Photon polarisation taken into account for Compton, Rayleigh and Photoelectric effects. Photohadron production: Vector Meson Dominance Model (Ranft (Ranft and Nelson, 1987)), modified and improved (Ferrari-Sala) using Peanut below 770 MeV (Fasso et al., 1994). Quasideuteron interactions, Giant Dipole Resonance. Note: the present lowest transport limit for photons is 100 eV. However, fluorescence emission may be underestimated at energies lower than the K-edge in high-Z materials, because of lack of Coster-Kronig effect. The minimum recommended energy for primary photons is about 1 keV.

7.4 Input File for Operations and Simulations with FLUKA

Before running the simulation FLUKA reads the *input file* that has been specified for certain purposes. The input file is an ASCII format text file with extension .inp that consists of a sequence of commands also called *options*, each of which contains one or more lines also called *cards*. Apart from FLUKA commands, the input file contains a geometry description of the simulated set-up. This description is provided using special format geometry *command cards*. Generally, the input file has the following structure:

- Titles and comments
- Geometry description (solid bodies and surfaces, combined to partition space into regions)
- Definition of the materials
- Material assignments
- Definition of the particle source
- Definition of the requested *detectors* for calculation of physical quantities such as dose, fluence, etc. By means of available detector cards detection of the particles can be done for various regions.
- Definition of biasing schemes
- Definition of physical settings such as energy cutoffs, transport threshold energies for particles, step size, physical effects not simulated by default, etc.
- Initialization of the random number sequence
- Starting signals and number of requested histories (Ferrari et al., 2005b)

To calculate the statistical error of the calculated results it is important to perform many other independent runs (minimum 5), each with different initialization. For this purpose, the random number of sequences is produced by FLUKA. The completed input file is run with the FLUKA executable. The output of the run provides a separate file for each detector that has been used in modeling. The output file has to be converted into formatted form by using codes provided in FLUKA for the extraction of data. The input file created for the simulations described in this thesis is given in the Appendix A.

7.4.1 Source of Electrons

All *histories* or *events* are initiated by the source of primary particles. In the simplest case the source is monoenergetic, monodirectional and starts from a single point in space having a shape of pencil beam. The FLUKA card BEAM defines the energy or momentum of the particle and the card BEAMPOS defines the starting position and direction of the beam. These commands are used also to define particle beams which can have simple angular or momentum distribution (Gaussian or rectangular), or a simple transverse profile (Gaussian, rectangular or annular), or different space distribution of starting point (spherical, cartesian or cylindrical shell). When it is required to simulate particle sources with more complex distributions in energy, space and direction or even with more than one type of particles, it can be realized with a special user-written subroutine adding a SOURCE card to the input file (Ferrari et al., 2005b).

The set of simulations has been carried out to estimate the bremsstrahlung, positron and electron yields for monoenergeric electron beams and for electron beams with Maxwellian energy distribution function. These simulations complemented the experimental data that were obtained from two global experiments P138 (2017) and P176 (2019) at the PHELIX laser. For modelling of the monoenergetic electron beam, various kinetic energies have been established with an option of BEAM card: 0.1 MeV, 0.175 MeV, 0.25 MeV, 0.375 MeV, 0.5 MeV, 0.75 MeV, 1 MeV, 1.75 MeV, 2.5 MeV, 3.75 MeV, 5 MeV, 7.5 MeV, 10 MeV, 15 MeV, 20 MeV, 25 MeV, 30 MeV, 40 MeV, 50 MeV, 75 MeV, 100 MeV. For the simulations of the electron beams with Maxwellian energy distribution function SOURCE card delivered electron kinetic energy 10 keV - 100 MeV. Initially, a cylindrical, monoenergetic and monodirectional electron beam was generated to simulate the response functions of the TLD spectrometer, which was applied in experiments P138 at the PHELIX laser. The electron beam had a radius of 7.6 cm in order to cover the area of the TLD spectrometer aperture window. For experiments P176 the propagation of electrons was simulated with Gaussian divergence type where the beam divergence $= 23.5°$. The divergence cone had minimum radius $R_{min} = 10 \mu m$ and the maximum radius $R_{max} = 160 \mu m$. The starting point of the electrons and their direction were declared by means of option BEAMPOS. It is important that the starting point is placed not on a boundary of the regions and not inside a black-hole region. In the Cartesian geometry used by FLUKA the electron beam is injected at X, Y, Z coordinates and is directed along the positive Z axis. X is a horizontal axis perpendicular to the beam. Y is a vertical axis pointing upward. For P138 the beam coordinates are $(0, 0, -88.3) cm$ and for P176 $(1.55, 2.2, -38.202) cm$. Additionally, 10^9 to 10^{10} primary particles were used to run the system in order to minimize the statistical errors in the simulation.

7.4.2 Combinatorial Geometry

The Combinatorial Geometry used by FLUKA is a modification of the program for the neutron and gamma-ray transport developed by MORSE (Emmett, 1984) which was based on the original combinatorial geometry by MAGI (Mathematical Applications Group Inc.) (Guber et al., 1967; Lichtenstein et al., 1979). The Combinatorial Geometry is based on four fundamental concepts: bodies, zones, regions and lattices. The first ones are basic convex objects or closed solid bodies (cylinders, spheres, parallelepipeds, etc.) or semi-infinite portion of space (half-spaces, infinite cylinders or planes) and generic quadric surfaces (surfaces described by 2nd degree equations). Zones are sub-regions defined only via bodies intersection and subtraction. The combinations of the bodies is realized by means of the boolean operations (addition, intersection and subtraction) to perform a complete partition of the space of interest into regions, namely cells of uniform material composition. Regions are defined as boolean operations on bodies (union of zones). Every point must belong to only one region inside the space of interest, defined by means of an external closed body. If the geometry of the simulated object contains some repetitions it is possible to use FLUKA's option - lattice capability. Lattice is a duplication of existing objects (translated and rotated). This allows to avoid describing repetitive structures in all details. Input for the geometry description contains between a GEOBEGIN and a GEOEND card (Ferrari et al., 2005b). Figure 7.1 represents 2D cross sections of the geometry of the TLD spectrometer in Flair geometry editor. The editor is used for viewing or debugging and editing FLUKA geometries in a graphical way.

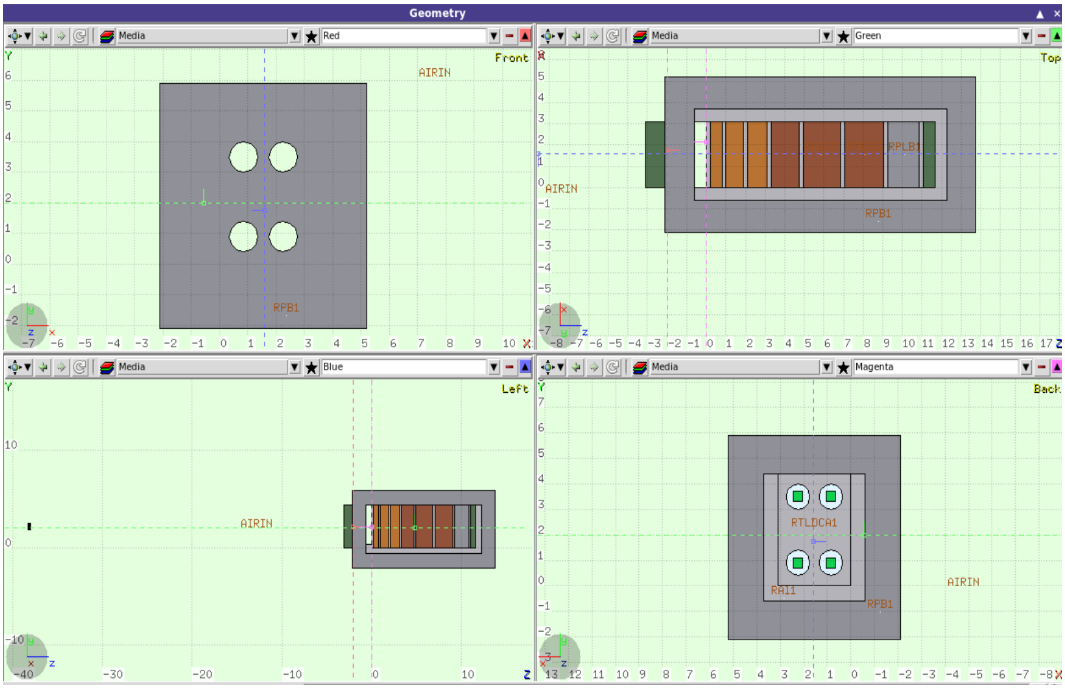

FIGURE 7.1: Representation of the 2D cross sections of the TLD spectrometer geometry in Flair geometry editor. The four view ports, clockwise from the top-left: front -red (X:Y), top -green (Z:X), back -magenta (-X:Y), left -blue (Z:Y).

7.4.3 Materials and Assignment to Regions

Each geometry region is supposed to be filled with a homogeneous material, or with vacuum, or with "blackhole". The latter is a fictitious material used to terminate particles trajectories: any particle is discarded when reaching a blackhole boundary. Materials can be used as simple elements or compounds, where an element can have either natural composition or consist of a single nuclide, and compound indicates a chemical compound or a mixture or an alloy of known composition. An element can be either pre-defined or defined by MATERIAL card giving its number, atomic weight, density, name and a material identification number. The 25 pre-defined materials are available with their default names, index numbers, density, atomic and mass numbers. If the material is not a single element or isotope, but a compound, mixtures or alloy, a command COMPOUND is needed to specify its atomic composition. All materials have to be assigned to the various geometry regions in order to specify of which material each region is made. This is done by command ASSIGNMAt (Ferrari et al., 2005b). For a description of the geometry of simulated experiments, the following materials were included in the model: isotopes of lithium 6 and lithium 7, fluorine, phosphor, chlorine, zinc, iron, aluminum, copper, titanium, tantalum, tungsten, gold and lead. The compound cards were included for the description of the compositions of the TLD cards, sand, brass, polyvinyl chloride, Teflon and air in the vacuum chamber.

7.4.4 Physical Settings, Transport and Production Thresholds

The important task of choosing the correct settings for a calculation problem is simplified by the existence of several "pre-packaged" sets of defaults, each of which is optimised for a particular type of application. Each set is chosen by option DEFAULTS, which has to be placed at the beginning of the input file, preceded only by TITLE or GLOBAL cards. FLUKA DEFAULT declarations contain different executable options suitable for specified kinds of problems. In current simulations PRECISIOn defaults for high precision of the simulations were selected. PRECISIOn contains the following options:

- EMF is activated
- Rayleigh scattering and inelastic form factor corrections to Compton scattering and Compton profiles are activated
- Detailed photoelectric edge treatment and fluorescence photons are activated
- Low-energy neutron transport on down to thermal energies included (high energy neutron threshold at 20 MeV)
- Fully analogue absorption for low-energy neutrons
- Particle transport threshold set at 100 keV, except for neutrons (10^{-5}) eVand (anti)neutrinos (0, but these values can be overwritten for the appropriate task conditions)
- Multiple scattering threshold at minimum allowed energy, for both primary and secondary charged particles
- Delta ray production on with threshold 100 keV
- Restricted ionisation fluctuations is activated, for both hadrons or muons and EM particles
- Tabulation ratio for hadron or muon dp/dx set at 1.04, fraction of the kinetic energy to be lost in a step set at 0.05, number of dp/dx tabulation points set at 80

- Heavy particle e^+, e^- pair production activated with full explicit production (with the minimum threshold= $2m_ec^2$)
- Heavy particle bremsstrahlung activated with explicit photon production above 300 keV
- Muon photonuclear interactions activated with explicit generation of secondaries
- Heavy fragment transport is activated (Ferrari et al., 2005b)

Additionally to these options, the EMFFLUO and EMFRAY cards were activated for all materials. These cards have essential meaning when the EMF option has been implicitly requested via option DEFAULTS. EMFFLUO provides a detailed treatment of photoelectric interactions and the following atomic de-excitation, with a production of fluorescence X-rays and a treatment of Auger electrons. Selection of EMFFLUO option is only meaningful for a material defined with electron and photon cutoffs lower than the highest K-edge in the elements of that material. When EMFFLUO is activated for a compound material, if the incident photon energy is lower than the highest K-edge for any constituent element, FLUKA uses separate parametrised representations of the photoelectric cross section between different edges of each constituent element (all levels are tabulated). If the photon energy is higher than the highest K-edge, average cross sections for the compound are used, but FLUKA still samples a single element on which to interact, in order to generate the correct fluorescence photon or Auger electron.

EMFRAY activates Rayleigh coherent scattering and Compton binding corrections and profile function corrections in selected regions. The full treatment of electron binding and motion in Compton scattering is activated. It is particular important for low energies and heavy materials, and in general for all problems where the best accuracy for photon transport is requested.

For activation of gamma interactions with nuclei PHOTONUC card was added to the input file. Because photonuclear cross sections are much smaller than photon cross sections for electromagnetic interactions with atoms and electrons, analogue simulations of photonuclear interactions are very inefficient. Therefore, PHOTONUC card was used in combination with LAM–BIAS to increase artificially the frequency of photonuclear interactions (Ferrari et al., 2005b).

Production thresholds and transport cutoffs in selected regions for electrons, positrons and photons must be explicitly set using the EMFCUT command for all materials in the model. In current FLUKA simulations the energy threshold for electron and positron production is 10 keV and for photons is 1 keV. Electron and positron transport energy cutoff is also 10 keV and for photons is 1 keV.

7.4.5 Estimators and Scorings

Monte Carlo simulation often means a “mathematical experiment”. The results of the Monte Carlo simulations are obtained by using estimators also called as "detectors" defined for certain purposes. A detector is an equivalent of a measurement instrument. Each detector is designed to estimate one or more radiometric quantities, and the final score is a statistical estimation of the average value of the corresponding population. As in experimental measurements, it is possible to calculate a standard deviation by running several independent calculations. In FLUKA no default detector is available and each scoring option must be explicitly requested. There are different input options corresponding to different types of detectors. FLUKA offers numerous different estimators, therefore the scoring the respective quantities has to be requested directly from the input file. The following scoring options were used for the quantities investigated in this thesis:

USRBIN is an detector for scoring the detailed spatial distribution of energy deposition, dose, star density, momentum transfer or integrated particle fluence distributions in a uniform spatial mesh independent of geometry. There are several types of binnings: Cartesian, 2D-cylindrical, 3D-cylindrical and even more complex phase space structures described by the user.

USRBDX is a the boundary-crossing detector, which estimates fluence or current, mono- or bi-directional, differential in energy and angle on any boundary between two selected regions. The normalisation area is needed to obtain a current in particles per cm^2. It is performed using an area value input by the user. If none is given, the area is assumed to be $= 1.0 cm^2$ and the option amounts simply to count the total number of particles crossing the boundary. Similarly, if fluence is scored, but in this case, each particle is weighted with the secant of the angle between the particle trajectory and the normal to the boundary surface at the crossing point.

USRYIELD is a multi-purpose estimator option, which can estimate several different double-differential quantities. The main one is an energy-angle double-differential yield of particles escaping from a target, the angle in this case being with respect to a fixed direction. The results are double-differential distributions with respect to a pair of variables, one is generally energy-like (kinetic energy, momentum, etc.) and the other is angle-like (polar angle, rapidity, Feynman-x, etc.) Energy and angle can be replaced by many other variables which are mostly of the same kind, such as momentum and rapidity. But it is possible also to score yields as a function of charge and Linear Energy Transfer (Ferrari et al., 2005b).

In the FLUKA simulations described in this thesis the USRBIN detector was applied to score energy deposition and distributions of photons, electrons and positrons fluences in space.The energy deposition results are normalized to [GeV/cm^3 per primary particles], the fluence results are normalized to [particles/cm^3 per primary particles]. Additionally the energy deposition, dose and the total particle fluences were calculated for each crystal of TLD cards, which were used in experiments of dose measurements in TLD spectrometers. USRBDX scoring card was used as boundary crossing estimator for the simulation of the fluences of bremsstrahlung photons, electrons and positrons from the external side of the target. Only one way scoring option was chosen, therefore no backscattered particles are counted by the estimator. The results from USRBDX estimator are given in terms of [particles/cm^2GeV per Steradian per primary particles]. USRYIELD detector was used to calculate the angular distributions of particles passing a given surface and the double differential distributions of the particles resulting from the interactions of electron beams with targets. The results are normalized as double differential [particles/GeV per Steradian per primary particles].

7.4.6 Particle Histories and Statistical Errors

At the end of the input file it is obligatory to use START card in order to begin the calculation.This card defines the termination conditions, gets a primary from a beam or from a source, identifies the number of particle histories requested and starts the transport. The result could be scored in single run, or in several runs. Distribution of scoring contributions by single run can be very asymmetric because many can histories contribute as zero. In Monte Carlo methods for calculation of the statistical errors of the results it is necessary to perform other independent runs (at least 4 or 5), each with a different independent initialization of random number sequence. Several runs are possible to perform in parallel or one after each other in a cycle mode. In case of cycle running the random number sequence used in a run is initialized by default by the seeds provided with the code. For the next run the seeds written by the program at the end of the previous run are used. For running several jobs in parallel the independent random number sequences has to be initialized by the user. The scoring of the distribution from batches of several histories tends to Gaussian distribution when number of samples $N \to \infty$, provided $\sigma^2 \neq \infty$ accordingly to CLT. The standard deviation of an estimator calculated from batches or from single histories is an estimate of the standard deviation of the actual distribution. The goodness is such estimation depends on the type of estimator and on the particular problem, but it converges to the true value for $N \to \infty$. The variance of the mean of an estimated quantity x calculated in N batches, is

$$\sigma^2_{<x>} = \frac{1}{N-1}\left[\frac{\sum_1^N n_i x_i^2}{n} - \left(\frac{\sum_1^N n_i x_i}{n}\right)^2\right] \tag{7.8}$$

where n_i is the number of histories in the i_{th} batch, $n = \sum n_i$ is the total number of histories in the N batches, x_i is average of x in the i_{th} batch $x_i = \sum_{j=1}^{n_i} \frac{x_{ij}}{ni}$ where x_{ij} is the contribution to x of the j_{th} history in the i_{th} batch (FLUKA, 2019b).

7.4.7 Variance Reduction and Importance of Biasing

The completeness of the Monte Carlo calculation is the degree to which the resulting data has converged to the average behaviour of the system. In practice, this convergence is very slow. There is usually a large variance in the histories of the primary particles, requiring a large number of primaries to be tracked before the average behaviour emerges. Furthermore, tracking a single primary particle can take a significant amount of processing time modelling the complexity of electromagnetic cascade. Therefore, to define the efficiency of the Monte Carlo calculations the quantities of speed and variance have to be taken into account. A useful quantity to measure the efficiency is a *figure of merit*, defined as

$$computer\, cost\, of\, an\, estimator = \sigma^2 \cdot t \tag{7.9}$$

where σ is the variance and t is the mean computing time per primary particle (FLUKA, 2019b). The figure of merit is a useful tool not only as an efficiency measure and tool for gauging the value of variance-reduction measures but also for estimation of the time needed to achieve a prescribed precision. Often reducing variance σ^2, the CPU time per primary particle t increases and vice versa. Therefore, minimizing $\sigma^2 \cdot t$ means to reduce σ at a faster rate that t increases or vice versa. That is so because t is proportional to the number of histories n and σ^2 is inversely proportional to that number $1/n$. Thus, applying a particular computational method to a certain problem, it is up to the user to minimize computer cost, because the method of its minimization is subject to the details of a given problem.

The analogue Monte Carlo particle transport calculations allow to study fluctuations and correlations, it samples from actual phase space distributions, predicts average quantities and all statistical moments of any order, but it is inefficient and converges very slowly, it also fails to predict important contributions due to rare events providing only a statistical estimate of the correct answer rather than a precise value. A very efficient way to reduce the probable error in an analogue calculation is to increase the number of histories. In this case the error decreases as the inverse of the square root of the number of histories, so that the computer time required may become very essential for a specified small probable error. In many cases it is important not to simulate exactly what occurs in reality, but to estimate in the most efficient way the desired response. This can be obtained by replacing the actual physical problem with a mathematically equivalent one and having the same solution but faster statistical convergence. FLUKA has available special biasing techniques for reduction of the error without increasing the computational efforts.

An analogue FLUKA simulation samples from true distributions of particle-matter interactions and particle transport, resulting in histories which are meant to accurately represent the histories of real particles. However, such realistic histories may be dominated by physics which leave out regions of phase space that are of interest, relegating these regions to be sampled only in rare events, and a large computer cost for a quantity of interest. A biased simulation samples from distributions which are biased, either in favour of above mentioned rare events, or in some other way which aims to reduce computer cost. Every particle that is tracked is given a statistical weight, and these weights are adjusted to compensate for whatever biasing is applied. In this way, biasing does not make influence on the solution, but how the calculation converges to the solution.

The efficiency of the Monte Carlo simulation is also affected by the type of scoring and the methods of sampling used for the random walks of particles. The central concept for improving the efficiency process is to assign to each particle a statistical weight or numerical value of its importance to the desired detector response. In the general physical situation or in the direct analogue mathematical simulation, the weight of each particle is unity. However, this is not necessary. If each particle is given some arbitrary weight or importance value, and if the detector response is defined in terms of the sum of all weights of the particles contributing to the response, the transport description of the particles is unchanged. Thus in a biased Monte Carlo simulation, the scoring of the particles at the detector must be modified from just the sum of the particles scores to the sum of the particles weighted scores. FLUKA offers the following biasing techniques: Importance Biasing (BIASING), Leading Particle Biasing (EMF-BIAS), Multiplicity Tuning (BIASING), Biasing Mean free paths (LAM-BIAS), Weight window (WW-FACTOr, WW-THRESh, WW-PROFIle), Biased down scattering for neutrons (LOW-DOWN), Non analogue absorption (LOW-BIAS), user defined biasing. The importance of biasing is based on the two complementary techniques Geometry Splitting (reduces σ but increases t) and Russian Roulette (does the opposite) (Ferrari et al., 2005b). For the FLUKA simulations described in this thesis the importance of biasing was requested by the option BIASING. Applying this option each geometry region is assigned to a number between 10^{-}4 and 10^4, proportional to the contribution that particles in that region are expected to give to the desired result. Additionally LAM–BIAS was used to sample with acceptable statistics photonuclear reactions which have a much lower probability than competing electromagnetic photon reactions, but are often very important for radiological applications.

7.5 Radiation Units Used in FLUKA and Experiments

For investigation and simulation of different physical effects in radiation fields it is important to specify the parameters of interest. The following physical quantities were used to describe radiation effects and particle transport:

N**:** number of identical particles

N_0**:** number of atoms per unit volume

$\lambda\ (cm)$**:** mean free path, the average distance passed by a particle in a material before an interaction.

$\Sigma = 1/\lambda\ (cm^{-1})$ **:** macroscopic cross section, probability of interaction per unit distance. Both λ and Σ depend on the material, particle type and energy.

$\sigma = \dfrac{\Sigma}{N_0}\ (barn = 10^{-24}cm^2)$**:** atom effective area, microscopic cross section is the area of an atom weighted with the probability of interaction or the probability of interaction per unit length, with the length measured in $atoms/cm^2$

$l\ (cm)$**:** total distance passed by a particle

$v\ (cm/s)$**:** average particle velocity

$F\ (particles \cdot cm^{-2} \cdot sec^{-1})$**:** flux is a term describing the number of particles passing through a unit area over a certain time.

$\Phi(r,v) = n(r,v)dl\ (cm^{-2})$**:** particle fluence is defined as the time integral of the particle flux and characterized as the number of particles per unit area that passed during certain time. The particle fluence is normalized per cm^2 and describes the density of particle tracks.

$\Phi_E = \dfrac{d\Phi}{dE}\ (cm^{-2}MeV^{-1})$**:** energy distribution of the particle fluence.

$\dot{R} = N\dfrac{dl}{dt}\Sigma = Nv\Sigma$**:** reaction rate

$\dfrac{\dot{R}}{dV} = \dfrac{dN}{dV}v\Sigma = n(r,v)v\Sigma$**:** reaction rate inside the volume element dV

$D = \dfrac{d\bar{E}}{dm}\ (J/kg, GeV/g, RAD, Gray)$**:** the absorbed dose is the amount of energy deposited in a medium by ionizing radiation. It is equal to the mean energy deposited per unit mass of medium. In the definition of the absorbed dose, the energy imparted by the ionising radiation to matter in a volume is given by $E = R_{in} - R_{out} + \sum Q$, where R_in is the radiant energy incident on the volume, the sum of all the energies (excluding rest energies) of all charged and uncharged ionising particles which enter the volume. R_{out} is the radiant energy emerging from the volume. $\sum Q$ is the sum of all changes of the rest mass energy of nuclei and elementary particles in any interactions that occur in the volume (Ferrari et al., 2005b).

Chapter 8

Characterization of Bremsstrahlung Radiations from Different Targets

This chapter presents the investigation of bremsstrahlung spectra for mono-energetic electron beams from different materials of low Z (Titanium $Z = 22$) to high Z (Gold $Z = 79$, Lead $Z = 82$) elements as an $e - \gamma$ targets. Simulations using Monte Carlo code FLUKA provided the results of positron and bremsstrahlung fluences from target surfaces of various thicknesses. The thickness of $e - \gamma$ targets has been varied from thin targets of $10\,\mu m$ to thick of $2\,mm$ thickness. Additionally the response functions of the TLD spectrometers to mono-energetic electron beams were simulated for the deconvolution of the electron spectra from the measured dose readings of the dosimeters. Using an unfolding algorithm based on a sequential enumeration of matching data series the electron spectra were calculated for all variants of targets that were used in the experiments. This method has been validated with the cross checking simulations of the TLD dose values. The characteristics of the simulated particle spectra were investigated. The electron distribution function was described by two temperature Maxwellian distribution function. The obtained from the modelling electron temperatures depended on the target material and thickness and were in agreement with electron temperature scaling laws.

8.1 Investigation of the $e - \gamma$ Targets

The investigation of bremsstrahlung is a very broad field for both theoretical and experimental research. In 1959 Koch and Motz presented a summary of theoretical formulae of various bremsstrahlung cross-sections, differentials of photon energy and photon scattering angle for thin targets and for a wide range of incident electron energies (Koch and Motz, 1959). The regimes of validity, in terms of incident energy, outgoing photon energy, angle and radiator atomic number are discussed and evaluated for thin targets. At the depth of a thick bremsstrahlung target, the intrinsic angular distribution of photons for a thin target should add up with the angular distribution of an electron formed by multiple scattering (Nordell and Brahme, 1984).

L. I. Schiff derived a formula for the angular photon distribution for semi-thin targets (Shiff, 1946). Seltzer and Berger have published a review that included extensive tables of bremsstrahlung photon spectra (Seltzer and Berger, 1985; Seltzer and Berger, 1986). A later survey of the various theoretical cross-sections that were used in the Monte Carlo codes is written by Salvata (Salvata et al., 2006). Despite numerous publications and the very advanced status of theoretical research, there are very few accurate experimental measurements of the photon bremsstrahlung spectrum produced by high-energy electrons. A number of measurements have been made for electrons with energies of 10 to 30 MeV incident on thick targets of Al and Pb (Faddegon, Ross, and Rogers, 1990; Faddegon, Ross, and Rogers, 1991). When the radiators of comparatively high thickness are used in experiments the comparison of the experimental results with analytically predicted becomes complicated since multiple scattering and secondary processes become important. Monte Carlo simulations can take into account the effects of radiator thickness and collimation on the photon spectrum and angular distribution.

Over the past several decades, many researches have been devoted to the investigation of the photon energy spectra. To determine the bremsstrahlung spectra, a wide range of methods have been proposed. There are analytical modeling (Shiff, 1946), Monte Carlo simulations (Rogers, Faddegon, and Ross, 1995; Fippel, 2003), the experiments on the unfolding of radiation data measured by spectrometry (Faddegon, Ross, and Rogers, 1990; Landry and Anderson, 1991). Reconstruction from measured transmission data, dosimetry data or dose depth curves are another popular techniques to determine the bremsstrahlung spectra (Bloch, 2000; Archer, Almond, and Wagner, 1985; Nisbet, 1998; Francois, 1997; Catala et al., 1995; Huang, Kase, and Bjarngard, 1983; Hinson and Bourland, 2002). Since each method has different advantages and disadvantages, it is important to have independent means to validate the results of any given approach. Additionally the knowledge about angular distributions of photons and production of positrons from thick targets is not sufficiently complete. Therefore, the Monte Carlo simulations using particle transport code FLUKA have been carried out to generate bremsstrahlung radiations by bombarding mono-energetic electron beams on different target materials of low to high Z of various thickness from 10 μm to $2 mm$.

8.2 Simulation of Bremsstrahlung Photons, Electrons and Positrons Generated due to Impact of Mono-Energetic Electron Beams with Ti, Ta, W, Au, Pb Targets of Different Thicknesses

The huge set of MC FLUKA simulations was carried out to estimate the fluences of bremsstrahlung photons, electrons and positrons produced as a result of the impact of the mono-energetic electron beams with Ti, Ta, W, Au, Pb targets of different thicknesses. The following parameters of electron beams and target materials were used in the performed simulations:

- **Electron energy :** 0.1 MeV, 0.175 MeV, 0.25 MeV, 0.375 MeV, 0.5 MeV, 0.75 MeV, 1 MeV, 1.75 MeV, 2.5 MeV, 3.75 MeV, 5 MeV, 7.5 MeV, 10 MeV, 15 MeV, 20 MeV, 30 MeV, 40 MeV, 50 MeV, 75 MeV and 100 MeV
- **Materials used as $e-\gamma$ target (Z) :** Ti (22), Ta (73), W (74), Au (79), Pb (82) (The materials with higher melting point were chosen for bremsstrahlung study.)
- **Target thickness :** 10 μm, 100 μm, 1 mm, 2 mm

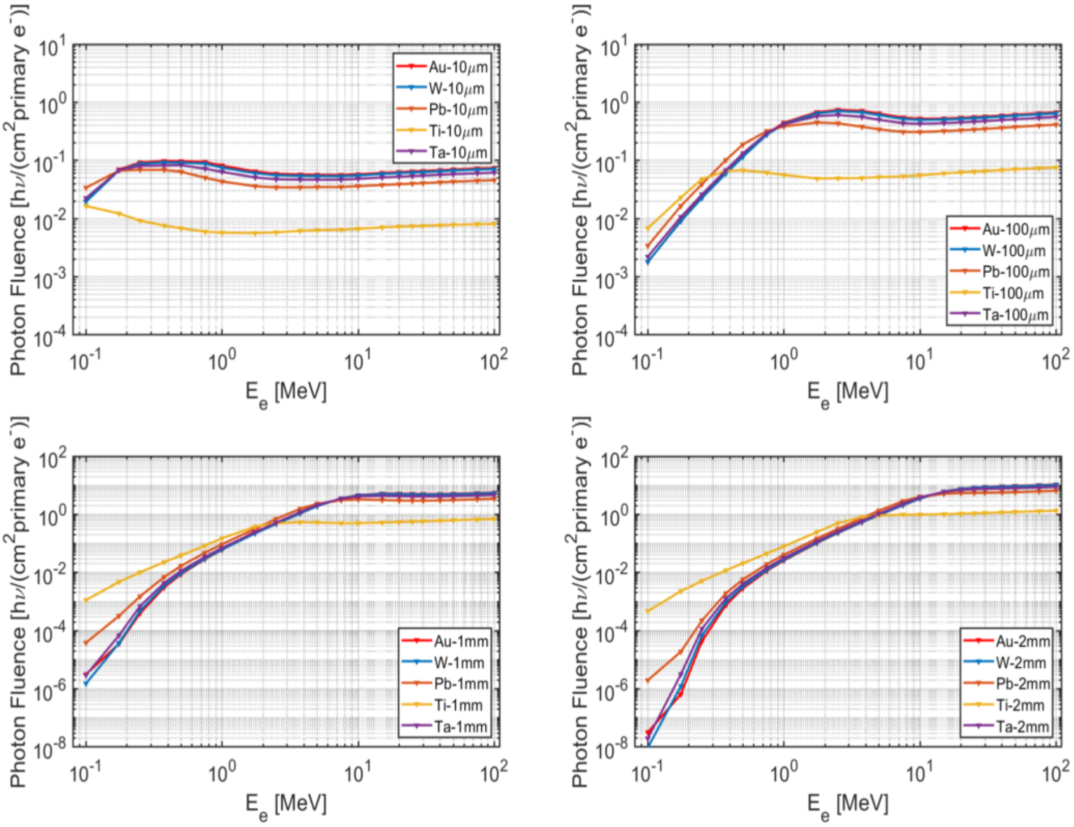

FIGURE 8.1: Integrated bremsstrahlung fluences versus energy of incident electrons on Ti (22), Ta (73), W (74), Au (79), Pb (82) targets of 10 μm, 100 μm, 1 mm, 2 mm thickness. The photon fluence was detected from the rear side of the target.

The configuration of the electron beam in FLUKA simulations is described with details in section 7.4.1. The targets had length and width of 0.7 cm each. The particle fluences were traversing throw the targets of 10 μm, 100 μm, 1 mm, 2 mm thickness. The virtual detector for registering of the resulting particle was placed on the rear side of the target. In order to minimise the statistical errors in the simulations 10^9 primary particles were used to run the system. The estimated percentage error was less than 0.1%. When a high-energy electron beam interacts with a target material electromagnetic cascade is developed, which produces electrons, positrons, and bremsstrahlung photons through the inelastic collisions of electrons. The variation of the integrated bremsstrahlung fluences with incident electron energy for different materials Ti ($Z = 22$), Ta ($Z = 73$), W ($Z = 74$), Au($Z = 79$), Pb($Z = 82$) is shown in Figure 8.1. It is observed that the bremsstrahlung fluence increases with increase of incident electron energy, since the collision energy losses of electrons are predominating at low electron energies while radiative losses start becoming essential at high electron energies. Also the bremsstrahlung fluence increases with the atomic number Z of the target except the lead Pb ($Z = 82$), where the bremsstrahlung fluence was found to be less compared to W ($Z = 74$) and Au ($Z = 79$). This is due to the smaller density value of the lead ($\rho = 11.34\, g/cm^3$) compared to the density values for tungsten ($\rho = 19.25\, g/cm^3$) and gold ($\rho = 19.30\, g/cm^3$), since the bremsstrahlung losses are proportional to the density of the target material. It is noted that for, higher density material the bremsstrahlung fluence peaks are shifted towards the low energy electrons for the targets of the lower thickness of 10 μm, 100 μm when Z number of the targets decreases. The energy losses of the high energy electrons moving through a material of small thickness are lower and in the low energy range the characteristic bremsstrahlung dominates. Therefore, the highest photon fluence is produced by the low energy electrons in case of thin targets and by high energy electrons in case of thick targets of the same matherial. The variation of the integrated positron fluence

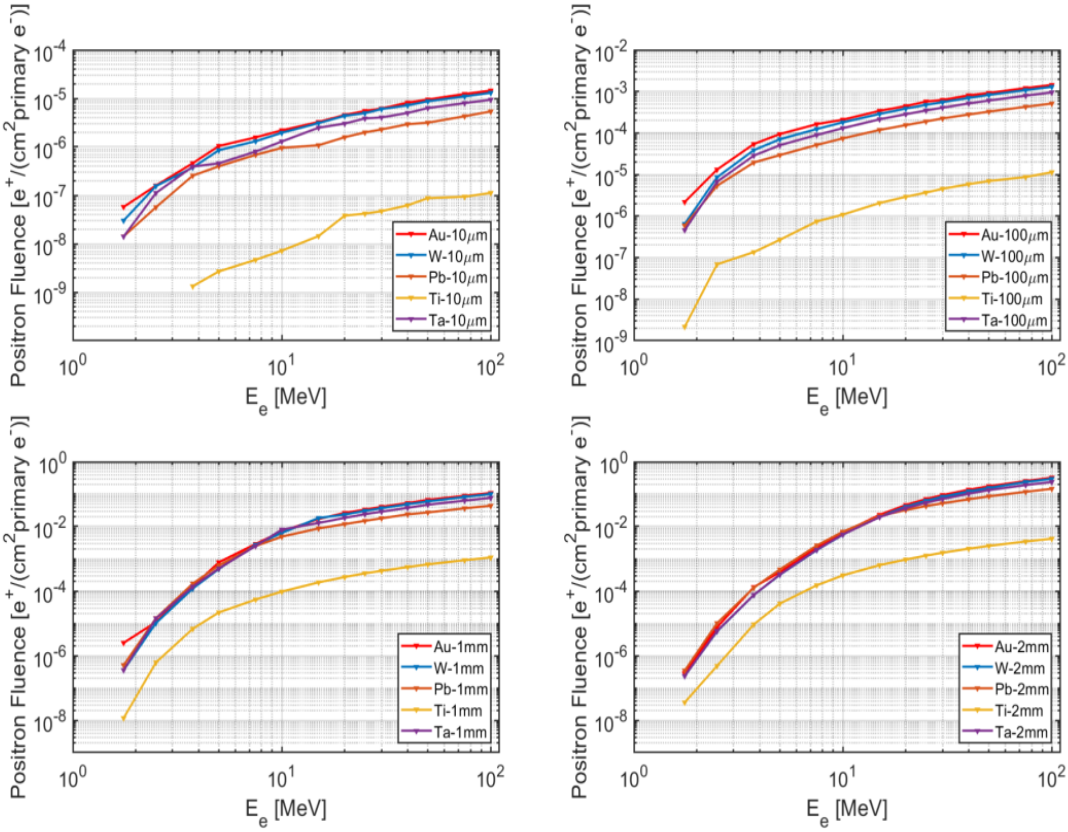

FIGURE 8.2: Integrated positron fluences versus energy of incident electrons on Ti (22), Ta (73), W (74), Au (79), Pb (82) targets of 10μm, 100μm, 1 mm, 2 mm thickness. The positron fluence was detected from the rear side of the target.

as a function of incident electron energy for targets of different thicknesses is shown in Figure 8.2. The contribution of positron is also estimated in the forward direction, which found to be 3 to 4 order less than the bremsstrahlung intensity. The targets produce positrons through the pair production process which has bigger cross section for higher energy of bremsstrahlung radiation. The grate number of positrons are produced in high Z targets since the cross section for pair production is directly proportional to Z^2 of the element. It is observed from the Figure 8.2 that as the target thickness increases the positron production also increases till a certain thickness and beyond that the positron contribution will fall due to the absorption of positron in the target itself. Figure 8.3 shows the variation of the electron fluence as a function

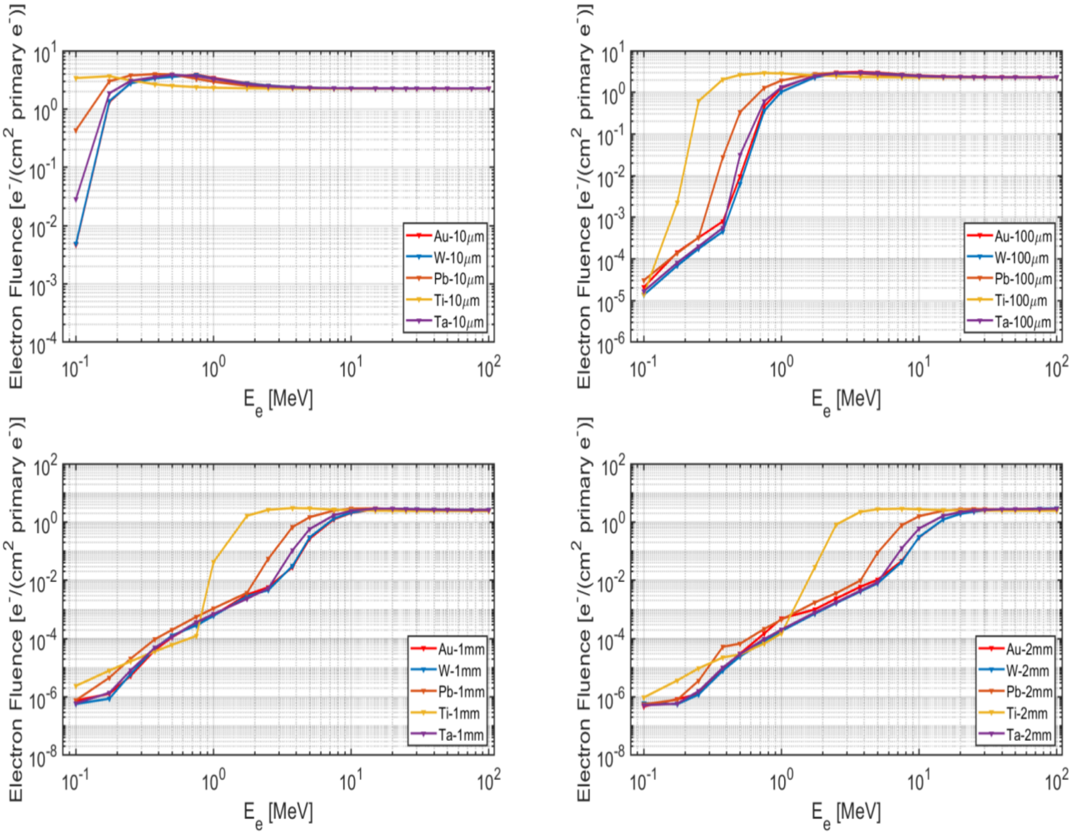

FIGURE 8.3: Integrated electron fluences versus energy of incident electrons on Ti (22), Ta (73), W (74), Au (79), Pb (82) targets of 10μm, 100μm, 1 mm, 2 mm thickness. The electron fluence was detected from the rear side of the target.

of incident electron energy for targets of different thicknesses. These results present the contribution of the direct transmitted electrons in the photon beam. It is found that when the thickness of the target increases, higher amount of the electrons gets absorbed in the target. This results in higher production of bremsstrahlung photons. For low Z material larger thickness is required to stop the incident electrons inside the target, while for high Z material smaller thickness is sufficient to stop the incident electrons.

The variation of the induced integrated fluences of bremsstrahlung photons and positrons with incident electron energy for **Au** targets is shown in Figure 8.4. It is observed that as the thickness of the target increases, the bremsstrahlung fluence also increases till certain energy of the incident electron beam and then stays almost constant with further increase of the electron energy. The production of positrons is getting higher in a case of thick targets and permanently increases with increase of electron energy in the selected electron energy range. Moreover, the production of positrons depends on the intensity of the bremsstrahlung radiation generated in the target. For each monoenergetic electron beam, there exists an optimal Au thickness to obtain the maximum photon and positron fluences. The results of FLUKA simulations of positrons and bremsstrahlung radiations generated in various targets (Ti, Ta, W, Au, Pb) for different energy of the incident electrons from 0.1 to 100 MeV are summarized and added to the Appendix B.

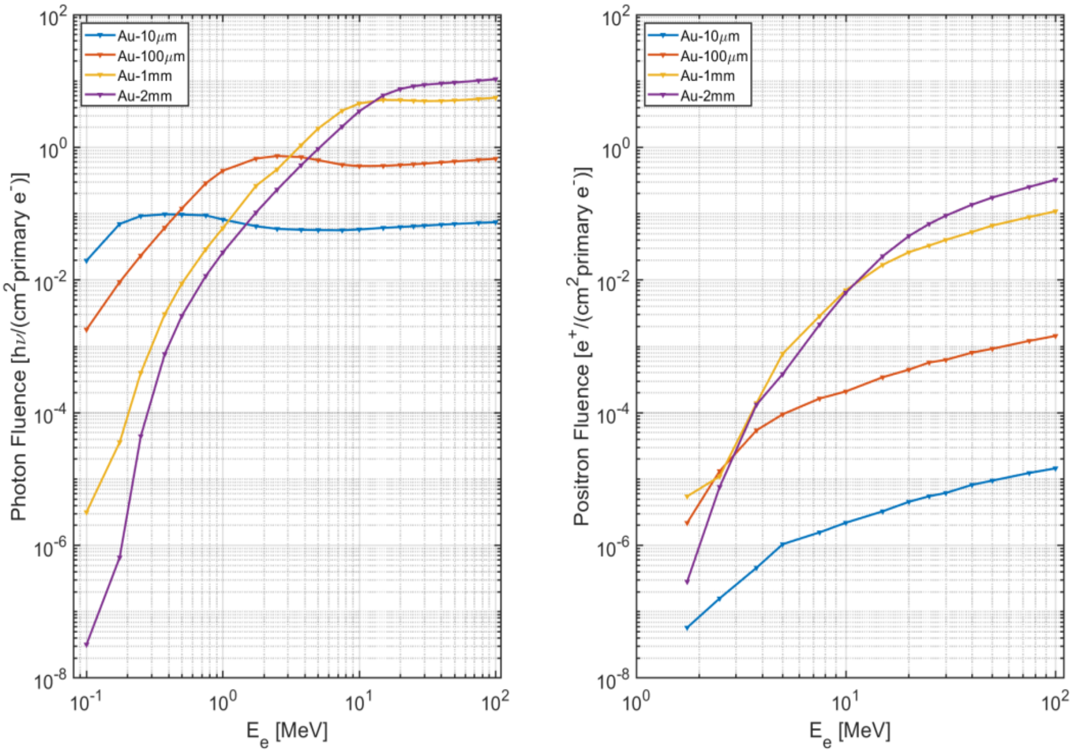

FIGURE 8.4: Integrated fluences of positrons and bremsstrahlung photons versus energy of incident electrons on Au targets of 10 μm, 100 μm, 1 mm, 2 mm thickness.

In the real physics process, the electron beams generated in the laser–plasma acceleration cannot be monoenergetic. If the electrons are produced by direct laser acceleration (DLA) regime or LWFA regime, their spectra are the superposition of exponential spectra with flat-top or quasi-monoenergetic spectra. Thus the results from monoenergetic electrons condition can be extended to the condition of flat-top spectra electron beams with specific energy bandwidth, and the comparison between these conditions improves understanding of the process.

8.3 FLUKA Simulations of Response Functions and Dose Distributions in TLD Spectrometer to Mono-Energetic Electron Beams

The dose readings measured in the different channels of the TLD-spectrometers resulted from contributions made by photons and electrons with different energies. Consequently, the deconvolution of the spectral distributions of the electrons requires information about the dose response functions of all the spectrometer layers to monoenergetic particle fluxes. The response matrix R_{ij} was calculated using the Monte Carlo multi-particle transport code FLUKA (Ferrari et al., 2005a) in the energy region between 100 keV and 100 MeV for electrons. The real geometry of the experimental set-up and environment were recreated for the simulations with help of the FLAIR interface for FLUKA. Figure 8.5 shows the simulated response functions of the ten channels TLD spectrometer to monoenergetic electron radiation. The dose reading per incident electron fluence depending on the electron energy is given. The obtained results are normalized to the primary particles. The different curves represent the responses for the different TLD layers (Figure 8.5 (a)). The TLDs in the front channels respond to lower particle energies than the TLDs in the rear channels. The fluctuations at low values of the electron energy have statistical nature. Figure 8.5 (b) shows that the low-energy electrons produce small dose values. The penetration depth of the electrons depends on their energy. Also the high energy electrons produce additional amount of the bremsstrahlung radiation in the rare layers of the TLD spectrometer. Figure 8.6 shows the complete response matrix simulated for the 10 channels TLD spectrometer.

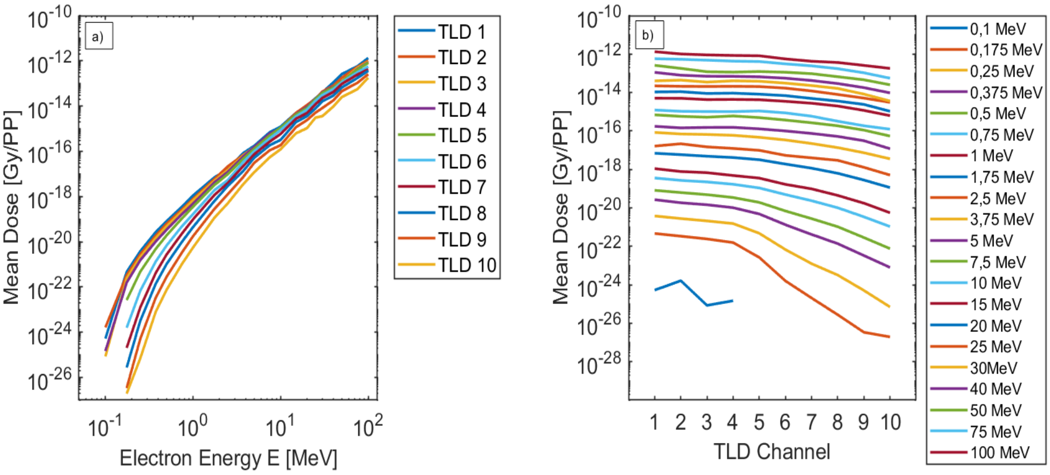

FIGURE 8.5: Simulated response functions of the ten channels TLD spectrometer to monoenergetic electron radiation in the experiment **P138**.

In the experiment **P176** the eight channel TLD-spectometer, described in section 5.4, was placed inside the vacuum chamber at 16° with respect to the laser axis.

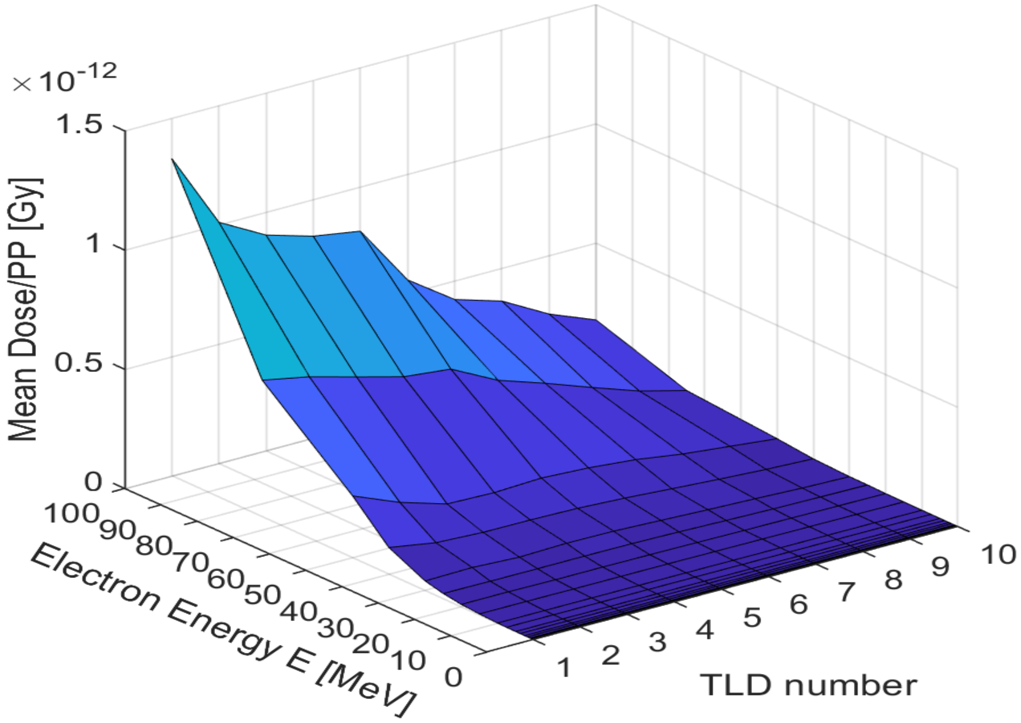

FIGURE 8.6: Response matrix calculated for electrons with energies between 10 keV and 100 MeV for the 10 channels TLD spectrometer in the experiment **P138**.

The distance between the spectrometer and the target was 36 cm. Therefore, new response functions to monoenergetic electron beams were simulated taking also into account the target material. Figure 8.7 shows the simulated response functions of the eight channels TLD spectrometer to monoenergetic electron radiation and Figure 8.8 shows the complete response matrix simulated for this spectrometer.

The approximate dose values for 20 energy intervals with different interval widths ΔE_j =[0.1; 0.175; 0.25; 0.375; 0.5; 0.75; 1; 1.75; 2.5; 3.75; 5; 7.5; 10; 15; 20; 25; 30; 40; 50; 75; 100] MeV were calculated by the following equation

$$D_{i\,calc} = \sum_{j=1}^{20} = \Phi_j(E) R_{ij} \Delta E_j \tag{8.1}$$

with an electron fluence $\Phi_j(E)$ and an average response R_{ij} of a channel i over the energy interval ΔE_j. The electron fluence depending on the energy was approximated by a Maxwell distribution function with two electron temperatures T_{e1} and T_{e2} and corresponding absolute numbers of electrons N_{e1} and N_{e2} (Rosmej et al., 2019).

$$\frac{dN_e}{dE_j} = \frac{N_{e1}}{T_{e1}} \exp\left(\frac{-E_j}{T_{e1}}\right) + \frac{N_{e2}}{T_{e2}} \exp\left(\frac{-E_j}{T_{e2}}\right). \tag{8.2}$$

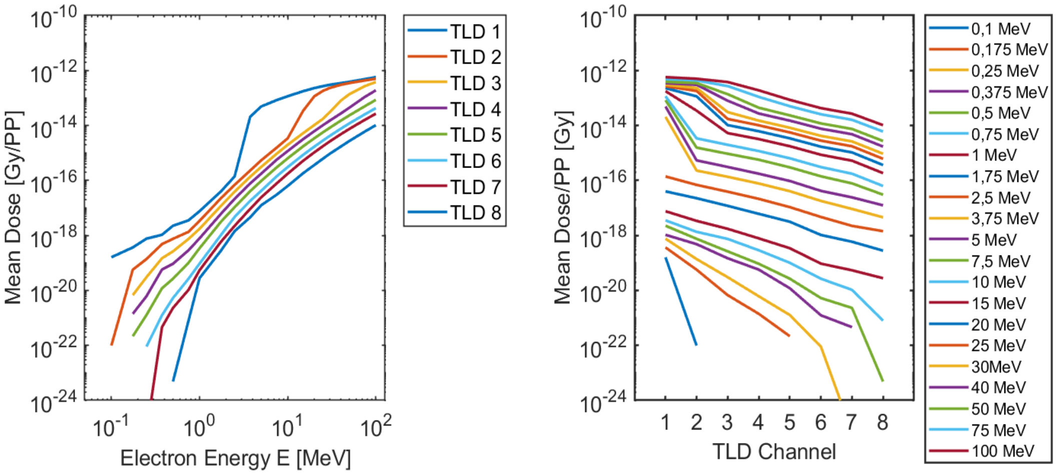

FIGURE 8.7: Simulated response functions of the eight channels TLD spectrometer to monoenergetic electron radiation in the experiment **P176**.

For the calculation of the electron spectrum, an unfolding-algorithm was created and applied, since the analytical calculation is impossible due to an inverse problem. The aim of the unfolding algorithm is to calculate a spectral fluence configuration $\Phi_j(E)$ according to equation 8.1 as precise as possible.

8.4 The Unfolding Algorithm

The unfolding algorithm was based on a sequential enumeration of matching data series and performed a best possible curve matching with the calculation of errors for deviations between the experimental and the simulated dose values. The task of the sequential enumeration is a listing of the all possible solutions of a given problem. The design of enumeration algorithms involved several important aspects that have to be taken into account in order to achieve correctness and effectiveness in the performance of the calculations. The enumeration algorithm had to prove that each solution output was only once created without duplication. A straightforward way to achieve this is to store in memory all found solutions, and whenever a new solution is encountered, then test whether it has been already output or not. But this approach is memory inefficient when the solutions are large with respect to the memory size, or if there are too many solutions. To solve this problem it would require a dynamic memory allocation mechanism and efficient search. For these reasons, that enumeration algorithm has to find out whether a solution has been already output without storing the already generated solutions. Additionally, the implicit forms of duplication should also be avoided. For this purpose it can be useful to define a canonical form of encoding for the solutions allowing easy comparisons. A very good approach to solve these problems is to use brute-force algorithm. Brute-force search, also known as generate and test algorithm, is a very general problem-solving technique that consists of systematic enumeration of all possible candidates for the solution and

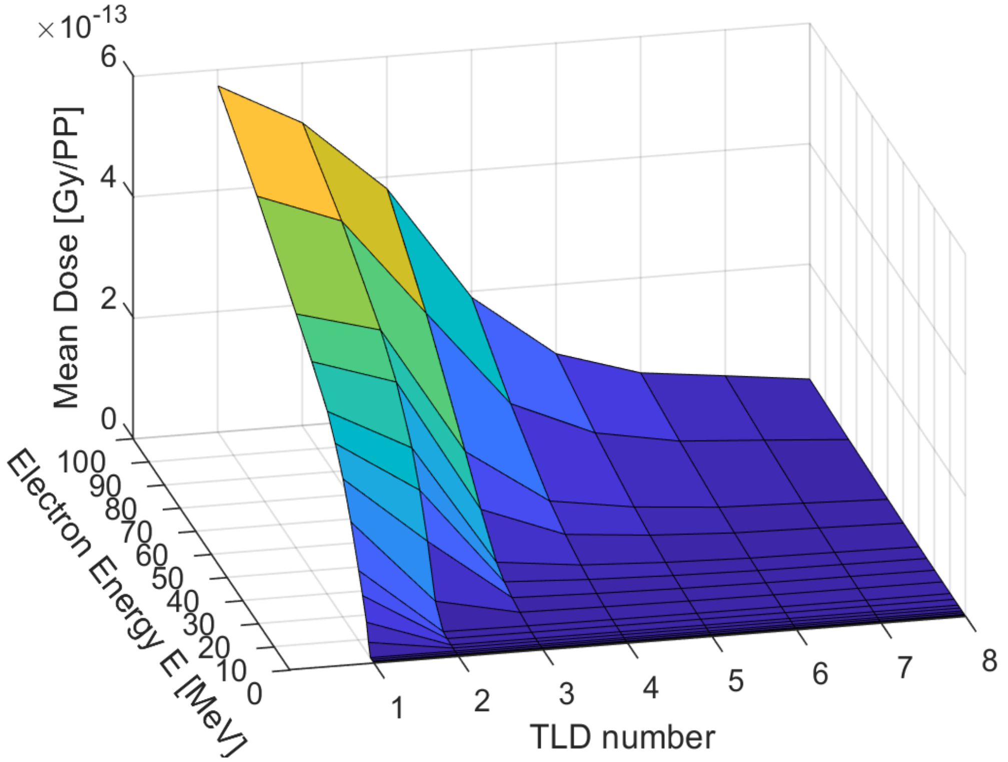

FIGURE 8.8: Response matrix calculated for electrons with energies between 10 keV and 100 MeV for the 8 channels TLD spectrometer in the experiment **P176**.

checking whether each candidate satisfies the problem's statement or not (Marino, 2015).

The unfolding algorithm was written using MATLAB language functions. The first step of this algorithm was to load the response matrix obtained from the simulations using Monte Carlo code FLUKA. The next step was to create an electron fluence according to the equation 8.2, varying the parameters T_1 and T_2 in the available range from 0.1 MeV till 30 MeV with a step interval of 0.2 MeV, varying the parameters N_1 and N_2 in the allowable range of $10^9 - 10^{13}$ and varying the coefficient that determines the ratio of N_1 and N_2 in the range of $0.01 - 0.5$ with a step interval 0.003. After every variation of one of the parameters the dose values D_{icalc} were calculated by the equation 8.1. These calculated dose values were used as an input for brute-force part of the unfolding algorithm for fitting with the measured dose values. The uncertainty of the fitted function is calculated by the mean absolute percentage error (MAPE), also known as mean absolute percentage deviation (MAPD), which is a measure of prediction accuracy of a forecasting method in statistics. MAPE expresses the accuracy of calculated doses in relation to the measured ones as a ratio defined by the following equation

$$MAPE = \frac{100\%}{n} \sum_{i=1}^{n} \left| \frac{D_{i\,meas} - D_{i\,calc}}{D_{i\,meas}} \right| \tag{8.3}$$

where $D_{i\,meas}$ is the measured values of the doses and $D_{i\,calc}$ is the simulated values of the doses.The absolute value in this ratio is summed for every forecasted results of the channel in TLD spectrometer and divided by the number of fitted points n. The procedure of variation of the input parameters was repeated till the $D_{i\,calc}$ with the smallest MAPE were found. Figure 8.9 shows the example of the obtained results of the reconstruction of the TLD-doses by the unfolding algorithm for eight channel TLD spectrometer simultaneously with the experimental results for laser shots on foam targets with Au foils of 10 μm, 1 mm and 2 mm thickness. The smallest MAPE was found of 0.89%, 1.12%, 0.28% for the corresponding calculated values in relation to the experimental results. These results confirm a very good agreement between the experiment and calculations.

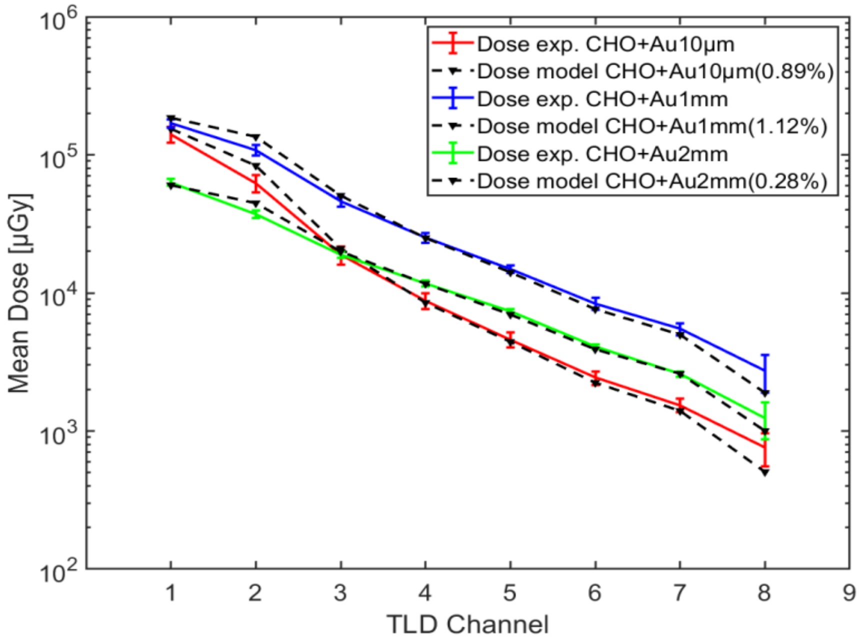

FIGURE 8.9: The results of the comparison of the reconstructed by the unfolding algorithm TLD-doses with experimental results for laser shots on foam targets with Au foils of 10 μm, 1 mm and 2 mm thickness.

The last step of the unfolding algorithm was the definition of the parameters of the electron fluence with two temperature exponential function. The configuration of the fluence values is used for further FLUKA simulations of the electron, photon and positron spectra from the targets of different thickness.

In order to validate the unfolding algorithm, the evaluated output electron spectra was used as an input data for cross-checking FLUKA simulation. The purpose of this modeling was the interaction of the obtained spectrum with the corresponding target which resulted in dose values on the simulated TLD detectors. Then to compare the results of doses obtained via the simulations and experiments. Figure 8.10 shows the results of the simulations which confirmed the coincidence of the simulated doses and experimentally measured ones. This proves the correctness of the calculations performed using the unfolding algorithm. Thus, the application of the unfolding algorithm makes it possible to use TLD diagnostics to obtain information about spectral distributions and use a combination of experimental and Monte Carlo simulation data.

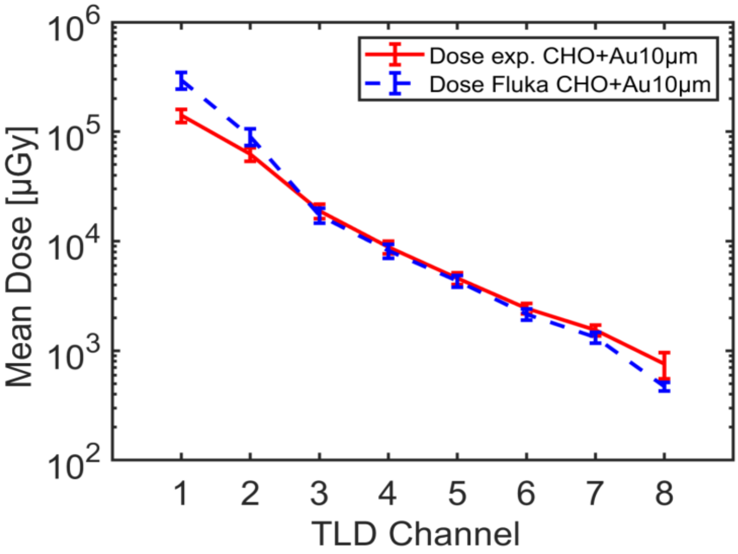

FIGURE 8.10: Comparison of simulation and experimental results The results of the comparison of the FLUKA simulated TLD-doses with experimental results for laser shots on foam targets with Au foils of 10 μm thickness.

8.5 Evaluation of the Electron Temperatures

The electron temperatures were evaluated from the measured TLD-doses by means of the unfolding algorithm procedure using FLUKA-simulations that accounted for a real geometry of the experimental set-ups and the environment and used a two electron temperatures approximation. The best fit was achieved by keeping the deviations of the simulated doses from measured values with the smallest MAPE for all detector channels of the TLD spectrometers simultaneously. Figure 8.11 shows the resulting values of T_{e1} and T_{e2} for selected laser shots on different targets in the experiment **P138**. Shots 31, 34, 38, 44 were made onto pre-ionized foam of 300 μm thickness in shots 31 and 34 and 500 μm thickness in shots 38 and 44. Shots 4, 25, 28, 37 were made onto foil or foam at the highest laser contrast. As expected, in the case of the foams, when the TLD doses reached their maximum value, both electron temperatures are essentially higher compared to T_{e1} and T_{e2} evaluated for the case of high contrast shots. In the case of the laser interaction with pre-ionized foams, the best fit of all ten TLD-signals was obtained for $T_{e1} \simeq 12$ MeV and $T_{e2} \simeq 2-5$ MeV. The application of CHO-foams as targets initiated essential increases the temperature and number of the accelerated in forward direction electrons, which is in agreement with the DLA-scaling while the temperature for electrons at large angles to the laser propagation direction matches the ponderomotive scaling. This observation of the

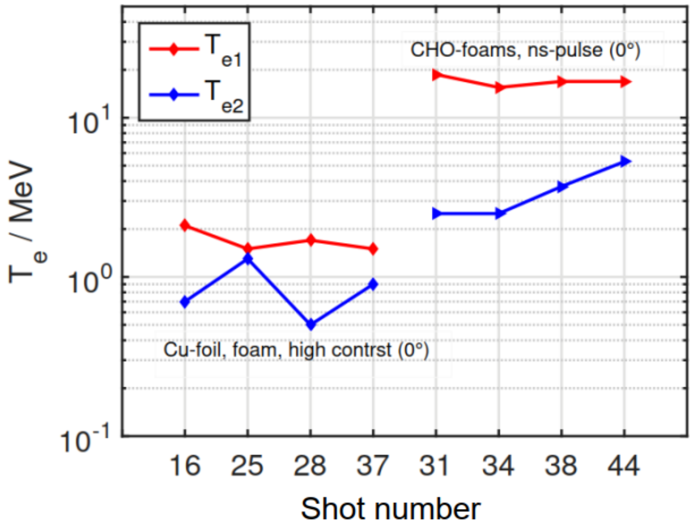

FIGURE 8.11: Electron temperatures evaluated from the measured TLD-doses (experiment **P138**) via the the unfolding algorithm using FLUKA-simulations results which were taking into accounted a real geometry of the experimental set-up and the environment and used a two electron temperatures approximation.

Targets	T_{e1} [MeV]	T_{e2} [MeV]
CHO + Au 10 μm	16.5	7.3
CHO + Au 1 mm	24.9	2.7
CHO + Au 2 mm	22.7	4.9

TABLE 8.1: Electron temperatures evaluated from the measured TLD-doses (experiment **P176**) via the the unfolding algorithm using FLUKA-simulations results

directionality of superponderomotive electrons generated in NCD plasmaswas was theoretically predicted (Pugachev et al., 2016; Pugachev et al., 2019). In the case of the shots at the highest laser contrast $T_{e1} \simeq T_{e2} \simeq 0.5 - 2.5$ MeV. These results show a very good correlation with the experimental conditions and with the results of the electron spectrometers (Zaehter, 2020). The measured doses allow retrieving N_{e1} and N_{e2} and then the absolute numbers of electrons N_e that interacts with the flange and produce a signal inside the TLD-cards. According to the experimental set-up and TLD geometry, these are electrons that propagate along the laser axis with a half angle divergence of $\theta = 3.3°$ and $N_e = 0.5 - 2 \times 10^{10}$ electrons, which is in good agreement with direct measurements made by means of two electron spectrometers. This number corresponds to up to 8 -16 nC of the well-directed super-ponderomotive electron beam (Rosmej et al., 2019).

In experiment **P176**, the eight channel TLD spectrometer (described in section 5.4) was used inside a vacuum chamber placed at an angle of 16° degrees. Applying an unfolding algorithm for TLD dose measurements after laser shots with an intensity of $1.9 \cdot 10^{19}\ W/cm^2$ on combination of CHO foams and Au foils of different thicknesses, the results presented in the Table 8.1 were obtained. These data are in a good agreement with the results of the electron spectrometer measured at 15° to the laser propagation axis for the same combinations of CHO foams and Au foils (Rosmej et al., 2020).

Chapter 9

FLUKA Simulations of Laser Driven Photon, Electron and Positron Spectra

When a high energy accelerated electron beam interacts with a high Z target material, it generates a cascade shower of bremsstrahlung radiation and the continuous spectra of photons, positrons and secondary electrons. The bremsstrahlung photons give possibility to perform different experiments such as investigation of the nuclear structures, various interaction mechanisms, developing and detecting different materials. Therefore, it is desirable that the photon beam has a maximal intensity and minimal scattering angle. As it is described in section 8.2 the intensity of the bremsstrahlung photons depends on the atomic number Z of material, density and material thickness. Therefore, by varying the target thickness in simulated models of the interactions of electron spectra with Maxwellian distribution with high Z targets, an optimal thickness can be defined that the photon flux will be maximal.

9.1 Simulation Results of the Laser-Driven Electrons

The results of the TLD measurements, FLUKA simulations of the spectrometer response functions and the unfolding algorithm made it possible to obtain the spectra of electrons produced during the interaction of the ultra-shot relativistic laser pulse with various targets. The evaluation of the electron spectra from the readings of 10 TLDs was resolved in 20 energy bins and was performed applying an unfolding algorithm based on a sequential enumeration of matching data series of the dose values measured by the dosimeters and calculated by means of FLUKA-simulations, as described in section 8.4. The electron spectra follow a Maxwell distribution function with two electron temperatures T_{e1} and T_{e2}. The results of evaluation of the electron temperatures are described in section 8.5. Figure 9.1 shows the electron spectra evaluated by means of unfolding algorithm using data measured by TLD spectrometer for the laser interaction with pre-ionized foam layer combined with Au-foil targets of $10\,\mu m$ thickness (laser shot 35, PHELIX beam-time P176, 2019). The electron spectra is described with a Maxwell distribution function with two electron temperatures

$T_{e1} = 16.5\,MeV$ and $T_{e2} = 7.3\,MeV$. This is also consistent with the experimental data of the electron spectrometer (Rosmej et al., 2020; Gyrdymov, 2020). According to results of the simulations, the total number of electrons with $E_e > 0.1\,MeV$ propagating forward in 2π solid angle reaches the value of $N_e = 2.515 \cdot 10^{13}$ that corresponds to $\approx 4\,\mu C$ of the electron charge.

Monte Carlo simulations were performed to study the process of generation of the photon beams and their characterization. In order to study the variation of bremsstrahlung spectra that is produced as a result of the impact of energetic electron beam with the targets of different Z number from Al, Ti, Fe, Ta, W, Au, Pb material and different thickness ranging from $10\,\mu m$ to $4\,mm$ the electron spectra evaluated for 35th laser shot was used as a source of incident electrons. The features of the target materials are given in Table 9.1.

Many different applications that use laser-generated photon beams require information about photon yields. The conversion efficiency between electrons and bremsstrahlung photons depends on the electron energy, the converter material and converter thickness. Hence, in order to obtain the largest photon yields, produced by the defined electron spectra, not only the atomic number of the material plays an important role but also its thickness. When the target thickness increases, the generated photons number also increases due to continuous interaction of electrons with

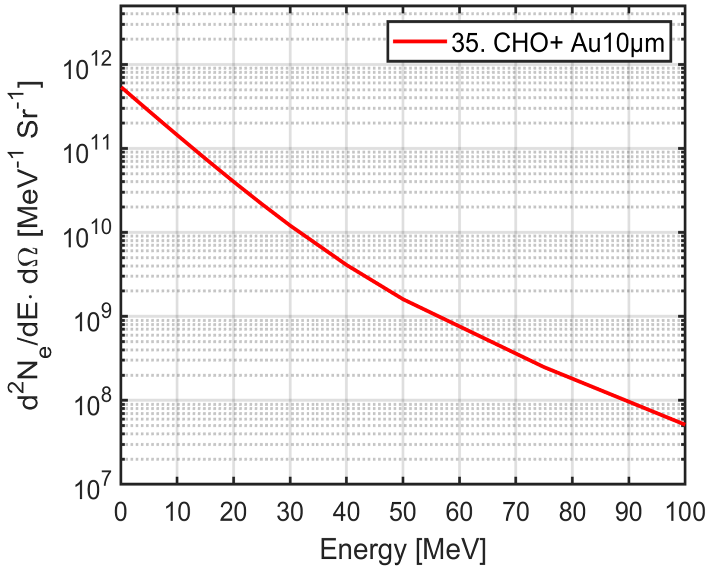

FIGURE 9.1: Electron spectra evaluated for laser shot of $10^{19}\,Wcm^{-2}$ laser intensity onto the pre-ionized foam layer combined with Au-foil targets of $10\,\mu m$ thickness (laser shot 35, PHELIX beam-time P176, 2019). The evaluation of the electron spectra from the readings of 10 TLDs was performed applying an unfolding algorithm based on a sequential enumeration of matching data series of the dose values measured by the dosimeters and calculated by means of FLUKA-simulations.

Target Material	Z number	Density $[g/cm^3]$	Melting point $[°C]$
Aluminum (Al)	13	2.7	660.32
Titanium (Ti)	22	4.506	1668
Iron (Fe)	26	7.874	1538
Tantalum (Ta)	73	16.69	3017
Tungsten (W)	74	19.25	3422
Gold (Au)	79	19.3	1064.18
Lead (Pb)	82	11.34	327.46

TABLE 9.1: Some features of the target materials

the target. However, the energetic photons will be attenuated as the thickness further increases, leading to the decreasing photon number. When these two processes get into balance it could result in the largest yield of gamma photons emitting from the different targets. Therefore, the information about the material and the thickness which maximise the photons yields or produces certain spectra of the irradiated particles is very important for the planning of the experiments. Repeating the simulations for several target thicknesses it was possible to determine the thickness which maximises the photon yields for the initial electron energy distribution function.

Positrons can be indirectly produced by laser-plasma accelerated electrons interacting with target also called as converter. The thickness of the high-Z solid targets is also important parameter for the positron yield since the generation and annihilation of positrons take place inside the target. More energy will be deposited with thicker targets, which favours positron generation. But increasing annihilation in thicker targets will decrease the resultant number of positrons. Thus, there should exist an optimal thickness to obtain the maximum positron yield for incident electron beams with a given spectrum.

The photon, electron and positron fluences were obtained from the simulation of the interaction of the described above electron spectra with Au targets of various thickness are shown in Figure 9.2. The differential over energy particle fluences were integrated over the solid angle in the region of particle propagation. The spectrum of photon energies produced through the bremsstrahlung interaction is continuous. This photon energy ranges from the energy of 100 keV up to a maximum value of energy which is equal to the maximum energy of the incident electron. The photon fluence decreases monotonically with increasing photon energy. The generated photon beam in turn generates ultrafast positron spectra. The resulting positron energy is not quite high although the photons and electrons have considerably high energies. The large numbers of low energy positrons have been stopped and annihilated inside the converter. Based on the obtained simulation results, it can be concluded that for efficient production and experimental measurements of positrons, it is necessary to use targets of a high Z number with a thickness of more than 1 mm.

Integrating the obtained particles spectra the total number of forward emitted

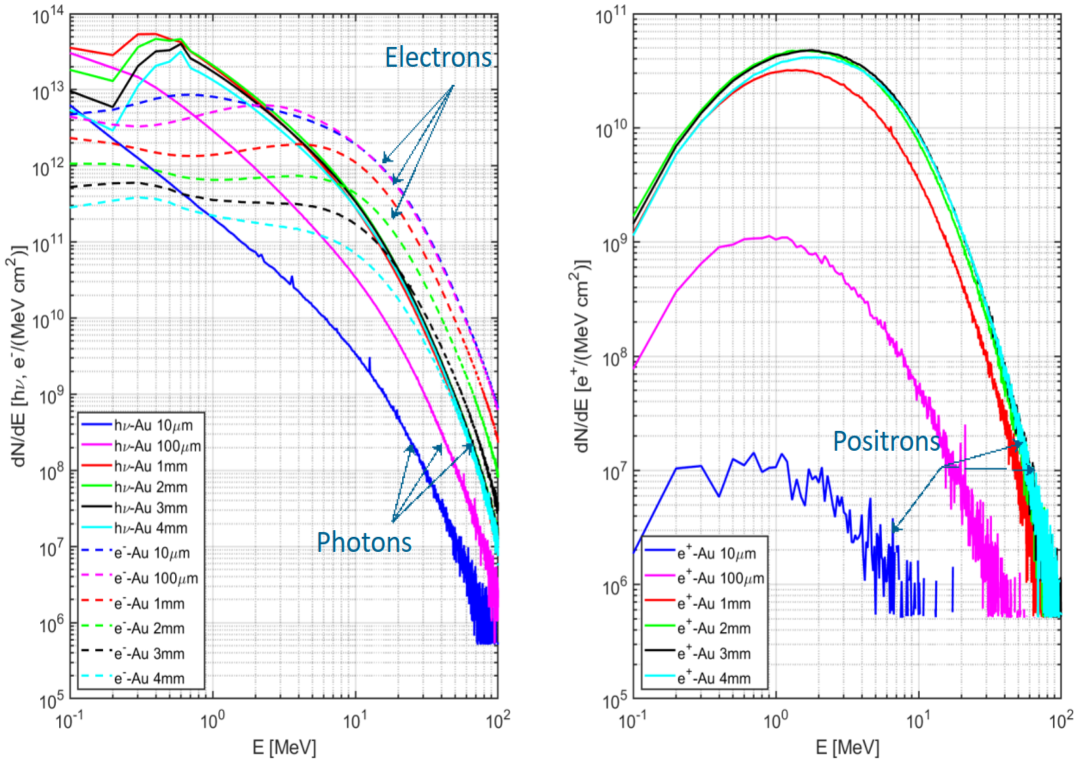

FIGURE 9.2: Differential fluences of photons, primary and secondary electrons and positrons as a function of the corresponding energy, integrated over solid angle 2π in forward direction, detected directly from the rear side of Au targets of 10 μm, 100 μm, 1 mm, 2 mm, 3 mm, 4 mm thickness.

photons, electrons and positrons can be found. Figure 9.3 shows the integrated fluences of bremsstrahlung photons and positrons from Al, Ti, Fe, Ta, W, Au, Pb targets versus target thickness of 10 μm, 100 μm, 1 mm, 2 mm, 3 mm, 4 mm. The results of the simulations showed that photon fluence increased quickly up to the certain thickness and then it decreased due to the photon attenuation process. It has been seen that the highest photon fluence is obtained for targets with the higher atomic number such as Au and W and least photon fluence is obtained from targets with the lowest atomic number such as Al. The photon beam reaches the maximum value with Au or W targets of 1 mm thickness. Our experiments with TLD spectrometer also showed the highest signal measured with TLD cards when Au foil of 1mm was used as a target. According to the simulations results the most efficient production of positrons was realized by using of Au or W targets of 2 - 3 mm thickness. Figure 9.4 (a) shows the total number of photons, electrons and positrons from Au targets of 10 μm, 100 μm, 1 mm, 2 mm, 3 mm, 4 mm thickness. The simulation results show the predominance of the electron fluence for thin Au targets of 10 μm, 100 μm thickness. The predominance of the photon fluence was obtained for thick targets of 1 - 4 mm thickness, which is explained by an increase of the interaction length in the process of generation of Bremsstrahlung photons. Figure 9.4 (b) shows the total number of photons in three energy intervals of $1\,keV - 1\,MeV$, $1\,MeV - 7.5\,MeV$,

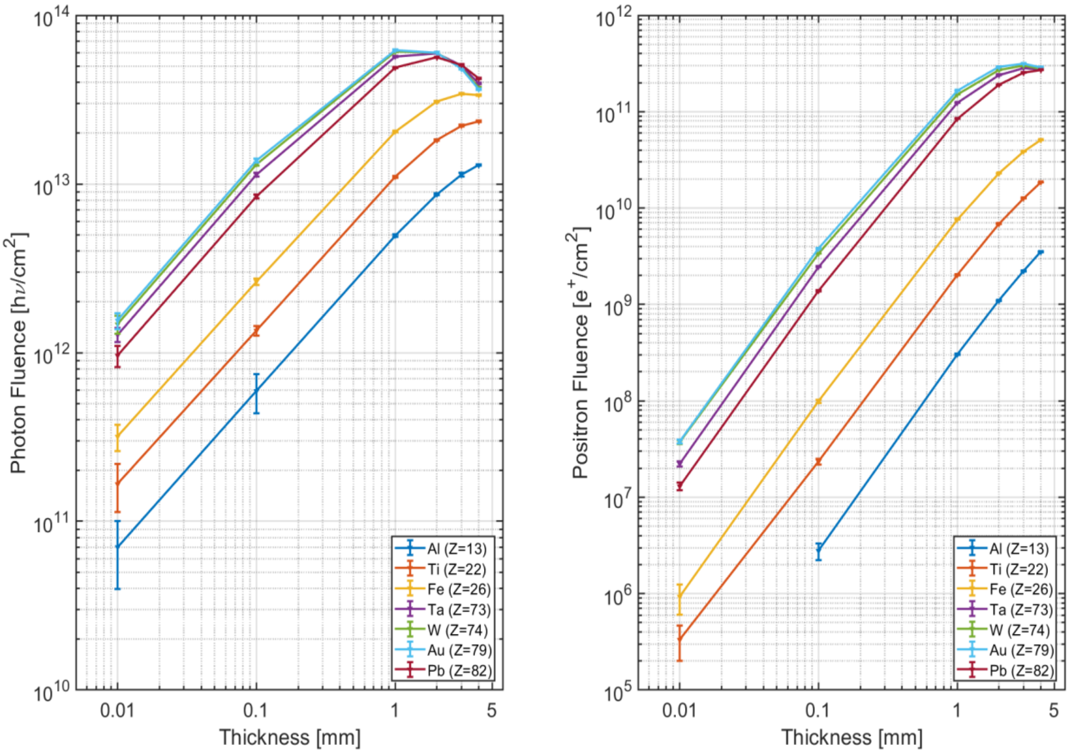

FIGURE 9.3: Integrated fluences of bremsstrahlung photons and positrons from Al, Ti, Fe, Ta, W, Au, Pb targets versus target thickness of 10 μm, 100 μm, 1 mm, 2 mm, 3 mm, 4 mm.

7.5 $MeV - 100\,MeV$ irradiated from Au targets of 10 μm, 100 μm, 1 mm, 2 mm, 3 mm, 4 mm thickness. It can be seen, that the maximal photon yields with energies of 1 $keV - 1\,MeV$ are emitted by the Au target of 1 mm thickness, the maximal photon yields with energies of 1 $MeV - 7.5\,MeV$ are emitted by the Au target of 2 mm thickness and the maximal photon yields with energies of 7.5 $MeV - 100\,MeV$ are emitted by the Au target of 2 - 3 mm thickness. Detection of the number of photons within certain energy intervals and looking at the maximum production in 2π forward direction gives possibility to investigate laser generated Bremsstrahlung photons for initiation of photonuclear reactions. The spectrum of the generated gammas is energetically broad and reaches the giant dipole resonance region. Thus it can serve as a source to generate ultrafast neutron beam through photo-nuclear reaction.

The results of these simulations were used to guide the selection of the target materials and thicknesses for the further laser experiments.

9.2 Simulation of Angular Distributions of Photons, Electrons and Positrons

The main concept of bremsstrahlung radiation and its results are discussed in sections 3.2.2 and 8.2. Based on the results of FLUKA simulations of interactions of monoenergetic electron beams with different studied materials, **gold** material was found to

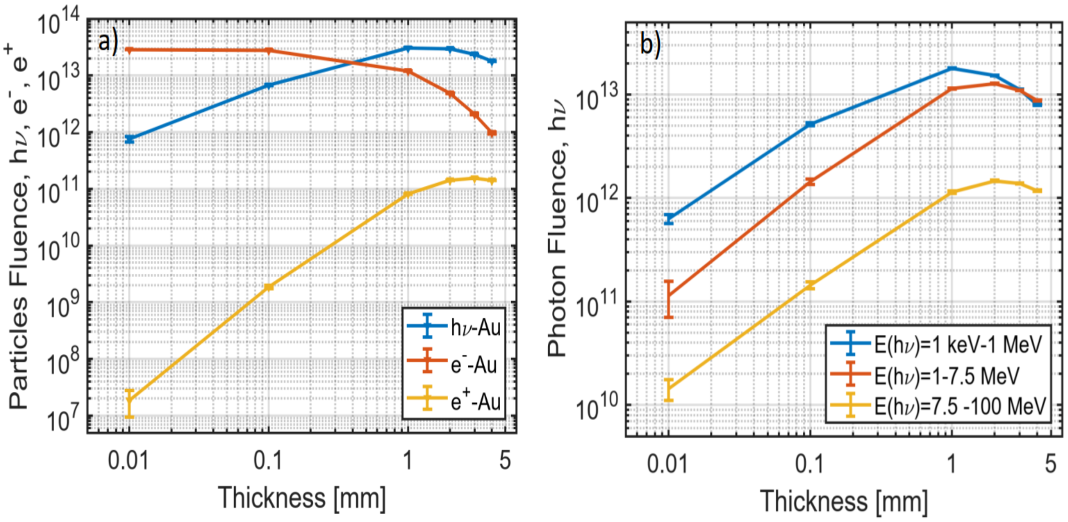

FIGURE 9.4: (a) Simulated photon electron and positron fluences from Au targets of 10 μm, 100 μm, 1 mm, 2 mm, 3 mm, 4 mm thickness. (b) Simulated photon fluences divided to three energy intervals. The photons, electrons and positrons number was detected in forward direction, 2π solid angle and normalised by the number of initial simulated electrons.

be the most suitable for the present experiments as $e-\gamma$ target because of its highest bremsstrahlung yield. Figures 9.5, 9.6 and 9.7 show the electron, photon and positron fluence distributions from Au targets of 10 μm, 1 mm and 2 mm thickness respectively. These plots are 2 dimensional Z-X projections of a 3 dimensional structure. The results are averaged over the third coordinate. Projection limits include area around target and TLD spectrometer (marked with a black rectangle). In the case of using thin gold foil of 10 μm thickness, electron beams have the smallest scattering angle. It can be seen that the majority of the electrons pass through the thin Au foil with less interactions compared to the thick Au radiators. Increase of the target thickness caused a larger angular distribution of out-coming electron beam. For Au targets of 1mm and 2mm thickness the electron energy is essentially deposited into production of bremsstrahlung photons. The highest photon fluence was generated for 1 mm Au target. The increase in the target thickness produced increase of the higher energy bremsstrahlung photons and large bremsstrahlung angular distribution. Due to the generation of a large number of energetic photons, the production of a large number of positrons is induced.

Figure 9.8 presents the simulations results of angular distributions of the Bremsstrahlung photons and electrons fluences produced by Au targets of different thickness, where $\Theta = 0^\circ$ is the direction of the laser axis. As expected, the angular distributions of the generated photons using the high energy electrons is extremely directed for thin converters of 10 μm and 100 μm. The electron fluence consisting of primary electrons and secondary electrons also has a moderate divergence angle. It was observed, that the increase of the target thickness causes to lager angular distribution of the emitted beams. In addition, it was determined that the electron fluence produced in

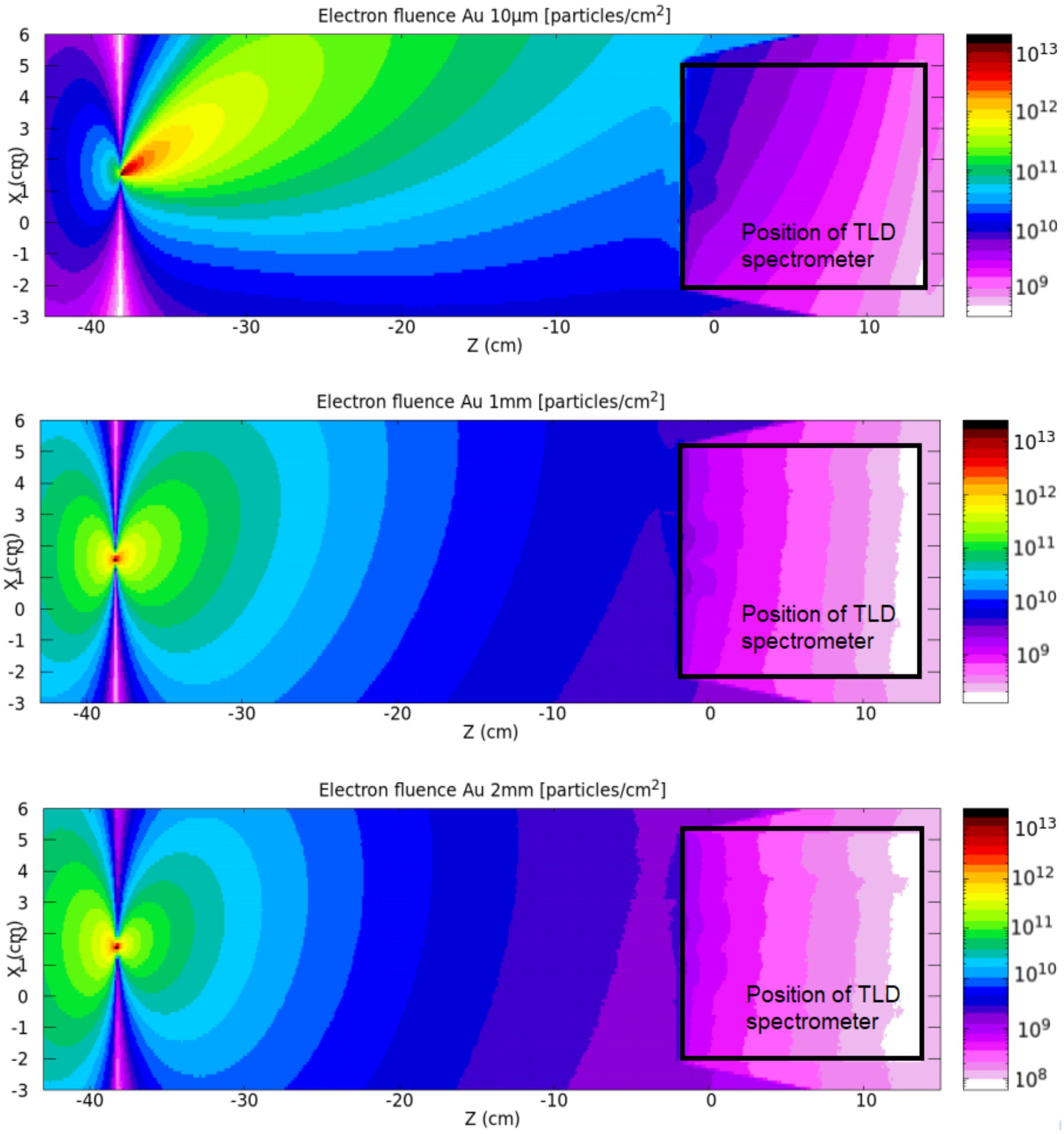

Figure 9.5: Spatial distribution of the total electron fluence from Au targets of 10 μm, 1 mm and 2 mm thickness. The plots are 2 dimensional Z-X projections of a 3 dimensional structure, the results are the averaged over the third coordinate.

the forward direction decreases faster with increasing of the angel compared to the bremsstrahlung fluence. Figure 9.9 shows a Full Width at Half Maximum (FWHM) or the angle at which the intensity of the simulated particles fluences decreases to half of the maximum for each thickness of the Au targets. These data give information about the divergence angle and therefore the intensity distribution of the simulated particles. According to the results, FWHM of the scattered photons increases till the 3 mm target thickness, then the divergence of the photon fluence saturates due to the attenuation of the low energy photons. At the same time the values of FWHM for angular distribution of the positrons saturated at 2 mm target thickness. These calculations provide important information for selection of the optimal thickness of the target at which the photon or positron fluences reach their maximum values with

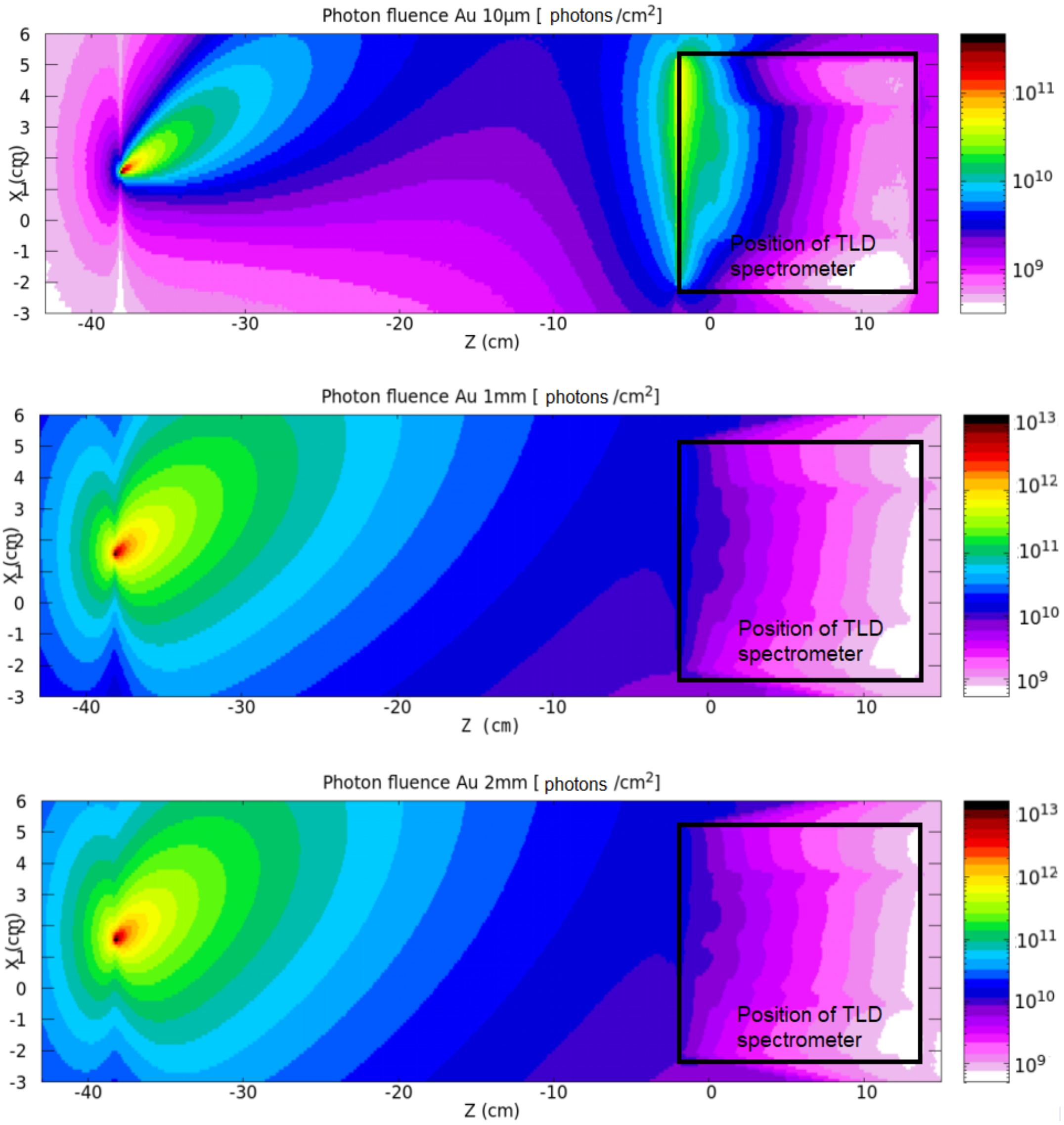

FIGURE 9.6: Spatial distribution of the total photon fluence from Au targets of 10 μm, 1 mm and 2 mm thickness. The plots are 2 dimensional Z-X projections of a 3 dimensional structure, the results are the averaged over the third coordinate.

corresponding angular distribution. Therefore, it can be concluded that the optimum thickness at which the maximum photon fluence and minimum angular distribution occurred from Au target of 1 mm thickness. The data obtained with the FLUKA simulations can be applied for selecting the Bremsstrahlung target in theoretical and practical areas were bremsstrahlung photons are generated and used.

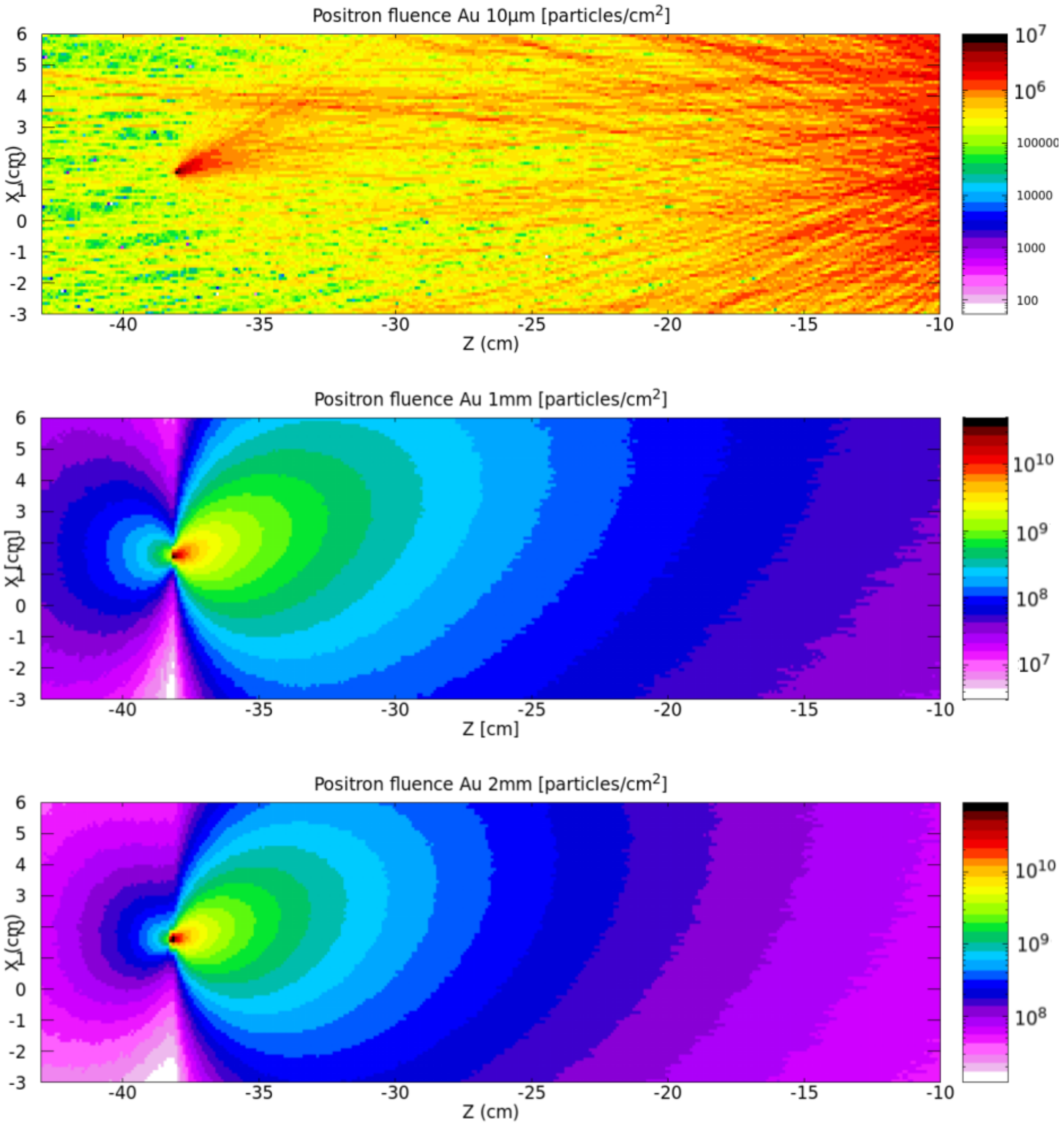

FIGURE 9.7: Spatial distribution of the total positron fluence from Au targets of 10 μm, 1 mm and 2 mm thickness. The plots are 2 dimensional Z-X projections of a 3 dimensional structure, the results are the averaged over the third coordinate.

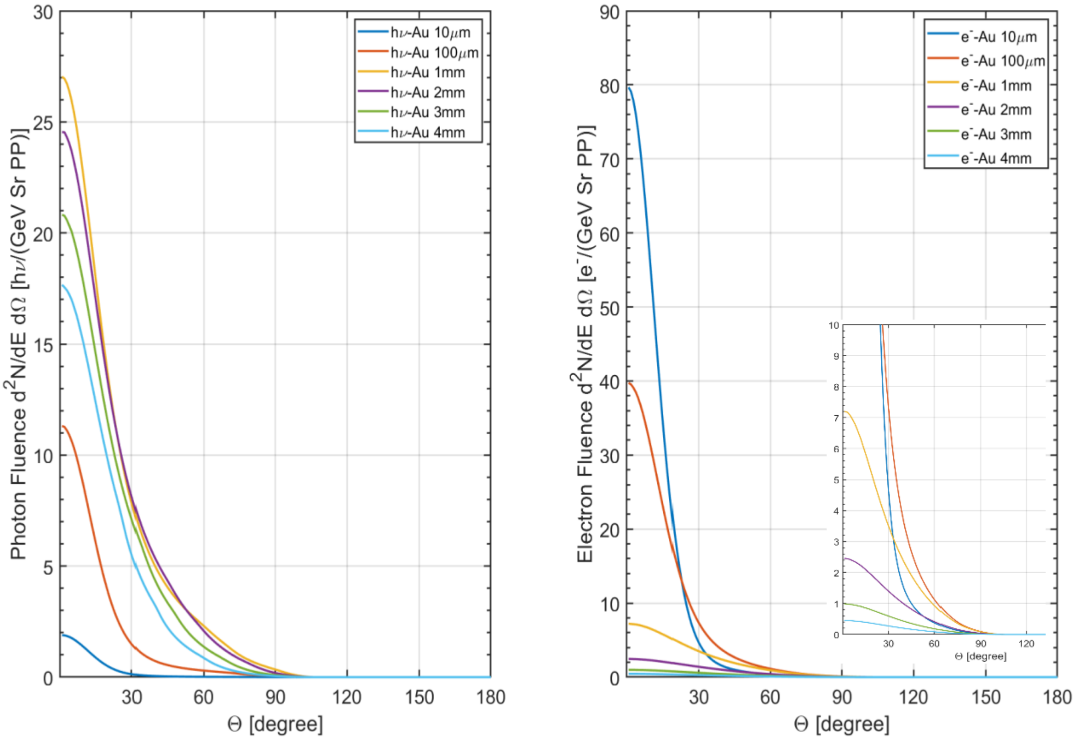

FIGURE 9.8: Angular distribution of photon and electron fluences for Au targets of various thickness.

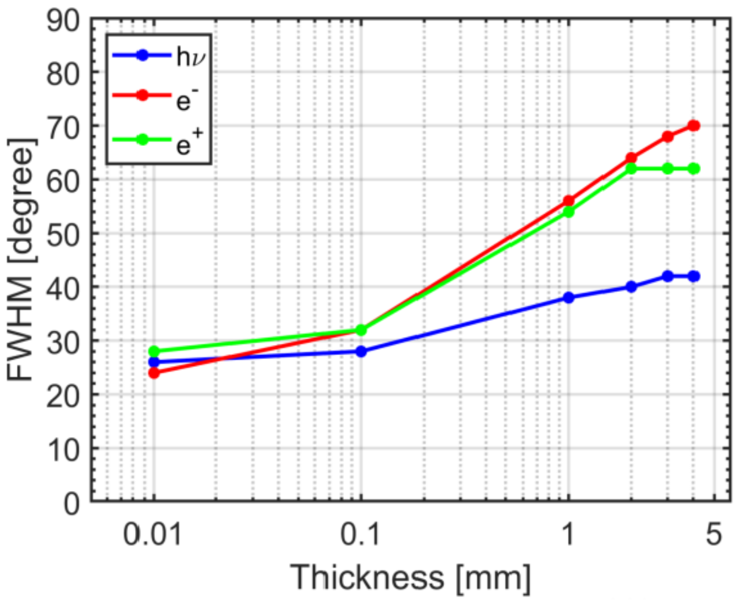

FIGURE 9.9: FWHM of the angular distributions of photons, electrons and positrons produced by the electron beam with Maxwellian energy distribution interacting with Au targets of different thickness.

Chapter 10

Enhancement of Efficiency of Laser-Driven Generation of MeV Particles and Photon Beams

This chapter demonstrates the advantages of long-scale plasmas of near critical density (NCD) to increase parameters of MeV particles and photon beams generated in relativistic laser-plasma interaction. The efficiency of laser-driven generation of MeV electrons and photons by application of low density polymer foams is essentially enhanced. These electrons are an excellent tool for many applications producing vast amount of MeV gamma radiation in interaction with high Z target-convertor. The convertor can be used to trigger gamma-driven nuclear reactions and electron-positron pair production. In this chapter, electron acceleration process in laser-plasma interactions was simulated with particle-in-cell (PIC) code for two laser energies of 20 J and 200 J, and the obtained electron beam parameters were imported into a Monte Carlo code FLUKA to simulate the production process of bremsstrahlung photons and positrons in Au converter. Monte Carlo FLUKA simulations show the record of conversion efficiency in MeV gammas can reach 10%, which reinforces the generation of positrons. Application of proposed robust target scheme, which does not require a high laser pointing stability, an ultra-high laser intensity and a high laser contrast, paves the way to a new level of diagnostic potential of kJ-class PW laser facilitates.

10.1 Electron Spectra Resulted from 3D-PIC Simulations

3D PIC simulations of the laser propagation in the NCD plasma were performed applying the Virtual Laser Plasma Laboratory (VLPL) code (Pukhov, 1999) for the calculation of energy and angular distribution of super-ponderomotive electrons generated in interaction of PHELIX laser pulse with NCD plasma. The first simulations were performed for laser energy of 20 J and showed an excellent agreement with experimental results of the electron energy and angular distributions (Rosmej et al., 2020). The next simulations were performed for the PHELIX up-grade laser system to simulate super-ponderomotive electrons generated in interaction of the laser with energy of $E_L = 200\,J$ in FWHM of the focal spot of $25\mu m$ in diameter (full energy on target 500J), 0.7 ps laser pulse with NCD plasma. The homogeneous plasma was composed of electrons and fully ionized ions of carbon, hydrogen and oxygen. Simulations accounted for the ion type and the ion fraction in accordance with the chemical composition of triacetate cellulose $C_{12}H_{16}O_8$ which was used as a target (Borisenko, 2007; Rosmej et al., 2019). The simulation box had sizes of $350 \times 75 \times 75\,m^3$. The first 10 and the last 15 μm from the total of 350 μm space in x-direction (the laser axis) were initially free of plasma. Sizes of the numerical cells were 0.1 μm along the x-axis and 0.5 μm along the y-axis and the z-axis. The number of particles per cell in the simulation were 4 for the electrons and 1 for the ions of each type. Boundary conditions were absorbing for particles and fields in each direction. The initial electron density profile (together with the neutralizing ion density) at the moment of the main pulse arrival was step-like. The created plasma had an electron density of $0.65 \cdot n_{cr}$. Previously, PIC-simulations were performed for a step-like density profile with n_{cr} and $0.5n_{cr}$ (Pugachev et al., 2016; Pugachev et al., 2019) and for a partially ramped density profile in order to account for plasma expansion toward the main laser pulse (Rosmej et al., 2019). The simulations result in a very similar overall behaviour of the energy and angular distributions of super-ponderomotive electrons in all mentioned cases. The results of these simulations showed that due to the direct laser acceleration in a sub-mm thick NCD plasma layer, electrons with effective temperature up to 10 times higher than ponderomotive potential and with a charge of 10 C can be produced. Such electrons are ideal for the production of grate amount of MeV gamma radiation in interaction with high Z convertor. These results demonstrated very high laser energy conversion into multi MeV electrons.

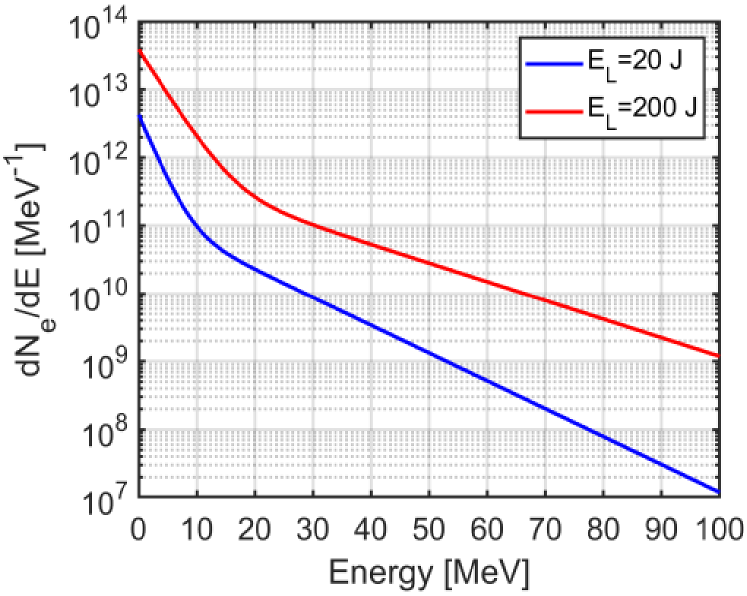

FIGURE 10.1: PIC simulated energy spectra of accelerated electron beams generated in laser–plasma interaction with laser energies of 20 J and 200 J.

Laser energy $E_L[J]$	$T_{e1}[MeV]$	$T_{e2}[MeV]$	N_{e1}	N_{e2}
20	10.6	2.16	$1.49 \cdot 10^{11}$	$4.17 \cdot 10^{12}$
200	15.8	3.23	$6.7 \cdot 10^{11}$	$3.84 \cdot 10^{13}$

TABLE 10.1: Components of the simulated electron spectra for laser energies of 20 J and 200 J.

The electron energy distributions obtained from PIC simulations were described by two exponent Maxwell distribution function: $dN/dE = N_{e1}exp(-E/T_{e1}) + N_{e2}exp(-E/T_{e2})$. The parameters of the simulated electron spectra for laser energies of 20 J and 200 J are presented in Table 10.1. According to the results of simulations, the total number of electrons with $E_e > 1\,keV$, propagating in 2π, for laser energy of 20 J reaches the value of $1.057 \cdot 10^{13}$ that corresponds to $\approx 1.7\,\mu C$ of the electron charge and for laser energy of 200 J reaches the value of $1.34 \cdot 10^{14}$ that corresponds to $\approx 22\,\mu C$ of the electron charge.

These PIC simulated spectra were imported into the Monte Carlo FLUKA as the primary particle energy spectrum for random sampling and used for further simulations of the bremsstrahlung spectra and investigation electron-positron pairs production.

10.2 FLUKA Simulation Results of MeV Bremsstrahlung Photons and Electron-Positron Pairs Production

Monte Carlo FLUKA simulations were performed to characterize MeV-bremsstrahlung spectra generated by super-ponderomotive electrons that propagate trough Au convertor attached to the foam of from the rear side. The PIC-simulated energy distribution of electrons was used as an input parameter. Therefore, Monte Carlo FLUKA simulations served as necessary means to get information about the generation MeV gammas and positrons. Figure 10.2 shows the comparison of spectral distributions of electrons and the bremsstrahlung photons produced by super-ponderomotive electrons spectra in Au-convertor generated in laser–plasma interaction with laser energies of a) 200 J and b) 20 J in dependence on the convertor thickness. These differential fluences of photons, electrons and positrons as a function of the corresponding energy are integrated over solid angle 2π in forward direction from rear side of Au targets of 1 mm, 2 mm, 3 mm, 4 mm, 5 mm thickness. The behaviour of the spectral distributions of particles do not have significant differences in each case. The particular interest of these simulations is the comparison of the order of magnitude of the corresponding spectra. Figure 10.3 presents the the comparison of spectral distributions of positrons produced by super-ponderomotive electrons spectra in Au-convertor generated in laser–plasma interaction with above mentioned laser energies. It was found that the electron energy contained in MeV electrons generated by the

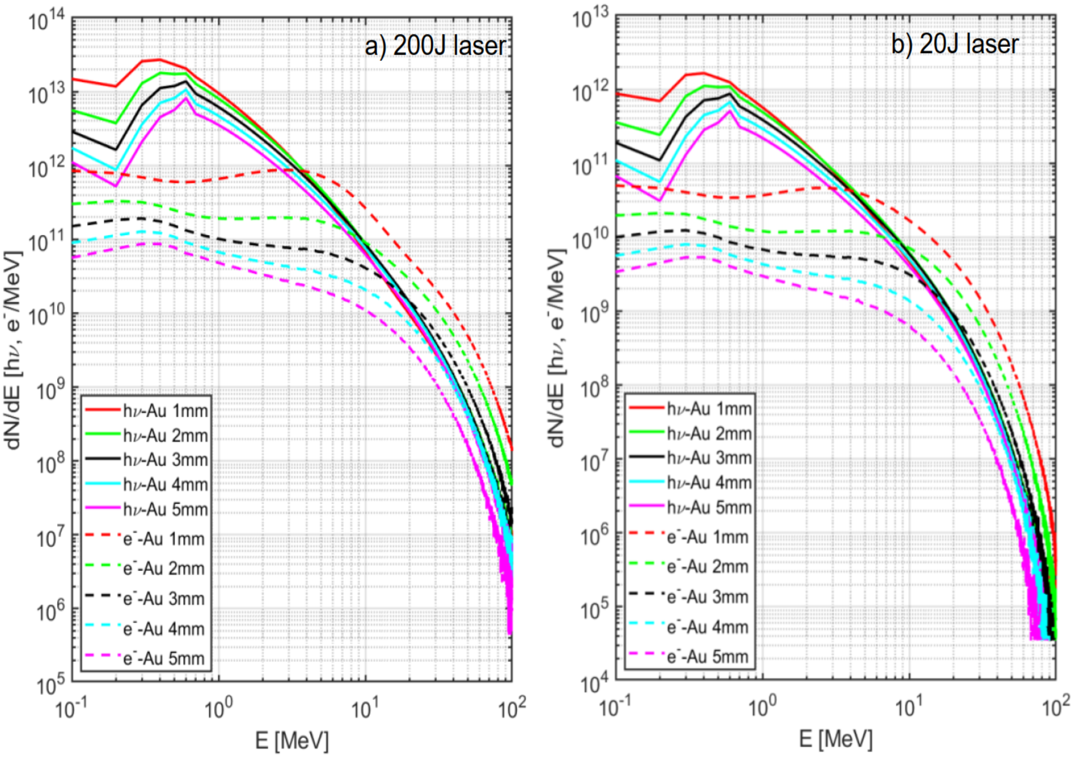

FIGURE 10.2: Differential fluences of primary and secondary electrons and bremsstrahlung photons as a function of the corresponding energy, integrated over solid angle 2π in forward direction from rear side of Au targets of 1 mm, 2 mm, 3 mm, 4 mm, 5 mm thickness. The electron spectra were generated in laser–plasma interaction with laser energies of a) 200 J and b) 20 J and used for MC FLUKA simulations.

laser with energy of 200 J is quite relevant not only for the effective production of Bremsstrahlung photons but also for the high yield of positrons which in turn can be experimentally measured with sufficient equipment.

The results of simulations of the bremsstrahlung radiation made it possible to calculate the effective temperatures of the bremsstrahlung spectrum, which was divided into three energy intervals. Table 10.2 shows the effective temperatures T_{eff1} and T_{eff2} of the bremsstrahlung spectrum generated by super-ponderomotive electrons in Au convertor in dependence on the penetration depth and the photon energy range. The electron spectra were simulated for laser energies of 20 J and 200 J. The effective temperatures of the bremsstrahlung radiation for three photon energy regions presented in table reflect the two-temperature distribution of the primary electron beams.

Figure 10.4 shows simulated photon electron and positron fluences from Au targets of 1 mm, 2 mm, 3 mm, 4 mm and 5 mm thickness produced by electron spectra with Maxwellian energy distribution. The electron spectra were generated in laser–plasma interaction with laser energies of a) 200 J and b) 20 J. The photons, electrons and positrons number was detected in forward direction, 2π solid angle and normalised by the number of initial simulated electrons. The peak photon numbers of $2.7 \cdot 10^{14}$ and $1.6 \cdot 10^{13}$ were reached after electron propagation in the 1 mm-thick Au-radiator

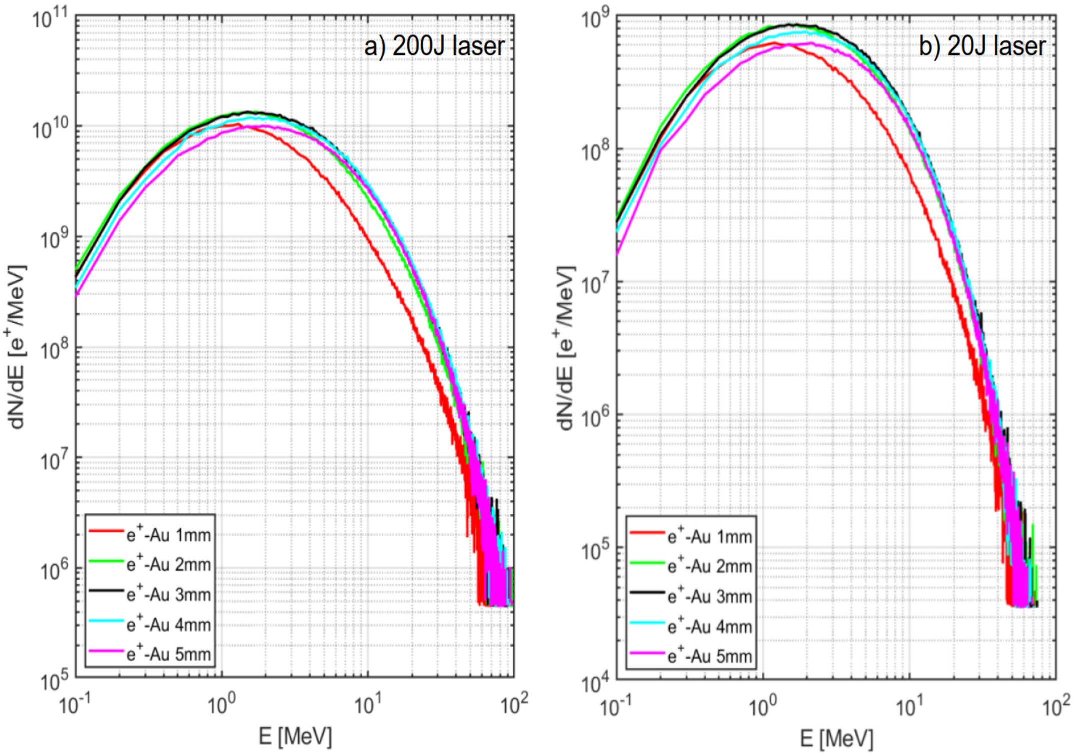

FIGURE 10.3: Differential fluences of positrons as a function of the corresponding energy, integrated over solid angle 2π in forward direction from rear side of Au targets of 1 mm, 2 mm, 3 mm, 4 mm, 5 mm thickness. The electron spectra were generated in laser–plasma interaction with laser energies of a) 200 J and b) 20 J and used for MC FLUKA simulations.

in case of 200 J and 20 J laser energy respectively. The peak positron numbers of $9.3 \cdot 10^{11}$ and $5.7 \cdot 10^{10}$ were calculated after electron propagation in the 3 mm-thick Au-radiator.

Figure 10.5 shows the total number of photons in three energy intervals of $0.1 - 1\,MeV$, $1 - 7.5\,MeV$, $7.5 - 100MeV$ irradiated from Au targets of 1 mm, 2 mm, 3 mm, 4 mm, 5mm thickness. It can be seen, that the maximal photon yields with energies of $0.1 - 7.5\,MeV$ are emitted by the Au target of 1 mm thickness and the maximal photon yields with energies of $7.5MeV - 100\,MeV$ are emitted by the Au target of 2 mm thickness. Figure 10.6 presents the angular distributions of photons electrons and positrons produced by electron beams with Maxwellian energy distribution on Au targets of different thickness. These are the results of Full Width at Half Maximum (FWHM) or the angle at which the intensity of the simulated particles fluences decreases to half of the maximum for each thickness of the Au targets. Comparing the results of both cases, one can note the high directionality of electrons with higher energy despite the increasing thickness of Au converter.

Considering the spectral distributions and corresponding divergence angles the conversion efficiency of the laser energy into the energy of gammas was calculated for both laser energies. Figure 10.7 shows the conversion efficiency of laser energy into photons production by electron beam with Maxwellian energy distribution on

Laser energy $E_L = 20J$					
Au-radiator thickness	1 mm	2 mm	3 mm	4 mm	5 mm
Energy range	$T_{eff1}[MeV]$				
0.1 - 1 MeV	0.36	0.42	0.78	0.51	0.55
1 - 7.5 MeV	2.06	2.37	2.54	2.66	2.75
7.5 - 100 MeV	6.62	6.54	6.53	5.54	5.61
Energy range	$T_{eff2}[MeV]$				
0.1 - 1 MeV	0.31	0.37	0.73	0.46	0.5
1 - 7.5 MeV	0.55	0.6	0.63	0.66	0.69
7.5 - 100 MeV	2.25	2.42	2.48	3.9	3.81
Laser energy $E_L = 200J$					
Au-radiator thickness	1 mm	2 mm	3 mm	4 mm	5 mm
Energy range	$T_{eff1}[MeV]$				
0.1 - 1 MeV	0.12	0.28	0.32	0.34	0.36
1 - 7.5 MeV	1.95	2.24	2.43	2.58	2.67
7.5 - 100 MeV	8.44	8.37	8.3	8.38	8.41
Energy range	$T_{eff2}[MeV]$				
0.1 - 1 MeV	0.43	0.28	0.32	0.34	0.36
1 - 7.5 MeV	0.54	0.59	0.62	0.65	0.68
7.5 - 100 MeV	2.3	2.49	2.57	2.65	2.69

TABLE 10.2: The effective temperatures T_{eff1} and T_{eff2} of the bremsstrahlung spectrum generated by super-ponderomotive electrons in Au convertor in dependence on the penetration depth and the photon energy range. The electron spectra were simulated for laser energies of 20 J and 200 J.

Au targets of different thickness for 20 J and 200 J laser energy. In the case of 200 J laser energy the maximal conversion efficiency reaches 9.8% for photon energy range of $E = 1 - 7.5\,MeV$, while for the region of the giant dipole resonance (GDR) with photon energies of $E > 7.5\,MeV$ it is of 2.7%. Compared with the case of PHELIX laser energy of 20 J, the conversion efficiency reaches 6.3% for photon energy range of $E = 1 - 7.5\,MeV$, which is 1.5 time smaller than in the case of 200 J laser energy. For photon energies of $E > 7.5\,MeV$ it is of 1.9%. This difference can be attributed to the higher laser intensity, which is in the case of 200 J laser energy of $\approx 8 \cdot 10^{19}\,W/cm^2$.

Summarizing the results of the numerical simulations, we can conclude that interaction of high-current well-directed relativistic electrons with Au targets leads to effective production of MeV bremsstrahlung radiation with the ultra-high fluence. The simulations demonstrated an extremely high capability of the well-directed high-current relativistic electron beams to be used in novel laser assisted applications using already existed high-energy sub-PW and PW-class laser systems. This approach is very important for applications that promise a strong improvement in the performance of laser sources of particles and photons.

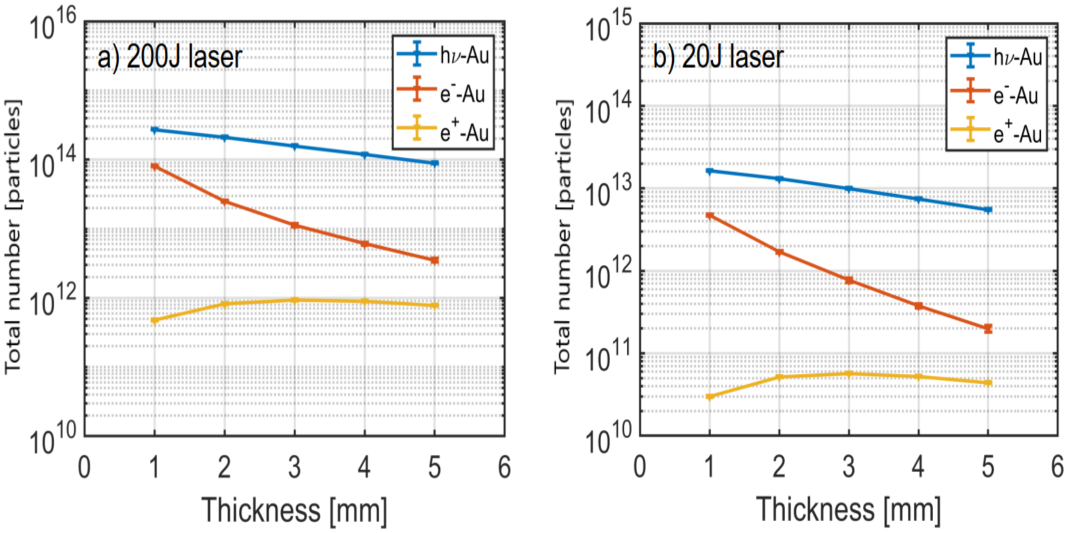

FIGURE 10.4: Simulated total number of photons, electrons and positrons from Au targets of 1 mm, 2 mm, 3 mm, 4 mm and 5 mm thickness produced by electron spectra with Maxwellian energy distribution. The electron spectra were generated in laser–plasma interaction with laser energies of a) 200 J and b) 20 J. The photons, electrons and positrons number was detected in forward direction, 2π solid angle and normalised by the number of initial simulated electrons.

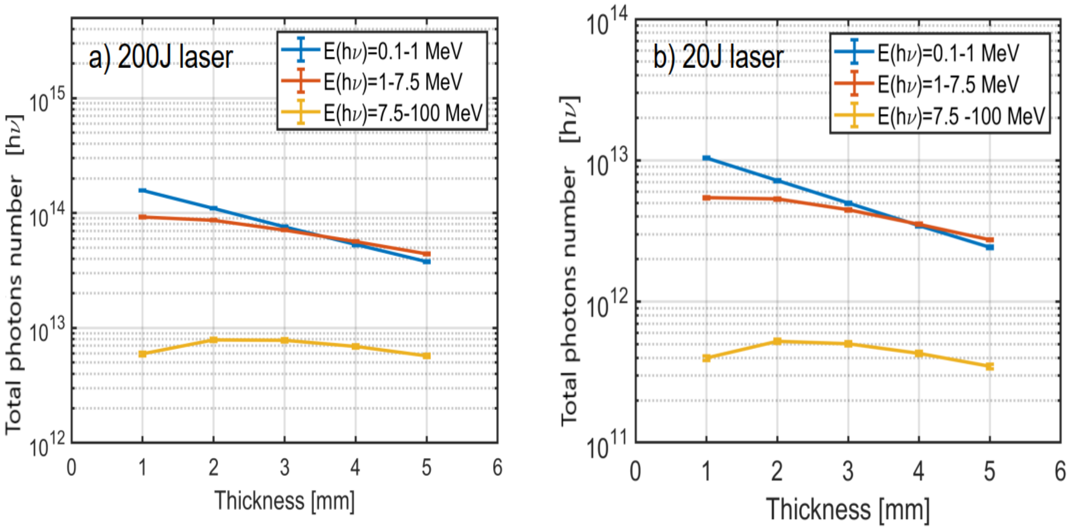

FIGURE 10.5: Simulated total photons number divided to three energy intervals. The electron spectra were generated in laser–plasma interaction with laser energies of a) 200 J and b) 20 J.

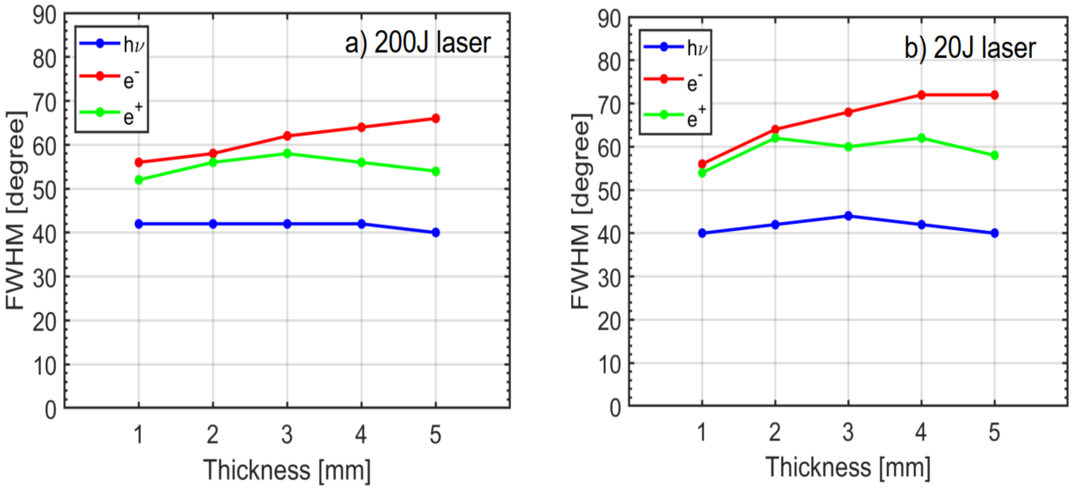

Figure 10.6: FWHM of the angular distributions of photons, electrons and positrons produced by the electron beam with Maxwellian energy distribution interacting with Au targets of different thickness. The electron spectra were generated in laser–plasma interaction with laser energies of a) 200 J and b) 20 J.

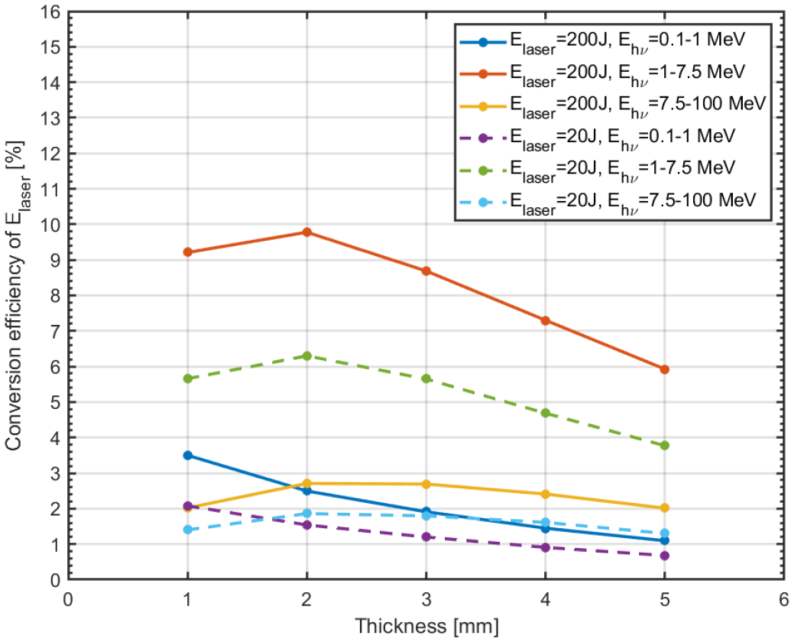

Figure 10.7: Conversion efficiency of laser energy into photons production by electron beam with Maxwellian energy distribution on Au targes of different thickness for 20 J and 200 J laser energy.

Chapter 11

Summary and Conclusion

The essential improvements in laser technology during last decade resulted in high intensities of laser reaching up to $10^{21}\,W/cm^2$. Already with intensities of $10^{18}\,W/cm^2$ the electron quiver energy in the laser field is fully relativistic that leads to the generation of high-intensity beams of energetic gamma rays via bremsstrahlung production. The laser induced photon beams make the high-intensity laser to be an effective tool for studying of nuclear reactions.

During the scope of this thesis, the experimental results on the interaction of relativistic sub-picosecond laser pulses produced by the PHELIX-system with extended, sub-mm long near-critical electron density plasmas were presented. In order to create the hydrodynamic stable, large scale, quasi-homogeneous plasmas low density polymer foam layers ($2\,mg/cc$ Triacetate-Cellulose $C_{12}H_{16}O_8$) with a thickness of 300 and $500\,\mu m$ were used as targets. Interaction of the relativistic laser pulse with large-scale NCD-plasmas ensured a long acceleration path and provided an effective coupling of the laser energy into fast MeV energetic electrons and resulting generation of the gamma bremsstrahlung and positrons in the targets of different materials and thickness.

The detailed description of the distribution of the photon emission induced by an interaction of relativistic electron beams with different target materials and definition of the characteristics of the produced bremsstrahlung photons such as energy, intensity and angular distribution is very important for optimization of the photon source and estimation of the corresponding conversion efficiency of the laser energy into the energy of gammas. The intensity of bremsstrahlung depends on the energy of the incoming electrons, the atomic number (Z) and the thickness of the radiator material. The optimization of the high-Z target geometry allows to reach an ultra-high MeV photon number of $\approx 10^{12}$ per shot at moderate relativistic laser intensity of $10^{19}\,W/cm^2$.

For the investigation of the generation and characterisation of ultra-relativistic hot electrons accelerated in under-dense pre-ionised foam targets and the following interactions of electrons with solid targets inducing the generation of high energetic photons in the form of bremsstrahlung two experimental campaigns at the PHELIX laser were carried out. The first pilot experiment **P138** on the generation of ultra-relativistic hot electrons accelerated by the direct laser acceleration (DLA) mechanism in pre-ionized foam targets showed the enormous increase of the total charge and energy of the laser-accelerated electrons as predicted by the theory (Pugachev et al., 2016), which is much higher than defined by Wilks law (Wilks et al., 1992). The aim of the subsequent experiment **P176** was to characterize MeV bremsstrahlung sources arising from the interaction of DLA electrons with high-Z converter targets.

In this work a TLD-spectrometer based on thermoluminescence dosimetry method was applied for the diagnostics in high intensity laser experiments. This spectrometer was developed and absolutely calibrated for an energy range from 30 keV to 100 MeV. The absorbers of different materials and thicknesses arranged as a stack caused a different response of every TLD detector, which then were used as information about the spectrum of the incident radiation beams. In the case of laser interaction with long-scale NCD-plasmas, the dose caused by the gamma-radiation measured in the direction of the laser pulse propagation showed a 1000-fold increase compared to the high contrast shots onto plane foils (see Fig. 11.1) and doses measured perpendicular to the laser propagation direction for all used combinations of targets and laser parameters. The measurements also showed high directionality of the acceleration process.

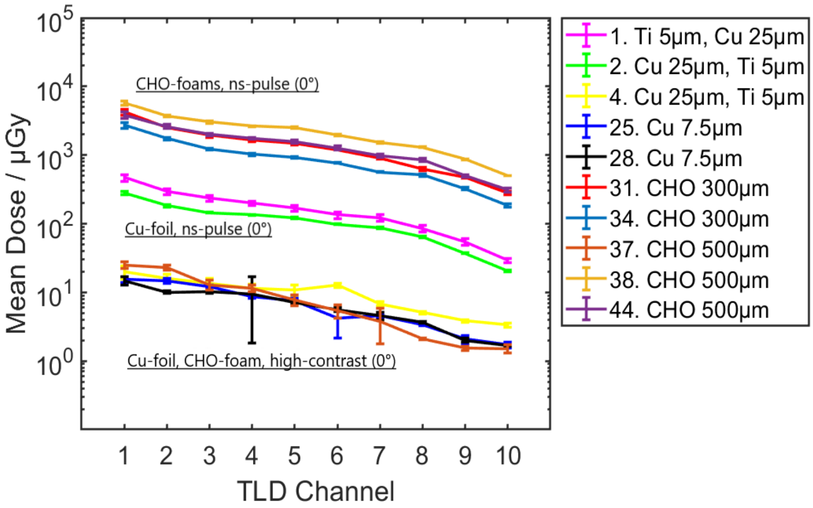

FIGURE 11.1: Dose distribution measured by the 10-channel TLD-spectrometer placed in the direction of the laser pulse propagation for shots made at different conditions. Shots 31, 34, 38, 44 were made onto pre-ionized foam. Shots 1, 2 were made onto pre-ionized foils. Shots 4, 25, 28, 37 were made onto foil or foam at the highest laser contrast.

The experiments supported by Monte Carlo simulations, which considered the target material and the geometry of the experimental setup. The response functions of the TLD spectrometer to mono-energetic electron radiation in the energy range of 100 keV - 100 MeV have been simulated using the Monte Carlo code FLUKA as dose values in the TLD detectors placed in a stack of different materials. Different gradients and thresholds of these response-functions allowed performing of the reconstruction (unfolding) of the electron spectra. The evaluation of the electron spectra from the readings of TLDs was resolved in 20 energy bins and was performed applying an unfolding algorithm based on a sequential enumeration of matching data series of the dose values measured by the dosimeters and calculated by means of FLUKA-simulations. The electron distribution functions were found to be described by two temperature Maxwellian distributions. The effective temperature of super-ponderomotive electrons retrieved from the measured TLD-doses by means of the combination of Monte-Carlo simulations and unfolding algorithm reached 11–12 MeV. Figure 11.2 shows the resulting values of T_{e1} and T_{e2} for selected laser shots on different targets in the experiment **P138**. In the case of the laser interaction with pre-ionized foams, the best fit of all ten TLD-signals was obtained for $T_{e1} \simeq 12$ MeV and $T_{e2} \simeq 2 - 5$ MeV. The application of CHO-foams as targets initiated essential increases of the temperature and number of the accelerated in forward direction electrons, which is in agreement with the DLA-scaling while the temperature for electrons at large angles to the laser propagation direction matches the ponderomotive scaling. This observation of the directionality of super-ponderomotive electrons generated in NCD plasmas was theoretically predicted (Pugachev et al., 2016; Pugachev et al., 2019). In the case of the shots at the highest laser contrast both electron temperatures are $T_{e1} \simeq T_{e2} \simeq 0.5 - 2.5$ MeV. These results represented a very good correlation with the experimental conditions and with the results of the direct measurements by the electron spectrometers (Zaehter, 2020).

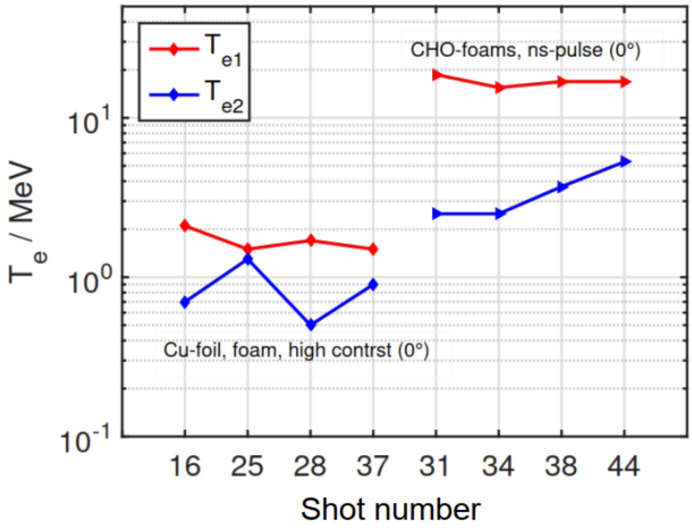

FIGURE 11.2: Electron temperatures evaluated from the measured TLD-doses (experiment **P138**) via the the unfolding algorithm using FLUKA-simulations results which were taking into account a real geometry of the experimental set-up and the environment and used a two electron temperatures approximation.

The high energy accelerated electron beam interacting with a high Z target material has generated a cascade shower of bremsstrahlung radiation and the continuous spectra of photons, positrons and secondary electrons. The generated by the interaction of the unfolded electrons spectra with different radiator materials bremsstrahlung spectra and exiting electron and positron spectra were simulated employing the Monte Carlo code FLUKA. The photon, electron and positron fluences obtained from the simulation of the interaction of the electron spectra with Au targets of various thickness are shown in Figure 11.3. The differential over energy particle fluences were integrated over the solid angle in the region of particle propagation. The bremsstrahlung

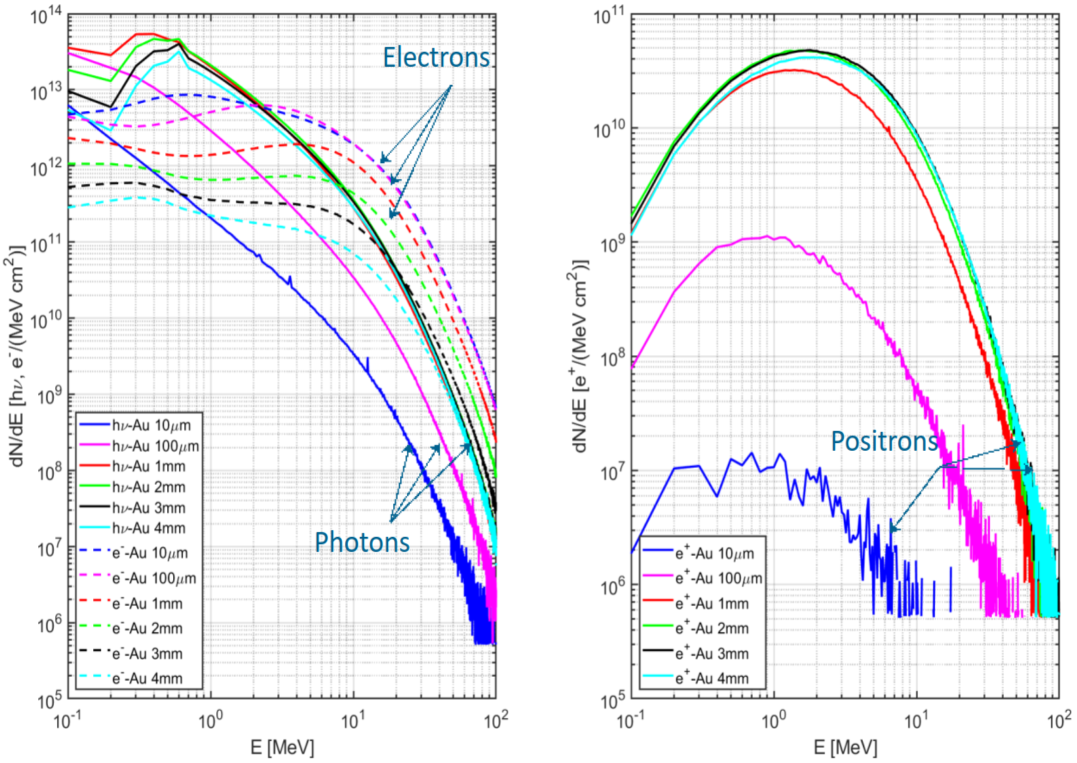

FIGURE 11.3: Differential fluences of photons, primary and secondary electrons and positrons as a function of the corresponding energy, integrated over solid angle 2π in forward direction, detected directly from the rear side of Au targets of 10 μm, 100 μm, 1 mm, 2 mm, 3 mm, 4 mm thickness.

photons give possibility to perform different experiments such as investigation of the nuclear structures, various interaction mechanisms, developing and detecting different materials. Therefore, it is desirable that the photon beam has a maximal intensity and minimal scattering angle. Since the intensity of the bremsstrahlung photons depends on the atomic number Z of material, density and material thickness, then by varying the target thickness in simulated models of the interactions of electron spectra with Maxwellian distribution with high Z targets, an optimal thickness was found when the photon and positron fluences were maximal. The results of the Monte Carlo simulation presented in Figure 11.4 showed that the photon fluence reached the maximum value when Au or W of 1 mm thickness were used as radiator-targets. The experiments with TLD spectrometer also confirmed the highest signal measured with TLD cards when Au foil of 1mm was used as a target. According to the simulations results the most efficient production of positrons was realized by using of Au or W targets of 2 - 3 mm thickness.

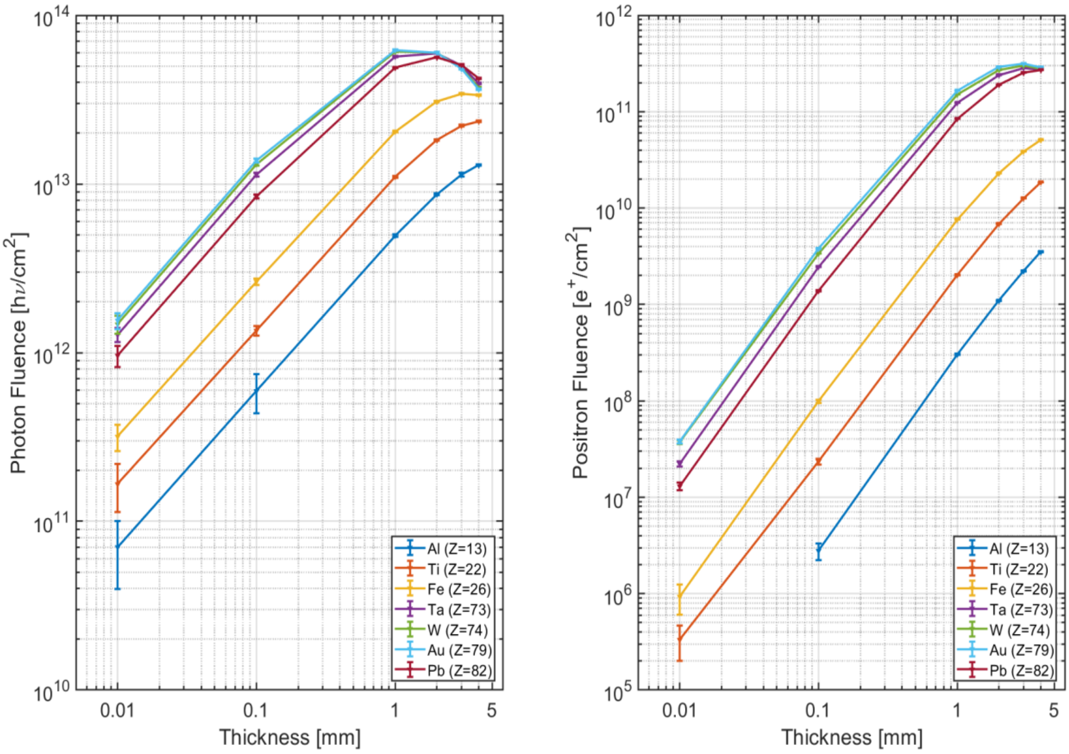

FIGURE 11.4: Integrated fluences of bremsstrahlung photons and positrons from Al, Ti, Fe, Ta, W, Au, Pb targets versus target thickness of 10 μm, 100 μm, 1 mm, 2 mm, 3 mm, 4 mm.

The simulations results of the optimization of high-Z target geometry showed an ultra-high MeV photon number of $\approx 10^{13}$ and positron number of $\approx 10^{11}$ per shot at moderate relativistic laser intensity of $10^{19}\, W/cm^2$. Figure 11.5 (a) shows the total number of photons, electrons and positrons from Au targets of 10 μm, 100 μm, 1 mm, 2 mm, 3 mm, 4 mm thickness. The simulation results showed the predominance of the electron fluence for thin Au targets of 10 μm, 100 μm thickness. The predominance of the photon fluence was obtained for thick targets of 1 - 4 mm thickness, which is explained by an increase of the interaction length in the process of generation of bremsstrahlung photons. Figure 11.5 (b) shows the total number of photons in three energy intervals of $1\, keV - 1\, MeV$, $1\, MeV - 7.5\, MeV$, $7.5\, MeV - 100\, MeV$ irradiated from Au targets of 10 μm, 100 μm, 1 mm, 2 mm, 3 mm, 4 mm thickness. The maximal photon yields with energies of $1\, keV - 1\, MeV$ were emitted by the Au target of 1 mm thickness, the maximal photon yields with energies of $1\, MeV - 7.5\, MeV$ were emitted by the Au target of 2 mm thickness and the maximal photon yields with energies of $7.5\, MeV - 100\, MeV$ were emitted by the Au target of 2 - 3 mm thickness. Detection of the number of photons within certain energy intervals and looking at the maximum production in 2π forward direction gives possibility to investigate laser generated bremsstrahlung photons for initiation of photonuclear reactions. The spectrum of the generated gammas is energetically broad and reaches the giant dipole resonance region. Thus, it can serve as a source to generate ultrafast neutron beam through photonuclear reaction. The results of these simulations can be used to guide the

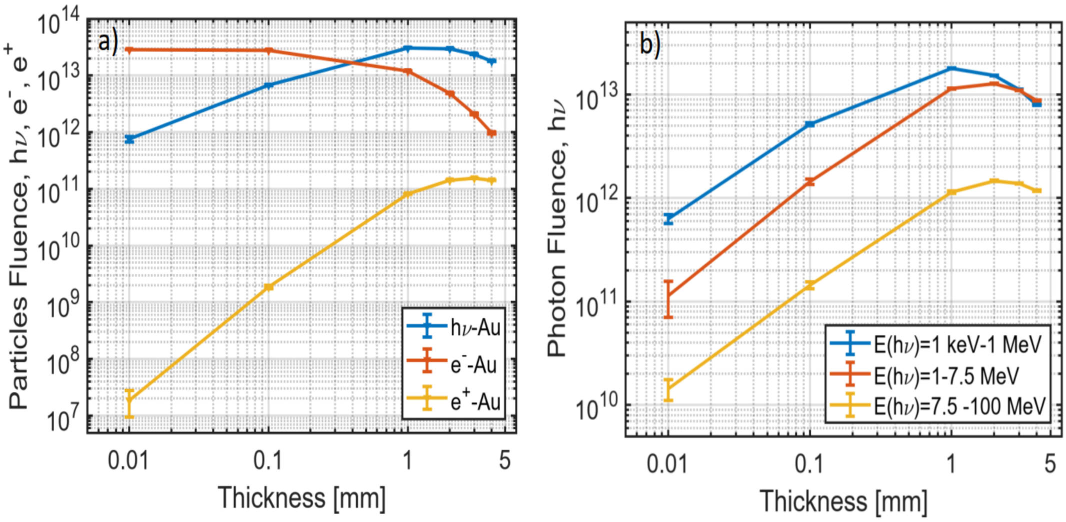

FIGURE 11.5: (a) Simulated photon, electron and positron fluences from Au targets of 10 μm, 100 μm, 1 mm, 2 mm, 3 mm, 4 mm thickness. (b) Simulated photon fluences divided to three energy intervals. The photons, electrons and positrons number was detected in forward direction, 2π solid angle and normalised by the number of initial simulated electrons.

selection of the target materials and thicknesses for the further laser experiments.

Additionally, the electron spectra parameters simulated with particle-in-cell (PIC) code for two laser energies of 20 J and 200 J were imported into a Monte Carlo code FLUKA to simulate the production process of bremsstrahlung photons and positrons in Au converter in order to compare the results of conversion efficiency of the high electron energy into photons. Figure 11.6 shows the conversion efficiency of laser energy into photons production by electron beam with Maxwellian energy distribution on Au targets of different thickness for 20 J and 200 J laser energy. The results of the simulations showed that the record of conversion efficiency in MeV gammas can reach 10%, which reinforces the generation of positrons. Further application of proposed robust target scheme, which does not require a high laser pointing stability, an ultra-high laser intensity and a high laser contrast, paves the way to a new level of diagnostic potential of kJ-class PW laser facilitates.

Summarizing the results of the Monte Carlo simulations, it was found that the interaction of high-current well-directed relativistic electrons with Au targets leads to effective production of MeV bremsstrahlung radiation with ultra-high fluence. The simulations demonstrated an extremely high capability of the well-directed high-current relativistic electron beams to be used in novel laser assisted applications using already existing high-energy sub-PW and PW-class laser systems. This approach is very important for applications that promise a strong improvement in the performance of laser sources of particles and photons.

In conclusion, the experimental results and the results of the numerical simulations reported in this thesis demonstrated the advantages of long-scale plasmas of near critical density (NCD) to increase parameters of MeV particles and photon

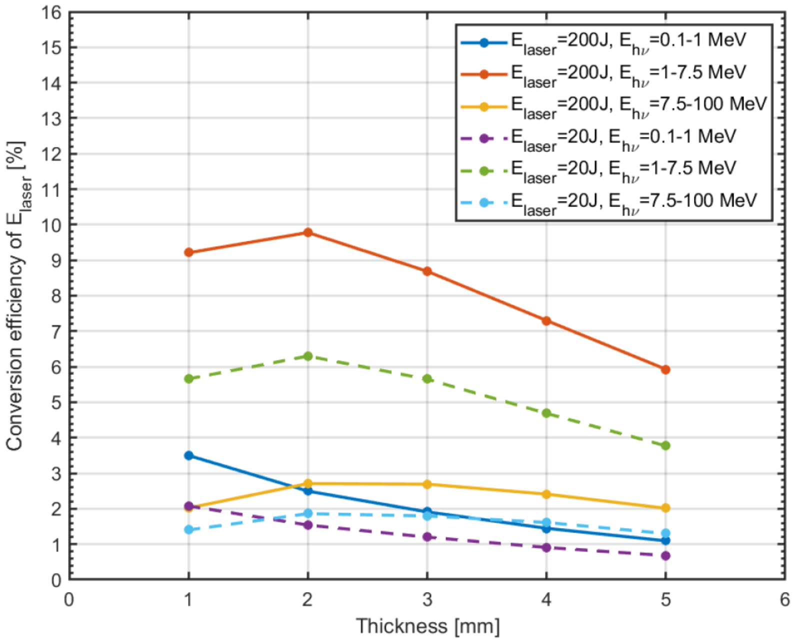

FIGURE 11.6: Conversion efficiency of laser energy into photons production by electron beam with Maxwellian energy distribution on Au targes of different thickness for 20 J and 200 J laser energy.

beams generated in relativistic laser-plasma interaction. The efficiency of laser-driven generation of MeV electrons and photons by application of low density polymer foams is essentially enhanced. These electrons are an excellent tool for many applications producing vast amount of MeV gamma radiation in interaction with high Z target-convertor, which can be used to trigger gamma-driven nuclear reactions and electron-positron pair production. This also brings new aspects concerning the laser-induced acceleration of electrons and generations of MeV gammas in future experiments.

Appendix A

FLUKA input file

This is a FLUKA input file used for simulations of the interactions of the electron beam with different targets. The electron beam was described by Maxwell distribution function with two electron temperatures by means of SOURCE routine written in fortran. The purpose of the simulation was to calculate electron, positron and photon fluences, their spatial distribution and total amount of particles for different targets materials and thicknesses. Additionally the results of the Monte Carlo simulations of LiF thermoluminescent dosimeters (TLDs) to the generated radiation were performed to calculate the doses in the channels of the TLD spectrometer and then to compare them with the results of the experiment und implement the results for unfolding algorithm.

```
TITLE
TLD spectrometer beam target
* Set the defaults for precision simulations
DEFAULTS

   PRECISIO
* Electron beam with 20e−6m diameter and 23.5 divergence
BEAM            −0.1       0.0    −410.2     0.016     0.001
         −1.ELECTRON
* Define the beam position
BEAMPOS         1.55       2.2  −42.102     0.276
EMFRAY            4.   BLKBODY  @LASTREG
*
PHYSICS           2.       0.0       0.0       0.0       0.0
         0.0EVAPORAT
EMFFLUO           1.  HYDROGEN  @LASTMAT
PHYSICS           1.
                                                    COALESCE
PHOTONUC          1.                      TITANIUM      LEAD
GEOBEGIN

   COMBNAME
```

```
    0      0             TLD spectrometer
* Black body
SPH blkbody      0.0 0.0 0.0 5000.
* Void sphere
SPH void         0.0 0.0 0.0 1000.
* vacuum chamber outside
RPP VACH1        −69.75 137.75 −51.75 51.75 −97.95 34.55
* vacuum chamber inside
RPP VACH2        −68. 136. −50. 50. −96.2 32.8
* Lead outside
RPP Pb1          −2.1 5.2 −2.1 5.9 −2.1 13.75
* Lead inside
RPP Pb2          −0.6 3.7 −0.6 4.4 −0.6 12.25
* PVH layer in front of lead cover
RPP PVHL2        0.0 3.1 0.0 4.4 −3.1 −2.1
* Target−Air initial region of electron spectra
RPP TARGAIR1     1.2 1.9 1.85 2.55 −42.102 −42.101
* Target
RPP TARGE        1.2 1.9 1.85 2.55 −42.101 −42.1
* Target−Air
RPP TARGEAIR     1.2 1.9 1.85 2.55 −42.1 −42.099
* 1st Apperture in Lead
RCC Pb7          0.85 0.9 −2.1 0.0 0.0 1.5 0.5
* 2nd Apperture in Lead
RCC Pb8          2.25 0.9 −2.1 0.0 0.0 1.5 0.5
* 3d Apperture in Lead
RCC Pb9          2.25 3.5 −2.1 0.0 0.0 1.5 0.5
* 4th Apperture in Lead
RCC Pb10         0.85 3.5 −2.1 0.0 0.0 1.5 0.5
* Aluminum left side
RPP Al1          −0.6 0.0 0.0 4.4 −0.6 11.65
* Aluminum right side
RPP Al2          3.1 3.7 0.0 4.4 −0.6 11.65
* Aluminum back side
RPP Al3          −0.6 3.7 0.0 4.4 11.65 12.25
* Aluminum bottom side
RPP Al4          −0.6 3.7 −0.6 0.0 0.0 12.25
* Aluminum front side
RPP Al5          −0.6 3.7 −0.6 0.3 −0.6 0.0
RCC TLD1         0.85 0.9 0.0 0.0 0.0 0.2 0.5
RCC TLD2         2.25 0.9 0.0 0.0 0.0 0.2 0.5
RCC TLD3         2.25 3.5 0.0 0.0 0.0 0.2 0.5
```

```
RCC TLD4         0.85 3.5 0.0 0.0 0.0 0.2 0.5
RPP KRIS1        0.65 1.05 0.7 1.1 0.0 0.1
RPP KRIS2        2.05 2.45 0.7 1.1 0.0 0.1
RPP KRIS3        2.05 2.45 3.3 3.7 0.0 0.1
RPP KRIS4        0.65 1.05 3.3 3.7 0.0 0.1
 $start_translat 0 0 0.8
RCC TLD5         0.85 0.9 0.0 0.0 0.0 0.2 0.5
RCC TLD6         2.25 0.9 0.0 0.0 0.0 0.2 0.5
RCC TLD7         2.25 3.5 0.0 0.0 0.0 0.2 0.5
RCC TLD8         0.85 3.5 0.0 0.0 0.0 0.2 0.5
RPP KRIS5        0.65 1.05 0.7 1.1 0.0 0.1
RPP KRIS6        2.05 2.45 0.7 1.1 0.0 0.1
RPP KRIS7        2.05 2.45 3.3 3.7 0.0 0.1
RPP KRIS8        0.65 1.05 3.3 3.7 0.0 0.1
 $end_translat
 $start_translat 0 0 1.9
RCC TLD9         0.85 0.9 0.0 0.0 0.0 0.2 0.5
RCC TLD10        2.25 0.9 0.0 0.0 0.0 0.2 0.5
RCC TLD11        2.25 3.5 0.0 0.0 0.0 0.2 0.5
RCC TLD12        0.85 3.5 0.0 0.0 0.0 0.2 0.5
RPP KRIS9        0.65 1.05 0.7 1.1 0.0 0.1
RPP KRIS10       2.05 2.45 0.7 1.1 0.0 0.1
RPP KRIS11       2.05 2.45 3.3 3.7 0.0 0.1
RPP KRIS12       0.65 1.05 3.3 3.7 0.0 0.1
 $end_translat
 $start_translat 0 0 3.1
RCC TLD13        0.85 0.9 0.0 0.0 0.0 0.2 0.5
RCC TLD14        2.25 0.9 0.0 0.0 0.0 0.2 0.5
RCC TLD15        2.25 3.5 0.0 0.0 0.0 0.2 0.5
RCC TLD16        0.85 3.5 0.0 0.0 0.0 0.2 0.5
RPP KRIS13       0.65 1.05 0.7 1.1 0.0 0.1
RPP KRIS14       2.05 2.45 0.7 1.1 0.0 0.1
RPP KRIS15       2.05 2.45 3.3 3.7 0.0 0.1
RPP KRIS16       0.65 1.05 3.3 3.7 0.0 0.1
 $end_translat
 $start_translat 0 0 4.75
RCC TLD17        0.85 0.9 0.0 0.0 0.0 0.2 0.5
RCC TLD18        2.25 0.9 0.0 0.0 0.0 0.2 0.5
RCC TLD19        2.25 3.5 0.0 0.0 0.0 0.2 0.5
RCC TLD20        0.85 3.5 0.0 0.0 0.0 0.2 0.5
RPP KRIS17       0.65 1.05 0.7 1.1 0.0 0.1
RPP KRIS18       2.05 2.45 0.7 1.1 0.0 0.1
```

```
RPP KRIS19      2.05 2.45 3.3 3.7 0.0 0.1
RPP KRIS20      0.65 1.05 3.3 3.7 0.0 0.1
$end_translat
$start_translat 0 0 6.85
RCC TLD21       0.85 0.9 0.0 0.0 0.0 0.2 0.5
RCC TLD22       2.25 0.9 0.0 0.0 0.0 0.2 0.5
RCC TLD23       2.25 3.5 0.0 0.0 0.0 0.2 0.5
RCC TLD24       0.85 3.5 0.0 0.0 0.0 0.2 0.5
RPP KRIS21      0.65 1.05 0.7 1.1 0.0 0.1
RPP KRIS22      2.05 2.45 0.7 1.1 0.0 0.1
RPP KRIS23      2.05 2.45 3.3 3.7 0.0 0.1
RPP KRIS24      0.65 1.05 3.3 3.7 0.0 0.1
$end_translat
$start_translat 0 0 9.05
RCC TLD25       0.85 0.9 0.0 0.0 0.0 0.2 0.5
RCC TLD26       2.25 0.9 0.0 0.0 0.0 0.2 0.5
RCC TLD27       2.25 3.5 0.0 0.0 0.0 0.2 0.5
RCC TLD28       0.85 3.5 0.0 0.0 0.0 0.2 0.5
RPP KRIS25      0.65 1.05 0.7 1.1 0.0 0.1
RPP KRIS26      2.05 2.45 0.7 1.1 0.0 0.1
RPP KRIS27      2.05 2.45 3.3 3.7 0.0 0.1
RPP KRIS28      0.65 1.05 3.3 3.7 0.0 0.1
$end_translat
$start_translat 0 0 10.85
RCC TLD29       0.85 0.9 0.0 0.0 0.0 0.2 0.5
RCC TLD30       2.25 0.9 0.0 0.0 0.0 0.2 0.5
RCC TLD31       2.25 3.5 0.0 0.0 0.0 0.2 0.5
RCC TLD32       0.85 3.5 0.0 0.0 0.0 0.2 0.5
RPP KRIS29      0.65 1.05 0.7 1.1 0.0 0.1
RPP KRIS30      2.05 2.45 0.7 1.1 0.0 0.1
RPP KRIS31      2.05 2.45 3.3 3.7 0.0 0.1
RPP KRIS32      0.65 1.05 3.3 3.7 0.0 0.1
$end_translat
* Air layer
RPP AIRL1       0.0 3.1 0.3 4.4 -0.6 0.0
* 1st TLD card
RPP TLDCA1      0.0 3.1 0.0 4.4 0.0 0.2
* 1st Cu layer
RPP CUP1        0.0 3.1 0.0 4.4 0.2 0.8
* 2nd TLD card
RPP TLDCA2      0.0 3.1 0.0 4.4 0.8 1.
* 2nd Cuprum layer
```

```
RPP CUP2        0.0 3.1 0.0 4.4 1. 1.9
* 3d TLD card
RPP TLDCA3      0.0 3.1 0.0 4.4 1.9 2.1
* 3d Cuprum layer
RPP CUP3        0.0 3.1 0.0 4.4 2.1 3.1
* 4th TLD card
RPP TLDCA4      0.0 3.1 0.0 4.4 3.1 3.3
* 1st Ferrum layer
RPP FER1        0.0 3.1 0.0 4.4 3.3 4.75
* 5th TLD card
RPP TLDCA5      0.0 3.1 0.0 4.4 4.75 4.95
* 2nd Ferrum layer
RPP FER2        0.0 3.1 0.0 4.4 4.95 6.85
* 6th TLD card
RPP TLDCA6      0.0 3.1 0.0 4.4 6.85 7.05
* 3d Ferrum layer
RPP FER3        0.0 3.1 0.0 4.4 7.05 9.05
* 7th TLD card
RPP TLDCA7      0.0 3.1 0.0 4.4 9.05 9.25
* Plumbum layer
RPP PLB1        0.0 3.1 0.0 4.4 9.25 10.85
* 8th TLD card
RPP TLDCA8      0.0 3.1 0.0 4.4 10.85 11.05
* PVH layer
RPP PVHL1       0.0 3.1 0.0 4.4 11.05 11.65
END
* Black hole
BLKBODY       5 +blkbody -void
AIROUT        5 +void -VACH1
WALLCH        5 +VACH1 -VACH2
AIRIN         5 +VACH2 -TARGE -PVHL2 -Pb1-TARGAIR1 -TARGEAIR
RPB1          5 +Pb1-Pb2-Pb7-Pb8-Pb9 -Pb10
RAl1          5 +Al1
                | +Al2
                | +Al3
                | +Al4
                | +Al5
RTARGE        5 +TARGE
RTARGEA       5 +TARGEAIR
RTARGEA1      5 +TARGAIR1
RCUP1         5 +CUP1
RCUP2         5 +CUP2
```

```
RCUP3        5 +CUP3
RFER1        5 +FER1
RFER2        5 +FER2
RFER3        5 +FER3
RPLB1        5 +PLB1
RPVHL1       5 +PVHL1
RPVHL2       5 +PVHL2
RAIRL1       5 +AIRL1
               | +Pb7
               | +Pb8
               | +Pb9
               | +Pb10
RKRIS1       5 +KRIS1
RKRIS2       5 +KRIS2
RKRIS3       5 +KRIS3
RKRIS4       5 +KRIS4
RKRIS5       5 +KRIS5
RKRIS6       5 +KRIS6
RKRIS7       5 +KRIS7
RKRIS8       5 +KRIS8
RKRIS9       5 +KRIS9
RKRIS10      5 +KRIS10
RKRIS11      5 +KRIS11
RKRIS12      5 +KRIS12
RKRIS13      5 +KRIS13
RKRIS14      5 +KRIS14
RKRIS15      5 +KRIS15
RKRIS16      5 +KRIS16
RKRIS17      5 +KRIS17
RKRIS18      5 +KRIS18
RKRIS19      5 +KRIS19
RKRIS20      5 +KRIS20
RKRIS21      5 +KRIS21
RKRIS22      5 +KRIS22
RKRIS23      5 +KRIS23
RKRIS24      5 +KRIS24
RKRIS25      5 +KRIS25
RKRIS26      5 +KRIS26
RKRIS27      5 +KRIS27
RKRIS28      5 +KRIS28
RKRIS29      5 +KRIS29
RKRIS30      5 +KRIS30
```

```
RKRIS31     5  +KRIS31
RKRIS32     5  +KRIS32
RTLD1       5  +TLD1  −KRIS1
RTLD2       5  +TLD2  −KRIS2
RTLD3       5  +TLD3  −KRIS3
RTLD4       5  +TLD4  −KRIS4
RTLD5       5  +TLD5  −KRIS5
RTLD6       5  +TLD6  −KRIS6
RTLD7       5  +TLD7  −KRIS7
RTLD8       5  +TLD8  −KRIS8
RTLD9       5  +TLD9–KRIS9
RTLD10      5  +TLD10–KRIS10
RTLD11      5  +TLD11–KRIS11
RTLD12      5  +TLD12  −KRIS12
RTLD13      5  +TLD13  −KRIS13
RTLD14      5  +TLD14  −KRIS14
RTLD15      5  +TLD15  −KRIS15
RTLD16      5  +TLD16  −KRIS16
RTLD17      5  +TLD17  −KRIS17
RTLD18      5  +TLD18  −KRIS18
RTLD19      5  +TLD19  −KRIS19
RTLD20      5  +TLD20  −KRIS20
RTLD21      5  +TLD21  −KRIS21
RTLD22      5  +TLD22  −KRIS22
RTLD23      5  +TLD23  −KRIS23
RTLD24      5  +TLD24  −KRIS24
RTLD25      5  +TLD25  −KRIS25
RTLD26      5  +TLD26  −KRIS26
RTLD27      5  +TLD27  −KRIS27
RTLD28      5  +TLD28  −KRIS28
RTLD29      5  +TLD29  −KRIS29
RTLD30      5  +TLD30  −KRIS30
RTLD31      5  +TLD31  −KRIS31
RTLD32      5  +TLD32  −KRIS32
RTLDCA1     5  +TLDCA1  −TLD1  −TLD2  −TLD3  −TLD4
RTLDCA2     5  +TLDCA2  −TLD5  −TLD6  −TLD7  −TLD8
RTLDCA3     5  +TLDCA3  −TLD9  −TLD10  −TLD11  −TLD12
RTLDCA4     5  +TLDCA4  −TLD13  −TLD14  −TLD15  −TLD16
RTLDCA5     5  +TLDCA5  −TLD17  −TLD18  −TLD19  −TLD20
RTLDCA6     5  +TLDCA6  −TLD21  −TLD22  −TLD23  −TLD24
RTLDCA7     5  +TLDCA7–TLD25  −TLD26  −TLD27  −TLD28
RTLDCA8     5  +TLDCA8  −TLD29  −TLD30  −TLD31  −TLD32
```

```
END
GEOEND
MATERIAL          3.  6.015122        1.       26.
                    6.LITHIU-6
MATERIAL          3.  7.016004        1.       27.
                    7.LITHIU-7
MATERIAL          9.  18.99840        1.       28.
                      FLUORINE
MATERIAL         15.  30.97376        1.       29.
                      PHOSPHO
MATERIAL         0.0       0.0      2.40       30.
                      TLD600H
COMPOUND     -0.2283  LITHIU-6  -0.01179  LITHIU-7    -0.002
    MAGNESIUTLD600H
COMPOUND    -0.00004    COPPER  -0.75487  FLUORINE    -0.003
     PHOSPHOTLD600H
MATERIAL         0.0       0.0      2.49       31.
                      TLD700H
COMPOUND   -0.000072  LITHIU-6   -0.2678  LITHIU-7    -0.002
    MAGNESIUTLD700H
COMPOUND    -0.00004    COPPER -0.727088  FLUORINE    -0.003
     PHOSPHOTLD700H
MATERIAL         0.0       0.0       1.3
                                Sand
COMPOUND          2.    OXYGEN        1.   SILICON
                      Sand
MATERIAL         30.     65.39     7.133
                                ZINC
* Brass (typical)
* Brass can have a wide variation of Cu/Zn content. Pb is not
* always present.
MATERIAL                            8.52
                                Brass
COMPOUND         58.    COPPER       39.      ZINC        3.
        LEADBrass
MATERIAL         17.   35.4527   .003214
                                CHLORINE
* Polyvinyl chloride (C2_H3_Cl)n
*
MATERIAL                            1.44
                                PVC
```

```
COMPOUND      -.04838   HYDROGEN     -.38436      CARBON    -.56726
     CHLORINEPVC
* 227 Teflon
* Chemical                  F      F
* Formula                   |      |
*                   ----- C -- C -----
*                           |      |
*                           F      F
MATERIAL                                   2.2
                                        Teflon
COMPOUND             2.      CARBON          4.   FLUORINE
                         Teflon
* 104 Air dry (near sea level)
*
MATERIAL                                  4.8E-9
                                       AIR1
COMPOUND    -1.248E-4      CARBON  -0.755267    NITROGEN  -0.231781
        OXYGENAIR1
COMPOUND    -0.012827       ARGON
                                                    AIR1
MAT-PROP          4E-6                                   AIR1
*
    ..+....1....+....2....+....3....+....4....+....5....+....6....+....7..

ASSIGNMA    BLCKHOLE    BLKBODY
ASSIGNMA         AIR     AIROUT
ASSIGNMA        IRON     WALLCH
ASSIGNMA        AIR1      AIRIN
ASSIGNMA     TLD700H     RKRIS1
ASSIGNMA     TLD700H     RKRIS2
ASSIGNMA     TLD700H     RKRIS3
ASSIGNMA     TLD700H     RKRIS4
ASSIGNMA     TLD700H     RKRIS5
ASSIGNMA     TLD700H     RKRIS6
ASSIGNMA     TLD700H     RKRIS7
ASSIGNMA     TLD700H     RKRIS8
ASSIGNMA     TLD700H     RKRIS9
ASSIGNMA     TLD700H    RKRIS10
ASSIGNMA     TLD700H    RKRIS11
ASSIGNMA     TLD700H    RKRIS12
ASSIGNMA     TLD700H    RKRIS13
ASSIGNMA     TLD700H    RKRIS14
```

```
ASSIGNMA     TLD700H   RKRIS15
ASSIGNMA     TLD700H   RKRIS16
ASSIGNMA     TLD700H   RKRIS17
ASSIGNMA     TLD700H   RKRIS18
ASSIGNMA     TLD700H   RKRIS19
ASSIGNMA     TLD700H   RKRIS20
ASSIGNMA     TLD700H   RKRIS21
ASSIGNMA     TLD700H   RKRIS22
ASSIGNMA     TLD700H   RKRIS23
ASSIGNMA     TLD700H   RKRIS24
ASSIGNMA     TLD700H   RKRIS25
ASSIGNMA     TLD700H   RKRIS26
ASSIGNMA     TLD700H   RKRIS27
ASSIGNMA     TLD700H   RKRIS28
ASSIGNMA     TLD700H   RKRIS29
ASSIGNMA     TLD700H   RKRIS30
ASSIGNMA     TLD700H   RKRIS31
ASSIGNMA     TLD700H   RKRIS32
ASSIGNMA         AIR     RTLD1
ASSIGNMA         AIR     RTLD2
ASSIGNMA         AIR     RTLD3
ASSIGNMA         AIR     RTLD4
ASSIGNMA         AIR     RTLD5
ASSIGNMA         AIR     RTLD6
ASSIGNMA         AIR     RTLD7
ASSIGNMA         AIR     RTLD8
ASSIGNMA         AIR     RTLD9
ASSIGNMA         AIR    RTLD10
ASSIGNMA         AIR    RTLD11
ASSIGNMA         AIR    RTLD12
ASSIGNMA         AIR    RTLD13
ASSIGNMA         AIR    RTLD14
ASSIGNMA         AIR    RTLD15
ASSIGNMA         AIR    RTLD16
ASSIGNMA         AIR    RTLD17
ASSIGNMA         AIR    RTLD18
ASSIGNMA         AIR    RTLD19
ASSIGNMA         AIR    RTLD20
ASSIGNMA         AIR    RTLD21
ASSIGNMA         AIR    RTLD22
ASSIGNMA         AIR    RTLD23
ASSIGNMA         AIR    RTLD24
```

```
ASSIGNMA         AIR    RTLD25
ASSIGNMA         AIR    RTLD26
ASSIGNMA         AIR    RTLD27
ASSIGNMA         AIR    RTLD28
ASSIGNMA         AIR    RTLD29
ASSIGNMA         AIR    RTLD30
ASSIGNMA         AIR    RTLD31
ASSIGNMA         AIR    RTLD32
ASSIGNMA    ALUMINUM   RTLDCA1
ASSIGNMA    ALUMINUM   RTLDCA2
ASSIGNMA    ALUMINUM   RTLDCA3
ASSIGNMA    ALUMINUM   RTLDCA4
ASSIGNMA    ALUMINUM   RTLDCA5
ASSIGNMA    ALUMINUM   RTLDCA6
ASSIGNMA    ALUMINUM   RTLDCA7
ASSIGNMA    ALUMINUM   RTLDCA8
ASSIGNMA      COPPER     RCUP1
ASSIGNMA      COPPER     RCUP2
ASSIGNMA      COPPER     RCUP3
ASSIGNMA        IRON     RFER1
ASSIGNMA        IRON     RFER2
ASSIGNMA        IRON     RFER3
ASSIGNMA        LEAD     RPLB1
ASSIGNMA         PVC    RPVHL1
ASSIGNMA        AIR1    RAIRL1
ASSIGNMA    ALUMINUM      RAl1
ASSIGNMA        LEAD      RPB1
ASSIGNMA         PVC    RPVHL2
ASSIGNMA        GOLD    RTARGE
ASSIGNMA        AIR1   RTARGEA
ASSIGNMA        AIR1  RTARGEA1
* Set transport cut off for electrons (10keV) and photon (1
  keV) in all regions
EMFCUT        -1E-05      1E-6             BLKBODY  @LASTREG
EMFCUT        -1E-05      1E-6      1E-5  HYDROGEN  @LASTMAT
          PROD-CUT
BIASING           2.                4000.     RPLB1
                     PRINT
BIASING           2.                4000.    RPVHL1
                     PRINT
BIASING           2.                4000.   RTLDCA8
                     PRINT
```

```
BIASING           2.                 4000.   RKRIS32
                        PRINT
BIASING           2.                 4000.   RKRIS31
                        PRINT
BIASING           2.                 4000.   RKRIS30
                        PRINT
BIASING           2.                 4000.   RKRIS29
                        PRINT
BIASING           2.                 4000.    RTLD32
                        PRINT
BIASING           2.                 4000.    RTLD31
                        PRINT
BIASING           2.                 4000.    RTLD30
                        PRINT
BIASING           2.                 4000.    RTLD29
                        PRINT
BIASING           2.                 2000.     RFER3
                        PRINT
BIASING           2.                 2000.   RTLDCA7
                        PRINT
BIASING           2.                 2000.   RKRIS28
                        PRINT
BIASING           2.                 2000.   RKRIS27
                        PRINT
BIASING           2.                 2000.   RKRIS26
                        PRINT
BIASING           2.                 2000.   RKRIS25
                        PRINT
BIASING           2.                 2000.    RTLD28
                        PRINT
BIASING           2.                 2000.    RTLD27
                        PRINT
BIASING           2.                 2000.    RTLD26
                        PRINT
BIASING           2.                 2000.    RTLD25
                        PRINT
BIASING           2.                  400.     RFER2
                        PRINT
BIASING           2.                  400.   RTLDCA6
                        PRINT
BIASING           2.                  400.   RKRIS24
                        PRINT
```

```
BIASING         2.                400.   RKRIS23
                     PRINT
BIASING         2.                400.   RKRIS22
                     PRINT
BIASING         2.                400.   RKRIS21
                     PRINT
BIASING         2.                400.    RTLD24
                     PRINT
BIASING         2.                400.    RTLD23
                     PRINT
BIASING         2.                400.    RTLD22
                     PRINT
BIASING         2.                400.    RTLD21
                     PRINT
BIASING         2.                200.     RFER1
                     PRINT
BIASING         2.                200.   RTLDCA5
                     PRINT
BIASING         2.                200.   RKRIS20
                     PRINT
BIASING         2.                200.   RKRIS19
                     PRINT
BIASING         2.                200.   RKRIS18
                     PRINT
BIASING         2.                200.   RKRIS17
                     PRINT
BIASING         2.                200.    RTLD20
                     PRINT
BIASING         2.                200.    RTLD19
                     PRINT
BIASING         2.                200.    RTLD18
                     PRINT
BIASING         2.                200.    RTLD17
                     PRINT
BIASING         2.                 20.     RCUP3
                     PRINT
BIASING         2.                 20.   RTLDCA4
                     PRINT
BIASING         2.                 20.   RKRIS16
                     PRINT
BIASING         2.                 20.   RKRIS15
                     PRINT
```

```
BIASING          2.                  20.   RKRIS14
                      PRINT
BIASING          2.                  20.   RKRIS13
                      PRINT
BIASING          2.                  20.    RTLD16
                      PRINT
BIASING          2.                  20.    RTLD15
                      PRINT
BIASING          2.                  20.    RTLD14
                      PRINT
BIASING          2.                  20.    RTLD13
                      PRINT
BIASING          2.                  20.     RCUP2
                      PRINT
BIASING          2.                  20.   RTLDCA3
                      PRINT
BIASING          2.                  20.   RKRIS12
                      PRINT
BIASING          2.                  20.   RKRIS11
                      PRINT
BIASING          2.                  20.   RKRIS10
                      PRINT
BIASING          2.                  20.    RKRIS9
                      PRINT
BIASING          2.                  20.    RTLD12
                      PRINT
BIASING          2.                  20.    RTLD11
                      PRINT
BIASING          2.                  20.    RTLD10
                      PRINT
BIASING          2.                  20.     RTLD9
                      PRINT
BIASING          2.                   4.     RCUP1
                      PRINT
BIASING          2.                   4.   RTLDCA2
                      PRINT
BIASING          2.                   4.    RKRIS8
                      PRINT
BIASING          2.                   4.    RKRIS7
                      PRINT
BIASING          2.                   4.    RKRIS6
                      PRINT
```

```
BIASING             2.                       4.      RKRIS5
                         PRINT
BIASING             2.                       4.       RTLD8
                         PRINT
BIASING             2.                       4.       RTLD7
                         PRINT
BIASING             2.                       4.       RTLD6
                         PRINT
BIASING             2.                       4.       RTLD5
                         PRINT
BIASING             2.                       2.      RAIRL1
                         PRINT
BIASING             2.                       2.     RTLDCA1
                         PRINT
BIASING             2.                       2.      RKRIS4
                         PRINT
BIASING             2.                       2.      RKRIS3
                         PRINT
BIASING             2.                       2.      RKRIS2
                         PRINT
BIASING             2.                       2.      RKRIS1
                         PRINT
BIASING             2.                       2.       RTLD4
                         PRINT
BIASING             2.                       2.       RTLD3
                         PRINT
BIASING             2.                       2.       RTLD2
                         PRINT
BIASING             2.                       2.       RTLD1
                         PRINT
BIASING             2.                       1.        RAl1
                         PRINT
BIASING             2.                     1E-1        RPB1
                         PRINT
BIASING             2.                     1E-1      RPVHL2
                         PRINT
BIASING             2.                       1.       AIRIN
                         PRINT
BIASING             2.                       1.      RTARGE
                         PRINT
BIASING             2.                       1.     RTARGEA
                         PRINT
```

```
BIASING             2.                       1.  RTARGEA1
                         PRINT
LAM−BIAS            0.0         0.1        GOLD  ELECTRON
LAM−BIAS            0.0         0.1        GOLD    PHOTON
LAM−BIAS            0.0         0.1    TITANIUM  ELECTRON
LAM−BIAS            0.0         0.1    TITANIUM    PHOTON
LAM−BIAS            0.0         0.1    TANTALUM  ELECTRON
LAM−BIAS            0.0         0.1    TANTALUM    PHOTON
LAM−BIAS            0.0         0.1    TUNGSTEN  ELECTRON
LAM−BIAS            0.0         0.1    TUNGSTEN    PHOTON
LAM−BIAS            0.0         0.1        LEAD  ELECTRON
LAM−BIAS            0.0         0.1        LEAD    PHOTON
* Target−spectrometer:energy deposition [GeV/cm3] and fluence
   ; 1bin=0.1cm
USRBIN              10.      ENERGY        −31.         6.          8.
           15.energdepos
USRBIN              −3.         −4.        −43.        90.        120.
          580. &
USRBIN              10.      PHOTON        −32.         6.          8.
           15.photbins
USRBIN              −3.         −4.        −43.        90.        120.
          580. &
USRBIN              10.    ELECTRON        −33.         6.          8.
           15.electbins
USRBIN              −3.         −4.        −43.        90.        120.
          580. &
USRBIN              10.    POSITRON        −34.         6.          8.
           15.positbins
USRBIN              −3.         −4.        −43.        90.        120.
          580. &
* Energy deposition on 1−8 TLD [GeV/cm3]
USRBIN              12.      ENERGY        −35.   RKRIS32
                         TLD_DO1
USRBIN          RKRIS1
                                                                 &
* Dose on 1 −8 TLDs Energy / unit mass [GeV/g]
USRBIN              12.        DOSE        −36.   RKRIS32
                         TLD_DO2
USRBIN          RKRIS1
                                                                 &
* Electron fluence [particles/cm2 per primary particles]
```

```
USRBIN             12.  ELECTRON        -37.   RKRIS32
                        TLD_DO3
USRBIN          RKRIS1
                                                                &
* Photon fluence [particles/cm2 per primary particles]
USRBIN             12.    PHOTON        -38.   RKRIS32
                        TLD_DO4
USRBIN          RKRIS1
                                                                &
* Positron fluence [particles/cm2 per primary particles]
USRBIN             12.  POSITRON        -39.   RKRIS32
                        TLD_DO5
USRBIN          RKRIS1
                                                                &
* Differential fluences of photons, electrons, positrons and
   protons as a function of energy by scoring track-length in
    a given region dF/dE. [Detect particles/ [GeV cm2] pro
   prim]
* Photons in Target region
USRTRACK            1.    PHOTON        -21.    RTARGE   0.00049
        1000.PhotSpecTr
USRTRACK           0.1        0.0
                                                    &
* Electrons in Target region
USRTRACK            1.  ELECTRON        -21.    RTARGE   0.00049
        1000.EleSpecTr
USRTRACK           0.1        0.0
                                                    &
* Positrons in Target region
USRTRACK            1.  POSITRON        -21.    RTARGE   0.00049
        1000.PosSpecTr
USRTRACK           0.1        0.0
                                                    &
* Differential fluences of photons, electrons, positrons and
   protons as a function of energy by scoring track-length in
    a given region dF/dE. [Detect particles/ [GeV cm2] pro
   prim]
* Photons in Target region
USRTRACK            1.    PHOTON        -30.    RTARGE   0.00049
        1000.PhotSpcTr
USRTRACK         0.001        0.0
                                                    &
```

```
* Differential fluences of photons, electrons, positrons and
   protons as a function of energy by scoring track-length in
    a given region dF/dE. [Detect particles/ [GeV cm2] pro
   prim]
* Photons in Target region
USRTRACK          1.  ELECTRON      -30.    RTARGE   0.00049
         1000.EleSpcTr
USRTRACK       0.001         0.0
                                                  &
* Differential fluences of photons, electrons, positrons and
   protons as a function of energy by scoring track-length in
    a given region dF/dE. [Detect particles/ [GeV cm2] pro
   prim]
* Photons in Target region
USRTRACK          1.  POSITRON      -30.    RTARGE   0.00049
         1000.PosSpcTr
USRTRACK       0.001         0.0
                                                  &
* Differential fluences of photons, electrons, positrons and
   protons as a function of energy by scoring track-length in
    a given region dF/dE. [Detect particles/ [GeV cm2] pro
   prim]
* Photons in Target region
USRTRACK          1.    PHOTON      -40.  RTARGEA1   0.00049
         1000.PhotSpbTr
USRTRACK         0.1         0.0
                                                  &
* Differential fluences of photons, electrons, positrons and
   protons as a function of energy by scoring track-length in
    a given region dF/dE. [Detect particles/ [GeV cm2] pro
   prim]
* Photons in Target region
USRTRACK          1.  ELECTRON      -40.  RTARGEA1   0.00049
         1000.EleSpbTr
USRTRACK         0.1         0.0
                                                  &
* Differential fluences of photons, electrons, positrons and
   protons as a function of energy by scoring track-length in
    a given region dF/dE. [Detect particles/ [GeV cm2] pro
   prim]
* Photons in Target region
```

```
USRTRACK            1.  POSITRON        -40.  RTARGEA1   0.00049
        1000.PosSpbTr
USRTRACK           0.1       0.0
                                          &
USRYIELD         2401.    PHOTON        -41.    RTARGE   RTARGEA
           1.YieldPh1
USRYIELD           0.1       0.0       1000.        4.       0.0
           3. &
USRYIELD         2401.    PHOTON        -41.    RTARGE   RTARGEA
           1.YieldPh2
USRYIELD           0.1       0.0       1000.        8.        4.
           3. &
USRYIELD         2401.    PHOTON        -41.    RTARGE   RTARGEA
           1.YieldPh3
USRYIELD           0.1       0.0       1000.       12.        8.
           3. &
USRYIELD         2401.    PHOTON        -41.    RTARGE   RTARGEA
           1.YieldPh4
USRYIELD           0.1       0.0       1000.       16.       12.
           3. &
USRYIELD         2401.    PHOTON        -41.    RTARGE   RTARGEA
           1.YieldPh5
USRYIELD           0.1       0.0       1000.       20.       16.
           3. &
USRYIELD         2401.    PHOTON        -41.    RTARGE   RTARGEA
           1.YieldPh6
USRYIELD           0.1       0.0       1000.       24.       20.
           3. &
USRYIELD         2401.    PHOTON        -41.    RTARGE   RTARGEA
           1.YieldPh7
USRYIELD           0.1       0.0       1000.       24.       0.0
           3. &
USRYIELD          124.    PHOTON        -42.    RTARGE   RTARGEA
           1.YieldPh8
USRYIELD          180.       0.0        180.       0.1       0.0
           3. &
* USRBDX scores double differential (energy and engle)
   particle distributions across a boundary surface d2F/dE*
   dOmega. [Detect particles/ (GeV cm2 Sr]
* Photon electron positron fluence exiting Au target
USRBDX            101.    PHOTON        -51.    RTARGE   RTARGEA
         0.49PhoTar
```

```
USRBDX            0.1       0.0     1000.
                                          &
USRBDX           101.  ELECTRON      -51.    RTARGE   RTARGEA
        0.49ElTar
USRBDX            0.1       0.0     1000.
                                          &
USRBDX           101.  POSITRON      -51.    RTARGE   RTARGEA
        0.49PosTar
USRBDX            0.1       0.0     1000.
                                          &
* primary incoming: fluence and current
USRBDX            99.    PHOTON      -52.    RTARGE   RTARGEA
        0.49PrimFF
USRBDX            0.1   0.00001     1000.    0.8418       0.0
          6. &
USRBDX           -1.   ELECTRON      -52.    RTARGE   RTARGEA
        0.49PrimC
USRBDX            0.1    0.0001     1000.    0.8418       0.0
          6. &
* Set the random number seed
RANDOMIZ          1.
* Set the number of primary histories to be simulated in the
   run
START      10000000.
STOP
```

Appendix B

Fluences of electrons, positrons, and bremsstrahlung photons

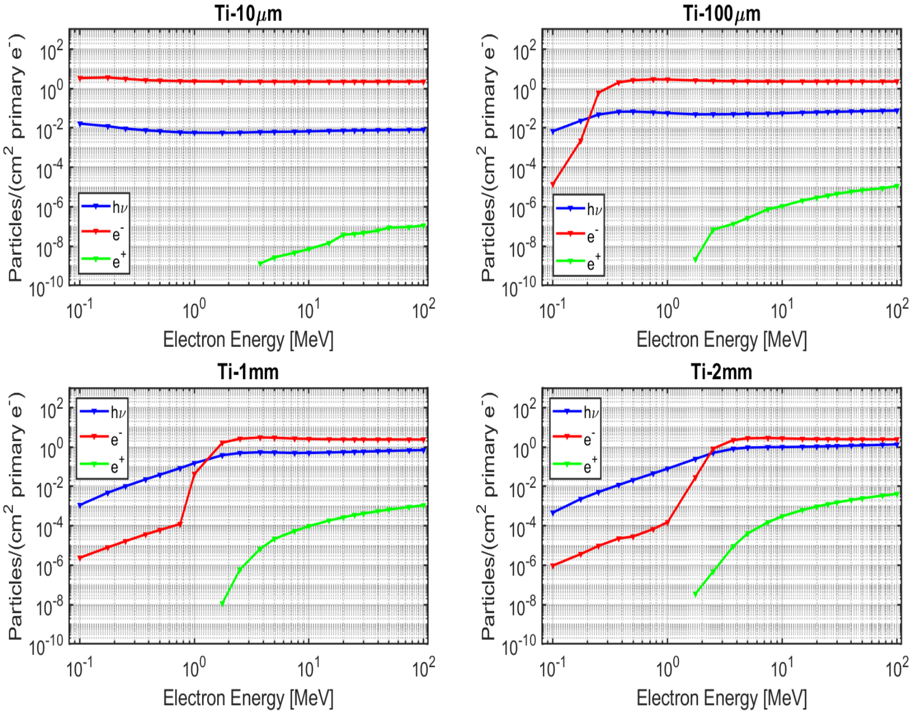

FIGURE B.1: Integrated fluences of electrons, positrons, and bremsstrahlung photons versus energy of incident electrons on Ti targets of 10μm, 100μm, 1 mm, 2 mm thickness.

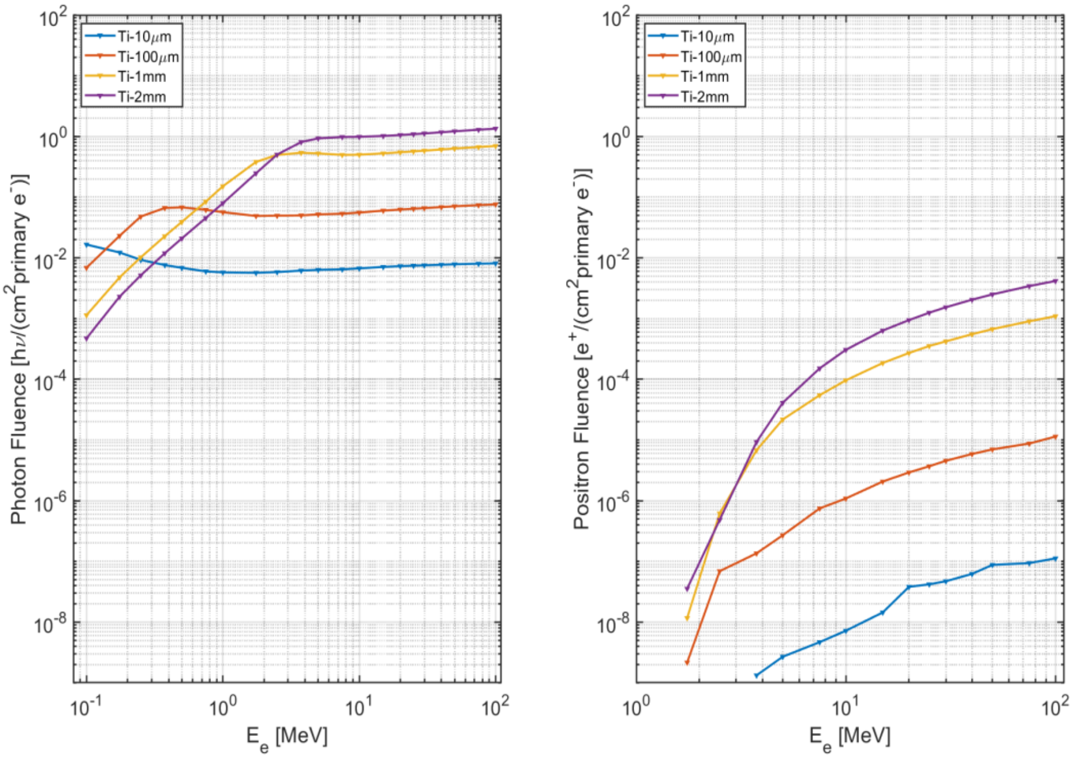

FIGURE B.2: Integrated fluences of positrons and bremsstrahlung photons versus energy of incident electrons on Ti targets of 10μm, 100μm, 1 mm, 2 mm thickness.

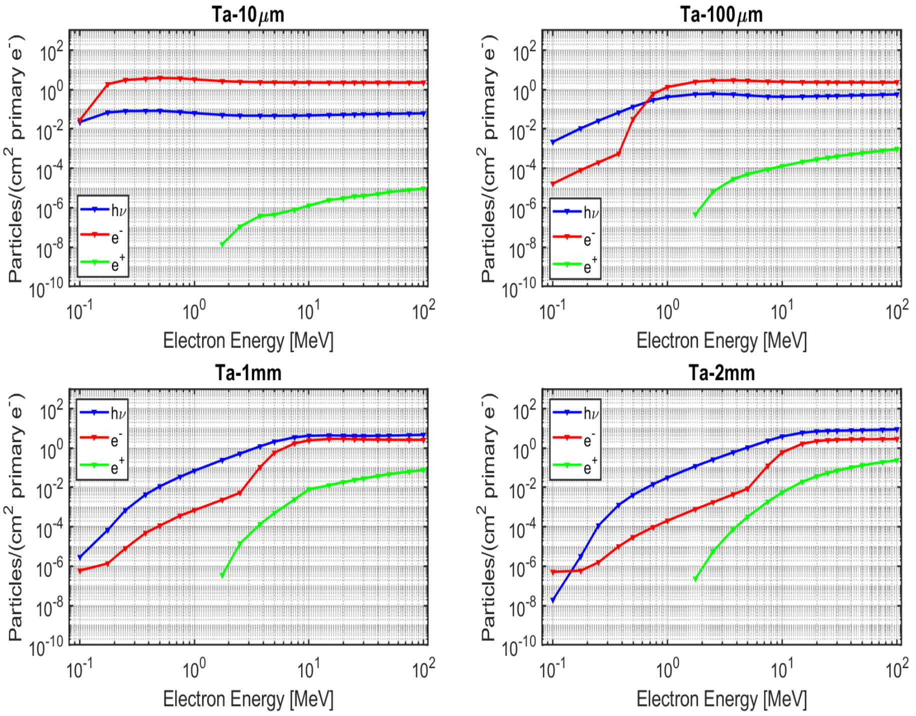

FIGURE B.3: Integrated fluences of electrons, positrons, and bremsstrahlung photons versus energy of incident electrons on Ta targets of 10μm, 100μm, 1 mm, 2 mm thickness.

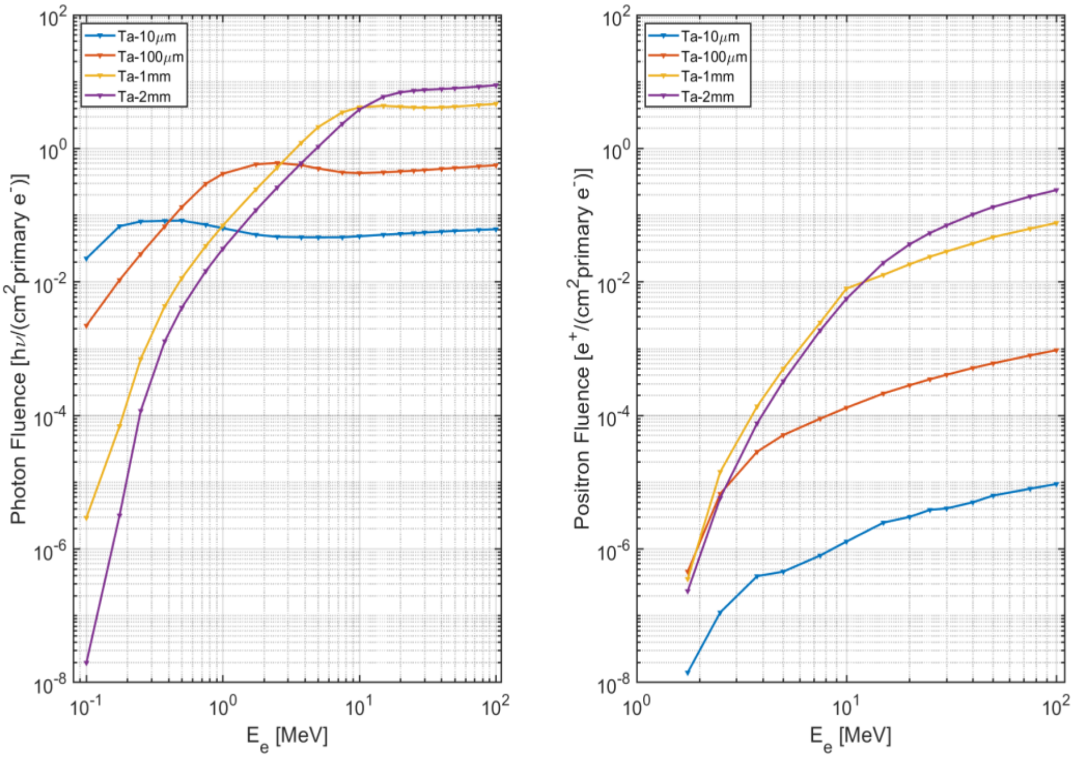

FIGURE B.4: Integrated fluences of positrons and bremsstrahlung photons versus energy of incident electrons on Ta targets of 10μm, 100μm, 1 mm, 2 mm thickness.

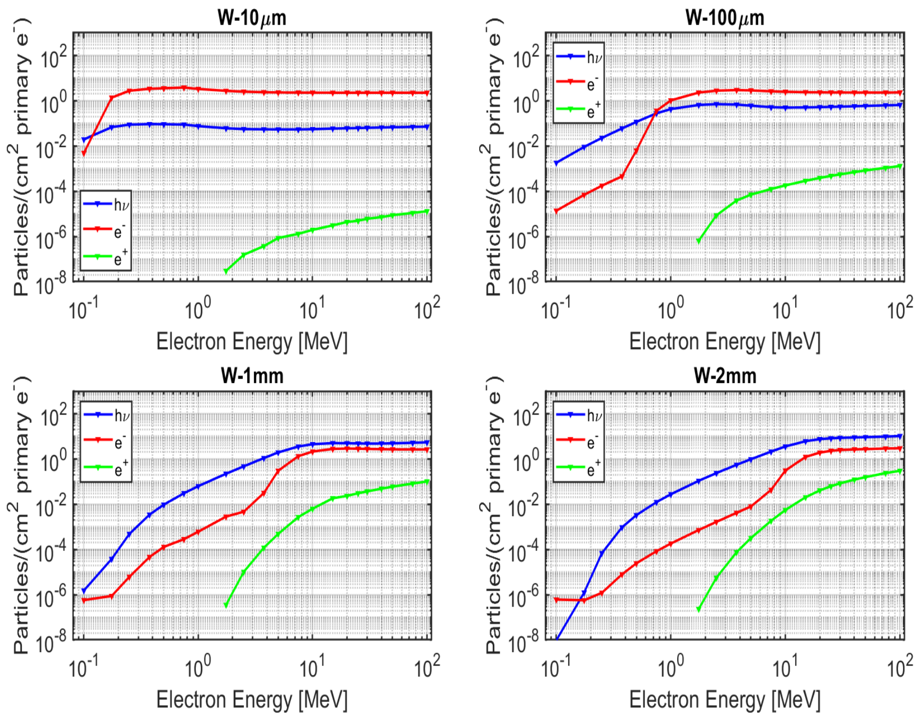

FIGURE B.5: Integrated fluences of electrons, positrons, and bremsstrahlung photons versus energy of incident electrons on W targets of 10μm, 100μm, 1 mm, 2 mm thickness.

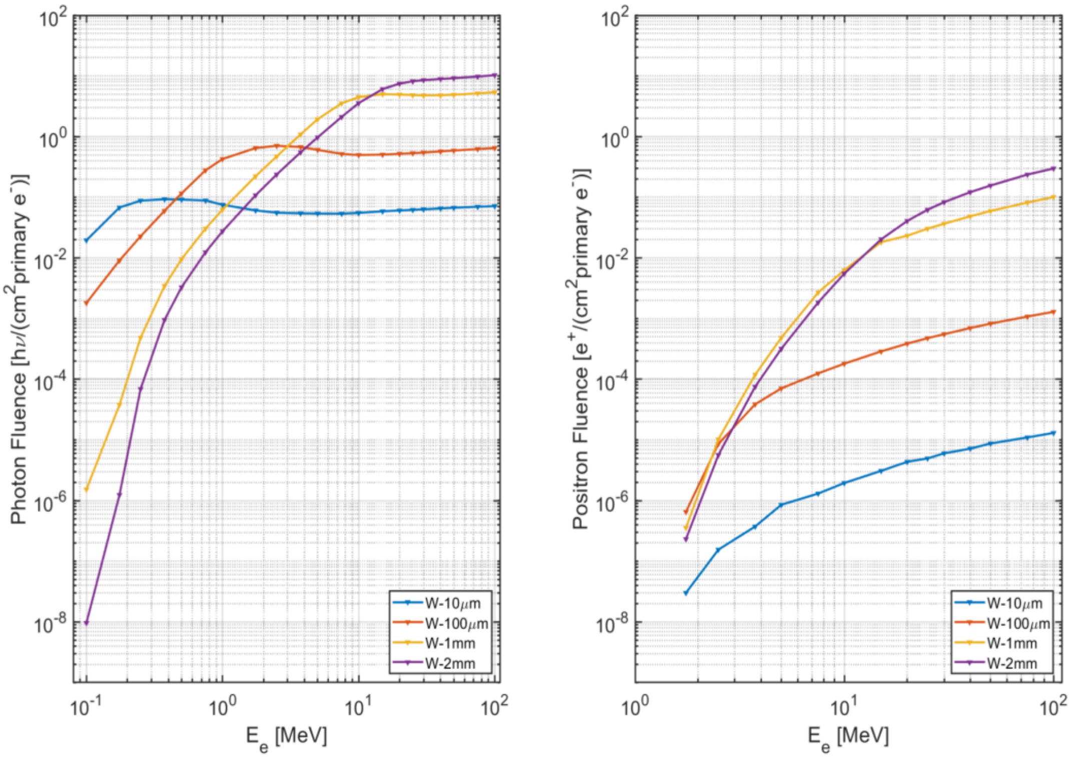

FIGURE B.6: Integrated fluences of positrons and bremsstrahlung photons versus energy of incident electrons on W targets of $10\mu m$, $100\mu m$, 1 mm, 2 mm thickness.

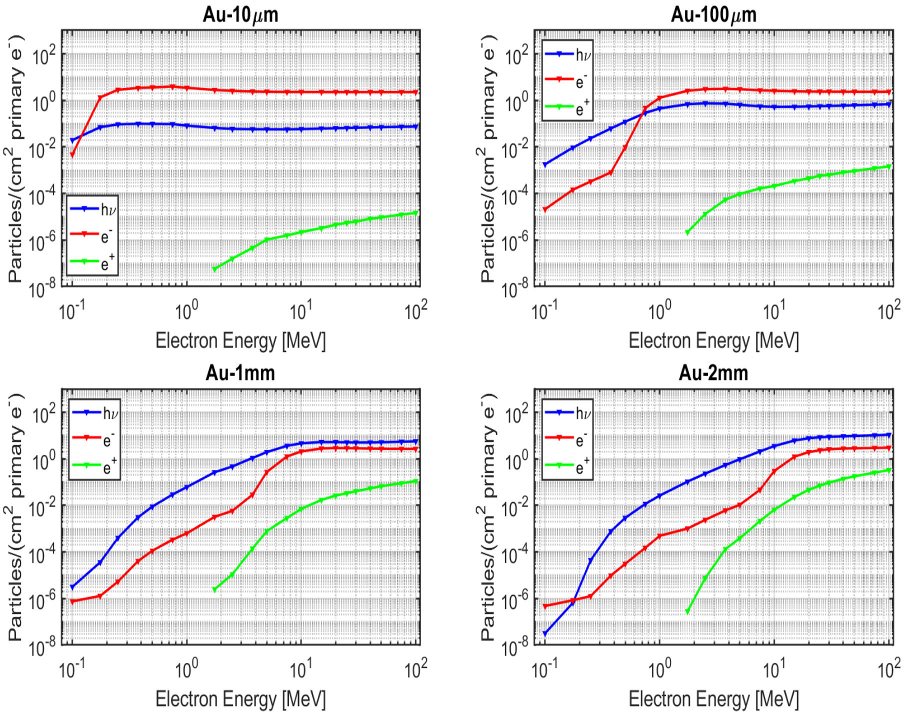

FIGURE B.7: Integrated fluences of electrons, positrons, and bremsstrahlung photons versus energy of incident electrons on Au targets of $10\mu m$, $100\mu m$, 1 mm, 2 mm thickness.

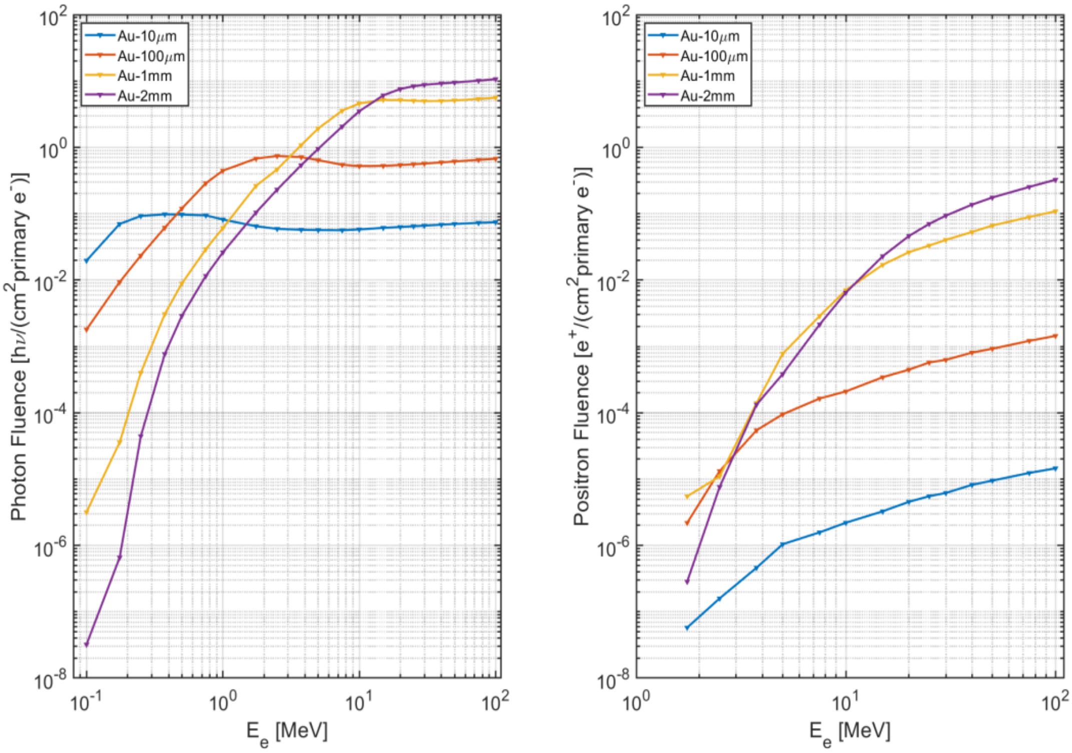

FIGURE B.8: Integrated fluences of electrons, positrons, and bremsstrahlung photons versus energy of incident electrons on Au targets of 10μm, 100μm, 1 mm, 2 mm thickness.

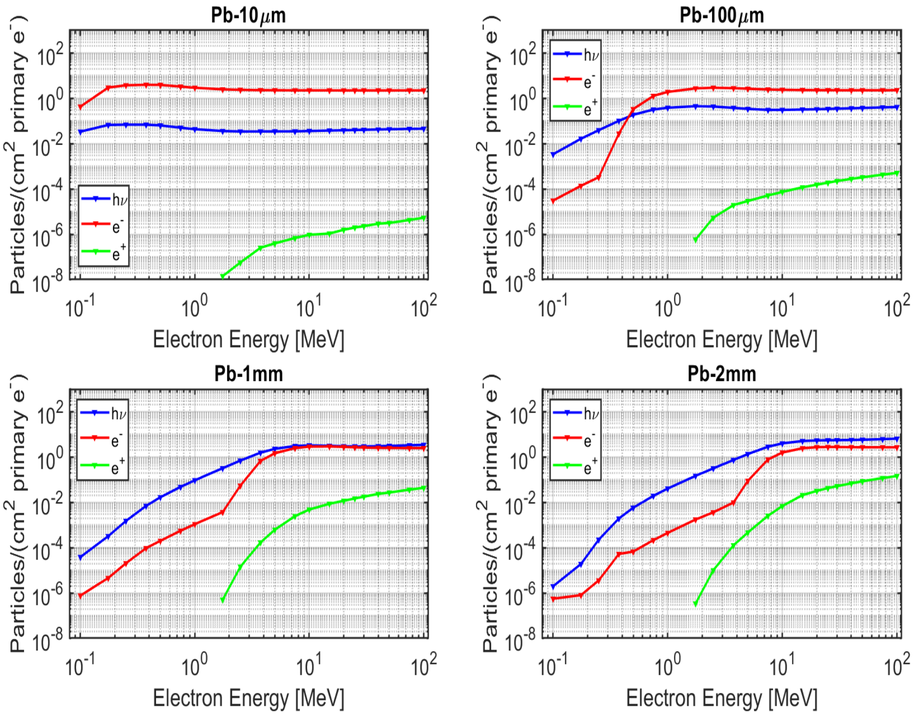

FIGURE B.9: Integrated fluences of positrons and bremsstrahlung photons versus energy of incident electrons on Pb targets of 10μm, 100μm, 1 mm, 2 mm thickness.

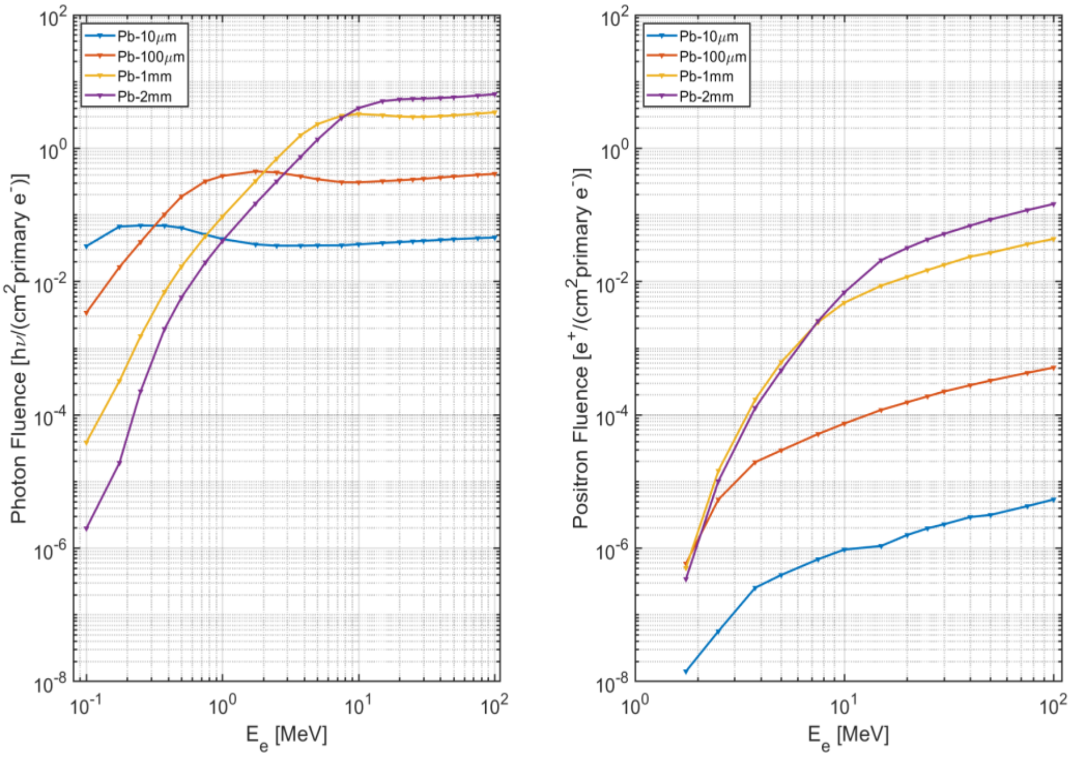

FIGURE B.10: Integrated fluences of electrons, positrons, and bremsstrahlung photons versus energy of incident electrons on Pb targets of $10\mu m$, $100\mu m$, 1 mm, 2 mm thickness.

Bibliography

Alfven, H. (1939). “On the motion of cosmic rays in interstellar space”. In: *Physical Review* 55, p. 429.

Archer, B.R., P.R. Almond, and L.K. Wagner (1985). “Application of a Laplace transform pair model for high x-ray spectral reconstruction.” In: *Med. Phys.* 12, p. 63034.

Arefiev A V Khudik V N, Robinson A P L Shvets G Willingale L and Schollmeier M (2016). “Beyond the ponderomotive limit: direct laser acceleration of relativistic electrons in sub-critical plasmas”. In: *Phys. Plasmas* 23, p. 056704.

Attix, F. H. (1986). *Introduction to radiological physics and radiation dosimetry.* WILEY-VCH Verlag. ISBN: ISBN 9780471011460. URL: `https://onlinelibrary.wiley.com/doi/book/10.1002/9783527617135`.

Atzeni, S. and J. Meyer ter vehn (2004). *The Physics of Inertial Fusion.* Clarendon, Oxford.

Bagnoud, V. (2010). “Commissioning and early experiments of the PHELIX facility”. In: *Appl. Phys. B* 100.4, p. 137.

Battistoni, G. et al. (2015). “Overview of the FLUKA code.” In: *Annuals of Nuclear Energy* 82.3, pp. 10–18.

Behrens, R. et al. (Feb. 2003). “A thermoluminescence detector-based few-channel spectrometer for simultaneous detection of electrons and photons from relativistic laser-produced plasmas”. In: *Review of Scientific Instruments* 74 (2), pp. 961–968. ISSN: 00346748. DOI: `10.1063/1.1532831`.

Ben-Ismail, A. et al. (2011). In: *Appl. Phys. Lett.* 98, p. 264101.

Berger, M. J. and S. M. Selzer (1968). “Etran Monte Carlo code system for electron and photon transport through extended media.” In: *Technical Report CCC-107, Radiation Schielding Information Center, Computer Code Collection, Oak Ridge National Laboratory.*

Berger, M.J. (1993). “National Institute of Standards and Technology, Gaithersburg, MD”. In: *NISTIR 4999.*

Bethe, H. A. (1930). “Theory of passage of swift corpuscular rays through matter.” In: *Ann. Physik* 5, p. 325.

— (1932). “Scattering of electrons.” In: *Z. fur Physik* 76, p. 293.

Bethe, H. A. and J. Ashkin (1953). “Passage of radiations through matter”. In: *Wiley, New York* 1.

Bethe, H. A. and W. Heitler (1934). “On the stopping of fast particles and on the creation of positive electrons.” In: *Proc. Roy. Soc.* A.11, p. 83.

Bethe, H. A. and Roman W. Jackiw (1973). “Intermediate Quantum Mechanics.” In: *W.A. Benjamin, Inc.* 93(1), 38–44.

Bhabha, H. J. (1935). In: *Proc. R. Soc. London* A 152, p. 559.

Biggs, F., L.B. Mendelsohn, and J.B. Mann (1975). “Hartree-Fock Compton profiles for the elements”. In: *At. Data Nucl. Data Tables* 16, pp. 201–309.

Bloch, P. (2000). “Determining clinical photon beam spectra from measured depth-dose curve with the Cimmino algorithm.” In: *Phys. Med. Biol.* 45, p. 17183.

Bohlen, T. et al. (2014). “The FLUKA Code: Developments and Challenges for High Energy and Medical Applications.” In: *Nuclear Data Sheets* 120, pp. 211–214.

Borisenko, N. G. (2006). In: *Fusion Sci. Technol.* 49, p. 676.

— (2007). In: *Fusion Sci. Technol.* 51, p. 655.

Bos, Adrie J.J. (Dec. 2006). “Theory of thermoluminescence”. In: *RADIATION MEASUREMENTS* 41, S45–S56.

Bote, D. and F. Salvat (2008). “Calculations of inner-shell ionization by electron impact with the distorted-wave and plane-wave Born approximations.” In: *Phys. Rev.* A.77, p. 042701.

Brambrink, E. et al. (2016). In: *High Power Laser Sci. Eng.* 4, p. 30.

Brunel, F. (1987). “Not-so-Resonant, Resonant Absorption”. In: *Physical Review Letters* 59, p. 52.

Buffon, G. L. (1749–1803). “Histoire Naturelle”. In: *Generali et Particular avec le Description du Cabinet du Roy, Paris* 44.

Burton, D. A. et al. (2017). “Observations on the ponderomotive force.” In: *Proc. SPIE* 10234, p. 1461. URL: `https://doi.org/10.1117/12.2270542`.

Cameron, J. R., N. K. Suntharalinharn, and G. N. Kenny (1968). *Thermoluminescence Dosimetry.* University of Wisconsin Press, Madison.

Catala, A. et al. (1995). “Reconstruction of 12 MeV bremsstrahlung spectra from measured transmission data by direct resolution of the numeric system”. In: *Med. Phys.* 22, p. 310.

Chen, F. F. (1974). *Introduction to Plasma Physics.* Plenum Press, New York.

Chen, R. (1969). “Glow Curves with General Order Kinetics”. In: *J. Electrochem. Soc.* 116, p. 1254.

Creagh, D. C. and J. H. Hubbell (1987). “Problems associated with the measurement of X-ray attenuation coefficients. I. Silicon. Report of the International Union of Crystallography X-ray Attenuation Project”. In: *Acta Crystallographica Section A: Foundations of Crystallography* 43.1, 102–112.

Cros, B. (2016). “Laser-driven Plasma Wakefield: Propagation Effects.” In: *Proceedings of the CAS-CERN Accelerator School: Plasma Wake Acceleration, Geneva.*

Daido, H., M. Nishiuchi, and A. S. Pirozhkov (2012). “Review of Laser-Driven Ion Sources and Their Applications”. In: *Rep. Prog. Phys.* 75, p. 056401.

Dam, J. V. and G. Morenello (2006). *Thermoluminescence Dosimetry.* ESTRO, Mounierlaan 83-12–1200 Brussels (Belgium).

Daniels, F., C. Boyd, and T. Saunders (1953). “Thermoluminescence as a research tool”. In: *Science* 117, 343–349.

Denham, D. H., R. L. Kathren, and J. P. Corley (1972). “A CaF2:Dy Thermoluminescent Dosimeter for Environmental Monitoring”. In: *Pacific Northwest Laboratory, Richland, Washington*, BNWL–SA–4191.

Edwards, C. et al. (Dec. 2005). “The low energy x-ray response of the LiF: Mg: Cu: P thermoluminescent dosemeter: a comparison with LiF: Mg: Ti”. In: *British journal of radiology* 78, 543–547.

Emmett, M. B. (1984). “The MORSE Monte Carlo radiation transport system”. In: *Oak Ridge National Laboratory report* R2, p. 4972.

Esarey, E., C. B. Schroeder, and W. P. Leemans (2009). “Physics of laser-driven plasma-based electron accelerators”. In: *Rev. Mod. Phys.* 81, p. 1229.

Evans, R. D. (1955). *The Atomic Nucleus*. McGraw-Hill, NewYork. ISBN: 9780070992993.

Faddegon, B. A., C.K. Ross, and D.W.O. Rogers (1990). “Forward-directed bremsstrahlung of 10- to 30-MeV electrons incident on thick targets of Al and Pb.” In: *Med. Phys.* 17, p. 77385.

— (1991). In: *Med. Phys.* 18, p. 727.

Fano, U. (1963). “Penetration of protons, alpha particles and mesons”. In: *Ann. Rev. Nucl. Sci.* 13, p. 1.

Fasso, A. (2005). “Photonuclear reactions in FLUKA: cross sectionsand interaction models.” In: *AIP conf. Proc.* 769, pp. 1303–1306.

Fasso, A. et al. (1994). “FLUKA: performances and applications in the intermediate energy range”. In: *Proc. of an AEN/NEA Specialists’ Meeting on Shielding Aspects of Accelerators, Targets and Irradiation Facilities, Arlington (Texas)* A257, pp. 28–29.

Ferrari, A. et al. (1992). “An improved multiple scattering model for charged particle transport”. In: *Nucl. Instr. Meth.* B71, pp. 412–426.

Ferrari, A. et al. (2005b). *FLUKA: a multi-particle transport code*. CERN-2005-10 (2005). ISBN: INFN-TC 05.11, SLAC-R-773. URL: `http://www.fluka.org/fluka.php?id=man_onl`.

Ferrari, A. et al. (2005a). “FLUKA: a multi-particle transport code.” In: *CERN-2005-10, INFN TC 05 11, SLAC-R-773* 10.

Fiorini, F. (2012). “Experimental and computational dosimetry of laser-driven radiation beams”. PhD Thesis. University of Birmingham.

Fippel, M. (2003). “A virtual photon energy fluence model for Monte Carlo dose calculation”. In: *Med. Phys.* 30, p. 30111.

FLUKA, Course (2019a). “Fundamentals of Monte Carlo simulations of radiation transport with FLUKA”. In: *21st Official FLUKA Course, ALBA Synchrotron (Spain)*.

— (2019b). “Statistics and Sampling”. In: *21st Official FLUKA Course, ALBA Synchrotron (Spain)*.

Francois, P. (1997). “Validation of reconstructed bremsstrahlung spectra between 6 MeV and 25 MeV from measured transmission data.” In: *Med. Phys.* 24, p. 76973.

Freeman, R. R., P. H. Bucksbaum, and T. J. McIlrath (1988). “The ponderomotive potential of high intensity light and its role in the multiphoton ionization of atoms.” In: *IEEE journal of quantum electronics* 24.7, p. 1461.

Geiß, O., M. Krämer, and G. Kraft (1998). “Efficiency of thermoluminescent detectors to heavy charged particles”. In: *Nuclear Instruments and Methods in Physics Research Section B: Beam Interactions with Materials and Atoms* 142.4, 592–598.

Gibbon, P. (2005). *Short Pulse Laser Interactions with Matter.* IMPERIAL COLLEGE PRESS. ISBN: ISBN 9781860941351.

Glenn, R. D. and P. E. Bramson (1977). “The Hanford Critical Radiation Dosimeter.” In: *Pacific Northwest Laboratory, Richland, Washington*, PNL–2276.

Gryaznykh, D., Y. Kandiev, and V. Lykov (1998). In: *JETP Lett.* 67, p. 257.

Gu, Y. et al. (2019). “Gamma photons and electron-positron pairs from ultra-intense laser-matter interaction: A comparative study of proposed configurations”. In: *Matter Radiat. Extremes* 4, p. 064403.

Guber, W. et al. (1967). “A geometric description technique suitable for computer analysis of both the nuclear and conventional vulnerability of armored military vehicles Mathematical Applications Group”. In: *Inc. Report MAGI*, p. 6701.

Günther, M. M. et al. (2011). “A novel nuclear pyrometry for the characterization of the high-energy bremsstrahlung and electrons produced in relativistic laser-plasma interactions.” In: *Physics of Plasmas* 18, p. 083102.

Gus’kov, S. Y. et al. (2011). “Laser-supported ionization wave in under-dense gases and foams”. In: *Phys. Plasmas* 18, p. 103114.

Gyrdymov, M. (2020). “Charakterisierung der Energie- und Winkelverteilung der laserbeschleunigten ultrarelativistischen Elektronen”. Master Thesis. Johann Wolfgang Goethe-Universität Frankfurt am Main.

Habs, D. and U. Köster (2011). “Production of medical radioisotopes with high specific activity in photonuclear reactions with gamma-beams of high intensity and large brilliance”. In: *Appl. Phys. B* 103, 501–19.

Hartemann, F. V. et al. (1995). “Nonlinear ponderomotive scattering of relativistic electrons by an intense laser field at focus.” In: *Physical Review* E.51, p. 4833.

Hartemann, F. V. et al. (1998). “Three-dimensional relativistic electron scattering in an ultra-high intensity laser focus.” In: *Physical Review* E.58, p. 5001.

Hatchet, S. P. (2000). “Electron, photon, and ion beams from the relativistic interaction of Petawatt laser pulses with solid targets”. In: *Phys. Plasmas* 7, p. 2076.

Heavy-Ion Research GmbH, GSI Helmholtz Centre for (2018). In: *PHELIX Lasersystem*. URL: https://www.gsi.de/work/forschung/appamml/plasmaphysikphelix/phelix.htm.

Hinson, W. H. and J. D. Bourland (2002). “Spectral reconstruction of high energy photon beams for kernel based dose calculations.” In: *Med. Phys.* 29, p. 178996.

Horowitz, Y. (1981). “The theoretical and microdosimetric basis of thermoluminescence and applications to dosimetry”. In: *Phys. Med. Biol.* 26, p. 765.

Horst, F. et al. (2015). “A TLD-based ten channel system for the spectrometry of bremsstrahlung generated by laser-matter interaction”. In: *Nuclear Instruments and Methods in Physics Research A* 782, 69–76.

Huang, P. H., K. R. Kase, and B. E. Bjarngard (1983). “Reconstruction of 4 MeV bremsstrahlung spectra from measured transmission data.” In: *Med. Phys.* 10, p. 77885.

ICRU (1984). “Stopping powers for electrons and positrons.” In: *Technical Report, International Commission on Radiation Units and Measurements, Bethesda* 37.

— (1992). *International Commission on Radiation Units and Measurements. Measurement of Dose Equivalents from External Photon and Electron Radiations.* ICRU Report 47. Bethesda, Maryland.

James, F. (1980). “Monte Carlo theory and practice”. In: *Rep. Prog. Phys.* 43, 1145–1189.

— (1990). “A review of pseudorandom number generators”. In: *Comput. Phys. Commun.* 60, 329–344.

Kalos, M. H. and P. A. Whitlock (2008). “Monte Carlo Methods”. In: *Wiley-VCH, Weinheim.*

Kaluza, Malte Christoph (2004). “Characterisation of Laser-Accelerated Proton Beams”. PhD Thesis. Technical University Munich.

Keldysh, L. V. (1965). “Ionization in the field of a strong electromagnetic wave.” In: *Sov. Phys. JETP* 20.5, 1307–1314.

Key, M. H. (1998). “Hot electron production and heating by hot electrons in fast igniter research”. In: *Physics of Plasmas* 5.5, 1966–1972.

Khalenkov, A. M. (2006). In: *Laser Part. Beams* 24, p. 283.

Kim, L. et al. (1986). “Ratio of positron to electron bremsstrahlung energy loss: an approximate scaling law”. In: *Phys. Rev.* A33, pp. 3002–3009.

Klein, O. and T. Nishina (1929). “Über die Streuung von Strahlung durch freie Electronen nach der neuen relativistischen Quantendynamik von Dirac.” In: *Zeitschrift für Physik* 52.11, pp. 853–868.

Kneubühl, Fritz Kurt and Markus Werner Sigrist (2005). *Laser.* B. G. Teubner Verlag.

Knoll, G. F. (2000). *Radiation Detection and Measurement.* 3rd ed, United States of America: John Wiley and Sons.

Koch, H. W. and J. W. Motz (1959). “Bremsstrahlung Cross-Section Formulas and Related Data”. In: *Rev. Mod. Phys.* 31.6, p. 920.

Königstein, T. (2013). “Optimierung und Anwendung der Beschleunigung von Elektronen in relativistischen Laser-Plasma.” PhD Thesis. Heinrich-Heine-Universität Düsseldorf.

Kron, T. (1994). “Thermoluminescence dosimetry and its applications in medicine. Part 1: Physics, Materials and Equipment”. In: *Austral. physical and Engineering Science in Medicine* 17.4, p. 175.

Kruer, W. L. (2003). *The physics of laser plasma interactions.* Westview Press. ISBN: DOI 10.2991 978-94-6239-097-3 2.

Lakshmanan, A., C. Raffnsre, and J. Tuyn (Dec. 1984). "Photon energy dependence of sensitized LiF (TLD-700) phosphor". In: *The International journal of applied radiation and isotopes* 35, 418–420.

Landau, L.D. and I.Ya. Pomeranchuk (1953a). "Electron-cascade processes at ultra-high energies (In Russian)". In: *Dokl. Akad. Nauk SSSR* 92, pp. 735–738.

— (1953b). "The limits of applicability of the theory of bremsstrahlung by electrons and of creation of pairs at large energies (In Russian)". In: *Dokl. Akad. Nauk SSSR* 92, p. 535.

Landry, D.J. and D.W. Anderson (1991). "Measurement of accelerator bremsstrahlung spectra with a high-efficiency Ge detector." In: *Med. Phys.* 18, p. 52732.

Laplace, P. S. (1812). "Analytical theory of probability". In: *Paris: Veuve Courcier* 44.

Lefebvre, E. and G. Bonnaud (2002). "Transparency Opacity of a Solid Target Illuminated by an Ultrahigh-Intensity Laser Pulse". In: *Physical Review Letters* 74, p. 1254.

Li, K. et al. (2014). "Developments toward hard X-ray radiography on heavy-ion heated dense plasmas". In: *Laser Part. Beams* 32, p. 631.

Li, Shun et al. (2017). "Ultrafast multi-MeV gamma-ray beam produced by laser-accelerated electrons". In: *Physics of Plasmas* 24, p. 093104.

Lichtenstein, H. et al. (1979). "The SAM-CE Monte Carlo system for radiation transport and criticality calculations in complex configurations (Revision 7.0)". In: *RSIC Computer Code Collection*, p. 187.

Llovet, Xavier et al. (2014). "Cross Sections for Inner-Shell Ionization by Electron Impact." In: *Journal of Physical and Chemical Reference Data* 43.1, p. 013102. URL: `https://doi.org/10.1063/1.4832851`.

Ma, Z. et al. (2019). "Photonuclear production of medical isotopes 62, 64 Cu using intense laser-plasma electron source". In: *Matter Radiat. Extremes* 4, p. 064401.

Macchi, A., M. Borghesi, and M. Passoni (2013). "Ion Acceleration by Superintense Laser-Plasma Interaction". In: *Rev. Mod. Phys.* 85, p. 751.

Malka, G. (1997). "Suprathermal electron generation and channel formation by an ultrarelativistic laser pulse in an underdense preformed plasma". In: *Physical Review Letters* 79.11, p. 2053.

Malka, G. and J. L. Miquel (1996). "Experimental Confirmation of Ponderomotive-Force Electrons Produced by an Ultrarelativistic Laser Pulse on a Solid Target". In: *Physical Review Letters* 77.4, p. 75.

Marino, A. (2015). *Analysis and Enumeration, Atlantis Studies in Computing 6.* Atlantis Press and the authors. ISBN: DOI 10.2991 978-94-6239-097-3 2.

McKinlay, A. F. (1981). *Thermoluminescence dosimetry-Medical Physics Handbooks.* Bristol: Adam Hilger Ltd.

Metropolis, N. (1987). “The beginning of the Monte Carlo method”. In: *Los Alamos Science Special Issue*, pp. 125–130.

Migdal, A.B. (1956). “Bremsstrahlung and pair production in condensed media at high energies”. In: *Phys. Rev.* 103, pp. 1811–1820.

— (1957). “Bremsstrahlung and pair production at high energies in condensed media”. In: *Zh. Exp. Teor. Fiz. SSSR* 32, pp. 633–646.

Miljanic, S., M. Ranogajec-Komor, and B. Vekic (Dec. 2002). “Main dosimetric characteristics of some tissue-equivalent TL detectors”. In: *Radiation protection dosimetry* 100, p. 437.

Mobley, R. C. and R. A. Laubenstein (1950). “Photoneutron thresholds of beryllium and deuterium.” In: *Phys. Rev.* 80.3, p. 309.

Moehring, H.J. (1989). “On the contribution of electroproduction off nuclei to the generation of energetic hadrons in electromagnetic showers”. In: *DESY*, pp. 89–150.

Moliere, Gert (1948). “Theorie der Streuung schneller geladener Teilchen II - Mehrfach- und Vielfachstreuung.” In: *Zeitschrift fuer Naturforschung* a.3, 78–97.

Moller., C. (1932). “Passage of hard beta rays through matter.” In: *Ann. Physik (Leipzig)* 14, p. 531.

Moore, C. I., J. P. Knauer, and D. D. Meyerhofer (1995). “Observation of the Transition from Thomson to Compton Scattering in Multiphoton Interactions with Low-Energy Electrons.” In: *Physical Review Letters* 74, p. 2439.

Motz, W., H. A. Olsen, and H. W. Koch (1969). “Bremsstrahlung Cross-Section Formulas and Related Data”. In: *Rev. Mod. Phys.* 41, p. 581.

Mulser, P. and D. Bauer (2010). *High Power Laser-Matter Interaction.* Springer Tracts in Modern Physics.

Myatt, J. et al. (2009). In: *Phys. Rev.* E 79, p. 066409.

Nakashima, K. and H. Takabe (2002). In: *Phys. Plasmas* 9, p. 1505.

Negoita, F. (2016). “Laser driven nuclear physics at ELI-NP”. In: *Rom. Rep. Phys.* 68.37, p. 144.

Nicolai, P. (2012). “Experimental evidence of foam homogenization”. In: *Phys. Plasmas* 19, p. 113105.

Nilgün Demir Zehra Nur Kuluöztürk, Iskender Akkurt (2013). “Monte Carlo simulations of bremsstrahlung photon yields from thin targets with electron beams between 10 and 40 MeV”. In: *Radiation Effects and Defects in Solids* 168.5, pp. 372–377.

— (2019). “FLUKA Monte Carlo calculations for angular distribution of bremsstrahlung photons from thin targets”. In: *Nuclear Instruments and Methods in Physics Research Section* 443.B, pp. 19–24.

Nisbet, A. (1998). “Spectral reconstruction of clinical megavoltage photon beams and implications of spectral determination on dosimetry of such beams.” In: *Phys. Med. Biol.* 43, p. 150721.

NIST (2017). “NIST: Appendix for ESTAR, PSTAR and ASTAR”. In: . URL: `https://physics.nist.gov/PhysRefData/Star/Text/appendix.html`.

Nordell, B. and A. Brahme (1984). “Angular distribution and yield from bremsstrahlung targets”. In: *Phys. Med. Biol.* 29.7, pp. 797–810.

Norreys, P. A. (1999). “Observation of a highly directional g-ray beam from ultrashort, ultraintense laser pulse interactions with solid”. In: *Phys. Plasmas* 6, p. 2150.

Paliwal, B. and P. Almond (1975). “Applications of cavity theories for electrons to LiF dosimeters”. In: *Phys. Med. Biol.* 20, pp. 547–558.

Podgorsak, E. B. (2005). *Radiation oncology physics: a handbook for teachers and students.* Vienna: International Atomic Energy Agency. ISBN: ISBN 92–0–107304–6.

Pomerantz, I. (2014). “Ultrashort pulsed neutron source”. In: *Phys. Rev. Lett.* 113, p. 184801.

Protopapas, M. Christoph, H. Keitel, and Peter L. Knight (1997). “Atomic physics with super-high intensity lasers”. In: *Reports on Progress in Physics* 4.60, p. 389.

Pugachev, L. P. et al. (2016). “Acceleration of electrons under the action of petawatt-class laser pulses onto foam targets”. In: *Nucl. Instrum. Methods Phys. Res. A* 829, pp. 88–93.

— (2019). “Characterization of accelerated electrons generated in foams under the action of petawatt lasers”. In: *Journal of Physics: Conference Series, IOP Publishing* 1147.1, p. 012080.

Pukhov, A. (1999). “Tree-dimensional electromagnetic relativistic particle-in-cell code VLPL (virtual laser plasma lab)”. In: *J. Plasma Phys.* 61, 425–433.

— (2003). “Strong field interaction of laser radiation”. In: *Reports on progress in Physics* 66, p. 47.

Pukhov, A., Z.M. Sheng, and J. Meyer ter Vehn (1999). “Particle acceleration in relativistic laser channels”. In: *Physics of Plasmas* 6.7, 2847–2854.

Pukhov, A. and J. Meyer ter Vehn (1996). “Relativistic magnetic self-channeling of light in near-critical plasma: three-dimensional particle-in-cell simulation”. In: *Physical Review Letters* 76, p. 3975.

— (1997). “Laser Hole Boring into Overdense Plasma and Relativistic Electron Currents for Fast Ignition of ICF Targets”. In: *Physical Review Letters* 79, p. 2686.

— (1998). “Relativistic laser-plasma interaction by multi-dimensional Particle-In-Cell simulations”. In: *Physics of Plasmas* 5, 1880–1886.

Randall, J. and M. Wilkins (1945). “Phosphorescence and electron traps. The interpretation of long period phosphorescence”. In: *Proc. R. Soc. London Ser. A* 184, pp. 390–407.

Ranft, J. and W.R. Nelson (1987). “Hadron cascades induced by electron and photon beams in the GeV energy range”. In: *Nucl. Instr. Meth.* A257, pp. 177–184.

Ravasio, A. (2008). “Hard x-ray radiography for density measurement in shock compressed matter”. In: *Phys. Plasmas* 15, p. 060701.

Remington, B. A. et al. (2000). “A Review of Astrophysics Experiments on Intense Lasers”. In: *Phys. Plasmas* 7, p. 1641.

Ribberfors, R. (1975). “Relationship of the relativistic Compton cross section to the momentum distribution of bound electron states”. In: *Phys. Rev.* B12, pp. 2067–2074.

Ridgers, C. P. (2012). “Dense electron-positron plasma and ultraintense g-rays from laser –irradiated solids”. In: *Phys. Rev. Lett.* 108, p. 165006.

Rogers, D.W.O., B. A. Faddegon, and C.K. Ross (1995). “BEAM: a Monte Carlo code to simulate radiotherapy treatment units”. In: *Med. Phys.* 22, p. 50324.

Rohrlich, F. and B. C. Carlson (1954). “Positron-electron differences in energy loss and multiple scattering.” In: *Phys. Rev.* 93(1), 38–44.

Rosmej, O. N. et al. (2019). “Interaction of relativistically intense laser pulses with long-scale near critical plasmas for optimization of laser based sources of MeV electrons and gamma-rays”. In: *New J. Phys.* 21, p. 043044.

Rosmej, O. N. et al. (2020). “High-current laser-driven beams of relativistic electrons for high energy density research”. In: *Plasma Phys. Control. Fusion* 62, p. 115024.

Rubinstein, R. Y. (1981). “Simulation and the Monte Carlo Method”. In: *Wiley, New York* 60.

Ruhl, H. et al. (1999). “Collimated Electron Jets by Intense Laser-Beam-Plasma Surface Interaction under Oblique Incidence”. In: *Physical Review Letters* 82, p. 743.

Saleh, B. E. and M.C. Teich (2007). *Fundamentals of Photonics.* John Wiley and Sons, Hoboken, NJ.

Salvat, Francesc (2015). “PENELOPE-2014. A Code System for Monte Carlo Simulation of Electron and Photon Transport”. In: *Workshop, NUCLEAR ENERGY AGENCY.*

Salvata, F. et al. (2006). In: *Radiation Physics and Chemistry* 75.120, p. 11219.

Sarri, G. et al. (2013). In: *Phys. Rev. Lett.* 110, p. 255002.

Sauter, F. (1931a). “Über den atomaren Photoeffect in der K-Schale nach der relativistischen Wellenmechanik Diracs.” In: *Ann. Physik* 11, pp. 454–488.

— (1931b). “Über den atomaren Photoeffekt bei grosser Härte der anregenden Strahlung.” In: *Ann. Physik* 9, pp. 217–247.

— (1931c). “Über den atomaren Photoeffekt in der K-Schale nach der relativistischen Wellenmechanik Diracs.” In: *Ann. Physik* 11, pp. 454–488.

Schlenvoigt, H. P. et al. (2008). In: *Nat. Phys.* 4, p. 130.

Schönlein, Andreas (2015). “Erzeugung von intensiver Röntgenstrahlung und Materie hoher Energiedichte durch laserbeschleunigte Elektronen”. PhD Thesis. Johann Wolfgang Goethe-Universität in Frankfurt am Main.

Scientific, Thermo Fisher (2010). *Harshaw Model 6600 PLUS TLD Reader Operator’s Manual.* Thermo Fisher Scientific. ISBN: 6600PC-W-O-1110-007. URL: `www.thermofisher.com/dosimetry`.

— (2016). *Thermo Scientific Harshaw TLD Materials and Dosimeters.* Dosimetry-Materials. URL: `www.thermofisher.com/dosimetry`.

Seltzer, S.M. and M.J. Berger (1982). “Stopping Powers and Ranges of Electrons and Positrons”. In: *NBSIR 82-2550.*

Seltzer, S.M. and M.J. Berger (1985). “Bremsstrahlung spectra from electron interactions with screened nuclei and orbital electrons”. In: *Nucl. Instr. Meth.* B12, pp. 95–134.

— (1986). “Bremsstrahlung spectra from electrons with kinetic energy 1 keV-10 GeV incident on screened nuclei and orbital electrons of neutral atoms with Z = 1-100”. In: *At. Data Nucl. Data Tables.* 35, pp. 345–418.

Selzer, S. M. (1991). “Electron-photon monte carlo calculations: The etran code.” In: *International Journal of Radiation Applications and Instrumentation. Part A. Applied Radiation and Isotops* 42.10, pp. 917–941.

Shiff, L.I. (1946). In: *Phys. Rev.* 70, p. 87.

Sun, G.Z. et al. (1987). “Self-focusing of short intense pulses in plasmas”. In: *Physics of Fluids* 30, p. 526.

Swinehart, D. F. (1962). “The Beer Lambert law.” In: *Journal of chemical education* 39.7, p. 333.

Tajima, T. and J. M. Dawson (1979). “Laser Electron Accelerator”. In: *Physical Review Letters* 69.43, p. 267.

Ter-Mikaelyan, M.L. (1954). “Bremsstrahlung radiation spectrum in a medium”. In: *Dokl. Akad. Nauk SSSR* 94, p. 1033.

Wagner, F. (2014). “Kontrolle des zeitlichen Kontrastes am Lasersystem PHELIX”. PhD Thesis. Technische Darmstadt.

Wang, T. et al. (2020). “Power scaling for collimated g-ray beams generated by structured laser-irradiated targets and its application to two-photon pair production”. In: *Phys. Rev. Appl.* 13, p. 054024.

Wharton, K. B. (1998). “Experimental measurements of hot electrons generated by ultraintense $(> 10^{1}9W/cm2)$ laser-plasma interactions on solid-density targets”. In: *Physical Review Letters* 81.4, p. 822.

Wilks, S. C. et al. (1992). “Absorption of ultra-intense laser pulses”. In: *Physical Review Letters* 69, pp. 1383–1386.

Williams, G. J. et al. (2016). “Target material dependence of positron generation from high intensity laser-matter interactions”. In: *Physics of Plasmas* 23.12, p. 123109. URL: `https://doi.org/10.1063/1.4971235`.

Willingale, L. (2018). “The unexpected role of evolving longitudinal electric fields in generating energetic electrons in relativistically transparent plasmas”. In: *New J. Phys.* 20, p. 093024.

Wilson, R. H. (1987). “Historical Review of Personnel Dosimetry Development and its Use in Radiation Protection Programs at Hanford”. In: *Pacific Northwest Laboratory, Richland, Washington*, PNL–6125.

Xiang, Roger Soh Cai (2013). “A TLD study of ACUROS XB for lung SBRT using a lung substitute material”. Bachelor Thesis. Nanyang Technological University.

Xu, T. J. et al. (2016). In: *Phys. Plasmas* 23, p. 033109.

Zaehter, Sero (2020). “Development of FAIR-Relevant X-Ray Diagnostics Based on the Interaction of Lasers and Particle Beams with Matter”. In: *Dissertation zur Erlangung des Doktorgrades der Naturwissenschaften.*

Zhu, X. L. et al. (2016). “Dense GeV electron-positron pairs generated by laser in near–critical density plasmas”. In: *Nat. Commun.* 7, p. 13686.

Zhu, X. L. et al. (2020). “Extremely brilliant GeV g-rays from a two-stage laser-plasma accelerator”. In: *Sci. Adv.* 6, p. 7240.

Acknowledgements

Gloria in excelsis Deo! (*Evangelium secundum Lucam, 2.14*)

First of all, I heartily thank my Almighty Lord for His grace and showering all His blessing of me on my way.

On completion of this dissertation I wish to deeply thank the various people, who provided me with useful assistance and guidance throughout my doctoral research.

I would like to express my sincere thanks to Prof. Dr. Joachim Jacoby and Prof. Dr. Olga Rosmej for giving me the possibility to be a part of the plasma physics research group at Goethe University Frankfurt and to do my PhD. I feel grateful to my supervisor, Prof. Dr. Olga Rosmej for her advices and guidance of this project and also for reading the whole book manuscript, making valuable suggestions.

Next, I would like to acknowledge the various interesting scientific discussions and the productive collaboration with Dr. Alexey Sokolov, who has been a great support for many theoretical questions and especially for the simulations with MC code FLUKA.

I would like to thank all those people who assisted me in completing the experimental research and provided their precious opinions. Especially, I have to pay a tribute to my colleague Felix Horst for his assistance during the work with TLD diagnostics in laboratory, giving me detailed information concerning the measurements and interpretation of the experimental results. I am also thankful to Dr. Ekaterina Kozlova for providing the TLD cards and assistance by the usage of TLD reader. Furthermore, I would like to thank all the colleagues with whom I worked over my PhD years and especially Dr. Sero Zähter for discussions about electron diagnostics and his responsive help in various matters.

I can't finish this thesis without expressing my extreme gratitude to my parents, who emphasized the importance of education, hard work and persistence, my dear sister who gave me the moral support to complete my study and my grandmother (she is unfortunately no longer with us), who instilled in me the inspiration to set high goals and the confidence to achieve them. They have never stopped believing in me.

And finally, I would like to give my special thanks to my husband Alexander Zahn for understanding, supports, inspiration and even sacrifice of his own interests. His patient love enabled me to complete this work. Without his care and consideration, this dissertation would likely not have matured.

Eidesstattliche Erklärung

Hiermit erkläre ich an Eides statt, dass diese Arbeit bisher von mir weder dem Fachbereich Physik der Johann Wolfgang Goethe Universität in Frankfurt am Main noch einer anderen wissenschaftlichen Einrichtung zum Zwecke der Promotion eingereicht wurde. Ferner erkläre ich, dass ich die vorliegende Arbeit selbständig und ohne fremde Hilfe angefertigt und alle Stellen, die wörtlich oder annähernd wörtlich aus Veröffentlichungen genommen sind, als solche kenntlich gemacht habe. Die Erklärung bezieht sich auch auf in der Arbeit gelieferte Zeichnungen, Skizzen, bildliche Darstellungen und dergleichen.

Frankfurt am Main, den 10.12.2022 Nadiya Zahn